DESY–THESIS–2001–044
September 2001.

Spin-Orbit Maps and Electron Spin Dynamics for the Luminosity Upgrade Project at HERA

Gun Zara Mari Berglund

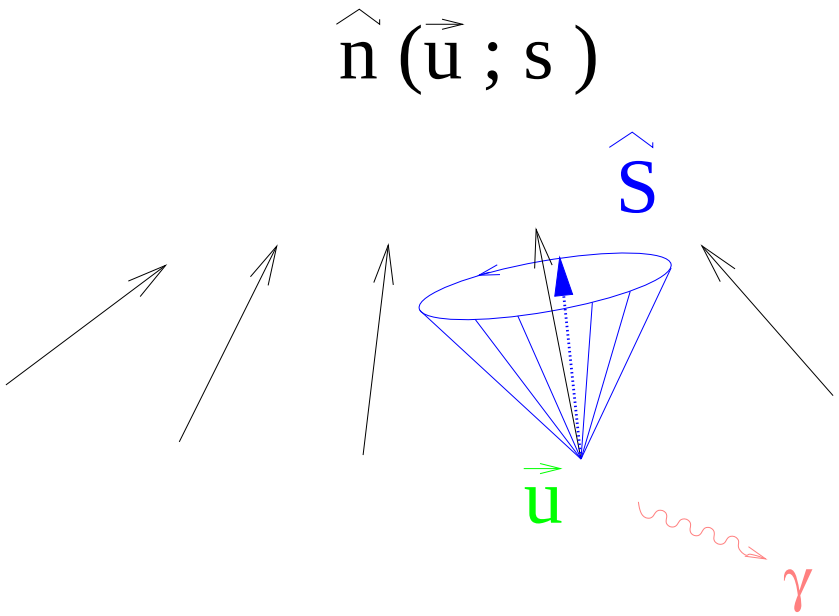

A thesis submitted in partial fulfillment of the requirements for the degree of Doctor of Philosophy [1]

at the

ALFVÉN LABORATORY
DIVISION OF ACCELERATOR TECHNOLOGY
ROYAL INSTITUTE OF TECHNOLOGY

STOCKHOLM, June 2001

[1] Updated version of the original (ISBN 91–7283–118–9).

For Max

and -ie

Abstract

HERA is the high energy electron(positron)–proton collider at Deutsches Elektronen–Synchrotron (DESY) in Hamburg. Following eight years of successful running, five of which were with a longitudinally spin polarized electron(positron) beam for the HERMES experiment, the rings have now been modified to increase the luminosity by a factor of about five and spin rotators have been installed for the H1 and ZEUS experiments. The modifications involve nonstandard configurations of overlapping magnetic fields and other aspects which have profound implications for the polarization. This thesis addresses the problem of calculating the polarization in the upgraded machine and the measures needed to maintain the polarization. A central topic is the construction of realistic spin–orbit transport maps for the regions of overlapping fields and their implementation in existing software. This is the first time that calculations with such fields have been possible. Using the upgraded software, calculations are presented for the polarization that can be expected in the upgraded machine and an analysis is made of the contributions to depolarization from the various parts of the machine. It is concluded that about 50 % polarization should be possible. The key issues for tuning the machine are discussed. The last chapter deals with a separate topic, namely how to exploit a simple unitary model of spin motion to describe electron depolarization and thereby expose a misconception appearing in the literature.

Descriptors

electron polarization, luminosity upgrade, overlapping fields, spin rotators, numerical spin–orbit maps, spin diagnostics, unitary model

Acknowledgements

My first dedication goes to my uncle Professor emeritus S. Berglund, without whom I probably would never have come to study physics. Already when I was a young child he kindled my interest in the natural sciences, although I have to admit that this interest was of a more philosophical nature to begin with.

I dare say, that my road through the world of science has been unusually squiggly for a PhD student. I started off at the The Svedberg Laboratory in Uppsala working on my Diploma on the Gustaf Werner cyclotron. After my graduation I moved to the Alfvén Laboratory (ALA) at the Royal Institute of Technology in Stockholm, but I continued to work in Uppsala on the CELSIUS storage ring under the supervision of D. Reistad, whom I owe many thanks. I then had the opportunity to spend six months at the Indiana University Cyclotron Facility (IUCF) in Bloomington, USA, working together with Professor S. Y. Lee, a visit which resulted in my first publication. Shortly after I came back from the US I happened to meet the scientists F. Willeke and G. Hoffstätter from the Deutsches Elektronen–Synchrotron (DESY) in Hamburg at a conference and they invited me to come to DESY. Thanks to a special arrangement between ALA and DESY, and to my very sympathetic supervisor S. Rosander at ALA, I have been able to carry out the last few years of my education at DESY. There I have been working on a large scale project for the upgrade of the electron(positron)/proton collider HERA. My area of interest has been electron beam polarization and I have been working closely together with a small team of experts studying the impact of the mentioned upgrade on the electron(positron) polarization, which is also the subject of my thesis.

I am most indebted to my supervisor and "polarization guru" at DESY Dr. D. P. Barber. His genuine interest in the subject of spin polarization dynamics has been a constant source of inspiration. Many, many thanks also goes to E. Gianfelice–Wendt who I am very happy to have had the opportunity to work with during my years at DESY. I would also like to mention my nice colleagues with whom I have shared my office at DESY: C. Montag, R. Glanz, M. Vogt, M–P. Zorzano and Š. Stres, and the entire Machine Physics group.

I am indebted to the Foundation BLANCEFLOR Boncompagni–Ludovisi, née Bildt for economical support, making my travels between Uppsala and Hamburg possible. A special thanks to L. Thuresson for repeatedly helping me with my Linux installation at home. And last but not least I want to thank my Tom for being so patient and seeing this through with me.

Contents

1 Introduction **6**

2 The HERA Luminosity Upgrade Project **11**

2.1 General 11

2.2 Upgrade concept and parameters 12

3 Radiative Spin Polarization **19**

3.1 Phenomenology 19

3.2 Methods of calculation 28

3.2.1 Linear approximation — the SLIM formalism 34

3.2.2 Alternative formulations of the linear radiative spin theory 39

3.2.3 Synchrotron sidebands 41

3.2.4 Higher order Monte Carlo simulations — SITROS 42

4 HERA Polarization in Light of the Upgrade **47**

4.1 Electron polarization — experience gathered at HERA 47

4.2 Impact of the upgrade on polarization 51

4.3 Polarimetry at HERA 52

4.3.1 Transverse Polarimeter 54

4.3.2 Longitudinal Polarimeter 55

5 Models for the new Interaction Regions **57**

5.1 Sandwich model for SLIM/SLICK 57

5.2 Maps from numerical integration 60

5.2.1 H1 and ZEUS solenoid field models 65

5.2.2 Implementation into SITROS 68

6 Polarization calculations for the upgraded HERA **73**

6.1 Limitations and remedies 73

6.1.1 Coupling compensation 74

6.1.2 Correction of distorted IR design trajectories 84

6.1.3 Local $\hat{n}_0$ tilt correction 87

6.1.4 Spin matching in the new lattice 88

6.2 Polarization in the non–distorted machine 89

6.3 Closed orbit distortions and misalignments 97

6.3.1 Investigations without solenoids 97

6.3.2 Investigations with solenoids 98

6.4 Effect of RF frequency shift on the polarization 101

6.5 Beam-beam effects on spin 102

7 A Unitary Model of Spin Depolarization **111**

7.1 The single resonance model (SRM) 112

7.2 The double resonance model 114

8 Conclusions **117**

A Equations of motion **119**

A.1 Orbit motion 119

A.2 Spin motion 121

B Characteristic times of processes **123**

C Updates of the SITROS code **125**

D Symplectification of maps via generating functions **127**

Chapter 1

Introduction

HERA is a 6.3 km long electron(positron)/proton double ring collider situated at Deutsches Elektronen Synchrotron, DESY, in Hamburg, Germany. The machine was commissioned during 1991 and has been providing luminosity since June 1992. The electron(positron) beam[1] is accelerated to an energy of 27.5 GeV and, since 1998, the proton beam energy used for routine operation has been 920 GeV. The ring has four experimental regions. The beams collide head–on at two interaction points, IP North and IP South, where the H1 and ZEUS experiments are located. Two further experimental stations make separate use of the $e^{+/-}$ and proton beams. HERMES, which is located in the East straight section, has since 1995 utilized the *longitudinally polarized* $e^{+/-}$ beam in collisions with a polarized gas target. The relatively new (1998) HERA B experiment, located in the West straight section, uses the proton beam halo interacting with a wire target. The physics studied at HERA spans a wide field including probing the internal structure of the proton and studies of the fundamental interactions between particles (H1 and ZEUS), measurements aiming to resolve the spin distributions of quarks and gluons in nucleons[2] (HERMES), and studies of CP–violation in B–meson systems (HERA B). The layout of HERA and the pre-accelerators is depicted in Figure 1.

The instantaneous polarization vector of an ensemble of N particles is defined as the ensemble average of the spin expectation values $\vec{S}_i$ ($\forall\, i \in \{1, \ldots, N\}$) through

$$\vec{P}(t) \equiv \frac{1}{N}\frac{2}{\hbar}\sum_{i=1}^{N}\vec{S}_i(t) = \langle \vec{S} \rangle_{ens}\,, \tag{1.1}$$

and the fact that it is possible to have polarized beams for HERMES is rooted in a discovery made at the beginning of the 1960's. In 1961 Ternov, Loskutov and Korovina [TLK62] made the first prediction of *radiation induced polarization* of electrons and positrons, caused by the quantum emission of synchrotron radiation when these particles travel in electromagnetic fields. This work was followed up a couple of years later by Sokolov and Ternov [ST64]. According to their theory, electrons circulating in the magnetic guide field of a storage ring gradually become polarized antiparallel to the field, whereas positrons become polarized parallel to the field. This naturally occuring polarization has been termed "vertical" or "transverse" polarization. Experiments soon followed and transverse, radiation induced polarization was first reported measured at the ACO storage ring in Orsay and at VEPP–2 in Novosibirsk [Be68, Ba72]. Since then high levels of vertical polarization in $e^{+/-}$ beams have been obtained at several high energy machines [Bb96]. This is largely due to work done in the late 70's and early 80's, especially at DESY [Ch81a, Br82, MR83, RS85, Bb85a], contributing to the practical

[1] In the following the abbreviation $e^{+/-}$ will be used to denote positrons and/or electrons.

[2] protons and neutrons

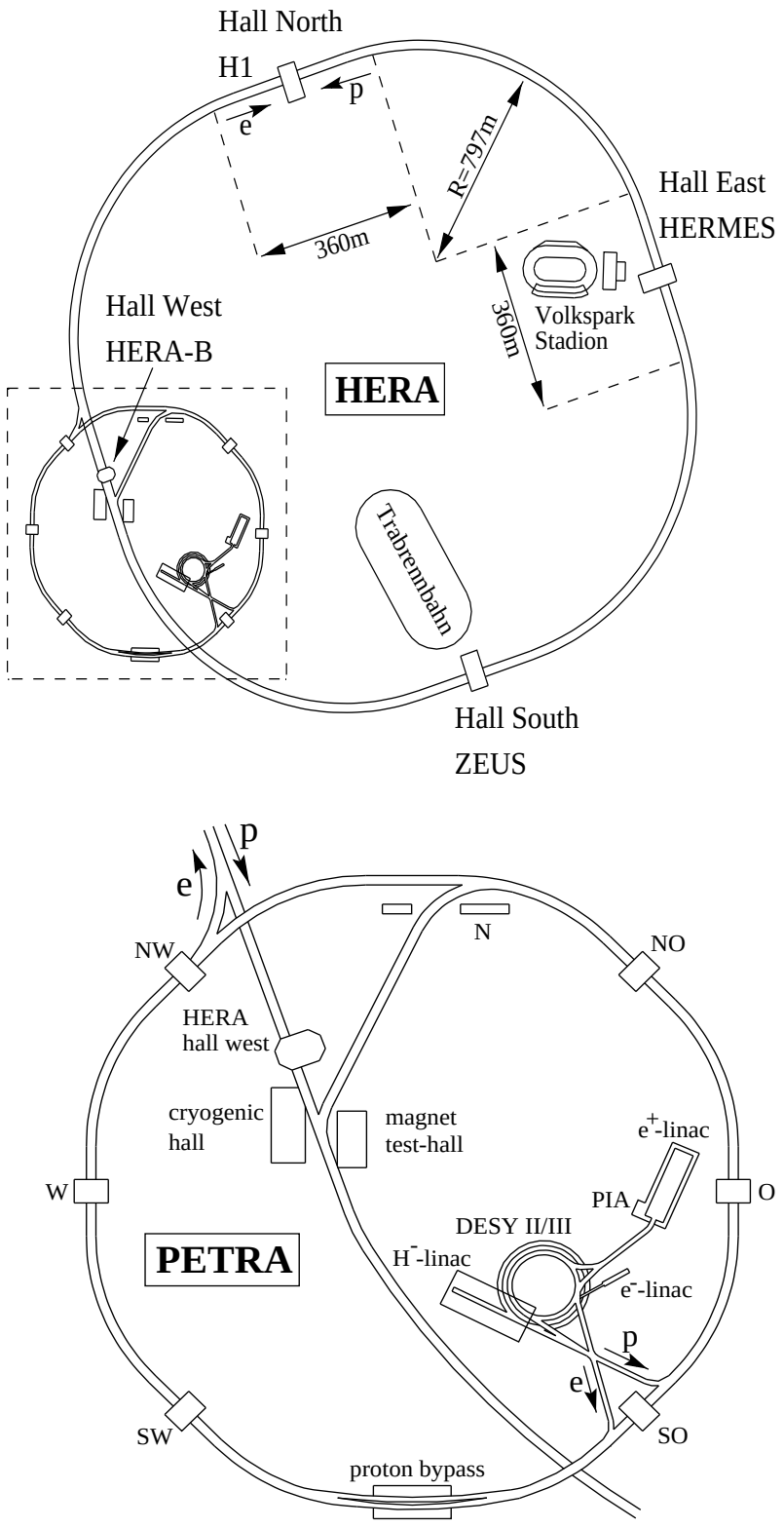

Figure 1.1: The HERA collider and the injector chain with PETRA.

realization of vertically, radiatively polarized beams, despite the inherent polarization limitations in real machines.

Unfortunately, although vertical polarization is useful as a means of making very precise beam energy calibrations (see for instance [Ar92]), it is not very attractive to experimentalists studying $e-p$ collisions. They require longitudinal polarization instead. This means that the natural vertical polarization must be rotated into the longitudinal direction just before an interaction point and then back to the vertical just after the interaction point, using special magnet configurations. A specific kind of such so called *spin rotators* will be described in some detail in Chapter 4. With the aid of spin rotators and with the implementation of a specially designed machine optic facilitating high polarization, using a technique which is also described in Chapter 4, longitudinal radiative electron polarization was achieved for the first time in the history of storage ring physics at the East IP of HERA in May 1994 [Bb95]. As already mentioned, HERMES has been using this unique feature of HERA since 1995 to study the spin structure of the nucleon. The spin of the nucleon can be broken down into four components

$$\frac{s_{_N}}{\hbar} = \frac{1}{2} = \frac{1}{2}(\Delta q_v + \Delta q_s) + \Delta g + L_{orb}$$

where Δq_v is the contribution from the valence quarks, Δq_s comes from the sea quarks, Δg is the gluon polarization and L_{orb} is a possible contribution from the orbital angular momentum of the partons. Measurements with HERMES have confirmed the original findings by the European Muon Collaboration (EMC) at CERN from 1988 [EMC88] that the total spin carried by the quarks only amounts to about 30 % of the nucleon spin. A special aspect of the HERMES experiment is that it, by the detection of the scattered hadrons in coincidence with the scattered leptons from deep inelastic scattering (DIS) processes, offers the possibility to pin down the spin contributions of the various quark flavours to the spin of the nucleon. Furthermore HERMES has been the first high energy physics experiment able to perform direct measurements of the gluon polarization. Crucial for these experiments is, apart from a highly specialized target and detector system, the provision of the high current longitudinally polarized $e^{+/-}$ HERA beam. The efficacy by these measurements for a given luminosity (see next chapter) scales like P_b^2 where P_b is the beam polarization.

As a tool for studying the internal structure of nucleons HERMES is, with its fixed target, limited to processes with centre of mass energies ($\sqrt{s}$) little more than 7 GeV. This has to be compared with the collision experiments H1 and ZEUS where $\sqrt{s} \approx 300$ GeV. Over the years, since these experiments started to collect data, H1 and ZEUS have contributed to the wealth of knowledge in elementary particle physics, especially on the inner structure of the proton and on the fundamental interactions between particles. DIS measurements at H1 and ZEUS show directly for the first time that at high momentum transfers, with Q^2 values[3] above 10^4 GeV^2, the electromagnetic and weak forces become similar in strength [Sc98]. However, despite the excellent performance of HERA in recent years (see Figure 2.1 in Chapter 2), the relatively low interaction rate has precluded detailed investigation of this hitherto unexplored high Q^2 region. An extension to smaller $x_{_B}$, which is the fractional momentum carried by the struck quark in a DIS scattering process (the so called Bjørken scaling variable), would open up new windows to QCD dynamics. There has therefore been a strong interest in increasing the kinematic range of the HERA experiments. The need for higher interaction rates has led to the decision to launch a *luminosity upgrade* of HERA. This requires the measures described in Chapter 2. The opportunity has also been taken to install two more pairs of spin rotators to serve H1 and ZEUS with longitudinal $e^{+/-}$ beam polarization.

There is also interest in storing polarized proton beams in HERA, which would add substantially to the physics potential of the collider. See [IRK96, pp99]. This however would require major and

[3] Q^2 is the negative square of the 4–momentum transfer.

costly modifications to both the preaccelerators and to HERA, and a decision on whether or not this will be implemented has not yet been taken. A study of the feasibility of providing polarized proton beams for HERA is given in [Vo00, Ho00a].

This work is not a document on high energy physics, but instead presents a study of the implications of the HERA luminosity upgrade on the $e^{+/-}$ polarization and suggested measures needed to obtain a high degree of longitudinal polarization for H1 and ZEUS and, in addition, maintain the high polarization for HERMES after the upgrade. The reader interested in the high energy physics should consult the literature from the HERA experiments.

The work is structured as follows. Chapter 2 gives an overview of the luminosity upgrade project and presents the most important machine parameters in this upgrade. In Chapter 3 an introduction to the necessary theoretical concepts for describing radiative spin polarization is given. A summary of the experience gathered at HERA on operation with $e^{+/-}$ polarization and a presentation of the impact that the upgrade will have on the latter is found in Chapter 4. The HERA polarimeters and their upgrade are also presented in Chapter 4. Methods developed for modelling the complicated field configurations in the new interaction regions are described in Chapter 5. Polarization calculations made for the upgraded HERA using these models in various computer codes are presented in Chapter 6. Chapter 7 contains an alternative model for describing polarization resonance phenomena, applicable under certain conditions, and is an extension of an earlier study to which the author has contributed. Finally, the conclusions are presented in Chapter 8.

A few words on conventions chosen for this thesis are in order. For Cartesian coordinates, the generic labelling (x, z, s) is used for right–handed systems. Note that this implies that quantities referring to the vertical plane are labeled with a z, whereas many authors prefer to use y. Variable length vectors are symbolized by arrows (e.g. $\vec{P}$), whereas unit vectors are symbolized by "hats" (e.g. $\hat{P}$). [4] SI units are used throughout. In Chapter 7 it was not possible to set the Pauli matrices occurring in some exponents in boldface font. Due to the finite number of Latin and Greek letters, the same symbols are sometimes used for different physical and mathematical quantities. The meaning should however always be clear from the context.

[4] Note that the quantity $\hat{a}$ which occurs in Chapter 7 is not a unit vector, but the symbol has been used so as to agree with a notation from the literature.

Chapter 2

The HERA Luminosity Upgrade Project

2.1 General

The HERA collider is a unique facility, the first of its kind, bringing high energy charged particle beams of totally different species into collision. The performance of HERA has steadily improved since the startup and has now reached or surpassed design goals for most key parameters. The luminosity delivered by HERA to the colliding beam experiments over the years illustrates this progress well, see Figure 2.1. In 2000 the peak luminosity exceeded the design value of $1.5 \cdot 10^{31}$ cm^{-2} s^{-1}. The averaged specific luminosity per bunch of $7.4 \cdot 10^{29}$ cm^{-2} s^{-1} mA^{-2} achieved in the same year is more than twice the original design value. The corresponding integrated luminosity delivered by HERA reached a value close to 70 pb^{-1}.

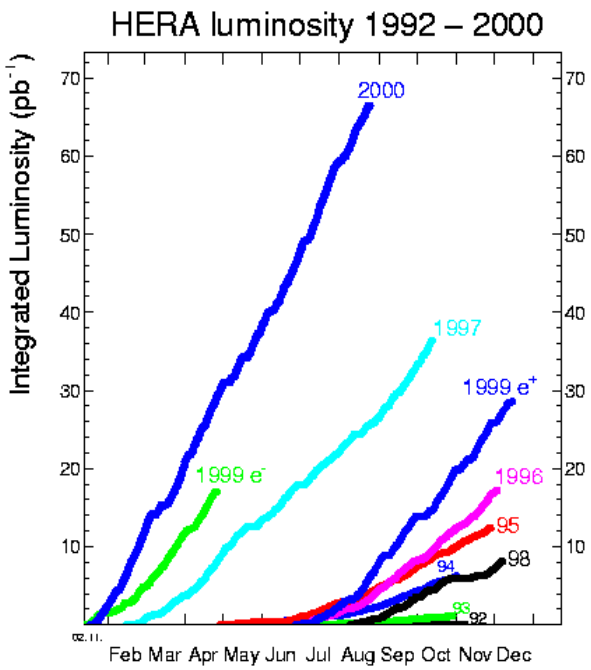

Figure 2.1: Integrated luminosity delivered by HERA to ZEUS versus time.

The margin for pushing these numbers further, given the original layout of the machine, has today largely been exhausted. As indicated in Chapter 1, there has however been a strong interest from

the users to widen the domain of physics accessible with HERA. During a workshop in 1995/1996 on "Future Physics at HERA" [IRK96] a discussion was held concerning the fields of high energy physics that could be reached within the potential of an upgraded HERA, if the machine could deliver an integrated luminosity of 1 fb^{-1} over an operational period of five years. Such a luminosity would make possible unique and sensitive tests of electroweak physics, QCD and physics beyond the Standard Model. Furthermore, the availability of longitudinally polarized electron and positron beams at the colliding beam experiments would add important features to the physics potential of the accelerator.

In order to match the investigations of the user groups, the HERA workshop also included a working group looking into the machine aspects of a luminosity upgrade of HERA. The conclusion arrived at by this group was that the most promising way of achieving the desired luminosity increase would be to reconstruct the interaction regions (IRs) so as to allow a substantial decrease of the β–functions of the beams in both transverse planes at the interaction points. A preliminary version of such a redesign of the IRs was layed out in the proceedings.

The work on the redesign of the HERA IRs and connected issues was continued after the "Future Physics at HERA" workshop by physicists from the DESY machine group and members of the H1 and ZEUS collaborations. Many different issues have been addressed such as magnet design and construction, lattice design, synchrotron radiation absorbers, vacuum systems, mechanical support structures, instrumentation, $e^{+/-}$ beam stability, and polarization. The goal of the luminosity upgrade project has been to devise a machine that allows an increase of the luminosity by a factor of about 5 compared to the original HERA design, while still delivering a high degree of longitudinal spin polarization to the HERMES experiment and, additionally, delivering longitudinal polarization to H1 and ZEUS. The project was officially approved in December 1997 and in September 2000 HERA was shut down for the rebuilding of the machine in accordance with the new design.

2.2 Upgrade concept and parameters

The HERA luminosity upgrade is described in detail in a project design report from August 1998 [Sc98]. To put the following chapters in context, and especially Chapter 6 that contains discussions on, and results of, polarization simulations for the HERA–e upgrade lattice, the general concept and the most important parameters of the luminosity upgrade will be presented here.

Apart from the beam energies the most important parameter at a colliding beam facility, as far as high energy physics is concerned, is the counting rate, $\mathcal{R}$. The counting rate for a particular process is expressed in terms of the *luminosity* $\mathcal{L}$, which describes the geometry and characteristics of the incident beams, by

$$\mathcal{R} = \sigma \, \mathcal{L} \, \mathcal{A} \tag{2.1}$$

The quantity σ is the total cross section for the process and $\mathcal{A}$ is the corresponding acceptance of the detector. The luminosity of HERA can be written as

$$\mathcal{L} = \frac{N_e N_p N_{b,col} \, f_{rev}}{2\pi \sqrt{\sigma_{xe}^2 + \sigma_{xp}^2} \sqrt{\sigma_{ze}^2 + \sigma_{zp}^2}} \tag{2.2}$$

where N_e is the number of leptons per bunch, N_p is the number of protons per bunch, $N_{b,col}$ is the number of colliding bunches per beam [1], f_{rev} is the revolution frequency and $\sigma_{x,z;e,p}$ are the rms beam

[1] In HERA a small number of non–colliding "pilot" bunches are used for background correction of the luminosity measurement.

sizes at the IP of the lepton and proton beams respectively. In order to understand the concept chosen for boosting the luminosity in HERA, it is instructive to write the luminosity in terms of the quantities limiting it.

The beam dynamics in an $e^{+/-}$ ring is strongly influenced by the emission of synchrotron radiation. Moreover, the energy lost per turn by an electron(positron) scales like E^4 where E is the energy. Thus the achievable $e^{+/-}$ energy and the beam current $I_e = eN_e N_{b,tot} f_{rev}$ (where $N_{b,tot}$ is the total number of lepton bunches, including pilot bunches) are restricted by the available RF power. Measures have been taken to soften this constraint in HERA by installing more RF accelerating cavities, but the high costs associated with a major upgrade of the RF system prevents this option from being extended further. At the highest energies there are also difficulties in obtaining stable beam conditions for the design current of 58 mA. In practice this means that the operating $e^{+/-}$ energy in HERA after the upgrade will be lower than the design value of 30 GeV. However, the need for longitudinally polarized beams puts a lower limit on the $e^{+/-}$ beam energy of approximately 27 GeV. I will elaborate on this point in Chapter 6.

For high energy physics an increase in luminosity is often equivalent to an increase in the energy. In 1998 the proton beam energy was successfully increased from the original design value of 820 GeV to 920 GeV. A further increase bringing the energy up to 1 TeV is not feasible however, since the superconducting proton magnets cannot be operated with sufficient safety at such high energy levels. Owing to space charge effects in the injector chain, especially in DESY III, the number of protons per bunch is restricted. The maximum beam "brightness", given here as N_p/ε_N^p, with ε_N^p being the normalized proton beam emittance, therefore poses another limitation to the attainable luminosity in HERA.

The experience accumulated from years of running colliders such as HERA shows that matching of the $e^{+/-}$ and proton beam sizes, as well as alignment of the beams at the IPs, are crucial for the luminosity [BW93]. Matching and alignment are necessary for reducing the nonlinear effects of the beam–beam interaction. In particular the proton beam in HERA suffers if the matching is poor, leading to emittance blowup, short lifetimes and large backgrounds. Hence

$$\sigma_{ye}^* = \sigma_{yp}^* = \sqrt{\varepsilon_{ye}\beta_{ye}} = \sqrt{\varepsilon_{yp}\beta_{yp}} = \sigma_y^* \tag{2.3}$$

where β is the envelope function of Courant and Snyder [CS58] and $\varepsilon_{y;e,p}$ are the $e^{+/-}$ and proton beam emittances, respectively. The general subscript y is used to denote either the horizontal plane x, or the vertical plane z. The superscript * is the conventional way of denoting a beam optical quantity at an IP. Imposing the restriction (2.3), together with the fact that $\varepsilon_{xp} \simeq \varepsilon_{zp}$, on the proton emittance enables the luminosity to be reexpressed thus

$$\mathcal{L} = \frac{\gamma_p}{4\pi e} \frac{I_e}{\sqrt{\beta_{xp}^* \beta_{zp}^*}} \frac{N_p}{\varepsilon_N^p} \tag{2.4}$$

where γ_p is the proton Lorentz factor.

From the above argumentation it is clear that the only feasible way to increase the luminosity is to decrease the proton β–functions at the IPs, and thus due to (2.3), the $e^{+/-}$ size at the IPs. However the β–functions in a drift space increase quadratically with distance s from the IP according to

$$\beta_y(s) = \beta_y^*(0) + \frac{s^2}{\beta_y^*(0)} \tag{2.5}$$

β^* is therefore limited from below by the need to accommodate the peaks of the transverse beam dimensions in the final focus magnets within the available aperture. Furthermore if β^* is made too

small, the β_y in the focusing quadrupoles will be so large that the necessary chromaticity correction becomes difficult.

It is important for the beam stability that the beams are separated early after collision. Moreover the $e^{+/-}$ beam must not be exposed to the strong focusing fields from the proton quadrupoles. In HERA, head–on collisions are achieved by bending the incoming $e^{+/-}$ beam into the path of the proton beam and then bending it out again after collision. This collision scheme is carried over to the new design. To achieve the strong focusing needed for small beam sizes at the IPs, and to obtain the early separation required, a solution employing superconducting separator magnets with gradient fields has been chosen. Such magnets have the advantage that they can be built with small outer dimensions while retaining relatively large apertures, thereby enabling them to be placed *partially inside* the experimental detectors — an unconventional solution. Note that the new IR design does not leave any space for the "anti–solenoids" which in the previous layout compensated for the effects of the experimental solenoids on orbit and spin motion. Part of this compensation will be taken over by correction coils contained within the superconducting magnets.

The first proton magnets are placed 11 m from the IPs. At this position the beams are separated by about 60 mm, which is sufficient to accommodate the first of the two proton septum quadrupoles. The maximum tolerable β–functions at this location, together with the apertures of the separator magnets, determine the minimum value of the proton β_y^*. The tight design, together with the matching condition, makes the horizontal $e^{+/-}$ beam size critical. However, it is planned to reduce the horizontal $e^{+/-}$ emittance in HERA from 41 nm rad to 20 nm rad, thereby allowing an aperture of $20\,\sigma_x$ to be maintained. The necessary emittance reduction can be achieved by increasing the focusing in the arcs or by changing the damping partition numbers via a small shift of the RF frequency. Simulations show [Ho99] that a combination of these two methods is advantageous. In the chosen solution the phase advance per FODO cell is increased from the pre–upgrade value of 60° to 72° and simultaneously the RF frequency is increased by about 250 Hz. For this choice of parameters the dynamic aperture is preserved. A discussion on the impact of the RF frequency shift on the polarization can be found in Chapter 6, Section 6.4.

A lower limitation on the proton beam size also comes from the so called "hourglass effect". Following eqn. (2.5), if the smallest of the proton β_y^* is comparable to the proton bunch length σ_s, the transverse dimension of the proton bunch varies strongly as the bunch passes through the IP. The average transverse dimension seen by an on–coming $e^{+/-}$ bunch can therefore be much larger than that suggested by the β_y^*, so that the gain in luminosity from the shrinking beam waist is counteracted by a loss from the broadening bunch tails.

Another important issue already mentioned is the beam–beam effect. Each time the electrons (positrons) collide with the counter–rotating proton beam, the particles are deflected by the electromagnetic forces of the on–coming bunches. These forces are very nonlinear functions of the transverse particle positions, but for small amplitudes the effect is merely a shift of the betatron tunes. This is quantified by the incoherent linear beam–beam tune shifts. The shifts per IP are given by

$$\Delta\nu_y^e = \frac{r_e N_p \beta_y^e}{2\pi\gamma_e(\sigma_x^p + \sigma_z^p)\sigma_y^p} \tag{2.6}$$

$$\Delta\nu_y^p = \frac{r_p N_e \beta_y^p}{2\pi\gamma_p(\sigma_x^e + \sigma_z^e)\sigma_y^e} \tag{2.7}$$

where r_e and r_p are the classical electron and proton radii respectively. Recent measurements in HERA [Bi99] indicate that the smaller emittances and higher beam currents [2] foreseen in the HERA

[2] The original design current for the $e^{+/-}$ beam of 58 mA has been kept as the goal for the upgrade. HERA has so far operated at a maximum of 86 % of this current.

upgrade can be tolerated without loss of luminosity. Note that the beam–beam tune shifts will be significantly higher than in the old optic. In particular the vertical tune shift of the $e^{+/-}$ beam will be large, $\Delta\nu_z^e = 0.052$ per IP. The betatron tune shifts and the nonlinear contributions from the beam–beam force influence the spin motion, and are therefore potential sources of depolarization. Further discussion on the topic is found in Chapter 6, Section 6.5.

The strong fields in the new IRs lead to strong synchrotron radiation emission from the $e^{+/-}$ beam, an important consideration that has required special attention during magnet and absorber design. The average bending radius of the separation magnets is decreased from the original 1200 m to 400 m and an estimated 28 kW of synchrotron radiation power will be produced in the detector areas. No collimation of the synchrotron radiation is possible in these regions implying that the geometry must be fashioned in a way that allows the radiation fan to pass through the detector areas with minimal losses and enter regions where it can be absorbed. The "warm" final focus magnets will therefore have gaps between the coils to let the synchrotron radiation through, and the first absorber will be located at 11 m from the IPs. To protect beamline and detector components from damage in case of spurious radiation losses in the detector areas, an extensive programme of measurement and correction of the orbit in the IRs is foreseen.

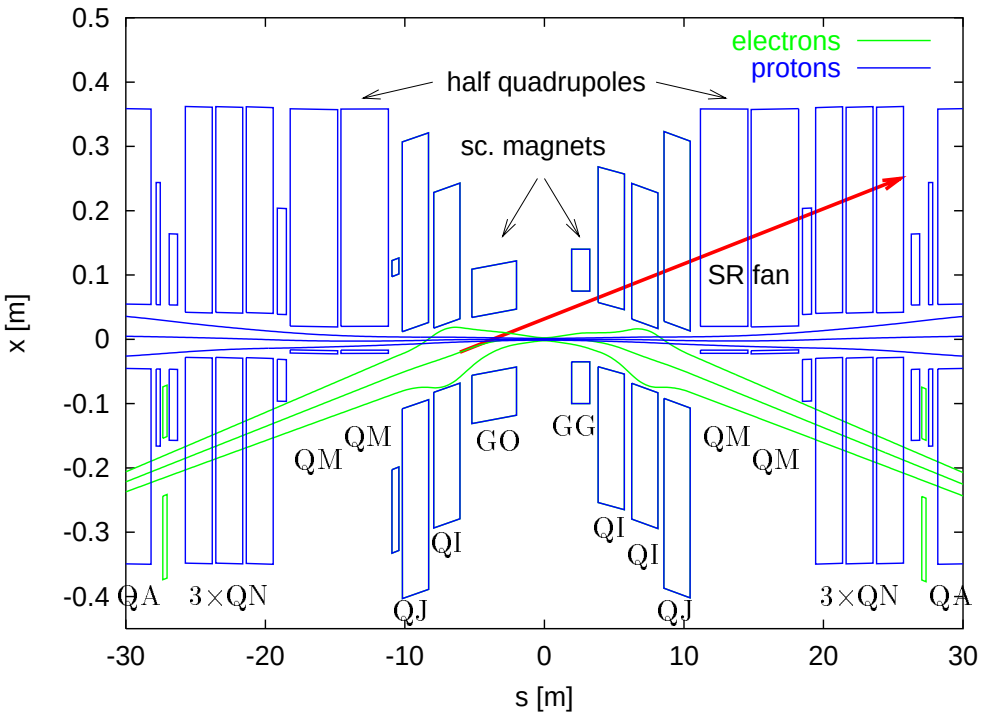

Figure 2.2: New interaction region layout. In the picture the $e^{+/-}$ are moving from left to right and the protons are moving from right to left.

The layout of the two upgraded interaction regions is illustrated in Figure 2.2. The superconducting separator magnets mentioned earlier (GO and GG) are placed inside the colliding beam detectors (not shown here, see instead the illustrations in Figures 5.1, 4.3 and 4.4) at a distance of 2 m on either side of the IPs. The geometry on the left side (upstream for the $e^{+/-}$ beam) and right side (downstream) differs, owing to asymmetries in detector component arrangements and the need to accommodate the synchrotron radiation fan on the downstream side. The layout is identical for both the North and South IRs. On the left side the 3.2 m long combined function magnet, GO, provides the necessary final focusing and a 8.2 mrad deflection to the $e^{+/-}$ beam. The right hand counterpart, GG, is only 1.3 m long and will nominally be used for deflection only. Following this magnet are two normalconducting combined function magnets of type QI, and one of type QJ. On the left side one of the QIs is missing.

	LUMINOSITY UPGRADE		DESIGN		2000 (average)	
	e-Beam	p-Beam	e-Beam	p-Beam	e-Beam	p-Beam
E [GeV]	27.5	920	30	820	27.5	920
I [mA]	58	140	58	160	45	95
N_{ppb} (N_e or N_p) $\times 10^{10}$	4.0	10.3	3.6	10.1	3.1	7.0
$N_{b,tot}$	189	180	210	210	189	180
$N_{b,col}$	174	174	210	210	174	174
ϵ_x [nm rad]	20	$\frac{5000}{\beta\gamma}$	48	$\frac{6000}{\beta\gamma}$	41	$\frac{5000}{\beta\gamma}$
ϵ_z/ϵ_x	0.17	1	0.05	1	0.1	1
β_x^* [m]	0.63	2.45	2.2	10.0	0.9	7.0
β_z^* [m]	0.26	0.18	0.9	1.0	0.6	0.5
$\sigma_x \times \sigma_z$ [μm^2]	112×30	112×30	325×46	262×83	192×50	189×50
σ_s [mm]	10.3	191	8.3	200 (85)	11.2	191
$\Delta\nu_x$/ IP	0.034	0.0015	0.019	$8 \cdot 10^{-4}$	0.012	0.0012
$\Delta\nu_z$/ IP	0.052	$4 \cdot 10^{-4}$	0.024	$6 \cdot 10^{-4}$	0.029	$3 \cdot 10^{-4}$
min. aperture [σ_x]	20	12	23	16	14	10
$\mathcal{L}_s$ [cm^{-2}s^{-1}mA^{-2}]	$1.8 \cdot 10^{30}$		$3.4 \cdot 10^{29}$		$7.4 \cdot 10^{29}$	
$\mathcal{L}$ [cm^{-2}s^{-1}]	$7.5 \cdot 10^{31}$		$1.5 \cdot 10^{31}$		$1.5 \cdot 10^{31}$	

Table 2.1: Luminosity upgrade parameters compared with the original design values and the averaged values for 2000 before the shutdown.

The GO magnet and the first QI on the right hand side are rotated around their midpoints in the horizontal plane by -4.1 mrad and $+2.4$ mrad respectively, to fit the apertures of the experiment detectors. The GG magnet is shifted outwards by 20 mm with respect to the detector axis (H1 and ZEUS) to provide the necessary space for the synchrotron radiation fan.

In the centre of the QJ magnet, at 9.5 m from the IP, the beam envelopes are completely separated. The first proton septum quadrupole, QM, located at 11 m is followed by a second QM, three QN type quadrupoles and two QA type quadrupoles. These proton magnets are specially designed to provide space for the $e^{+/-}$ beam and for the synchrotron radiation fan. The magnets that follow are all of HERA standard types. In the electron ring, the first standard focusing element after the IR combined function magnets is found at 55 m. A total of 4 new superconducting magnets and 56 new normalconducting magnets is needed for the luminosity upgrade.

An important feature of HERA I has been the possibility to collide the proton beam with either electrons *or* positrons. This possibility is maintained in the upgraded machine. The switching between lepton types will however be more difficult than in the old design. A change from electrons to positrons (or vice versa) requires the polarity of the separation magnets to be switched. This causes a disturbance of the trajectory and optic of the proton beam. While the optical errors can be compensated by changing quadrupole currents, there can be no local compensation of the proton trajectory by dedicated dipoles due to lack of space. Instead, some of the $e^{+/-}$ low–β magnets must be repositioned. In the solution adopted, the IPs are shifted horizontally with respect to the magnetic axes of the final focus superconducting magnets as well as with respect to the detector solenoids, the shift depending on lepton type and experiment solenoid.

By implementing the modifications described above the goal of the upgrade programme, an increase of the HERA luminosity by a factor of about 5, should be achieved. Table 2.1 summarizes the most important parameters of the luminosity upgrade. A comparison is also made with the original design and the beam parameters used immediately before the shutdown. The optical functions in the IRs for the upgrade lattice and the lattice used in the year 2000 runs are illustrated in Figures 2.3 and 2.4.

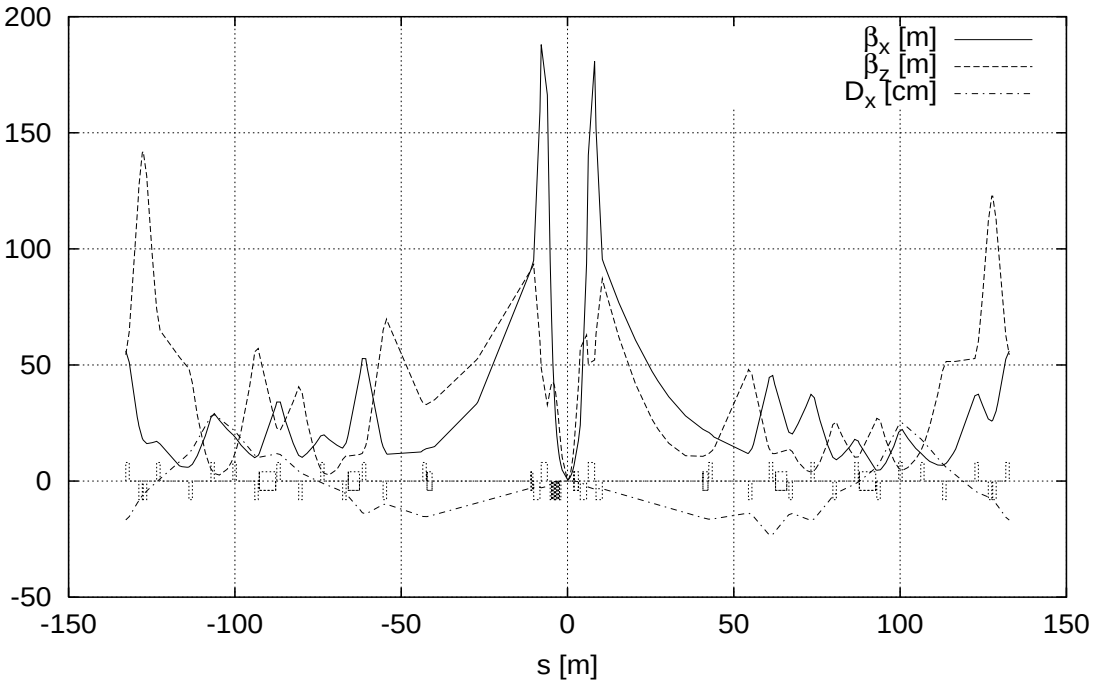

Figure 2.3: Optical functions for the e^- in the luminosity upgraded IRs. The boxes indicate magnet positions.

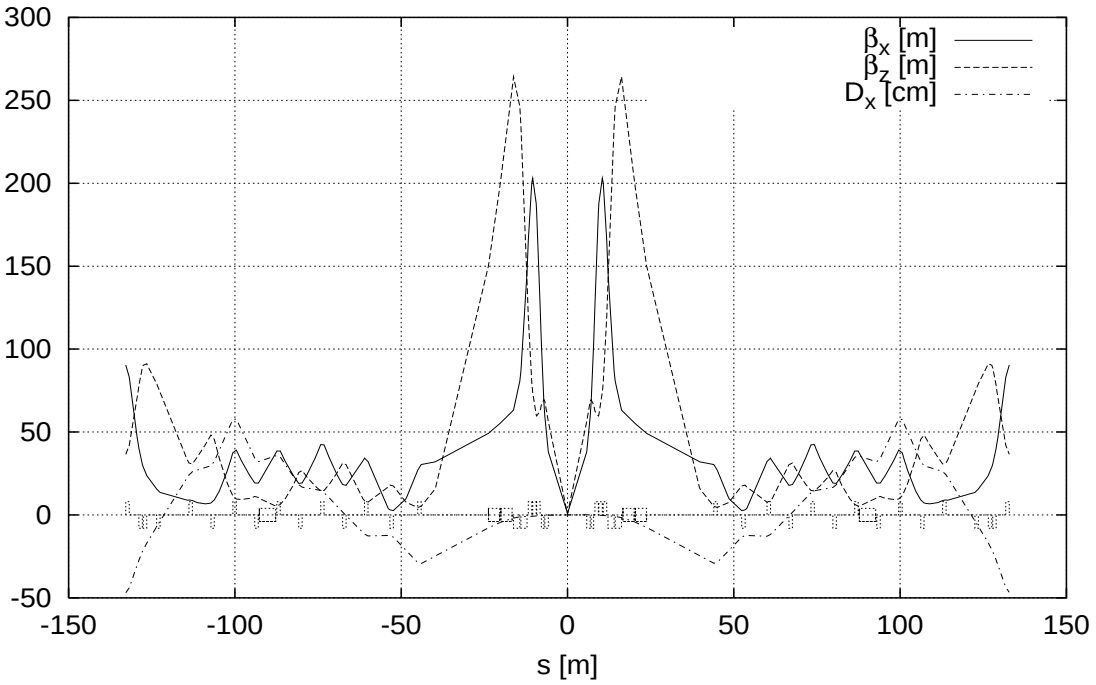

Figure 2.4: Optical functions for the e^- in pre–upgrade HERA IRs. The boxes indicate magnet positions.

Chapter 3

Radiative Spin Polarization

3.1 Phenomenology

The theory of radiative spin polarization in storage rings is now fairly well understood and has been treated in many publications. However, even for linear orbital motion the evaluation of the polarization from the resulting formulae can be a difficult task in practical cases. In the presence of strong nonlinearities in the orbital motion, as for example in the case of the beam–beam interaction, there is no analytical formalism. The aim of this section is to give an overview of the subject and to develop the terminology that will be used throughout this thesis to describe the physics of polarized electron and positron beams in storage rings. In particular I want to provide the necessary theoretical background in preparation for describing the impact that the luminosity upgrade will have on the $e^{+/-}$ beam polarization in HERA. Comparisons with non–radiative polarization theory and other relevant observations will be made.

The starting point for our description of polarized electrons in a storage ring is the concept of *spin–flip synchrotron radiation emission*, the celebrated Sokolov–Ternov effect [ST64]. When electrons (positrons) are moving on curved orbits, such as those prescribed by the magnetic guide fields of a storage ring, they emit synchrotron radiation. By calculating transition rates in terms of exact Dirac wavefunctions for electrons moving in a homogenous magnetic field, it is found that a very small fraction of the emitted photons will cause a spin–flip between the "up" and "down" quantum states of the electrons' spin. For electrons with spins initially aligned along the magnetic field the probabilities for transitions from the up–to–down state and down–to–up state differ, leading to the build–up of polarization antiparallel to the field. Positrons become polarized parallel to the field. The transition rates for electrons are

$$\begin{aligned} W_{\uparrow\downarrow} &= \frac{5\sqrt{3}}{16}\frac{r_e\gamma^5\hbar}{m|\rho|^3}\left(1+\frac{8}{5\sqrt{3}}\right) \\ W_{\downarrow\uparrow} &= \frac{5\sqrt{3}}{16}\frac{r_e\gamma^5\hbar}{m|\rho|^3}\left(1-\frac{8}{5\sqrt{3}}\right) \end{aligned} \tag{3.1}$$

where the arrows indicate the relative directions of the spin in the initial and final states. For positrons plus and minus signs are interchanged here and elsewhere. An initially unpolarized stored $e^{+/-}$ beam gradually becomes polarized following the exponential law

$$P_{ST}(t) = P_{eq,ST}\left(1-e^{-t/\tau_{ST}}\right) \tag{3.2}$$

where the maximum attainable (equilibrium) polarization is given by

$$P_{_{eq,ST}} = \frac{W_{\uparrow\downarrow} - W_{\downarrow\uparrow}}{W_{\uparrow\downarrow} + W_{\downarrow\uparrow}} = \frac{8}{5\sqrt{3}} \simeq 0.9238 \tag{3.3}$$

and the build–up rate is

$$\tau_{_{ST}}^{-1} = \frac{5\sqrt{3}}{8} \frac{r_e \gamma^5 \hbar}{m|\rho|^3} \tag{3.4}$$

Here ρ is the (local) radius of curvature of the orbit, and the other symbols have their usual definitions. It should be emphasized that due to the smallness of the spin–flip transition probability [1], the time scale of polarization build–up is large compared to other processes taking place, such as synchro–betatron oscillations and radiation damping. The build–up rate depends strongly on energy (γ^5) and bending radius (ρ^{-3}). Its reciprocal, the build–up time $\tau_{_{ST}}$, is typically of the order of minutes or hours. For HERA at an operating energy of 27.5 GeV is $\tau_{_{ST}} \approx 40$ min.

A generalization of the Sokolov–Ternov build–up rate to electrons moving in arbitrary magnetic field configurations and with spins initially aligned along an arbitrary unit vector $\hat{\xi}$, has been given by Baier and Katkov using semiclassical methods [BK67]

$$\tau_{_{BK}}^{-1} = \tau_{_{ST}}^{-1} \left(1 - \frac{2}{9} (\hat{\xi} \cdot \hat{s})^2 \right) \tag{3.5}$$

where $\hat{s}$ denotes the direction of motion.

A second fundamental property of an electron (positron) moving in the electromagnetic guide fields of a storage ring is the *spin precession*. This physical phenomenon also applies to other particles, such as protons and deuterons in which cases synchrotron radiation emission is normally negligible so that spin–flip induced polarization is usually not observed.

Neglecting radiation, the evolution of the centre–of–mass spin expectation value, $\widehat{S}$, [2] of a relativistic charged particle moving in the electromagnetic fields of a storage ring is contained in the Thomas–Bargmann–Michel–Telegdi (T–BMT) equation [Th27, BMT59]

$$\frac{d\widehat{S}}{dt} = \vec{\Omega}_{_{BMT}}(\vec{r}, \dot{\vec{r}}; t) \times \widehat{S} \tag{3.6}$$

where

$$\vec{\Omega}_{_{BMT}} = -\frac{e}{\gamma m} \left((1 + a\gamma)\, \vec{\mathcal{B}} - \frac{a\gamma^2}{1+\gamma} \frac{1}{c^2} \left(\dot{\vec{r}} \cdot \vec{\mathcal{B}} \right) \dot{\vec{r}} - \left(a\gamma + \frac{\gamma}{1+\gamma} \right) \dot{\vec{r}} \times \frac{\vec{\mathcal{E}}}{c^2} \right)$$

$\vec{\Omega}_{_{BMT}}$ is the *spin precession vector* evaluated in the laboratory frame, with time t used as the independent variable. $\vec{\mathcal{B}}$ and $\vec{\mathcal{E}}$ are the magnetic and electric fields given in this frame. The position vector $\vec{r}$ and its time derivative $\dot{\vec{r}}$ evolve according to the Lorentz equation [Ja98]. The parameter

[1] For the HERA electron ring at an energy of $E \sim 27.5$ GeV, the ratio of the probabilities $\frac{\Pi_{spin-flip\ rad.}}{\Pi_{non-flip\ rad.}}$ is of the order $1 \cdot 10^{-10}$.

[2] For the rest of this thesis we will work with the vector $\widehat{S} = \frac{2}{\hbar}\vec{S}$. This vector will often be referred to as simply "the spin".

$a = (g-2)/2$ is the particle's gyromagnetic anomaly, which for electrons and positrons has the numerical value $a \approx 0.0011597$, while for protons the value is approximately 1.7928. In the proton case, the symbol G instead of a is commonly used to represent the gyromagnetic anomaly. By expressing the T–BMT equation in terms of components perpendicular and parallel to the particle momentum $\vec{p}$ and comparing with the Lorentz equation of motion (ignoring the electric fields, which normally in storage rings are non–zero only in the accelerating cavities)

$$\frac{d\vec{p}}{dt} = -\frac{e}{\gamma m}\vec{\mathcal{B}}_\perp \times \vec{p} \tag{3.7}$$

$$\frac{d\widehat{S}}{dt} \simeq -\frac{e}{\gamma m}\left((1+a\gamma)\,\vec{\mathcal{B}}_\perp + (1+a)\,\vec{\mathcal{B}}_{||}\right) \times \widehat{S} \tag{3.8}$$

several conclusions can be drawn. From eqs. (3.7) and (3.8) it is seen that for motion perpendicular to the field, the spin precession around $\vec{\mathcal{B}}_\perp$ is a factor $(1+a\gamma)$ larger than the corresponding orbit deflection

$$\delta\theta_{spin} = (1+a\gamma)\,\delta\theta_{orbit} \tag{3.9}$$

The term "1" corresponds to the relativistic cyclotron frequency, $\omega_c = -\frac{e\mathcal{B}_\perp}{\gamma m}$, and is eliminated in a transformation to a frame rotating with the particle orbit according to eqn. (3.7). The remaining factor $a\gamma$, which is referred to as the *naïve spin tune*, is simply the instantaneous rate of precession in the rotating frame. In a perfectly flat ring, while particles complete a full turn with 2π of orbit deflection, the spins are rotated $a\gamma$ times around the vertical direction with respect to the orbit. Inspection of eqn. (3.8) also reveals that the precession rate around a fixed transverse field at high energies is essentially independent of energy ($1/\gamma \ll 1$), whereas for longitudinal fields (as in solenoids) the precession rate is inversely proportional to the energy, an important observation when it comes to the design of spin manipulating devices such as spin rotators and Siberian Snakes [Mo84]. For spin motion in purely transverse magnetic fields a few more points can be noted using HERA as an example:

- Relation (3.9) implies that an orbit deflection angle of 1 mrad in a transverse magnetic field for electrons (positrons) operated at the HERA nominal energy of 27.5 GeV gives rise to a spin rotation of approximately 3.6°. For protons operated at 920 GeV the same orbit deflection leads to a spin rotation of 100°.
- The naïve spin tune $a\gamma$ increases for electrons (positrons) by one unit every $\Delta E \approx 441$ MeV ($= \frac{m_e c^2}{a}$), whereas for protons the corresponding value is $\Delta E \approx 523$ MeV ($= \frac{m_p c^2}{G}$). For HERA–e at 27.5 GeV, $a\gamma \approx 62.5$.
- For a fixed transverse orbit deflection (and hence fixed ratio $\vec{\mathcal{B}}_\perp/\gamma$), the spin precession rate increases linearly with energy. Spin motion is therefore more sensitive to (transverse) orbit distortions at higher energies.

The laboratory frame, in which the T–BMT equation was originally derived, is not a suitable reference frame for the description of orbital motion in circular accelerators. Therefore, as a standard procedure, a transformation is made to a reference frame where the particles are described with respect to a moving curvilinear coordinate system, associated with a fictitious ideal particle. The six dimensional vector describing the particle positions in *phase space* in this reference frame will be denoted by $\vec{u}$. Here we will choose the coordinates such that $\vec{u} \equiv (x, x', z, z', \ell, \delta)$, where x, x', z, z' are

the horizontal and vertical (transverse) positions and directions and ℓ, δ are the longitudinal deviation and fractional energy deviation with respect to the synchronous particle (at the centre of the bunch) respectively. At high energies the coordinate pairs (x, x'), (z, z') and (ℓ, δ) are nearly canonically conjugate and we can write $x' \simeq \frac{p_x}{p}$ and $z' \simeq \frac{p_z}{p}$, except inside solenoids where these relationships have to be replaced by $x' \simeq \frac{p_x}{p} + z\,\frac{ec}{2E_0}\mathcal{B}_s^{d.o}$ and $z' \simeq \frac{p_z}{p} - x\,\frac{ec}{2E_0}\mathcal{B}_s^{d.o}$, where $\vec{\mathcal{B}}^{d.o} = \left(\mathcal{B}_x^{d.o}, \mathcal{B}_z^{d.o}, \mathcal{B}_s^{d.o}\right)$ is the magnetic field on the design orbit. [3] The change of coordinates means that $\vec{\Omega}_{BMT}(\vec{r}, \dot{\vec{r}}; t)$ must be transformed to a corresponding $\vec{\Omega}(\vec{u}; s)$, where s is the distance along the design orbit, and that the components of the spin vectors now refer to the curvilinear coordinate system $\widehat{S} = (S_x, S_z, S_s)^T$. The details of the transformation are outlined in Appendix A. After transformation to curvilinear coordinates, the T–BMT equation of spin motion reads as

$$\frac{d\widehat{S}}{ds} = \vec{\Omega}(\vec{u}; s) \times \widehat{S} \tag{3.10}$$

Further insight into the implications of the T–BMT equation can be gained by writing the rotation vector $\vec{\Omega}$ as

$$\vec{\Omega}(\vec{u}; s) \;=\; \vec{\Omega}^{c.o} + \vec{\omega}^{s.b} \tag{3.11}$$

The vector $\vec{\Omega}^{c.o}$ contains the fields along the periodic *closed orbit* and satisfies the periodicity condition $\vec{\Omega}^{c.o}(s + C) = \vec{\Omega}^{c.o}(s)$, where C is the circumference of the ring. This can be written as $\vec{\Omega}^{c.o} = \vec{\Omega}^{d.o} + \vec{\omega}^{imp}$, where $\vec{\Omega}^{d.o}$ contains the design fields and $\vec{\omega}^{imp}$ represents the effects of magnet misalignments, correction fields etc. along the closed orbit. The term $\vec{\omega}^{s.b}$ contains the contribution due to synchrotron and/or betatron motion with respect to the closed orbit. This term is in general not one–turn periodic.

Since the length $|\widehat{S}|$ is invariant during precession, the most intuitive way of representing the spin evolution in a storage ring is through the real orthogonal 3×3 rotation matrices of the SO(3) group. [4] In this formalism it is convenient to parametrize the rotations via the unit rotation axis $\hat{r}$ and the rotation angle φ. However, it is often more efficient to use other representations for the spin rotations, especially for spin tracking. We will return to this point later on in the text. By introducing the anti–symmetric matrix

$$\mathbf{\Omega}(\vec{u}; s) = \begin{pmatrix} 0 & -\Omega_s & \Omega_z \\ \Omega_s & 0 & -\Omega_x \\ -\Omega_z & \Omega_x & 0 \end{pmatrix}$$

eqn. (3.10) can be expressed as

$$\frac{d\widehat{S}}{ds} = \mathbf{\Omega}(\vec{u}; s)\, \widehat{S} \tag{3.12}$$

The solution to this ordinary differential equation (ODE) can be written in terms of an orthogonal matrix $\mathbf{R}_{\vec{u}}$: $\widehat{S}(s) = \mathbf{R}_{\vec{u}}(s, s_i)\, \widehat{S}(s_i)$, for transport of a spin vector $\widehat{S}$ from s_i to s. In particular, on the closed orbit the equation of spin motion and its solution takes the form

$$\frac{d\widehat{S}}{ds} = \vec{\Omega}^{c.o} \times \widehat{S} \tag{3.13}$$

and

$$\widehat{S}(s) = \mathbf{R}^{c.o}(s, s_i)\, \widehat{S}(s_i) \quad \text{with} \quad \mathbf{R}^{c.o}(s_i, s_i) = \mathbf{I} \tag{3.14}$$

[3] Any momenta p that occur are now calculated in the curvilinear coordinate system.

[4] The orthogonality condition for SO(3) matrices $\mathbf{R}$ is expressed as $\mathbf{R}^T\,\mathbf{R} = \mathbf{R}^{-1}\,\mathbf{R} = \mathbf{I}$, where $\mathbf{I}$ is the (3×3) unit matrix.

As the next step, we need to find the unit length periodic solution on the closed orbit. This is accomplished by solving the eigenvalue problem for the one turn rotation matrix: $\mathbf{R}^{c.o}(s+C,s)\vec{r}_\mu(s) = \lambda_\mu \vec{r}_\mu(s)$. The solution we are looking for is the unit length eigenvector with unit eigenvalue. This periodic solution is parallel to the effective one turn rotation axis, and away from resonances (see eqn. (3.42) and the accompanying text) it is unique. It is denoted by $\hat{n}_0$ in the literature [5] and is a central object for the description of polarization in storage rings. The remaining two eigenvalues of the one turn rotation matrix form a complex conjugate pair: $e^{\pm i 2\pi\nu_0}$. The *closed orbit spin tune* ν_0, appearing in the exponent, is the number of spin precessions around $\hat{n}_0$ in one turn around the machine. For a perfectly aligned flat ring without solenoids $\nu_0 = a\gamma$. It should be noted that only the fractional part of the spin tune can be extracted from the numerical values of the complex pair of eigenvalues. The integer part must be found by following the spin motion for one turn around the machine. For the definition of spin tune away from the closed orbit, see [VBH98]. Suffice it to say that the spin tune at some arbitrary amplitude in phase space cannot be extracted as an eigenvalue of some generalized eigenvector problem, since particle orbits are not one–turn periodic.

Just as a suitable coordinate frame is necessary for the description of the orbital motion in storage rings, an appropriate coordinate frame is needed for the description of the spin motion. The unit eigenvector $\hat{n}_0$ of the one–turn spin rotation matrix on the closed orbit, together with the eigenvectors associated with the complex conjugate eigenvalue pair lend themselves to the construction of such a frame. Writing the latter pair as $\hat{m}_0 \pm i\,\hat{l}_0$ we can extract two new basis vectors $\hat{m}_0$ and $\hat{l}_0$ which are both orthogonal to $\hat{n}_0$, $\hat{m}_0 = \hat{l}_0 \times \hat{n}_0$, $\hat{l}_0 = \hat{n}_0 \times \hat{m}_0$, and obey the relation

$$\hat{m}_0(s+C) + i\,\hat{l}_0(s+C) = e^{\,i\,2\pi\nu_0}\left[\hat{m}_0(s) + i\,\hat{l}_0(s)\right] \tag{3.15}$$

It should be observed that $\hat{m}_0$ and $\hat{l}_0$ are solutions to the T–BMT equation on the closed orbit, eqn. (3.13). With these new unit vectors, we have a righthanded coordinate system $(\hat{n}_0, \hat{m}_0, \hat{l}_0)$ in which spin motion can be described with respect to the "ideal particle" on the closed orbit. This spin basis will be needed in Section 3.2.

By studying the equation of motion of the spin expectation value in the synchrotron radiation field one obtains the general evolution equation for the polarization given by Baier, Katkov and Strakhovenko (BKS) [BKS70], [6] which for motion on the closed orbit takes the form

$$\left(\frac{d\vec{P}}{dt}\right)_{BKS} = \vec{\Omega}^{c.o}(\vec{r},\dot{\vec{r}};t)\times\vec{P} - \frac{1}{\tau_{ST}(s)}\left(\vec{P} - \frac{2}{9}(\vec{P}\cdot\hat{s})\hat{s} + \frac{8}{5\sqrt{3}}\hat{b}(s)\right) \tag{3.16}$$

The first term on the right hand side describes precession and the second term describes radiative build–up of polarization. This equation is valid under the simplifying assumption that even when a synchrotron radiation photon is emitted, the particle stays on the closed orbit. The unit vector $\hat{b}$ is perpendicular to both the velocity and the acceleration, $\hat{b} = (\hat{s}\times\dot{\hat{s}})/|\dot{\hat{s}}|$, and is the direction of the magnetic field in the case of no electric fields and motion perpendicular to the magnetic field. Note the difference in time scales of the terms in eqn. (3.16): the first term varies like $\tau_{rev}/a\gamma$ where τ_{rev} is the revolution time, whereas the characteristic time of the second term, τ_{ST}, is many orders of magnitude larger. This fact simplifies the mathematical analysis of the spin motion, making averaging techniques permissible. By integration of the BKS equation, and by letting $t \to \infty$ the generalization of the Sokolov–Ternov formula for the asymptotic electron polarization in arbitrary magnetic field configurations along the closed orbit is obtained

[5] In early publications the notation $\hat{n}$ is common. This is an unlucky choice, since the same symbol is also used for the invariant spin field appearing in the Derbenev–Kondratenko formula (3.20).

[6] Here we choose t as the independent variable in conformity with the original paper.

$$P_{BKS} = P_{ST} \frac{\oint \frac{\hat{n}_0(s) \cdot \hat{b}(s)}{|\rho(s)|^3} ds}{\oint \frac{\left(1 - \frac{2}{9}(\hat{n}_0 \cdot \hat{s})^2\right)}{|\rho(s)|^3} ds} \tag{3.17}$$

and

$$\vec{P}_{BKS} = -P_{BKS}\, \hat{n}_0 \tag{3.18}$$

The build–up rate is

$$\tau_{BKS}^{-1} = \frac{5\sqrt{3}}{8} \frac{r_e \gamma^5 \hbar}{m} \frac{1}{C} \oint \frac{\left(1 - \frac{2}{9}(\hat{n}_0 \cdot \hat{s})^2\right)}{|\rho(s)|^3} ds \tag{3.19}$$

At equilibrium, the polarization is aligned with $\hat{n}_0$ on the closed orbit. In a perfectly flat ring, without solenoids, $\hat{n}_0$ is vertical. In rings containing vertical bends (e.g. dipole spin rotators) there are regions where $|\hat{n}_0(s) \cdot \hat{b}(s)| \neq 1$ and the radiative polarization can usually not reach the 92.38 % of the Sokolov–Ternov formula. Nevertheless, the polarization is still parallel to $\hat{n}_0$.

Unfortunately in the inhomogeneous fields of storage rings the Sokolov–Ternov effect is accompanied by depolarization. Soon after the discovery of radiative polarization is was realized that synchrotron radiation not only creates polarization, but that it can also destroy the polarization! This *radiative depolarization* was predicted in 1965 by Baier and Orlov [BO66] and a few years later it was observed and studied for the first time at the ACO storage ring at Orsay [Be68]. To complete this introduction to the theory of electron spin dynamics the important matter of radiation induced depolarization will now be addressed.

In an electron storage ring energy is continuously lost through the emission of synchrotron radiation in the bending magnets. This, together with replenishment of energy loss by the RF cavities leads to a *damping* of the synchro–betatron motion. The emission of the individual synchrotron radiation photons is a stochastic process. Each photon emission is accompanied by a discontinuous change in energy of the emitting electron and a corresponding disturbance of the electron's trajectory. For the beam as a whole, the random disturbances introduce noise into the synchrotron oscillations and then via the dispersion into the betatron oscillations causing a *diffusion* of all orbital amplitudes. The classical description of the orbit dynamics thus leads to stochastic differential equations [MR83, EMR99] for the evolution of the dynamical phase space variables. The balance between radiation damping and diffusion determines the equilibrium electron beam emittances. See Appendix A also.

The evolution of the electron polarization shows some similarities with the orbit dynamics. While the synchrotron radiation emission gives rise to a polarization build–up through the Sokolov–Ternov effect, which is the spin dynamical parallel to orbital damping, the stochastic nature of the individual emissions can bring *spin diffusion*. Photon emission imparts both transverse and longitudinal recoils to the electron, so that the electron changes its position in phase space. However, since a photon is typically emitted within an angle $1/\gamma$ with respect to the direction of the electron the effect of the longitudinal recoil, i.e. the energy jump, dominates. The transverse recoil is therefore often neglected in calculations. In the motion that follows after every such emission event, the electrons will experience fields in the quadrupoles (and higher order multipoles) that appear to contain a stochastic component. Imagining, in a classical sense, that the spins are passengers on the electrons, the stochastic journey will impart stochastic precessions to the spins through the term $\vec{\omega}^{s.b}$ of the T–BMT equation (eqs. (3.10) and (3.11)). If after a photon emission, the electron would eventually return to its original phase space position, owing to the damping, the spin would not point in the same direction as before the emission. For an initially fully polarized ensemble of electrons, the cumulative effect on the polarization of a large number of uncorrelated photon emission events is an incoherent summation of disturbances resulting in a spread of the spin vectors and decreased polarization.

This is a naïve picture, but nevertheless instructive. It emphasizes that the orbit dynamics has a strong influence on the spin motion and also that the electron polarization achieved is the result of a competition between the radiation induced polarization due to the Sokolov–Ternov effect and spin diffusion. But spin is by nature a purely quantum mechanical concept. Therefore this description of classical spin diffusion mixed with quantum mechanical spin–flip should be replaced by an approach unifying the various aspects of electron spin dynamics. I will now outline how this can be achieved by using more quantitative arguments to describe the interplay between polarization build–up and diffusion in $e^{+/-}$ storage rings.

The most elegant way to proceed is to consider the *stationary* (i.e. equilibrium) *polarization state* of the machine. The beam phase space density, w, is a function of the phase space position $\vec{u}$ and azimuth s: $w(\vec{u};s)$. If the beam is stable, the phase space density of a bunch is a periodic function of s so that we can write $w_{eq}(\vec{u};s) = w_{eq}(\vec{u};s+C)$. Likewise at equilibrium the polarization at each point in phase space should repeat itself from turn to turn, $\vec{P}_{eq}(\vec{u};s) = \vec{P}_{eq}(\vec{u};s+C)$. Note that $\vec{P}_{eq}$ need not in general be parallel to $\hat{n}_0$ for $\vec{u} \neq \vec{0}$. In the absence of spin–flip synchrotron radiation spin motion is, as we have seen, described by the T–BMT equation (3.6). In analogy with eqn. (3.16) we expect that a general evolution equation for the polarization under the influence of stochastic radiation should contain a T–BMT like term. Moreover, because of the time scales (and hence the strengths) of the processes involved this term is expected to dominate the spin motion: The Sokolov–Ternov effect and the spin diffusion leading to depolarization operate on a time scale of minutes to hours, whereas the radiation damping is measured in milliseconds and the spin precession in fractions of microseconds. A visual representation of characteristic time scales for a typical 25 GeV electron storage ring is found in Appendix B.

Because of the dominance of the T–BMT term, the stationary polarization direction $\vec{P}_{eq}/\|\vec{P}_{eq}\|$ at each point in phase space should, to a good approximation, be parallel to the direction we would get for a stationary (periodic) polarization distribution without the radiative effects [BH01]. We denote this latter direction by $\hat{n}$ [7] and by definition it satisfies the periodicity condition $\hat{n}(\vec{u};s) = \hat{n}(\vec{u};s+C)$. The unit vector field $\hat{n}(\vec{u};s)$ obeys the T–BMT equation along particle trajectories in the sense that $\hat{n}(\vec{M}(\vec{u};s);s+C) = \mathbf{R}(\vec{u};s)\,\hat{n}(\vec{u};s)$, where $\vec{M}(\vec{u};s)$ is the new phase space vector after one turn starting at $\vec{u}$ and s and $\mathbf{R}(\vec{u};s)$ is the corresponding spin transfer matrix. Observe that a spin initially parallel to $\hat{n}$ at some starting phase space position $\vec{u}$ and azimuth s is generally not transformed into itself in one turn around the machine, whereas the whole field $\hat{n}(\vec{u};s)$ is! We therefore call $\hat{n}(\vec{u};s)$ the *invariant spin field* [VBH98, Bb99]. The vector field $\hat{n}(\vec{u};s)$ is uniquely defined [8] except at spin–orbit resonances to be discussed later. If a spin $\widehat{S}$ is followed along a phase space trajectory in the absence of radiation, the scalar product $\widehat{S}\cdot\hat{n}$ of $\widehat{S}$ with the local $\hat{n}$ is an invariant since both vectors obey the T–BMT precession equation. Note that because orbital motion is in general not one–turn periodic, $\hat{n}(\vec{u};s)$ cannot usually be derived as an eigenvector of the spin transfer matrix $\mathbf{R}(\vec{u};s)$. On the other hand $\hat{n}(\vec{u};s)$ reduces to $\hat{n}(\vec{0};s) \equiv \hat{n}_0(s)$ on the closed orbit, and of course $\hat{n}_0(s) = \hat{n}_0(s+C)$. The meaning of the invariant spin field is illustrated in Figure 3.1.

If we now include the effects of radiation, following the treatments of either Derbenev and Kondratenko [DK73] or Mane [Ma86a] we obtain the generalization of the BKS equation (3.16). Before doing so, and again stressing the importance of time scales in the field of radiative spin polarization, it must be pointed out that under the assumption of "well behaved" integrable orbital motion, the absolute *value* of the electron polarization is essentially independent of azimuth and position in phase space. Neglecting the effect of transverse recoil by photon emission [9], the equilibrium electron polarization is given by

[7] Sometimes $\hat{n}$ will be referred to as the "$\hat{n}$–axis".

[8] For comments upon existence and uniqueness of $\hat{n}(\vec{u};s)$, see for example [Bb99].

[9] The effect of transverse recoil can also be included but contributes extra terms containing derivatives of $\hat{n}$ w.r.t. x' and z' which are typically a factor γ smaller than $\frac{\partial\hat{n}}{\partial\delta}$ [BR99].

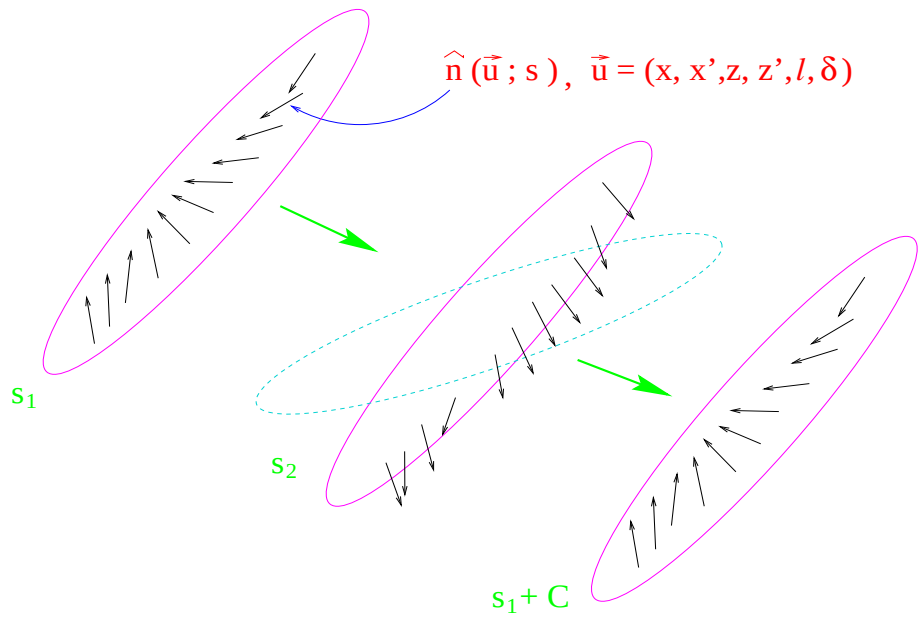

Figure 3.1: The invariant spin field $\hat{n}(\vec{u};s)$: an s–periodic unit vector field at each point in phase space, illustrated here for the same region of phase space (solid line ellipses) at three different azimuths. The dashed ellipse indicates the rotation of *particle phase space* associated with a bunch of particles travelling around the accelerator.

$$P_{DK} = P_{ST}\,\frac{\oint \left\langle \frac{1}{|\rho(s)|^3}\,\hat{b}\cdot\left(\hat{n}-\frac{\partial\hat{n}}{\partial\delta}\right)\right\rangle_s ds}{\oint \left\langle \frac{1}{|\rho(s)|^3}\left(1-\frac{2}{9}(\hat{n}\cdot\hat{s})^2+\frac{11}{18}\left(\frac{\partial\hat{n}}{\partial\delta}\right)^2\right)\right\rangle_s ds} \tag{3.20}$$

and

$$\langle \vec{P}_{DK}\rangle_{ens} = -P_{DK}\,\langle\hat{n}\rangle_s \tag{3.21}$$

where $\langle\,\rangle_s$ denotes an average over phase space. The corresponding build–up rate is

$$\tau_{DK}^{-1} = \frac{5\sqrt{3}}{8}\frac{r_e\gamma^5\hbar}{m}\frac{1}{C}\oint\left\langle\frac{1-\frac{2}{9}(\hat{n}\cdot\hat{s})^2+\frac{11}{18}\left(\frac{\partial\hat{n}}{\partial\delta}\right)^2}{|\rho(s)|^3}\right\rangle_s ds \tag{3.22}$$

The ensemble average $\langle\,\rangle_{ens}$ of the equilibrium polarization, eqn. (3.21), is given by P_{DK} times the average across phase space of $\hat{n}(\vec{u};s)$ at azimuth s, $\langle\hat{n}\rangle_s$. The expressions differ from those in eqs. (3.17) and (3.19) by the inclusion of terms with $\frac{\partial\hat{n}}{\partial\delta}$ and by the exchange of $\hat{n}_0$ for $\hat{n}$. The partial derivative $\frac{\partial\hat{n}}{\partial\delta}$ is a measure of the change of $\hat{n}$ caused by the fractional energy jumps δ. [10] Note that the statement that the value of the polarization to a good approximation is the same at all phase space positions and azimuths does not generally hold true for protons, especially at high energies. Even at HERA energies, there is essentially no radiation from a proton beam and hence no mechanism similar to the "spin damping" of the Sokolov–Ternov effect is in play. There is also only little exchange of particles between different phase space tori. In fact the polarization times for proton beams are very much larger than for electron beams, making self–polarization practically impossible. For instance the build–up time in HERA–p at 920 GeV would be $7\cdot 10^{10}$ years! It is therefore customary to inject a prepolarized proton beam that is then accelerated. Polarization lost at some orbital amplitudes during

[10] The original notation used by Derbenev and Kondratenko for this derivative, $\gamma\frac{\partial\hat{n}}{\partial\gamma}$, is not used here since it is open to misinterpretation.

the acceleration cannot be replenished, and the polarization can therefore vary across the beam phase space. Furthermore $\langle \hat{n} \rangle_s$ can vary significantly with the azimuth s [Vo00, Ho00a].

Far from resonances (see below) the invariant spin field $\hat{n}$ is very nearly aligned along $\hat{n}_0$, hence

$$P_{DK} \langle \hat{n} \rangle_s \approx P_{DK} \hat{n}_0 \tag{3.23}$$

but when the spin tune is sufficiently close to a spin–orbit resonance (see next section) the spin field $\hat{n}(\vec{u}; s)$ starts to "open up". In our unified model it is therefore not adequate to talk about diffusion away from $\hat{n}_0$ but away from $\hat{n}$ instead. In $e^{+/-}$ beams the opening angle between $\hat{n}(\vec{u}; s)$ and $\hat{n}_0(s)$ can be tens of milliradians near resonances at a few tens of GeV and increases with particle amplitude and naïve spin tune $a\gamma$. Observe that for electrons $|\langle \hat{n} \rangle_s|$ has a value close to one even in the vicinity of resonances and the beam polarization is mainly influenced by the value of P_{DK}. In the Derbenev–Kondratenko–Mane formalism, the depolarization is quantified by the square of the *spin–orbit coupling function* $\frac{\partial \hat{n}}{\partial \delta}(\vec{u}; s)$, in the denominator of eqn. (3.20). To attain high polarization, $(\frac{\partial \hat{n}}{\partial \delta})^2$ has to be kept small ($\ll 1$) in the dipole magnets of the machine. Methods to achieve this are referred to as *spin matching* and amount to organizing the machine optic in such a way that certain criteria are fulfilled. Details about several spin matching schemes can be found in Chapter 4, Chapter 6 and [BR99].

Derbenev and Kondratenko derived their expression for the equilibrium polarization already in 1973 using a complete semi–classical quantum mechanical treatment. It should be mentioned that it took a long time before the implications and correct usage of this formula were fully appreciated by the physics community. Mane gave an important contribution to the understanding of the underlying physics when in 1987 he rederived the Derbenev–Kondratenko formula from a statistical viewpoint. The evaluation of $\hat{n}(\vec{u}; s)$ and the partial derivative $\frac{\partial \hat{n}}{\partial \delta}(\vec{u}; s)$ are today the key tasks in most computer algorithms written for deriving the equilibrium polarization in storage rings. However, rewriting the Derbenev–Kondratenko build–up rate (eqn. (3.22)) in the form

$$\tau_{DK}^{-1} \;=\; \tau_{BKS}^{-1} + \tau_{dep}^{-1} \;\simeq\; \tau_{ST}^{-1} + \tau_{dep}^{-1} \tag{3.24}$$

where τ_{dep}^{-1} is the depolarization rate given by

$$\tau_{dep}^{-1} = \frac{5\sqrt{3}}{8} \frac{r_e \gamma^5 \hbar}{m} \frac{1}{C} \oint \left\langle \frac{\frac{11}{18} \left(\frac{\partial \hat{n}}{\partial \delta} \right)^2}{|\rho(s)|^3} \right\rangle_s ds \tag{3.25}$$

suggests another route to arrive at the equilibrium electron polarization, without introducing the concept of the invariant spin field $\hat{n}$ necessary in the Derbenev–Kondratenko–Mane formalism. In particular τ_{dep} can be estimated by a spin–orbit tracking simulation. This is the strategy adopted in the Monte Carlo program SITROS [Ke85]. The equilibrium polarization in this approximation is extracted using eqs. (3.17) and (3.19) as

$$P_{eq} \simeq P_{BKS} \frac{\tau_{dep}}{\tau_{BKS} + \tau_{dep}} \;=\; P_{BKS} \frac{\tau_{DK}}{\tau_{BKS}} \tag{3.26}$$

The contribution from the usually small term $\hat{b} \cdot \frac{\partial \hat{n}}{\partial \delta}$ in the numerator of the Derbenev–Kondratenko formula is neglected here. This term represents a correlation between the spin orientation and the radiation power and it is normally negligible since $\frac{\partial \hat{n}}{\partial \delta}$ is usually essentially perpendicular to the main bending field. However in the case of a ring with dipole spin rotators such as HERA $\hat{b} \cdot \frac{\partial \hat{n}}{\partial \delta} \neq 0$ in the rotator dipole fields. In addition, since in such a case the periodic spin solution $\hat{n}_0$ by design is horizontal in some straight sections, $\hat{b} \cdot \frac{\partial \hat{n}}{\partial \delta}$ need not vanish in any dipole in these "straight sections".

This can lead to a build–up or "build–down" (i.e a shift) of polarization separate from the Sokolov–Ternov effect. The phenomenon is called *kinetic polarization* [Mo84] and is a manifestation of the unified treatment.

The time dependence of polarization build–up, starting from an initial polarization P_0 (for $t \leq t_0$) is given by

$$P(t) = \langle P_{DK} \rangle_{ens} \left(1 - e^{-(t-t_0)/\tau_{DK}}\right) + P_0 \, e^{-(t-t_0)/\tau_{DK}} \tag{3.27}$$

The formula can be used in combination with eqn. (3.26) to calibrate polarimeters. In such a *rise time calibration* (a short description of the procedure is given in Section 4.3) the polarization is measured as a function of time and the parameters P_{eq}, τ_{DK} and P_0 are fitted to the expression in (3.27). The measurements should be made with a flat machine to minimize the effect of the kinetic polarization, which in practice is difficult to predict with high accuracy.

An intuitive way of understanding depolarization and spin diffusion, but now in terms of the $\hat{n}$–axis, may be gained through the following visualization. See Figure 3.2. Consider an electron with spin vector $\widehat{S}$ aligned along $\hat{n}(\vec{u}; s)$ at some initial phase space position $\vec{u}_0$: $S_n = |\widehat{S} \cdot \hat{n}| = 1$. Suppose that the electron undergoes a stochastic photon emission. After the emission (which can be regarded as an instantaneous process since $\tau_\gamma \approx \rho/c\gamma \sim 10^{-10}$ s), the spin finds itself at a new phase space position $\vec{u}_1$ due to the electron recoil. At this new position, the spin field vector $\hat{n}$ is generally pointing in some other direction compared to the direction of $\hat{n}$ at the initial phase space point. The spin vector $\widehat{S}$ on the other hand has *not* changed direction. The projection of $\widehat{S}$ upon $\hat{n}$ is therefore decreased: $S_n = |\widehat{S} \cdot \hat{n}| < 1$. Usually the angle between $\widehat{S}$ and $\hat{n}$ created by such a discontinuous jump is small, unless we are close to a spin–orbit resonance. At the new phase space position $\widehat{S}$, obeying the T–BMT equation, will rotate around the stable spin solution $\hat{n}$. After a short time, the electron will emit another photon. At the moment of emission the spin is pointing in a direction determined by the cone of rotation and the exact emission time. The projection of $\widehat{S}$ upon $\hat{n}$ may be increased or decreased following the second recoil, depending on the direction of $\hat{n}$ at the electron's new phase space point. The result of a large number of such stochastic emission events is a random walk where the total probability of a decrease of S_n results in an exponential decay of the polarization.

The above picture of spin diffusion has overseen an important factor, namely the damping. Without damping, the orbital phase space would grow indefinitely and no polarization could be observed. In general, following a disturbance, an electron beam will return to its original phase space distribution after a few damping times. [11] The damping is a slow process, compared to the time scale of photon emission and the effective change of orbital amplitude of individual electrons due to damping can therefore be regarded as being adiabatic. In [Ho00a] a proof is given that $S_n = |\widehat{S} \cdot \hat{n}|$ is an *adiabatic invariant* along a particle trajectory when a parameter such as orbit amplitude changes slowly. Thus the angle between the spin vector and $\hat{n}$ is essentially "locked" as the electron slowly moves towards lower amplitudes under the damping.

3.2 Methods of calculation

In the previous section we have briefly touched upon different philosophies for the calculation of the equilibrium polarization for electrons in storage rings. We have learned of the central role for estimating the polarization played by the calculation of $\hat{n}$ and of $\frac{11}{18}(\frac{\partial \hat{n}}{\partial \delta})^2$ in the dipoles, where the

[11] This property can be understood by studying the Fokker–Planck equation for the evolution of the electron phase space density [Bb91, Ri89].

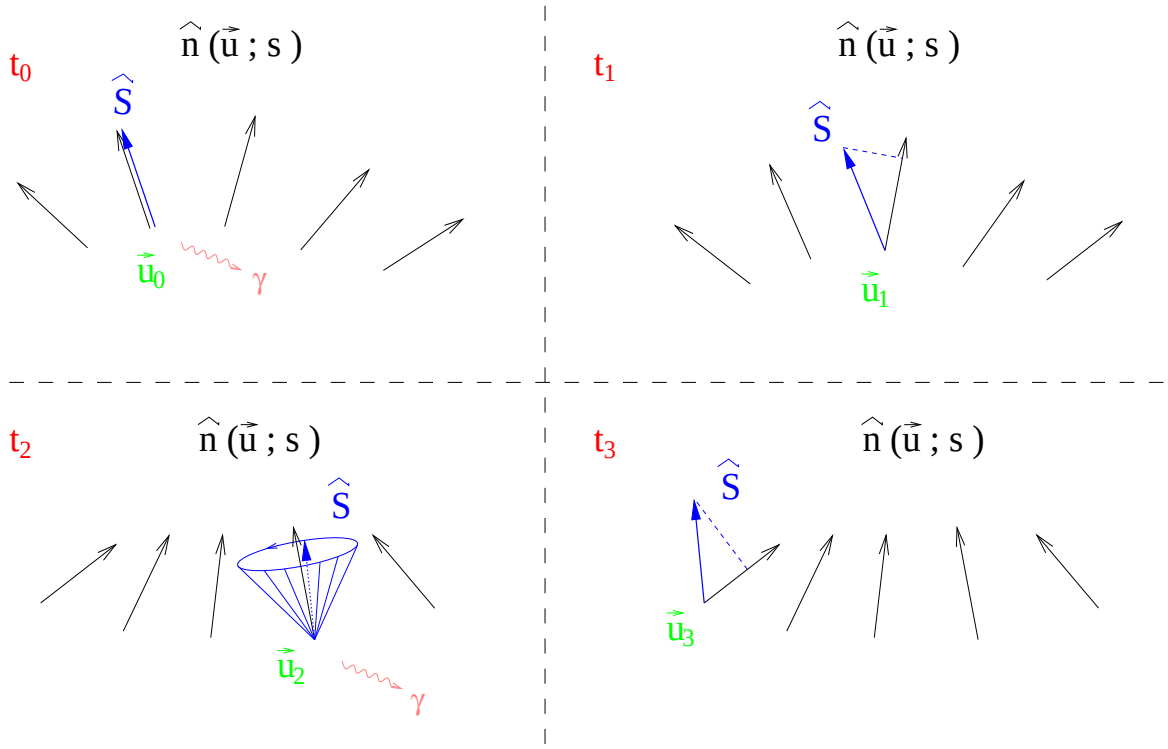

Figure 3.2: A simple model illustrating spin diffusion away from $\hat{n}$. At time t_0 a photon (γ) is emitted and the particle makes a discontinous jump in phase space due to the recoil. In the time interval t_1 to t_2 the particle coordinates changes smoothly as the particle travels from azimuth s_1 to s_2 under the influence of synchro–betatron motion and damping. At time t_2 another photon is emitted. The influence on the particle spin during these processes is described in the text. Observe that the spread of $\hat{n}(\vec{u};s)$ has been exaggerated in the picture (assuming that we are not close to a spin–orbit resonance).

radiation takes place. To proceed further, we need to discuss ways to integrate spins along non–periodic orbital trajectories, so that we can calculate these quantities. The starting point for this is the T–BMT equation of spin motion (3.10) or (3.12)

$$\frac{d\widehat{S}}{ds} \;=\; \vec{\Omega}(\vec{u};s)\times\widehat{S} \;=\; \mathbf{\Omega}(\vec{u};s)\,\widehat{S}$$

Since the elements of $\mathbf{\Omega}$ depend on the phase space position $\vec{u}$, so does the spin motion and it is in general not possible to find analytical solutions for all initial orbital conditions. In the spirit of the treatment of orbital motion with respect to the closed orbit, to facilitate perturbation calculations, we separate $\vec{\Omega}(\vec{u};s)$ into a periodic part $\vec{\Omega}_0(s)$ and a small part $\vec{\omega}(\vec{u};s)$ due to the synchro–betatron motion, as in eqn. (3.11)

$$\vec{\Omega}(\vec{u};s) \;=\; \vec{\Omega}_0(s) + \vec{\omega}(\vec{u};s) \tag{3.28}$$

We now recall that we expect the polarization $\vec{P}_{eq}(\vec{u};s)$ to be closely aligned along $\hat{n}$ and that away from resonances (see eqn. (3.42) or (3.44)) $\hat{n}$ is nearly parallel to $\hat{n}_0$. We therefore write the general solution to the T–BMT equation in the form

$$\widehat{S}(\;) = \gamma_0(\;)\,\hat{n}_0(s) + \alpha_0(\;)\,\hat{m}_0(s) + \beta_0(\;)\,\hat{l}_0(s) \tag{3.29}$$

where the spin variables $\alpha_0 = \widehat{S} \cdot \hat{m}_0$ and $\beta_0 = \widehat{S} \cdot \hat{l}_0$ are expected to be small, so that $\gamma_0 = \widehat{S} \cdot \hat{n}_0 = \sqrt{1 - \alpha_0^2 - \beta_0^2} \approx 1$. [12] To obtain the equations of motion for α_0, β_0 and γ_0 we write the above equation as $\widehat{S} \rightarrow \mathbf{R}_0^T \widehat{S}$, where

$$\mathbf{R}_0 = \begin{pmatrix} \hat{n}_{0x} & \hat{m}_{0x} & \hat{l}_{0x} \\ \hat{n}_{0z} & \hat{m}_{0z} & \hat{l}_{0z} \\ \hat{n}_{0s} & \hat{m}_{0s} & \hat{l}_{0s} \end{pmatrix} \tag{3.30}$$

This transformation implies the companion transformation

$$\begin{aligned} \mathbf{\Omega} \rightarrow \mathbf{W} &= \mathbf{R}_0^T \, \mathbf{\Omega} \, \mathbf{R}_0 + \frac{d\mathbf{R}_0^T}{ds} \mathbf{R}_0 \\ &= \mathbf{R}_0^T \boldsymbol{\omega} \mathbf{R}_0 \end{aligned} \tag{3.31}$$

for which the orthogonality of $\mathbf{R}_0$ has been used. The matrix $\boldsymbol{\omega}$ is here the anti–symmetric matrix of components in $\vec{\omega}$, in analogy with $\mathbf{\Omega}(\vec{u}; s)$ in eqn. (3.12). In an accelerator $\vec{\Omega}_0$ is normally piecewise constant and one–turn periodic to a good approximation and the derivation of $\mathbf{R}_0$ is hence straightforward (cf. eqn. (3.14) and following text). After the transformation we are left with a coupled system of nonlinear differential equations in the spin components α_0, β_0 and γ_0

$$\begin{aligned} \frac{d}{ds} \left(\mathbf{R}_0^T \widehat{S} \right) &= \mathbf{W} \left(\mathbf{R}_0^T \widehat{S} \right) \\ &\Longleftrightarrow \\ \frac{d}{ds} \begin{pmatrix} \gamma_0 \\ \alpha_0 \\ \beta_0 \end{pmatrix} &= \begin{pmatrix} 0 & -\hat{l}_0 \cdot \vec{\omega} & \hat{m}_0 \cdot \vec{\omega} \\ \hat{l}_0 \cdot \vec{\omega} & 0 & -\hat{n}_0 \cdot \vec{\omega} \\ -\hat{m}_0 \cdot \vec{\omega} & \hat{n}_0 \cdot \vec{\omega} & 0 \end{pmatrix} \begin{pmatrix} \gamma_0 \\ \alpha_0 \\ \beta_0 \end{pmatrix} \end{aligned} \tag{3.32}$$

The nonlinearities are buried in the dependence of $\vec{\omega}$ on phase space position $\vec{u}$ and the fact that only two of the spin variables can vary independently. Moreover, since $\vec{\omega}$ depends on s, the $\mathbf{W}$–matrices calculated at different azimuths do not commute. A perturbative solution to (3.32) can be found in the form of an azimuth–ordered [13] exponential, analogous to the von Neumann expansion in quantum mechanics [Ne55]

$$\begin{aligned} \begin{pmatrix} \gamma_0 \\ \alpha_0 \\ \beta_0 \end{pmatrix}_f &= \mathrm{A} \exp \left(\int_{s_i}^{s_f} \mathbf{W}(\vec{u}_i; s') ds' \right) \begin{pmatrix} \gamma_0 \\ \alpha_0 \\ \beta_0 \end{pmatrix}_i \\ &\equiv \left[\mathbf{I} + \int_{s_i}^{s_f} \mathbf{W}(\vec{u}_i; s') ds' + \int_{s_i}^{s_f} \mathbf{W}(\vec{u}_i; s') \int_{s_i}^{s'} \mathbf{W}(\vec{u}_i; s'') ds'' ds' \right. \\ &\quad \left. + \int_{s_i}^{s_f} \mathbf{W}(\vec{u}_i; s') \int_{s_i}^{s'} \mathbf{W}(\vec{u}_i; s'') \int_{s_i}^{s''} \mathbf{W}(\vec{u}_i; s''') ds''' ds'' ds' + \ldots \right] \begin{pmatrix} \gamma_0 \\ \alpha_0 \\ \beta_0 \end{pmatrix}_i \end{aligned} \tag{3.33}$$

[12] The empty braces indicate the dependence of $\widehat{S}$ and $\gamma_0, \alpha_0, \beta_0$ on the initial coordinates and the transport therefrom, $(\,) = (\vec{u}_i; s, s_i)$

[13] here implied by the operator A

However we are interested in a special solution to the T–BMT equation, namely $\hat{n}$. There are a handful of methods available for the derivation of this quantity. In order to illustrate the origin of spin–orbit resonance structures I will concentrate mainly on one of them, namely the perturbative SMILE formalism by Mane [Ma86b]. Before embarking on this, I should mention a few of the other schemes. Two newer non–perturbative methods are especially interesting. The SPRINT algorithm [Vo00, Ho00a] computes an approximation of $\hat{n}$ using a technique developed by Heinemann and Hoffstätter called stroboscopic averaging [HH96]. In the SPRINT code, multi–turn spin–orbit tracking is performed for linearized orbital motion, but fully nonlinear spin motion and all orders of resonance (see below) emerge automatically. The code has been optimized for the spin–orbit tracking of protons but unfortunately lacks a description of the features specific to radiating particles such as electrons. At the moment the code does not handle the calculation of $\frac{\partial \hat{n}}{\partial \delta}(\vec{u};s)$. In the SODOM algorithm [Yo92] $\hat{n}$ is represented by a spinor $\Psi_{\hat{n}}$. [14] By utilizing the periodicity condition $\hat{n}(\vec{u};s) = \hat{n}(\vec{u};s+C)$ and the corresponding periodicity condition for the one–turn 2×2 spinor transfer matrix $\mathbf{T}$ on a synchro–beta orbit

$$\mathbf{T}(\phi_k)\Psi_{\hat{n}}(\phi_k) = e^{-i\nu_{\vec{u}}/2}\,\Psi_{\hat{n}}(\phi_k + 2\pi\nu_k) \qquad \forall\, k \in \{x,z,s\} \tag{3.34}$$

where the ϕ_k are the initial orbital phases, ν_k are the tunes of the three orbital degrees of freedom k, and $\nu_{\vec{u}}$ is the so called amplitude dependent spin tune [Vo00, Ho00a], an eigen problem in the Fourier components of $\mathbf{T}(\phi_k)$ and $\Psi_{\hat{n}}(\phi_k)$ can be formulated. The Fourier coefficients are obtained numerically from spin–orbit tracking data and the eigenvector of Fourier components of $\hat{n}$ allows the invariant spin field to be reconstructed. By constructing $\hat{n}$ at many points in phase space $\frac{\partial \hat{n}}{\partial \delta}(\vec{u};s)$ can be obtained by numerical differentiation. However, in order to calculate this derivative at the nodes of a sufficiently fine phase space mesh, so that reliable results can be extracted for its use in the Derbenev–Kondratenko formula, very large computer power is needed. The same holds true if this derivative is to be calculated with the SPRINT code. Ways to derive $\hat{n}$ using Lie algebraic methods have also been developed [Yo87, EY94, BG98].

Now, let us return to the SMILE algorithm. Following Mane [Ma86b] we define the spherical components

$$V_0 = \gamma_0\,, \quad V_\pm = \frac{1}{\sqrt{2}}\,(\alpha_0 \pm i\beta_0) \tag{3.35}$$

and write

$$\omega_0 = \hat{n}_0 \cdot \vec{\omega}\,, \quad \omega_\pm = \left(\hat{m}_0 \pm i\hat{l}_0\right)\cdot\vec{\omega} \tag{3.36}$$

which leads to the form

$$\begin{aligned}
\frac{d}{ds}\begin{pmatrix} V_+ \\ V_0 \\ V_- \end{pmatrix} &= \begin{pmatrix} \omega_0 & -\frac{\omega_+}{\sqrt{2}} & 0 \\ -\frac{\omega_-}{\sqrt{2}} & 0 & \frac{\omega_+}{\sqrt{2}} \\ 0 & \frac{\omega_-}{\sqrt{2}} & \omega_0 \end{pmatrix}\begin{pmatrix} V_+ \\ V_0 \\ V_- \end{pmatrix} \\
&= i\left(\vec{\omega}\cdot\vec{J}\right)^T\begin{pmatrix} V_+ \\ V_0 \\ V_- \end{pmatrix}
\end{aligned} \tag{3.37}$$

for the equation of motion for the components of $\hat{n}$, where $\vec{J}$ is a vector of spin–1 angular momentum matrices. The solution for $\hat{n}$ is then given in the form of a von Neumann expansion as

[14] For an introduction to SU(2) spinor algebra, see [Mo84].

$$\begin{pmatrix} V_+ \\ V_0 \\ V_- \end{pmatrix}(s) \;=\; \lim_{\lambda\to 0_+} \mathrm{A}\,\exp\left(i\int_{-\infty}^{s} \left(\vec{\omega}\cdot\vec{J}\right)^T e^{\lambda s'} ds' \right) \begin{pmatrix} 0 \\ 1 \\ 0 \end{pmatrix} \tag{3.38}$$

where the inclusion of the damping factor $e^{\lambda s'}$ ($\lambda > 0$) ensures that the solution $\hat{n}$ has the correct periodicity property $\hat{n}(\vec{u};s) = \hat{n}(\vec{u};s+C)$. The incorporation of the damping factor can also be interpreted in terms of the adiabatic invariance of $S_n = |\widehat{S}\cdot\hat{n}|$. Suppose that we start at "$-\infty$" with a spin aligned parallel to $\hat{n}_0$ on the closed orbit. As the spin evolution is followed (tracked) forward in time, the orbit amplitude is slowly increased until it reaches full size. Provided that the increase of the orbit amplitude is slow enough, the spin will stay aligned with, and be an approximation of, the pre–established invariant spin field $\hat{n}(\vec{u};s)$ during this *anti–damping* procedure.

To illustrate the properties of the derived vector field a perturbative expansion in powers of $\vec{\omega}$ is made and we will look at the structure of the integrals for the first few orders. In order to emphasize the key features I will restrict the description to the case of linear orbital motion and be quite symbolic. To first order in $\vec{\omega}$ eqn. (3.38) reads

$$\begin{pmatrix} V_+ \\ V_0 \\ V_- \end{pmatrix}(s) \;=_1\; \begin{pmatrix} 0 \\ 1 \\ 0 \end{pmatrix} + \lim_{\lambda\to 0_+} \frac{i}{\sqrt{2}} \int_{-\infty}^{s} \begin{pmatrix} -\omega_+ \\ 0 \\ \omega_- \end{pmatrix} e^{\lambda s'} ds' \tag{3.39}$$

Note that in the linear approximation $\vec{\omega}$ is linear in the orbital amplitudes, A_k, and we can write $\vec{\omega} =_1 \sum_k A_k \vec{\omega}_k$, where now $k \in \{1,\ldots,6\}$ labels the six orbital normal modes. Due to the quasi–periodicity of the synchro–betatron oscillations and the rotation of the spin basis, the integrand is a quasi–periodic function obeying $\omega_{k\pm}(s+C) = e^{\,i\,2\pi(\nu_k\pm\nu_0)}\omega_{k\pm}(s)$ for each k, so that [15]

$$\begin{aligned} V_\pm(s) \;&=_1\; \lim_{\lambda\to 0_+} \mp\frac{i}{\sqrt{2}} \sum_k A_k \int_{-\infty}^{s} \omega_{k\pm}(s')\, e^{\lambda s'} ds' \\ &=\; \lim_{\lambda\to 0_+} \mp\frac{i}{\sqrt{2}} \sum_k A_k \sum_{N=0}^{\infty} e^{\,-i\,2\pi N(\nu_k\pm\nu_0)}\, e^{-\lambda NC} \int_{s-C}^{s} \omega_{k\pm}(s')\, ds' \\ &=\; \lim_{\lambda\to 0_+} \mp\frac{i}{\sqrt{2}} \sum_k A_k \frac{1}{e^{\,i\,2\pi(\nu_k\pm\nu_0)+\lambda C}-1} \int_{s}^{s+C} \omega_{k\pm}(s')\, e^{\lambda s'} ds' \end{aligned} \tag{3.40}$$

In this particular perturbation expansion, we see that in the first order terms (of which there are six) the summation of the geometrical series of phase factors leads to first order resonance denominators. If the expansion is taken to second or higher order, similar resonance denominators will emerge. For example, at second order and with an obvious notation

$$\begin{pmatrix} V_+ \\ V_0 \\ V_- \end{pmatrix}_2 (s) \;=\; \lim_{\lambda\to 0_+} i\int_{-\infty}^{s} \left(\vec{\omega}\cdot\vec{J}\right)^T \begin{pmatrix} V_+' \\ V_0' \\ V_-' \end{pmatrix}_1 e^{\lambda s'}\, ds' \tag{3.41}$$

[15] Note that the periodicity condition for the components ω_{k0} read as $\omega_{k0}(s+C) = e^{\,i\,2\pi\nu_k}\,\omega_{k0}(s)$.

Observe that as before each nonzero element in $\left(\vec{\omega}\cdot\vec{J}\right)^T$ is a sum of 6 terms and the $V_{\pm,0}$ are themselves sums of 6 terms (cf. eqn. (3.40)). At second order we therefore have $6\times 6 = 36$ groups of integrals. [16] In analogy with the first order case, each integral from $-\infty$ to s can be written as a sum of one turn integrals. Then, owing to the quasi–periodicity of the integrand one finds that in addition to the first order resonance denominators contained in the first order V's in the integrand, each of the terms acquires a second order resonance denominator of the kind $\exp\left[\,i\,2\pi(\sum_k m_k\nu_k \pm \nu_0)\,\right]-1$ with $\sum|m_k| = 2$. In the same way higher order resonance denominators emerge from the integration of terms containing resonance denominators of all lower orders.

Note that when the perturbative solution is transformed back into the machine coordinates, it satisfies the periodicity condition $\hat{n}(\vec{u};s) = \hat{n}(\vec{u};s+C)$ order by order. The resonance denominators appearing in this perturbative formulation clearly show, as expected, that when the spin motion is coherent with the orbital motion the $\hat{n}$–axis is strongly tilted away from $\hat{n}_0$ and the spin motion becomes extremely sensitive to small changes in the orbit variables. Then $\frac{\partial\hat{n}}{\partial\delta}(\vec{u};s)$ can be large so that spin diffusion can be strong. In this perturbation theory the resonance condition is written as

$$\nu_0 = m + m_x\,\nu_x + m_z\,\nu_z + m_s\,\nu_s \tag{3.42}$$

where the m's are integers and the ν's are the tunes of the three orbital modes. The appearance of ν_0 in the resonance condition (3.42) is an artifact of the perturbative treatment. A non–perturbative treatment would deliver the condition $\nu = m + m_x\,\nu_x + m_z\,\nu_z + m_s\,\nu_s$ where ν is the amplitude dependent spin tune [VBH98, Vo00, Ho00a] and can differ from ν_0. At HERA energies the difference is negligible.

The resonances can be classified into several groups. Synchro–betatron resonances with $|m_x| + |m_z| + |m_s| \neq 0$ are sometimes referred to as "intrinsic resonances". The integer $|m_x| + |m_z| + |m_s|$ is called the order of the resonance. Hence the condition $|m_x| + |m_z| + |m_s| = 1$ corresponds to first order resonances which, as we have seen, emerge from first order integrals as in eqn. (3.40). Another type of resonance may appear when $\nu_0 =$ integer, i.e. a zeroth order resonance in the adopted terminology. In a real storage ring unavoidable magnet misalignments and field errors give rise to horizontal and longitudinal fields on the closed orbit, that cause $\hat{n}_0$ to tilt away from its nominal direction. This tilt is especially large near such "integer resonances". If ν_0 would be an integer, the one–turn spin rotation matrix evaluated on the closed orbit would be a unit matrix and $\hat{n}_0(s)$ would not be unique. Note that *this* kind of zeroth order resonance (called "imperfection resonances" in the field of polarized protons) does not appear here, because we are calculating depolarization rates with respect to $\hat{n}_0$ (or $\hat{n}$) at a fixed energy or for a narrow range of energies. [17] The effects of closed orbit distortions are therefore best accounted for already in the calculation of $\hat{n}_0$. A loss of polarization may nonetheless appear at integer values of ν_0, because a strong tilt of $\hat{n}_0$ away from its nominal direction can cause terms in the so called **G** matrix (see Section 3.2.1 and Chapter 4) to switch on and lead to strong depolarization related to the synchrotron motion. An example of this can be seen in Chapter 6, Figure 6.9 (top left) where the broad first order synchrotron resonances have swept away the polarization at the positions of integer ν_0. Moreover, *very* close to integer values of ν_0 imperfections can cause $\hat{n}_0$ to be so strongly tilted away from the vertical in the arcs that the numerator in eqn. (3.17) becomes small. Then the Sokolov–Ternov effect itself becomes weak and the attainable polarization is small independently of depolarization effects. This is also illustrated in Figure 6.9.

In practice the dominant higher order resonances are the *synchrotron sidebands* of first order parent betatron resonances

[16] Note that, because of the multiplication in these integrals of terms linear in A_k , the $\begin{pmatrix} V_+ \\ V_0 \\ V_- \end{pmatrix}_2$ is second order in the orbital amplitude.

[17] But the imperfection resonances *are* important for the acceleration of polarized protons.

$$\nu_0 = m \pm \nu_y + m_s\,\nu_s \tag{3.43}$$

(recall the generic use of the symbol ν_y, representing either ν_x or ν_z). These originate in the synchrotron part of the term $\hat{n}_0 \cdot \vec{\omega}$ in eqn. (3.32) (see also eqn. (3.51) and the paragraph following), which represents a modulation of the instantaneous rate of spin precession around $\hat{n}_0$ due to energy oscillations. More details on synchrotron sidebands and estimates of their strengths will be given in Section 3.2.3 but since we have been discussing integer resonances, it is already appropriate to point out here that synchrotron sidebands of parent first order synchrotron resonances can also occur and that they can produce integer resonances [Ma90, Ma92, Yo83, Yo92]. But these can occur even in the *absence* of imperfections, namely if the ring is not properly spin matched for synchrotron motion.

So far in our treatment the simplifying assumption has been made that the horizontal, vertical and longitudinal oscillation modes of the particles are uncoupled. However, in practice a more or less strong inter–mode coupling always exists and the perturbative spin–orbit resonance criterion becomes

$$\nu_0 = m + m_I\,\nu_I + m_{II}\,\nu_{II} + m_{III}\,\nu_{III} \tag{3.44}$$

where ν_I, ν_{II} and ν_{III} are the orbit eigentunes in the presence of coupling. At this point, it should be emphasized that neither coupling nor inclusion of higher order terms in $\vec{\omega}$, viz. nonlinear fields, are a prerequisite for the occurrence of higher order resonances. The dominant contribution to *all* orders instead comes from *noncommutation* between spin rotations around different axes. The influence of noncommutation is manifested in the nontrivial structure of the azimuth–ordered integrals used for the perturbative derivation of $\hat{n}(\vec{u}; s)$ just summarized. [18] Observe also that the higher order integrals describe the *combined* effects of *independent* orbital modes.

Equation 3.38 has been implemented by Mane in the SMILE code. The SMILE perturbation expansion is a power series in the orbital amplitudes, which after averaging over the beam distribution becomes a series in the emittances. It is a unified approach where all resonances are treated on equal footing. Unfortunately the algorithm suffers from convergence problems at large $a\gamma$ and is therefore not a practically useful tool for calculations of $\hat{n}$ and its partial derivative $\frac{\partial \hat{n}}{\partial \delta}$ at HERA energies.

3.2.1 Linear approximation — the SLIM formalism

As we have seen, solving the general equation of spin motion (3.10) with the purpose of finding the special solution $\hat{n}$, and being able to calculate $\frac{\partial \hat{n}}{\partial \delta}$, can be far from trivial. It is therefore valuable to approximate by formulating a simplified problem equivalent to first order SMILE, for which it is possible to find closed analytical solutions. This is achieved by linearizing the orbit and the spin motion. Here I will follow the route layed out in [MR83] and start with the orbit motion.

In Appendix A a presentation of the Abraham–Lorentz equation of motion is made, and the design orbit reference trajectory is introduced. The linear formalism I will discuss here is based upon an extension of the well known 6×6 matrix formalism for describing particle motion through lattice elements, in which a transformation to the closed orbit as a new reference trajectory is made. In the absence of radiation, the transport of a phase space vector $\vec{u}$ from azimuth s_0 to s_1 can be described by a *symplectic*, i.e. phase space volume preserving, transfer matrix $\mathbf{M}$. Introducing the notation $\vec{X}(s_0) = \vec{u}_{s=s_0}$ and $\vec{X}(s_1) = \vec{u}_{s=s_1}$ this transport is given by

$$\vec{X}(s_1) = \mathbf{M}(s_1, s_0)\,\vec{X}(s_0) \tag{3.45}$$

[18] An alternative, but equivalent perturbation formulation is given in [BHR92].

The periodic closed orbit in a circular accelerator is generally *not* identical with the design orbit. RF cavities are necessary in the lattice to compensate for the radiation losses, mainly occurring in the arcs. This causes the azimuthal variation of the energy of the circulating particles to attain a "sawtooth" shape. A real machine always suffers from misalignments of the magnets and compensation magnets are therefore usually needed. There can also be other perturbing fields in the lattice coming from insertion devices, experimental stations, beam kickers for injection etc. By extending the six–dimensional phase space vector with a seventh component equal to unity, $\vec{X}_7 \equiv (\vec{u}, 1)$, and correspondingly enlarging the transfer matrix $\mathbf{M}_{6\times 6} \rightarrow \mathbf{M}_{7\times 7}$, the closed orbit can be calculated. The transformation through a lattice element then reads as

$$\vec{X}_7(s_1) = \mathbf{M}_{7\times 7}(s_1, s_0)\, \vec{X}_7(s_0) \tag{3.46}$$

$$\mathbf{M}_{7\times 7} = \begin{pmatrix} \mathbf{M}_{6\times 6} & \vec{N}_6 \\ \mathbf{0} & 1 \end{pmatrix} \tag{3.47}$$

where the vector $\vec{N}_6$ depends on the perturbing electromagnetic fields along the design orbit. Imposing the periodicity condition: $\vec{X}_7(s_0 + C) = \vec{X}_7(s_0)$ gives for the closed orbit vector at the initial position s_0

$$\vec{X}_0(s_0) = \Big(\mathbf{I} - \mathbf{M}_{6\times 6}(s_0 + C, s_0)\Big)^{-1} \vec{N}_6(s_0 + C, s_0) \tag{3.48}$$

By using eqn. (3.46) the closed orbit $X_0(s)$ can be found at every position in the lattice. In principle the sextupoles have to be included in the calculation of the closed orbit. This gives rise to a nonlinear problem and it has to be solved by iteration. The elements of the enlarged transfer matrix $\mathbf{M}_{7\times 7}$ for various magnet types can be found in [Ch79] or [MR83]. With the knowledge of the closed orbit, the synchro–betatron oscillations can be described using this periodic orbit as a new reference trajectory.

Already in Section 3.1 a decomposition of the spin motion into a closed orbit contribution and a synchro–beta contribution was introduced, and at the beginning of this section a transformation was made to a frame rotating with the spin on the closed orbit, so that the spin evolution could be described in terms of the small quantities α_0 and β_0. The particular spin basis chosen for that discussion however is not one–turn periodic, but for the following description we will need a periodic spin basis. Such a spin basis can most easily be constructed from the non–periodic basis $(\hat{n}_0, \hat{m}_0, \hat{l}_0)$ by introducing an additional backward rotation around $\hat{n}_0$ by an angle $\psi_0(s)$ thus

$$\hat{m}(s) + i\,\hat{l}(s) = e^{-i\psi_0(s)} \Big[\hat{m}_0(s) + i\,\hat{l}_0(s)\Big] \tag{3.49}$$

and requiring that $\psi_0(s + C) - \psi_0(s) = 2\pi\nu_0$. The new unit vectors $\hat{m}$ and $\hat{l}$, together with $\hat{n}_0$, then form a s–periodic righthanded set $(\hat{n}_0, \hat{m}, \hat{l})$ with period C. The $\hat{n}$–axis can be expressed in terms of this new spin basis as

$$\hat{n}(\vec{u}; s) = \gamma(\vec{u}; s)\, \hat{n}_0(s) + \alpha(\vec{u}; s)\, \hat{m}(s) + \beta(\vec{u}; s)\, \hat{l}(s) \tag{3.50}$$

with $\gamma = \sqrt{1 - \alpha^2 - \beta^2}$, where the γ, α and β are, like $\hat{n}$, periodic in s at fixed $\vec{u}$. The components α and β satisfy the nonlinear system of differential equations (compare eqn. (3.32))

$$\begin{aligned} \alpha' &= \sqrt{1 - \alpha^2 - \beta^2}\, \vec{\omega} \cdot \hat{l} \; - \beta\, (\hat{n}_0 \cdot \vec{\omega}) + \beta\, \psi_0'(s) \\ \beta' &= -\sqrt{1 - \alpha^2 - \beta^2}\, \vec{\omega} \cdot \hat{m} + \alpha\, (\hat{n}_0 \cdot \vec{\omega}) - \alpha\, \psi_0'(s) \end{aligned} \tag{3.51}$$

Now, assuming that $\hat{n}$ remains close to $\hat{n}_0$ (a reasonable assumption away from resonances, as pointed out earlier), implying that α and β can be assumed to be small quantities, the above expressions can be simplified. In the approximation of linear orbit and spin motion, i.e. linearizing $\vec{\omega}$ in the orbital coordinates such that $\vec{\omega} =_1 \mathbf{F}_{3\times 6}\,\vec{u}$ (equivalent to the ansatz $\vec{\omega} =_1 \sum_k A_k \vec{\omega}_k$ used earlier), and dropping terms of higher order in α and β, the differential equations for α and β reduce to

$$\begin{aligned} \alpha' &= \vec{\omega}\cdot\hat{l} + \beta\,\psi_0' \\ \beta' &= -\vec{\omega}\cdot\hat{m} - \alpha\,\psi_0' \end{aligned} \tag{3.52}$$

which can be straightforwardly solved. In this linear approximation the Derbenev–Kondratenko $\hat{n}$–axis is given by

$$\hat{n}(\vec{u};s) = \hat{n}_0(s) + \alpha(\vec{u};s)\,\hat{m}(s) + \beta(\vec{u};s)\,\hat{l}(s) \tag{3.53}$$

valid as long as $\sqrt{\alpha^2+\beta^2} \ll 1$.

By combining the orbit and spin descriptions in a fashion that was first done by Chao [Ch81a], we arrive at a compact 8×8 matrix notation. In this formalism the orbit and spin motions through the various lattice elements are represented by 8×8 matrices acting on an 8–dimensional spin–orbit "phase space vector" $(\vec{u},\alpha,\beta)^T$, effectively describing the motion with respect to an 8–dimensional closed orbit:

$$\frac{d}{ds}\begin{pmatrix} \vec{u} \\ \alpha \\ \beta \end{pmatrix} = \mathbf{A}_{8\times 8}\begin{pmatrix} \vec{u} \\ \alpha \\ \beta \end{pmatrix} \tag{3.54}$$

where $\mathbf{A}_{8\times 8}$ is a coefficient matrix, whose form is given for various ring elements for example in [MR83]. The general solution to this equation is written in terms of the 8×8 transfer matrix

$$\mathbf{M}_{8\times 8} = \begin{pmatrix} \mathbf{M}_{6\times 6} & \mathbf{0}_{6\times 2} \\ \mathbf{G}_{2\times 6} & \mathbf{D}_{2\times 2} \end{pmatrix} \tag{3.55}$$

Recall that $\mathbf{M}_{6\times 6}$ is a symplectic matrix, describing the "Hamiltonian part" of the orbital motion with respect to the closed orbit. The radiation is taken into account in a second step of the calculations. The $\mathbf{G}_{2\times 6}$ matrix describes the coupling of the spin variables to the orbital motion. It is the transfer matrix of the spin variables α and β, giving the solution of the linearized equation (3.52)

$$\begin{pmatrix} \alpha(s) \\ \beta(s) \end{pmatrix} = G_{ij}\,X_j(s_0) + \mathbf{D}_{2\times 2}\begin{pmatrix} \alpha(s_0) \\ \beta(s_0) \end{pmatrix} \tag{3.56}$$

with

$$\begin{aligned} G_{1j} &= \frac{\partial\alpha}{\partial x_j} \\ G_{2j} &= \frac{\partial\beta}{\partial x_j} \end{aligned} \qquad \forall\, j\in\{1,\ldots,6\}$$

The elements G_{ij} of the $\mathbf{G}$ matrix generally depend upon the orientation of the spin base vectors $\hat{l}(s)$ and $\hat{m}(s)$ as well as on characteristics of the field of the particular lattice element. For later use I introduce the notation $\mathbf{G} = (\mathbf{G}_x, \mathbf{G}_z, \mathbf{G}_s)$, where the $\mathbf{G}_x$, $\mathbf{G}_z$ and $\mathbf{G}_s$ are 2×2 matrices associated with the spin coupling to the orbital motion in the horizontal, vertical and longitudinal planes, respectively. The $\mathbf{G}$ matrix plays a vital role in some formulations of spin matching conditions, see Chapter 4

and [BR99]. Examples of $\mathbf{G}$ matrices for various magnet types are given in [Bb85b]. This formalism usually does not take into account the weak Stern–Gerlach forces causing the spin motion to act back on the orbital motion, hence the $\mathbf{0}_{6\times 2}$ in the last two columns of $\mathbf{M}_{8\times 8}$. The $\mathbf{D}_{2\times 2}$ in the bottom right corner is a rotation matrix related to the spin phase manipulation needed to satisfy the spin basis periodicity requirement. We choose to apply this backward rotation $\Delta\psi_0 = 2\pi\nu_0$ to $\hat{m}_0$, $\hat{l}_0$ and $\mathbf{G}$ at the end of each turn.

$$\mathbf{D}_{2\times 2}(s+C,s) = \begin{pmatrix} \cos 2\pi\nu_0 & \sin 2\pi\nu_0 \\ -\sin 2\pi\nu_0 & \cos 2\pi\nu_0 \end{pmatrix} \tag{3.57}$$

Solving the eigen problem posed by the one turn map: $\mathbf{M}_{8\times 8}(s+C,s)\,\vec{q}_\mu(s) = \hat{\lambda}_\mu\,\vec{q}_\mu(s)$, gives eigenvectors of the form

$$\begin{aligned} \vec{q}_k(s) &= \begin{pmatrix} \vec{v}_k(s) \\ \vec{w}_k(s) \end{pmatrix}, \quad \vec{q}_{-k}(s) = [\vec{q}_k(s)]^* \qquad \forall\, k \in \{I, II, III\} \\ \vec{q}_k(s) &= \begin{pmatrix} \vec{0}_6 \\ \vec{w}_k(s) \end{pmatrix}, \quad \vec{q}_{-k}(s) = [\vec{q}_k(s)]^* \qquad k = IV \end{aligned} \tag{3.58}$$

The eigenvectors associated with the orbital motion, $\vec{v}_k$ are normalized according to $\vec{v}^{\,\dagger}_{\pm k}\mathbf{S}\,\vec{v}_{\pm k} = \pm i$ [19], whereas the spin parts of the eigenvectors, $\vec{w}_k$ are given by

$$\begin{aligned} \vec{w}_k(s) &= -\left[\mathbf{D}(s+C,s) - \hat{\lambda}_k\right]^{-1}\mathbf{G}(s+C,s)\,\vec{v}_k(s) \qquad \forall\, k \in \{I, II, III\} \\ \vec{w}_k(s) &= \frac{1}{\sqrt{2}}\begin{pmatrix} 1 \\ -i \end{pmatrix} e^{-i\psi_0(s)} \qquad k = IV \end{aligned} \tag{3.59}$$

with

$$\vec{w}_{-k}(s) = [\vec{w}_k(s)]^* \qquad \forall\, k \in \{I, II, III, IV\}$$

The corresponding eigenvalues of $\mathbf{M}_{8\times 8}(s+C,s)$ are $\hat{\lambda}_k = e^{\,i\,2\pi\nu_k}$, where ν_k are the orbital tunes ($k \in \{I, II, III\}$) and $\nu_{IV} = \nu_0$; $\nu_{-k} = -\nu_k$ ($k \in \{I, II, III, IV\}$).

In the absence of radiation

$$\vec{u}(s) = \sum_{k=I,II,III} \{A_k\,\vec{v}_k(s) + A_{-k}\,\vec{v}_{-k}(s)\} \tag{3.60}$$

where the amplitudes A_k are constants of motion. However, the synchrotron radiation adds a non–Hamiltonian part to the problem. But the radiation effects in a storage ring are usually weak (in HERA for example the radiation losses in one turn are only a fraction of a percent of the total energy) and can therefore be treated as a perturbation. Hence using perturbation theory the full problem, including radiation, can be solved and then [Ch79, MR83, EMR99] in the linear approximation the solution to the orbital part of the problem has the general form

[19] $\vec{v}^{\,\dagger} = (\vec{v}^{\,*})^{\mathrm{T}}$ and $\mathbf{S}$ is the unit symplectic matrix defined by $\mathbf{S} = \begin{pmatrix} 0 & -1 & 0 & 0 & 0 & 0 \\ 1 & 0 & 0 & 0 & 0 & 0 \\ 0 & 0 & 0 & -1 & 0 & 0 \\ 0 & 0 & 1 & 0 & 0 & 0 \\ 0 & 0 & 0 & 0 & 0 & -1 \\ 0 & 0 & 0 & 0 & 1 & 0 \end{pmatrix}$

$$\vec{u}(s) \;=\; \sum_{k=I,II,III} \{A_k(s)\,\vec{v}_k(s) + A_{-k}(s)\,\vec{v}_{-k}(s)\} \tag{3.61}$$

where again the $A_k(s)$ are the amplitudes for the orbital modes k but are now s dependent stochastic variables. It was pointed out earlier that the electron beam size is determined by the balance between quantum diffusion and radiation damping. Because of the statistical character of the radiation, the only relevant quantities which can be evaluated are moments of statistical distributions. The equilibrium values of the beam dimensions can be calculated from eqn. (3.61) using the expression originally given by Chao [Ch79, MR83, Bb91, EMR99]

$$\langle |A_k|^2 \rangle \;=\; \frac{55 r_e \hbar \gamma^5}{48\sqrt{3} mc \alpha_k} \oint \frac{|v_{k5}|^2}{|\rho(s)|^3} ds \tag{3.62}$$

which is independent of azimuth s and where the α_k are the radiation damping constants

$$\alpha_k \;=\; \frac{T}{\tau_k} \;=\; -2\pi\, \Im\mathfrak{m}\{\,\partial\nu_k\,\}, \qquad (\,k \in \{I, II, III\}\,) \tag{3.63}$$

with T the revolution time and τ_k the radiation damping times. Further, the $\partial\nu_k$ are the complex tune shifts caused by the (non–symplectic) damping.

Moreover, in the linear approximation $\hat{n}(\vec{u};s)$ is given by a simple expression in terms of (undamped!) eigenvectors and amplitudes [Ma85, BHR92]

$$\hat{n}(\vec{u};s) - \hat{n}_0(s) \;\equiv\; \begin{pmatrix} \alpha(\vec{u};s) \\ \beta(\vec{u};s) \end{pmatrix} = \sum_{k=I,II,III} \{A_k\,\vec{w}_k(s) + A_{-k}\,\vec{w}_{-k}(s)\} \tag{3.64}$$

where the amplitudes are determined by the position in phase space $\vec{u}$ through (3.60). Recall from our previous heuristic picture that the non–flip spin motion is not directly affected by the radiation, but only indirectly through the orbital motion. The explicit dependence of $\hat{n}$ on $\vec{u}$ can be seen by writing eqn. (3.64) as

$$\begin{pmatrix} \alpha(\vec{u};s) \\ \beta(\vec{u};s) \end{pmatrix} = -2\,\Re\mathfrak{e}\left\{ \sum_{k=I,II,III} i\,\vec{w}_k(s) \cdot \vec{v}_k^{\dagger}(s)\,\mathbf{S} \right\} \vec{u}(s) \;=\; \mathbf{H}_{2\times 6}\,\vec{u}(s) \tag{3.65}$$

The linearized version of the spin–orbit coupling function, given in the $(\hat{n}_0, \hat{m}, \hat{l}\,)$ frame reads [Ma85]

$$\frac{\partial \hat{n}}{\partial \delta}(s) \equiv i \sum_{k=I,II,III} \{v_{k5}^*\,\vec{w}_k - v_{k5}\,\vec{w}_k^*\} = -2\,\Im\mathfrak{m} \sum_{k=I,II,III} v_{k5}^*\,\vec{w}_k \tag{3.66}$$

Note that to first order the spin–orbit coupling function does not depend on the phase space position $\vec{u}$. Each term in the sum in (3.66) essentially describes the product of the sensitivity of an orbit amplitude to a fractional energy change (v_{k5}^*) with the sensitivity of $\hat{n}$ to that orbit amplitude ($\vec{w}_k$). The linearization of $\hat{n}$ and $\frac{\partial \hat{n}}{\partial \delta}$ has the effect that only resonances of the first order can be reproduced (cf. eqn. (3.44))

$$\nu_0 = m + m_I\,\nu_I + m_{II}\,\nu_{II} + m_{III}\,\nu_{III}$$

where $|m_I| + |m_{II}| + |m_{III}| = 1$. These arise from the denominator matrix in eqn. (3.59). Observe that the theory is only valid for $\sqrt{\alpha^2+\beta^2} \ll 1$.

Finally, the depolarization rate in this approximation is given using eqn. (3.25) by

$$\tau^{-1}_{dep,lin} = \frac{55\sqrt{3}}{36}\frac{r_e\gamma^5\hbar}{m}\frac{1}{C}\oint \frac{1}{|\rho(s)|^3}\sum_{j=1,2}\left(\Im\mathfrak{m}\sum_{k=I,II,III} v^*_{k5}(s)\,w_{kj}(s)\right)^2 ds \tag{3.67}$$

The linear formulation presented here is usually called the SLIM formalism since it makes use of the 8×8 matrix and the eigenvectors introduced by Chao [Ch81a, Ch81b] in the code SLIM. There, instead of being used to describe $\hat{n}$ the matrices and eigenvectors are used to estimate the depolarization rate for spins which are initially on the closed orbit and diffuse away from $\hat{n}_0$, but the same expression as in eqn. (3.67) for $\tau^{-1}_{dep,lin}$ is obtained.

3.2.2 Alternative formulations of the linear radiative spin theory

Until now our description of coupled linear spin–orbit motion has been carried out using the particle coordinates $\vec{u} \equiv (x, x', z, z', \ell, \delta) \simeq \left(x, \frac{p_x}{p}, z, \frac{p_z}{p}, \ell, \delta\right)$. However, additional valuable insight into spin–orbit dynamics can be gained by rewriting the SLIM formalism in terms of "betatron–dispersion" coordinates, namely by defining

$$x_\beta \,=\, x - \delta\, D_1\,, \qquad z_\beta \,=\, z - \delta\, D_3 \tag{3.68}$$

Here $\vec{D} \equiv (D_1, D_2, D_3, D_4)$ is the dispersion vector [20] and x_β, z_β are the free betatron oscillations about the instantaneous orbit $\delta\, D_{1,3}(s)$. The corresponding 8×8 matrix formalism is obtained by making a canonical transformation of the coordinates thus [BR99]

$$\vec{\tilde{u}} = \mathbf{K}\cdot\vec{u} \tag{3.69}$$

where

$$\mathbf{K}(s) = \begin{pmatrix} 1 & 0 & 0 & 0 & 0 & -D_1 \\ 0 & 1 & 0 & 0 & 0 & -D_2 \\ 0 & 0 & 1 & 0 & 0 & -D_3 \\ 0 & 0 & 0 & 1 & 0 & -D_4 \\ D_2 & -D_1 & D_3 & -D_4 & 1 & 0 \\ 0 & 0 & 0 & 0 & 0 & 1 \end{pmatrix} \tag{3.70}$$

For instance the new 6×6 orbit transfer matrix $\tilde{\mathbf{M}}$ is obtained via

[20] $\vec{D}$ is the periodic solution of the linearized equations of motion for $\left(x, \frac{p_x}{p}, z, \frac{p_z}{p}\right)$ when $\delta = 1$ and without the RF cavities.

$$\tilde{\mathbf{M}}(s_1, s_0) = \mathbf{K}(s_1) \cdot \mathbf{M}(s_1, s_0) \cdot \mathbf{K}^{-1}(s_0) \tag{3.71}$$

$$\Longrightarrow \qquad \vec{v}_k(s) = \mathbf{K}(s)\, \vec{v}_k(s) \tag{3.72}$$

and the corresponding matrix for the spin, $\tilde{\mathbf{G}}$, is given by

$$\tilde{\mathbf{G}}(s_1, s_0) = \mathbf{G}(s_1, s_0) \cdot \mathbf{K}^{-1}(s_0) \tag{3.73}$$

The spin components of the eigenvectors can now be expressed as

$$\vec{w}_k(s) = -\Big[\mathbf{D}(s+C, s) - \hat{\lambda}_k\Big]^{-1} \tilde{\mathbf{G}}(s+C, s)\, \vec{v}_k(s) \qquad \forall\, k \in \{I, II, III\} \tag{3.74}$$

Note that the eigenvalues (tunes) are unchanged under this transformation, and that $\vec{w}_k = \vec{w}_k$. As a result of the separation of the transverse coordinates into betatron and dispersion contributions, columns $1-4$ of $\tilde{\mathbf{G}}$ for a magnet only contain terms depending on the betatron coordinates, whereas the sixth column contains terms depending on the dispersion. This circumstance can be used when analyzing the origin of first order resonances.

Spin–orbit coupling can now also be discussed in terms of $\tilde{\mathbf{G}}$, but the use of betatron–dispersion coordinates also allows us to discuss spin–orbit coupling directly in terms of Courant–Snyder parameters. Assuming now that the transverse phase space planes are decoupled, then $\vec{\omega}$ in the linear approximation can be decomposed into its contributions due to radial betatron (x_β), vertical betatron (z_β) and longitudinal (s) motion

$$\vec{\omega}(\vec{u}; s) =_1 \vec{\omega}_{x_\beta}(\vec{u}; s) + \vec{\omega}_{z_\beta}(\vec{u}; s) + \vec{\omega}_s(\vec{u}; s) \tag{3.75}$$

In analogy with our previous decomposition into amplitudes and eigen modes (see eqn. (3.40) and accompanying text) we rewrite this as

$$\vec{\omega}(\vec{u}; s) =_1 \frac{1}{2} \sum_j \Big(\tilde{A}_{+j}\, \vec{\omega}_{+j}(s) + \tilde{A}_{-j}\, \vec{\omega}_{-j}(s) \Big) \qquad \forall\, j \in \{x_\beta, z_\beta, s\} \tag{3.76}$$

where $\tilde{A}_{\pm j}$ are new orbit amplitudes for the modes j. By taking into account only the dominant contributions, namely from the quadrupoles, we are left with [CY81, BS86, BR99]

$$\begin{aligned}
\vec{\omega}_{\pm x_\beta}(s) &= (a\gamma + 1)\, g(s) \sqrt{\beta_x(s)}\, e^{\pm i \psi_x(s)}\, \hat{e}_z \\
\vec{\omega}_{\pm z_\beta}(s) &= -(a\gamma + 1)\, g(s) \sqrt{\beta_z(s)}\, e^{\pm i \psi_z(s)}\, \hat{e}_x \\
\vec{\omega}_{\pm s}(s) &= (a\gamma + 1)\, g(s) \left[\hat{e}_z D_x(s) - \hat{e}_x D_z(s)\right] e^{\pm i \psi_s(s)}
\end{aligned} \tag{3.77}$$

where $g = \frac{ec}{E_0}\Big(\frac{\partial \mathcal{B}_z}{\partial x}\Big)_{x=z=0}$ are the normalized quadrupole field gradients. We define the one–turn linear *spin–orbit coupling integrals* as

$$
\begin{aligned}
J_{\pm x}(s) &= \int_s^{s+C} \left[\hat{m}_0(s') + i\,\hat{l}_0(s')\right] \cdot \vec{\omega}_{\pm x_\beta}(s')\, ds' \\
J_{\pm z}(s) &= \int_s^{s+C} \left[\hat{m}_0(s') + i\,\hat{l}_0(s')\right] \cdot \vec{\omega}_{\pm z_\beta}(s')\, ds' \\
J_{\pm s}(s) &= \int_s^{s+C} \left[\hat{m}_0(s') + i\,\hat{l}_0(s')\right] \cdot \vec{\omega}_{\pm s}(s')\, ds'
\end{aligned}
\tag{3.78}
$$

An accelerator lattice is said to be *linearly spin matched* at an azimuth s_0 if for all $k \in \{\pm x, \pm z, \pm s\}$ the $J_k(s_0)$ vanish. These spin matching conditions are equivalent to requiring that $\tilde{\mathbf{G}}(s+C,s)\,\vec{v}_k(s) = 0$ in eqn. (3.74) for one turn, starting at $s = s_0$ (see also eqn. (3.59)). Spin matching in terms of the $\mathbf{G}$ matrix will be discussed in Chapter 4. The relevance of the spin–orbit coupling integrals is illustrated by the fact that in the betatron–dispersion formalism, and considering just the effect of quadrupoles, eqn. (3.66) becomes

$$
\frac{\partial \hat{n}}{\partial \delta}(s) \;=_1\; \frac{1}{2}\,\Im\mathfrak{m} \sum_{k=\pm x,\pm z,\pm s} \left[\hat{m}_0(s) + i\,\hat{l}_0(s)\right]^* \Delta_k(s) \tag{3.79}
$$

where

$$
\begin{aligned}
\Delta_{\pm x}(s) &= \frac{e^{\mp i\psi_x(s)}}{e^{\,i\,2\pi[\nu_0 \pm \nu_x]} - 1}\, J_{\pm x}(s)\, \frac{[-D_x(s) \pm i\{\alpha_x(s) D_x(s) + \beta_x(s) D_x{}'(s)\}]}{\sqrt{\beta_x(s)}} \\
\Delta_{\pm z}(s) &= \frac{e^{\mp i\psi_z(s)}}{e^{\,i\,2\pi[\nu_0 \pm \nu_z]} - 1}\, J_{\pm z}(s)\, \frac{[-D_z(s) \pm i\{\alpha_z(s) D_z(s) + \beta_z(s) D_z{}'(s)\}]}{\sqrt{\beta_z(s)}} \\
\Delta_{\pm s}(s) &= \frac{e^{\pm i\psi_s(s)}}{e^{\,i\,2\pi[\nu_0 \pm \nu_s]} - 1}\, J_{\pm s}(s)
\end{aligned}
\tag{3.80}
$$

Thus $\frac{\partial \hat{n}}{\partial \delta}(s_0)$ vanishes if the lattice is linearly spin matched at s_0. Note that α and β appearing in the third factor in the first two equations above are the Courant–Snyder parameters and should not be confused with the spin variables introduced in eqn. (3.50). The expression for $\frac{\partial \hat{n}}{\partial \delta}$ in eqn. (3.79) in terms of spin–orbit coupling integrals is identical to the expression for the vector $\vec{d}$ given by Chao and Yokoya [CY81] in their calculation of spin diffusion with respect to $\hat{n}_0$.

3.2.3 Synchrotron sidebands

The depolarization rate associated with sidebands of isolated parent resonances, $\nu_0 = m \pm \nu_y$, is approximately proportional to the depolarization rate of the parent resonance. For example, using betatron–dispersion coordinates, one finds that the modification, due to sidebands, to the depolarization rate associated with an isolated parent betatron resonance can be represented symbolically as [21]

$$
\tau_{dep}^{-1} \propto \frac{A}{(\nu_0 \pm \nu_y)^2} \quad \rightarrow \quad \tau_{dep}^{-1} \propto \sum_{m_s=-\infty}^{\infty} \frac{A\, B(\xi; m_s)}{(\nu_0 \pm \nu_y \pm m_s\, \nu_s)^2} \tag{3.81}
$$

[21] Analogous but different formulae can also be derived for the effect of synchrotron sidebands of a parent first order synchrotron resonance.

where A is an energy dependent factor originating in the non–resonant factors in eqn. (3.79) when evaluating the depolarization rate using eqn. (3.25). The $B(\xi; m_s)$'s, which are called *enhancement factors*, contain modified Bessel functions $I_{|m_s|}(\xi)$ and $I_{|m_s|+1}(\xi)$ depending on the *modulation index* $\xi = \left(\frac{a\gamma\sigma_\delta}{\nu_s}\right)^2$. The explicit expression for $B(\xi; m_s)$ can be found in [Ma90, Ma92]. See also the derivation in [Yo83]. The underlying strength parameter ξ increases strongly with energy and energy spread. Using HERA parameters, we find that $\xi \approx 1$ (with $a\gamma = 62.5$, $\sigma_\delta \simeq 1 \cdot 10^{-3}$ and $\nu_s \simeq 0.06$). Taking $\xi = 1$ we find the values 0.88, 0.72 and 0.27 for $B(\xi;0), B(\xi;1)$ and $B(\xi;2)$ respectively. For $\xi = 2$ the corresponding values would be 1.17, 1.02 and 0.58. We see that $B(\xi; m_s)$ falls off as $|m_s|$ increases, but also that as ξ increases higher order sidebands become more and more significant. In any case it is clear that synchrotron sidebands are important for HERA. It should be emphasized that this approximation for synchrotron sidebands is based on the assumption that the parent resonances are well separated, and does not account for interference effects. But it is nevertheless a useful guide. An alternative model for treating synchrotron sidebands is presented in Chapter 7.

3.2.4 Higher order Monte Carlo simulations — SITROS

The linear approximation which is the basis for the SLIM formalism, as has been emphasized, only reproduces first order resonances. This is equivalent to saying that in the SLIM approximation the $\boldsymbol{\omega}$ at different azimuths commute. However, we know from the multiple integrals discussed earlier in this chapter that we cannot neglect non–commutation. The sideband effect is a good example of this. In order to get a realistic picture of the spin dynamics in a storage ring it is therefore necessary to go to higher order. But as we have seen, most of the codes available for the calculation of high order spin–orbit motion are either not customized for radiating particles and/or require very large computing capacity. What we need is an algorithm where these shortcomings have been overcome by some reasonable simplifying assumptions and a code that can calculate the equilibrium polarization for electrons.

The SLIM family of programs as well as SMILE, SODOM and SPRINT are all based on calculations of the quantities $\hat{n}$ and $\frac{\partial \hat{n}}{\partial \delta}$ in the Derbenev–Kondratenko formula (3.20). A more pragmatic way of treating spin polarization in rings is employed in the Monte Carlo tracking code SITROS. Here the central concept is the estimation of the depolarization time from tracking data of a sample of test particles with spins attached to them, under the influence of radiation damping and stochastic excitation of the orbit motion. Hence SITROS simulates the heuristic model of spin diffusion that I pictured earlier. The SITROS code was originally written and described by Kewisch [Ke85]. A presentation of the code and the approximations used in the calculations can also be found in [Bö94], but for the sake of clarity the main concepts and connections to relevant underlying physics will be repeated here. An account of recent updates to the program is given in Appendix C.

In SITROS an ensemble of electrons (positrons) is tracked in the electromagnetic fields of a storage ring for many turns. The tracking takes place in two stages. First only orbital tracking is performed, to establish an equilibrium phase space distribution, and in a second stage spin motion is added. The basic equations of motion for the orbit and the spin are given in Appendix A: eqs. (A.1) with (A.2) and (A.13). Performing direct integration of these equations for many particles over thousands of turns in an accelerator is not practical and therefore some form of transfer matrix formalism should be adopted. In SITROS, the transformation of the orbital coordinates through the main lattice elements is represented by 6×6 first order maps with built in damping, i.e. δ dependent effects corresponding to the term $\vec{R}^D$ in eqn. (A.2) are taken into account. The nonlinearities in the lattice (sextupoles and beam–beam effects) are included as thin lens kicks. In order to reduce the computing time, the ring structure in SITROS is divided into sections. The elements in a section of the ring are lumped together such that the individual orbit and spin maps are concatenated into just one map for the orbit and one map for the spin, representing the entire section. Therefore stochastic radiation can only take

place between the sections. The subdivision is chosen by the user, but requires that at least one dipole (or combined function magnet) is contained in each division.

The radiation damping built into the orbit matrices of SITROS reflects the non–Hamiltonian character of the problem and implies non–symplecticity. For a pure dipole field, the smooth averaged radiation leads to a damping of the sixth orbital coordinate δ (transverse recoils affecting x' and z' are ignored), whereas in combined function magnets the dissipation can cause antidamping of the transverse motion. The phases and voltages of the accelerating cavities are set so that the energy lost in the bending fields is compensated by the average energy gain in the cavities. The weak radiation coming from quadrupoles, sextupoles and solenoids is neglected. The stochastic part of the synchrotron radiation process, $\delta\vec{\mathcal{R}}$ in Appendix A, is usually modelled as a white noise process with the properties given in eqn. (A.11)

$$\begin{aligned} \langle\, \delta\vec{\mathcal{R}} \,\rangle &= 0 \\ \langle\, \delta\vec{\mathcal{R}}(s)\, \delta\vec{\mathcal{R}}(s') \,\rangle &= \frac{55 r_e \hbar \gamma^5}{24\sqrt{3} mc} \frac{1}{|\rho(s)|^3} \delta(s-s') \end{aligned}$$

SITROS approximates the stochastic radiation effects by emitting a small number of "high energy" photons, which in practice means that a random kick chosen from a truncated centered Gaussian distribution is given to the energy offset coordinate δ at the beginning of each section. The tracking is started with all particles on the closed orbit. From our simple diffusion model with damping and noise, assuming that all initial transients have died away, we expect the beam size σ_k ($k \in \{I, II, III\}$) to develop with time as [He97]

$$\sigma_k(t) \approx \sigma_k^{lin} \sqrt{1 - \exp(-\frac{t}{\tau_k})} \tag{3.82}$$

where σ_k^{lin} and τ_k are beam size and damping time for mode k from linear theory (eqs. (3.62) and (3.63)). Writing the random energy change $\Delta\delta$ as a product of a strength factor, K, and a random variable, η, an estimate for the excitation strength needed at the radiation points in the tracking to reproduce the correct beam dimensions is given by [Bö94]

$$\begin{aligned} K &= 2\sqrt{\frac{T\langle\, \delta^2 \,\rangle}{\tau_s \langle\, \eta^2 \,\rangle N_R}} \\ \langle\, \eta^2 \,\rangle &= 1 - \frac{\frac{n_c}{\sqrt{2}} \exp\left(-\frac{n_c^2}{2}\right)}{\frac{\sqrt{\pi}}{2} \operatorname{erf}\left(\frac{n_c}{\sqrt{2}}\right)} \end{aligned} \tag{3.83}$$

provided that the centered Gaussian random distribution, $g(\eta)$ describing the emissions has unit variance and is cut off at n_c standard deviations. In SITROS the cut off is made at $n_c = 1$. Here $\langle\, \delta^2 \,\rangle$ and $\langle\, \eta^2 \,\rangle$ are the second moments of the energy offset variable δ and the random variable η respectively, N_R is the number of radiation points, erf( ) is the error function [AS70], and T is again the revolution time. Note the explicit use of the index s in τ_s, indicating an uncoupled or only weakly coupled optic. To make sure that the model, with only a restricted number of radiators representing the stochastic part of the radiation process, returns the expected beam sizes, the excitation strength

is adjusted during the tracking. The simulated rms beam size [22] in one dimension, preferably in the longitudinal plane, is monitored during the tracking and compared with the predicted value from linear theory σ_y^{lin} at fixed time intervals, which are taken to be multiples of the damping time in that plane. If the tracked rms beam size has not converged to the linear value for a given K at the end of the time interval, the excitation strength is modified by subtracting from it $f_g \left(\sigma_y^{tracked} - \sigma_y^{lin}\right)/\sigma_y^{lin}$, where f_g is an appropriately chosen scale factor.

The SITROS section matrices describing the transformations of the orbital coordinates in the tracking contain the lattice nonlinearities up to second order. This means that an input particle trajectory is described by a 28 component vector $\vec{X}_{(2)}$ made up of all first and second order monomials of the phase space coordinates with respect to the closed orbit, plus an entry for the closed orbit itself

$$\vec{X}_{(2)} \;=\; \left(1, x, x', z, z', \ell, \delta, x^2, x'^2, \ldots, z'\delta, \ell\delta\right) \tag{3.84}$$

Thus the section matrices, relating the output phase space coordinates to the input $\vec{X}_{(2)}$ vector, are of dimension 6×28 and consist of the differential quotients of the 6 output first order monomials with respect to the 28 input first and second order monomials. The section matrices are calculated prior to the "real" tracking in a "test" tracking of a set of particles through the sections, starting at representative positions. $\pm 1\sigma$ is the pragmatic choice used in SITROS. Counting all possible sign combinations at the starting point, 73 test trajectories are needed. The test trajectories are obtained by using 6×6 matrices for the linear elements and nonlinear kicks from the sextupoles. An analogous method is used for the determination of the coefficients of the transfer maps for the spin motion in Chapter 5.

The spin transformations in SITROS are represented using a *quarternion formalism*, which is closely connected to SU(2) spinor algebra. In this formalism, the basic quantity is the unit–quarternion defined as

$$\bar{q} \;\equiv\; (q_0, q_1, q_2, q_3) \equiv \left(\cos\frac{\varphi}{2}, \sin\frac{\varphi}{2}\hat{q}\right) \tag{3.85}$$

with $\|\bar{q}\| = 1$. The rotation angle φ and the unit vector $\hat{q}$ are related to the spin precession vector $\vec{\Omega} = \sum \Omega_j \, \hat{e}_j$ ($j \in \{x, z, s\}$), integrated over some short distance Δs for which $\vec{\Omega} \approx$ const., through

$$\begin{aligned} \varphi &= \int_{\Delta s} \|\vec{\Omega}\| \, ds \\ \hat{q}_j &= \frac{\int_{\Delta s} \Omega_j \, ds}{\|\int_{\Delta s} \vec{\Omega} \, ds\|} \qquad \forall\, j \in \{x, z, s\} \end{aligned} \tag{3.86}$$

The spin transformation across a lattice element in the language of unit–quarternions is given by the composition of two quarternions and can be expressed as a product of a real 4×4 matrix with an initial quarternion

[22] $\sigma_y \equiv \sqrt{\dfrac{\sum_{i=1}^{N} (y_i - \langle y \rangle)^2}{N-1}}$ $\quad (y = x, z, s)$ where $\langle y \rangle = 0$ (the closed orbit).

$$\begin{pmatrix} q_0 \\ q_1 \\ q_2 \\ q_3 \end{pmatrix}_f = \begin{pmatrix} q_0 & -q_1 & -q_2 & -q_3 \\ q_1 & q_0 & -q_3 & q_2 \\ q_2 & q_3 & q_0 & -q_1 \\ q_3 & -q_2 & q_1 & q_0 \end{pmatrix}_{l.e} \begin{pmatrix} q_0 \\ q_1 \\ q_2 \\ q_3 \end{pmatrix}_i \tag{3.87}$$

A summary of the rules for quarternion algebra and a discussion on its relation to the SO(3) formalism and SU(2) spinor algebra is given in [Vo00]. See also [Mo84].

We have seen earlier that even in the case of linear orbit motion, the spin motion is nonlinear (cf. eqn. (3.51)). To handle these nonlinearities economically, the following approximations are made in SITROS

- For dipoles there is only a minor dependence of $\vec{\Omega}$ on the transverse coordinates (introduced by the weak focusing of these magnets). The phase space dependence can therefore to a good approximation be averaged over the element length. The dipole fields due to correction coils and to orbit offsets with respect to the centres of quadrupoles and sextupoles are also treated in this way.
- For quadrupoles and higher order multipoles (mainly sextupoles) the phase space dependence of $\vec{\Omega}$ cannot be neglected. See, for example, eqn. (3.33). On the other hand, the spin rotations in these magnets are usually small and rotations around different axes in a magnet can therefore be treated as if they would commute. For purely transverse fields the following relationship between the spin rotation and the particle deflection hold: $\int \vec{\Omega}\, ds = (a\gamma + 1)\,(-\Delta z', \Delta x', 0)^T$. Note that the spin rotation experienced in solenoid end fields and due to the (linearized) beam–beam effect is given by this same expression.

The tracking in SITROS is typically done for an energy range of 441 MeV (spanning the interval of one integer in $a\gamma$). For this the quarternion spin maps, parametrized as second order polynomials in the orbital coordinates at each energy step, and the orbit maps for the central energy point [23] are combined into a matrix of dimension $(6 + 4 \cdot N_E) \times 28$, multiplying onto the vector $\left(\vec{X}_{(2);1}, \ldots, \vec{X}_{(2);N_E}\right)^T$, where N_E is the number of energy steps. The parametrization of the maps leads to extra artificial nonsymplecticity in the orbital maps. Moreover it changes the length of the spin quarternions slightly, thereby violating the orthogonality of the rotation matrices. [24] The additional nonsymplecticity is usually quite small compared to the damping related nonsymplecticity and can be neglected, but the unitarity of the spin quarternions must be restored in each step by normalizing them to avoid an unphysical blowup or shrinking of the spin vectors during the course of the multi–turn tracking.

Although the spin transformations through individual lattice elements as well as the concatenated transformations for sections of the ring in SITROS are described by quarternions and compositions thereof, which are new quarternions, the actual spin transport across a section is carried out by using a 3×3 rotation. Given a spin vector $\widehat{S} = (S_x, S_z, S_s)$, the transformation across a section of the ring, represented by the quarternion map $\bar{q}$ is

$$\widehat{S}_f = \mathbf{R}_{\bar{q}}\, \widehat{S}_i \tag{3.88}$$

$$\mathbf{R}_{\bar{q}} = 2 \begin{pmatrix} q_0^2 + q_1^2 - \frac{1}{2} & q_1 q_2 - q_0 q_3 & q_1 q_3 + q_0 q_2 \\ q_2 q_1 + q_0 q_3 & q_0^2 + q_2^2 - \frac{1}{2} & q_2 q_3 - q_0 q_1 \\ q_3 q_1 - q_0 q_2 & q_3 q_2 + q_0 q_1 & q_0^2 + q_3^2 - \frac{1}{2} \end{pmatrix} \tag{3.89}$$

[23] The change in the orbital maps for this energy range is negligible.

[24] Recall that the unitarity or, equivalent, orthogonality condition for the unit–quarternion simply reads $\|\bar{q}\| = 1$.

The final spin tracking in SITROS is carried out with the phase space distribution in equilibrium with all spins initially parallel to the stable closed orbit spin solution $\hat{n}_0$. Then the polarization with respect to $\hat{n}_0(s_{o.p})$ at some observation point $s_{o.p}$ is monitored for a large number of turns. In this way it is possible to get an estimate of the depolarization rate and by combining it with the polarization build–up rate eqn. (3.19) an estimate for the equilibrium polarization is obtained (eqn. (3.26))

$$P_{eq} \simeq P_{BKS} \frac{\tau_{dep}}{\tau_{BKS} + \tau_{dep}} = P_{BKS} \frac{\tau_{DK}}{\tau_{BKS}}$$

In practice, the depolarization rate is obtained from the tracking data via a fit of the relation

$$\tau_{dep}^{-1}(t_i) = \frac{\ln(P_{\tau_{dep}}(t_0)) - \ln(P_{\tau_{dep}}(t_i))}{t_i - t_0} \qquad \forall\, i \in \{1, \ldots, N_T\} \tag{3.90}$$

where

$$P_{\tau_{dep}}(t_i) = P_{BKS} \frac{1}{N_P} \sum_{j=1}^{N_P} \widehat{S}_j(t_i) \cdot \hat{n}_0(s_{o.p}) \tag{3.91}$$

Here $t_i = \frac{i\,C}{c}$ for all $i \in \{1, \ldots, N_T\}$, where N_T is the number of tracking turns, and N_P is the number of particles.

The sectioning technique used in SITROS has the obvious disadvantage of potentially poor representation of the nonlinearities in the optic and the stochastic radiation process. These disadvantages have become apparent in calculations with SITROS for the HERA luminosity upgrade electron optic. For this optic the small number of sections used in past calculations for HERA [Li88, Bö94] (a few times 10) is not enough to accurately reproduce the equilibrium beam sizes and to calculate the equilibrium polarization. The maximum number of allowed sections has therefore been increased so that each section (and hence radiation point) contains only one dipole or combined function magnet in HERA. Moreover, the spin representation in the parametrized maps now contains the quarternion components instead of spins parametrized in the vector–angle representation, which was implemented in an older version of the code. For more details on recent upgrades of SITROS, see Appendix C.

The SITROS package consists of a number of modules, each with its own main program (named SITA, SITB, SITC, SITD, SITE and SITF), that is responsible for a part of the algorithm. A flow diagram illustrating the connections between the different parts can be found in Appendix C. The tasks of the different modules can be summarized as follows:

- In SITA a PETROS [Ke78] optic file (with or without distortions, corrections and harmonic bumps – see next chapter) is read and the basic optic parameters, such as optical functions, closed orbit and emittances are calculated using linear orbit theory. $\hat{n}_0$ is computed as well as the asymptotic polarization P_{BKS} and the polarization build–up time τ_{BKS}, for the chosen energy points. Section matrices for the orbit and the spin are constructed in the way previously described.

- The starting value for the excitation strength K is set in SITB. Other quantities needed for the tracking are also initialized here, among them the number of particles N, the starting particle distributions (all particles set on the closed orbit as default) and the beam–beam parameters.

- The first stage of the tracking is carried out in SITC. The particle orbits are tracked for a few damping times, typically 5000 turns, in order to achieve the correct equilibrium beam sizes.

- Simultaneous spin and orbit tracking is performed in SITD, starting as mentioned with all spins initially parallel to $\hat{n}_0$. For each of typically 5000 tracking turns the projections of the individual spin vectors onto the $\hat{n}_0$ basis vector at the starting azimuth are noted and an ensemble average is calculated.

- Finally in SITE, an estimate of the depolarization time τ_{dep} is evaluated from the tracking data and P_{eq} can be calculated from eqn. (3.26).

- SITF differs from the other modules in that it is a "stand–alone" program, calculating the polarization in the linear approximation, using the SLIM technique.

Chapter 4

HERA Polarization in Light of the Upgrade

4.1 Electron polarization — experience gathered at HERA

In the last chapter we have learned that the electron polarization in a storage ring such as HERA is the result of a competition between radiation induced build–up due to the Sokolov–Ternov effect and spin diffusion. At HERA the polarization reaches equilibrium in a few tens of minutes. It has been argued that this equilibrium polarization should be nearly parallel to the $\hat{n}$–axis, which in turn is closely aligned along $\hat{n}_0$, except very close to resonances. In a perfectly planar ring without solenoids $\hat{n}_0$ is vertical. Vertical electron beam polarization was first observed in HERA in November 1991, and polarization values of over 70 % were achieved only a few months later after dedicated machine tuning [Bb95].

As pointed out in Chapter 1, most of the high energy physics that can be done with polarized beams requires polarization in the beam direction, i.e. longitudinal polarization. This is achieved by bringing the natural transverse polarization of the arcs into the longitudinal direction at the interaction points using special magnet arrangements — so called spin rotators. Since the generation and maintenance of the naturally occurring polarization requires that the polarization direction be vertical in the arcs, spins rotated into the longitudinal direction at an IP must be rotated back to the vertical direction before entering the next machine arc. Spin rotators therefore always come in pairs. The provision of longitudinally polarized $e^{+/-}$ beams for the collider experiments was one of the features of the original HERA design. After successful operation with vertically polarized beams, a first pair of spin rotators of the Buon–Steffen Mini–Rotator type [BS86] was installed in the East straight section of HERA in 1993–94 to serve the HERMES experiment with longitudinal spin polarization. A rotator consists of a chain of interleaved horizontal and vertical bending magnets, replacing two ordinary bending magnets at the end of the regular arc structure on either side of the IP. The vertical bending magnets of the two rotators in the pair form closed bumps on each side of the IP, the left and the right side bumps being asymmetric with respect to the IP. The HERA rotators are designed to operate in an energy range from 26.8 GeV to 39 GeV and they allow the change of spin helicity at the IP by reversing the signs of the vertical bumps. To facilitate this the magnets are mounted on remotely controlled jacks, so that the magnet elevation follows the vertical profile of the orbit, allowing operation within the specified energy range. The adjustment of the horizontal geometry necessary for changes in the beam energy greater than ± 100 MeV must however be performed manually. An illustration of the magnet lattice and the spin transformations in the rotator region on the upstream (left) side of the East IP is seen in Figure 4.1.

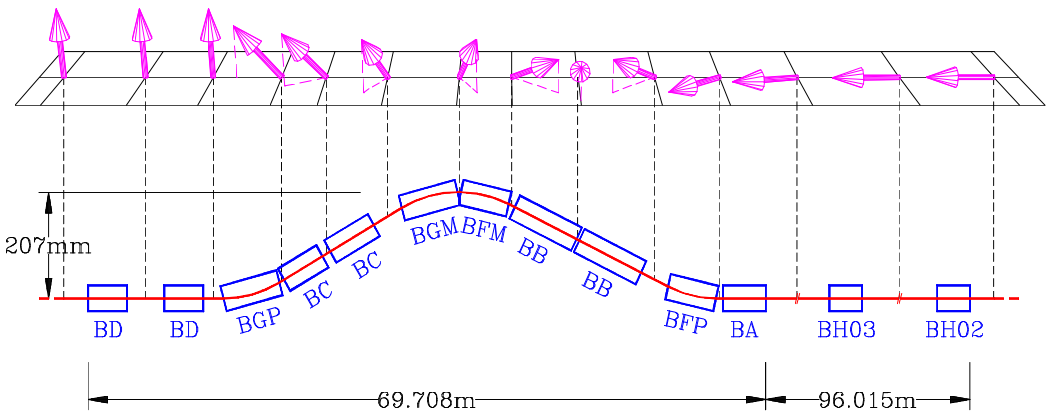

Figure 4.1: The left half of the rotator pair in the East. The magnets BH03 and BH02 are not an integral part of the rotator, but are needed to complete the spin rotation into the longitudinal direction. On the opposite side of the IP a similar magnet arrangement with reversed radial fields (BF and BG magnets) brings the polarization back to the vertical direction. Courtesy of M. Wendt.

A characteristic of dipole spin rotators is their effect on the maximum attainable equilibrium polarization. In a perfectly flat ring (without solenoids) $P_{_{eq,ST}} = 92.38\,\%$, but in a ring with rotators this upper limit is decreased since $\hat{n}_0$ is not antiparallel to the magnetic field at all positions along the closed orbit. See eqn. (3.17). The main part of this drop comes from the tilt of $\hat{n}_0$ in the rotator region itself, but for rings with dipole fields in the "straight sections" (such as in the HERA upgrade lattice) these sections also contribute to this loss. For HERA at a nominal energy of 27.5 GeV the drop is about 3 % for one pair of rotators. Hence, the starting condition for attaining a high level of spin polarization in a ring containing spin rotators is worse than in a ring without rotators. To this comes the effects of spin diffusion for particles in the fields of a real accelerator.

Spin diffusion can be particularly strong in a ring with spin rotators. One reason is that in the section between the rotators in a pair, $\hat{n}_0$ is horizontal and can hence be considered to be maximally tilted from the vertical. I will elaborate on the implications of a tilted $\hat{n}_0$ in the following pages. Another reason is that synchrotron radiation emitted in the rotators, where the vertical bends create a local vertical dispersion bump, excites vertical betatron oscillations. To achieve the highest possible polarization for the experiments, the detrimental effects of spin diffusion have to be minimized. This can be accomplished through the procedures of *spin matching* described in [BR99]. In practice spin matching is carried out in stages. Using available quadrupoles, not only should the usual optical conditions be fulfilled, but also additional requirements have to be met, forcing the spin–orbit coupling to vanish in the sense to be explained below. This is the first stage in setting up a spin matched optic. The method is called *strong synchro–beta spin matching* and is based on linearized spin–orbit theory for perfectly aligned machines. To illustrate the concept of strong linear synchro–beta spin matching and at the same time facilitate the description of the analysis carried out in Chapter 6 I will remind the reader here of some basic facts.

From the discussion in Section 3.2 it is clear that to maximize the polarization, $\tau_{dep,lin}^{-1}$ must be minimized. By eqn. (3.67) this is equivalent to saying that v_{k5}^* ($k \in \{I, II, III\}$) or the components of $\vec{w}_k$ should be minimized at azimuths where $\frac{1}{|\rho(s)|^3}$ is large. The v_{k5}^* determine the orbit excitation caused by synchrotron radiation (cf. eqs. (3.61) and (3.62)). In a ring with no transverse inter–mode coupling v_{II5}^* usually vanishes in the arcs, since there the vertical dispersion D_z vanishes. However, in rings with spin rotators v_{II5}^* does not vanish in the rotator regions, if the rotators contain vertical bends. The v_{I5}^* on the other hand, generally does not vanish in the arcs since the horizontal dispersion $D_x \neq 0$. Finally v_{III5}^* essentially never vanishes. The conclusion to draw from this is that one should at least try to minimize $\vec{w}_k$ for azimuths in the ring where $\frac{|v_{k5}^*|^2}{|\rho(s)|^3}$ gives a substantial contribution

to $\tau^{-1}_{dep,lin}$. Examination of eqn. (3.59) shows that the spin eigenvectors $\vec{w}_k$ for $k \in \{I, II, III\}$ are proportional to the one–turn $\mathbf{G}$ matrix. The strong spin matching therefore boils down to bringing the elements of $\mathbf{G}(s_f, s_i)$ to zero for the appropriate regions (going from azimuth s_i to s_f) or, if that is not possible, minimizing the product $\mathbf{G}(s_f, s_i) \cdot \vec{v}_k(s_i)$. Now, since in a perfectly flat ring without solenoids $\hat{n}_0$ is vertical, the vertical components of the two remaining base vectors of the periodic spin frame, $\hat{m}_z$ and $\hat{l}_z$, are zero. By inspection of the $\mathbf{G}$ matrix elements for horizontal bends and combined function magnets, quadrupoles and RF cavities (see for instance [Bb85b]) we find that in the absence of coupling, columns 1, 2, 5 and 6 of the one–turn $\mathbf{G}(s + C, s)$ vanish. Moreover, the one–turn orbit matrix and its corresponding eigenvectors have the general structure

$$\mathbf{M}_{6\times 6} = \begin{pmatrix} \star & \star & 0 & 0 & \star & \star \\ \star & \star & 0 & 0 & \star & \star \\ 0 & 0 & \star & \star & 0 & 0 \\ 0 & 0 & \star & \star & 0 & 0 \\ \star & \star & 0 & 0 & \star & \star \\ \star & \star & 0 & 0 & \star & \star \end{pmatrix} \quad ; \quad \vec{v}_x = \begin{pmatrix} \star \\ \star \\ 0 \\ 0 \\ \star \\ \star \end{pmatrix} \quad ; \quad \vec{v}_z = \begin{pmatrix} 0 \\ 0 \\ \star \\ \star \\ 0 \\ 0 \end{pmatrix} \quad ; \quad \vec{v}_s = \begin{pmatrix} \star \\ \star \\ 0 \\ 0 \\ \star \\ \star \end{pmatrix} \tag{4.1}$$

where $\star$'s symbolize nonzero components. Hence, by eqn. (3.59) $\vec{w}_I(s)$ and $\vec{w}_{III}(s)$ are zero in this case, and we already know that $v^*_{II5} \equiv v^*_{z5}$ vanishes in an uncoupled ring without rotators. The depolarization rate $\tau^{-1}_{dep,lin}$ is therefore automatically zero. In rings with rotators, the 90° tilt of $\hat{n}_0$ in the region between the rotators in a pair results in additional nonzero entries in the $\mathbf{G}$ matrix for this region for $\mathbf{G}_x$ and $\mathbf{G}_s$. Thus the one–turn $\mathbf{G}_x(s + C, s)$ and $\mathbf{G}_s(s + C, s)$, in addition to $\mathbf{G}_z(s + C, s)$, can be nonzero for any dipole inside or outside the rotator region. Observe that the one–turn elements of $\mathbf{G}_x$ and $\mathbf{G}_s$ everywhere in the ring arise solely from the rotator region, since $\hat{n}_0$ is vertical in the arcs. The task of synchro–beta spin matching of rings with rotators in terms of the $\mathbf{G}$ matrix can be summarized as follows [1]

- Minimize $\mathbf{G}_x$, $\mathbf{G}_z$ and $\mathbf{G}_s$ for the region between the rotators in a pair.
- Minimize $\mathbf{G}_z$ for an arc, i.e. from the centre of one rotator to the centre of the next rotator.

A section of a ring which has been spin matched according to these guidelines is said to be *spin transparent*. Note that the use of the $\mathbf{G}$ matrix for spin matching emphasizes the *local nature* of spin transparency. At DESY the SPINOR code [HS85] is traditionally used for designing the spin matched HERA optics in the presence of rotators, making the lattice spin transparent by fulfilling all the above conditions.

Creating a spin transparent optic for the perfectly aligned machine is usually not enough to assure a high degree of polarization. There is a limit to the precision with which the machine magnets in a real ring can be aligned and positioned with respect to the design values. Modern storage rings are equipped with beam position monitors and correction coils so that the closed orbit can be directly measured and corrected. Nevertheless, even after careful orbit corrections have been applied, there will always be a residual distortion of the closed orbit caused by the misalignments, field errors and their corrections. This will generate a tilt $\delta\hat{n}_0$ of the periodic closed orbit spin solution $\hat{n}_0$ from its nominal direction. In HERA with transverse alignment tolerances of 0.3 mm, an rms value of $\delta\hat{n}_0$ of

[1] This is a very general recipe and it should be pointed out that each case has to be treated individually, taking into account such things as ring (a)symmetries and number of independently powered quadrupoles available. For example in HERA we do not try to spin match between radiating dipoles in the straight sections, but only across whole straight sections. I will return to this point when discussing results of polarization simulations for the HERA luminosity upgrade in Chapter 6.

the order of $30 - 40$ mrad is expected after standard orbit corrections. Simulations show that in such a situation, even with a good (strong synchro–beta) spin matched optic, the polarization is usually very low and of no practical value to the experiments. This is simply so because in a real ring with misalignments and errors the spin match of the perfectly aligned ring is broken! In a ring with tilted $\hat{n}_0$ in the arcs, the elements of columns 1, 2, 5 and 6 of the one–turn $\mathbf{G}$ matrix are generally non–zero. Equivalently, the spin–orbit coupling integrals $J_{\pm x}$ and $J_{\pm s}$ in eqn. (3.78) become non–zero due to this tilt. Synchrotron and horizontal betatron oscillations can therefore contribute to the spin diffusion. It is found numerically that the term in $J_{\pm s}$ related to the horizontal dispersion dominates. Further examples of how the various terms contribute to the depolarization will be given in Chapter 6. To counteract the sometimes strong spin diffusion connected to the tilt of $\hat{n}_0$ a dedicated minimization of the distortion $\delta\hat{n}_0$ is needed. This is the second step of the spin matching. If there would be enough beam position monitors (BPMs) and correction coils in the lattice so that each quadrupole would have its own BPM and correction coil, and the positions of the BPMs with respect to the quadrupoles would be well known (from, for example, beam–based calibration [Sa99]), one could minimize the combined vertical kick applied to the orbit by each quadrupole and its correction coil, in effect reducing the tilt of $\hat{n}_0$ deterministically [BB94]. [2] However in practice, this is usually not the case and therefore some empirical correction scheme has to be applied. The method used at HERA for optimizing the polarization in a ring with orbit distortions is called *harmonic closed orbit spin matching* and is described in [Bb85a, Bb94]. The technique was first developed for and applied to the $e^{+/-}$ storage ring PETRA [RS85], but has since been improved for HERA. Introducing the notation $\delta\hat{n}_0 = \delta n_{0m}\,\hat{m} + \delta n_{0l}\,\hat{l}$, where the tilt of $\hat{n}_0$ from the design orientation is expressed in terms of the periodic frame $(\hat{n}_0, \hat{m}, \hat{l})$ calculated on the design closed orbit, $\delta\hat{n}_0$ can be expressed as

$$\delta n_{0m}(s) - i\,\delta n_{0l}(s) \;=\; -i\,\frac{C}{2\pi}\sum_p f_p \frac{e^{\,i\,2\pi p s/C}}{p-\nu_0} \tag{4.2}$$

where the f_p are the Fourier coefficients of a "spin–orbit function" $f(s) = f_1(s) - i\,f_2(s)$ given by

$$f_p \;=\; \frac{1}{C}\int_s^{s+C} f(s')\,e^{-\,i\,2\pi p s'/C}\,ds'$$

and

$$\begin{pmatrix} f_1 \\ f_2 \end{pmatrix} \;=\; \begin{pmatrix} l_s & l_x & l_z \\ -m_s & -m_x & -m_z \end{pmatrix} \left\{ \mathbf{F}_{3\times 6}\cdot\vec{u}^{\,c.o} - \frac{ec}{E_0}\begin{pmatrix} \Delta\mathcal{B}_s\,\frac{1+a\gamma_0}{1+\gamma_0} \\ \Delta\mathcal{B}_x\,(1+a\gamma_0) \\ \Delta\mathcal{B}_z\,(1+a\gamma_0) \end{pmatrix} \right\}$$

where the $\Delta\mathcal{B}_y$ $(y = x, z, s)$ are field errors and $\vec{u}^{\,c.o}$ is the deviation of the six–dimensional (distorted) closed orbit from the design orbit. The principle of the harmonic spin–orbit correction scheme is to use a small number of vertical correction coils to reduce the rms value of the $\delta\hat{n}_0$ distortion by minimizing the most detrimental harmonics in the above expression. Before the shutdown for the upgrade of HERA a total of eight closed vertical orbit bumps, the "harmonic bumps", located in the arcs of the machine, were used to control the real and imaginary parts of the harmonics -1, 0, 1 and 2 of f, found to be the most important in simulations. Closed bumps, consisting of three vertical correction coils each, have been used in order to avoid perturbing the vertical orbit everywhere and creating vertical dispersion. Moreover, in this way the luminosity is not effected. The optimal settings of the bump amplitudes are found through empirical tuning by observing the polarization. To this end, fast

[2] Such "kick minimization" will not be efficient if the ring dipoles are significantly tilted.

polarimeters are of utmost importance. The harmonic closed orbit spin matching used in HERA I was able to reduce the rms value of $\delta\hat{n}_0$ to $10-20$ mrad and greatly improved the polarization. This can be understood by recalling that the depolarization associated with a tilt of $\hat{n}_0$ roughly scales as $\delta\hat{n}_0^2$, due to the term $(\frac{\partial\hat{n}}{\partial\delta})^2$ in the depolarization rate, eqn. (3.25). In the years 1995–2000 HERA had the capability to routinely deliver longitudinally spin polarized $e^{+/-}$ to HERMES, with polarization values lying between 50 and 60 % and with peak values reaching 65 %. The HERA electron ring is so far the only high energy ring that gives access to longitudinal spin polarization.

The polarization in HERA is measured at two locations in the ring: in the West straight section, where the polarization direction is vertical, and in the East straight section close to HERMES, where the polarization direction is almost longitudinal. These devices are briefly described in Section 4.3.

4.2 Impact of the upgrade on polarization

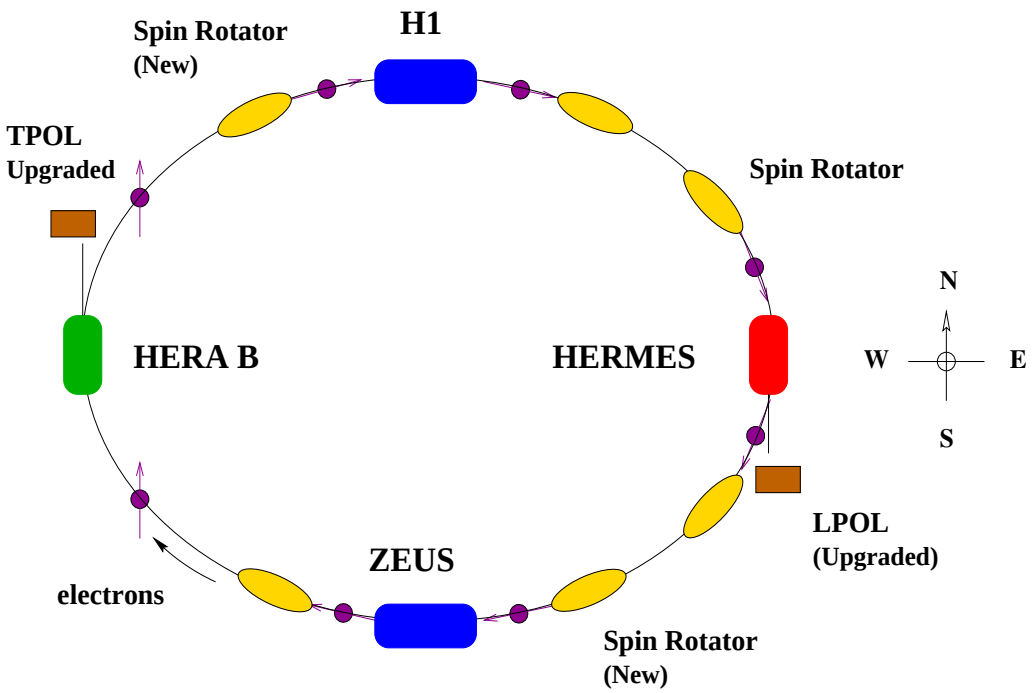

Figure 4.2: Schematic representation of HERA–e after the Luminosity Upgrade.

As we have seen in Chapter 2, the luminosity upgrade of HERA will have a profound impact on the lattices of the proton and $e^{+/-}$ rings. By now it should be clear that since the spin and orbital dynamics are intimately connected, the changes implemented to influence the orbital dynamics in favour of higher luminosity will have repercussions on the spin motion. In this section these changes will be discussed further with emphasis on their importance for operation with polarized $e^{+/-}$ beams.

Two additional pairs of spin rotators have been available for inclusion in the ring since 1997. These have, at the time of writing, been installed at the beginnings and ends of the North and South straight sections respectively, giving access to longitudinal $e^{+/-}$ spin polarization at the colliding beam experiments H1 and ZEUS. Due to the lack of space in the interaction regions the anti–solenoids, previously used to compensate for the effects of the experimental solenoids on orbit and spin motion, will be removed. [3] This calls for an alternative solution. In the tight layouts of the new interaction zones the superconducting separator magnets GO and GG are placed partially inside the detector

[3] A discussion on the effects of (uncompensated) solenoids on the polarization is found in Chapter 6.

solenoids, giving rise to overlapping magnetic fields. The positions of the GO and GG magnets with respect to the detectors are shown in Figures 4.3. and 4.4. This has some unpleasant effects on the orbit and spin motion. The increased horizontal and vertical phase advances, from 60° to 72°, and the shift of the RF frequency to reduce the horizontal emittance will also influence the polarization. The new interaction region quadrupoles are stronger than the old ones and the design is no longer mirror symmetric with respect to the IPs. As a result of these changes the new e^+ and e^- optics are subject to tougher constraints than previously and the asymmetries in the lattice make spin matching an intricate business. It should be pointed out that a good spin match becomes especially important with additional rotators operating in the ring, because of the effects described earlier in this chapter. Another area expected to have a significant impact on the polarization is the interaction with the high intensity proton beam. The construction of optical solutions that permit a high degree of $e^{+/-}$ spin polarization in the upgraded HERA presents many challenges. A basic requirement for calculating the polarization is the ability to model the complicated field configurations in the interaction regions. A detailed description of how this problem has been solved is given in Chapter 5.

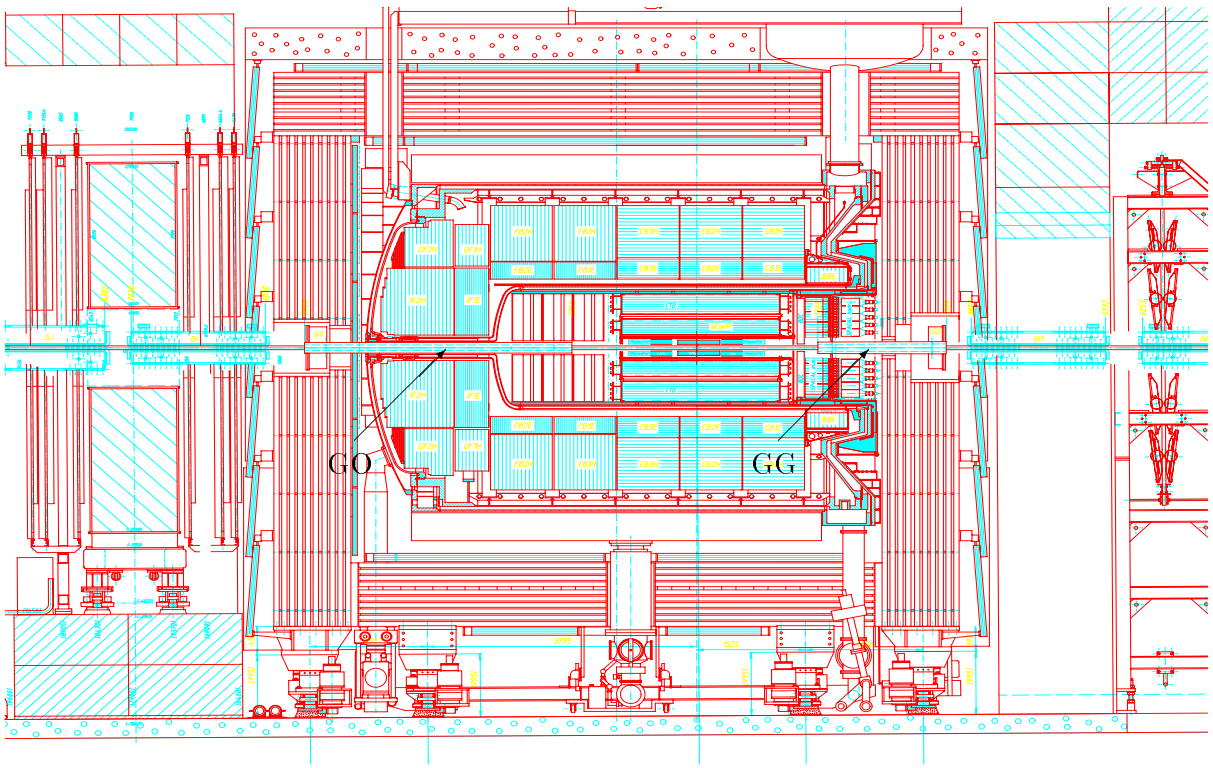

Figure 4.3: The H1 solenoid with the overlapping machine magnets. Courtesy of H. D. Brück.

4.3 Polarimetry at HERA

In the past, two polarimeters have been used to measure the electron spin polarization in HERA, measuring transverse and longitudinal beam polarization in the West and East straight sections respectively. [4] The two devices rely on the same basic physical principle: spin dependent Compton

[4]Recall that although the direction of the polarization can vary around the ring, the value of the polarization is the same at all azimuths.

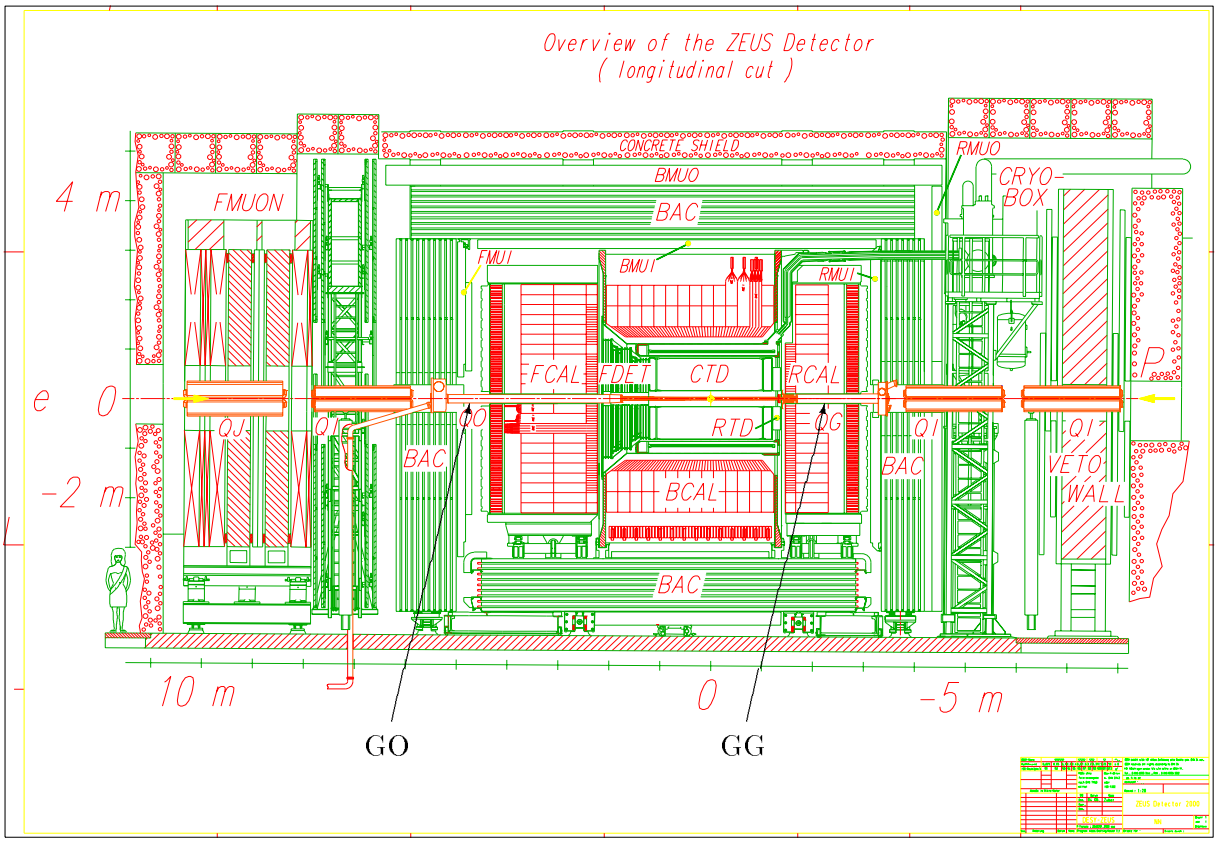

Figure 4.4: The ZEUS solenoid with the overlapping machine magnets. Courtesy of U. Schneekloth.

scattering of circularly polarized laser light off polarized $e^{+/-}$. However they differ in construction and the measurement techniques employed [Bb93, Be00a] and therefore complement each other.

After the luminosity upgrade, with two more spin rotator pairs installed in the HERA lattice, the default operation mode for HERMES, H1 and ZEUS will be with longitudinally polarized $e^{+/-}$. Spin dependent physics will become an integral part of the programme of the colliding beam experiments in addition to HERMES, where this has been the case since the startup of the experiment. Access to longitudinal $e^{+/-}$ spin polarization in combination with a luminosity increase by a factor of about 5 opens up new possibilities for studying the physics of the electroweak and strong interactions. Precision measurements to permit tests of physics beyond the Standard Model will also become feasible. In these new studies, measured quantities such as structure functions and asymmetries will be very sensitive to the beam polarization. The monitoring of the spin polarization will thus become as important for H1 and ZEUS as monitoring luminosity. Given an accuracy of the luminosity measurements of $1-2$ %, the polarization measurements after the upgrade should be capable of a precision of $\Delta P/P \leq 2$ % for $P = 50-70$ %. Measures will have to be taken so that continuous, reliable beam polarization measurements are available throughout the HERA collision programme. It should be pointed out that the physics experiments done at H1 and ZEUS are based on the colliding bunches only, whereas at HERMES all electron bunches are used. A system of polarimeters should therefore be able to separately measure the polarization of the colliding and the non–colliding bunches. In the old setup, only one of the polarimeters (the longitudinal polarimeter) was able to accomplish this.

Parallel to the work done by the Luminosity Upgrade group, a special working group, "the Polarization 2000 Project" group, has been looking into the potential for upgrading the existing HERA polarimeters to meet these requirements.

4.3.1 Transverse Polarimeter

Located in the HERA West straight section, where the nominal polarization direction is vertical, the transverse polarimeter (TPOL) measures the vertical component of the electron polarization. The polarimeter became operational in 1991 and until the summer of 1999 it was the primary device for measurement of polarization in HERA. TPOL measures *spatial asymmetries* in the vertical plane of the distribution of single backscattered Compton photons arising when circularly polarized photons scatter off vertically polarized electrons. The shift of the mean vertical position of the photon distribution, when switching between left (L) and right (R) circular laser light polarization, is proportional to the vertical polarization component P_z of the electrons. In particular at the position of the photon detector, 65 m away from the point of interaction, the photon spot size is of the order of 0.3 mm in the vertical plane and the shift between the centroids is typically about 140 μm. The vertical positions of the photons are recorded with a vertically segmented calorimeter by energy sharing in the upper and lower halves. By forming the shower energy asymmetry $\eta = (E_{up} - E_{down})/(E_{up} + E_{down})$, where η is related to the vertical position through a parametrization, P_z can be obtained through the difference of the mean values $\langle\eta\rangle$ when switching the light polarization

$$\Delta\eta(E_\gamma) \;=\; \frac{\langle\eta\rangle_L - \langle\eta\rangle_R}{2} \;=\; P_z \Delta S_3 \Pi_\eta(E_\gamma) \tag{4.3}$$

Here ΔS_3 is the difference in the circular polarization of the laser light. $\Pi_\eta(E_\gamma)$ is the so called analyzing power, which depends on the Compton cross section as well as detector and electron beam parameters and has to be checked through calibration.

An alternative method has been developed, in which the measured energy distributions in the calorimeter are used, and an asymmetry is formed by comparing distributions for left and right polarized laser light. The systematic errors of the two methods are of different nature: the means method is dominated by the spatial calibration of the calorimeter, whereas the asymmetry method is mostly sensitive to the exact knowledge of the interaction point of the lepton and laser beams.

Since precise knowledge of polarization is so important, the absolute value delivered by a polarimeter must be checked through calibration. Before the shutdown for the upgrade, the calibration of TPOL was relying on experimental data through *rise time measurements*. In such a measurement the electron beam is deliberately depolarized by means of a radial RF–field and the subsequent build–up of the polarization is recorded. The asymptotic polarization (P_{eq}) from the fit mentioned in Chapter 3 is then used to rescale the measured asymptotic polarization. An example of a rise time curve is given in Figure 4.5.

The rise time calibration method is time consuming and requires dedicated beam time under stable machine conditions. No recent measurements have been made and it is desirable that alternative methods be found, so that the calibration of the polarimeter can be done independently of rise time measurements. A new method to improve the use of the TPOL data has been proposed in which a position sensitive detector in front of TPOL could be used as an in–situ device to calibrate the energy – position relation, parametrized in the so called $\eta - y$ transformation (in a coordinate system where y refers to the vertical direction). A silicon strip detector is currently under development for this purpose and the goal is to have it installed at the time of turn on of HERA II in summer 2001.

Recent studies have resulted in a much improved understanding of the detector calorimeter and the energy distributions as a function of the polarization. Together with an improved description of the spatial calibration this has allowed a recalibration of TPOL and the systematic errors are now approaching the 1 % level [Be00b]. Up to now, the errors from the asymmetry method have been slightly larger, favouring the means method.

The most extensive upgrade of TPOL concerns the data acquisition (DAQ) system. With the old DAQ system used before the shutdown, TPOL was only capable of measuring the average polarization

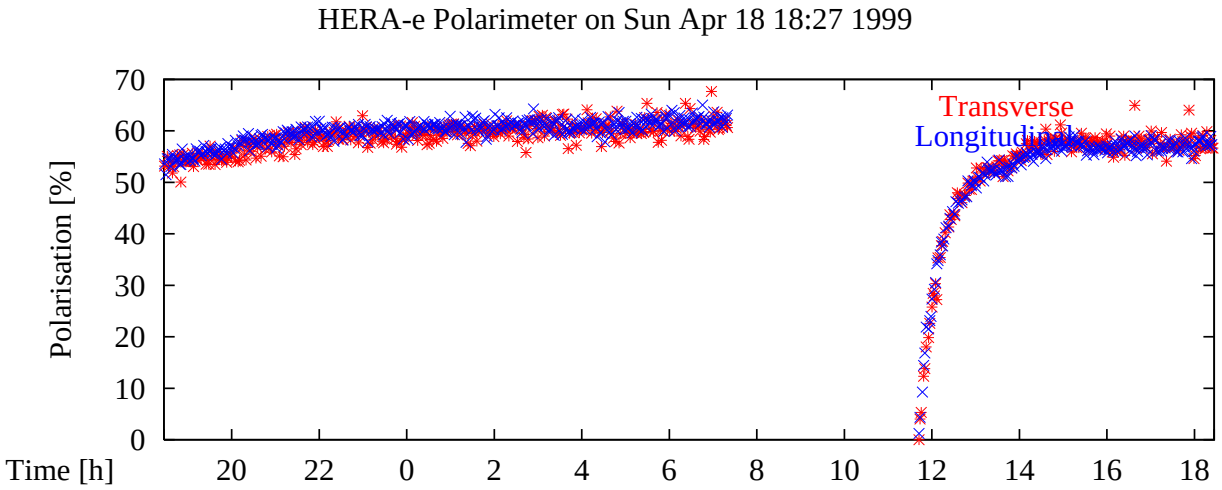

Figure 4.5: An example of the electron polarization in HERA as a function of time, as measured by the transverse (TPOL) and longitudinal (LPOL) polarimeters. Note that as expected TPOL and LPOL deliver the same value for the polarization within errors.

of all the electron bunches in the ring. Experience with the longitudinal polarimeter (LPOL) shows that colliding and non–colliding bunches can have different polarization patterns and that the values obtained depend strongly on the tuning of the machine. The provision of fast and flexible systems, capable of measuring the polarization of any combination of bunches is therefore a key issue for the polarimetry in HERA after the upgrade. The new DAQ for TPOL has been designed with these considerations in mind. The new system will enable TPOL to measure the polarization bunch–by–bunch, with a statistical accuracy close to 1 % per bunch in 15 minutes and about 1 % accuracy for all colliding bunches in 1 minute. The work on the new system has now reached a mature state and it has been demonstrated that it allows the measurement of the polarization of individual bunches. The goal is to have a debugged and operational system for TPOL at the start of experimental data taking in 2001.

4.3.2 Longitudinal Polarimeter

The determination of the electron polarization with an absolute accuracy of 1 % requires approximately 10^6 scattered photons. The detection of individual photons is referred to as the "single photon" method. It can be used if the background from beam–gas bremsstrahlung is low. At the position of TPOL in the West straight section this is the case, and TPOL is operating in this mode. In cases where the background is large, the "multi photon" method is preferred. By using a pulsed, high power laser to produce thousands of backscattered photons for each interaction with an electron bunch, the Compton scattering can be made to dominate over the background.

In 1996 a second polarimeter built by the HERMES collaboration was taken into operation at HERA. This polarimeter measures the longitudinal component of the $e^{+/-}$ polarization, P_s, [5] in the region between the HERMES spin rotators. Unfortunately the bremsstrahlung background rate in the HERMES straight section is relatively high at the position of LPOL, so the polarimeter is designed to operate in the multi photon mode. The polarization measurement is based upon large asymmetries in the energy distributions of the backscattered photons. A high intensity pulsed Nd:YAG laser delivers photons whose interactions with individual electron bunches are detected. The energy weighted cross

[5] Note that in Chapter 6 the symbol P_s refers to the polarization associated with longitudinal orbital motion in the SLIM formalism.

sections of the backscattered Compton photons — about 1000 per laser pulse — are then used to extract the value of the longitudinal polarization. The expression for the energy weighted asymmetry $\mathcal{A}$ reads

$$\mathcal{A} = \Delta S_3 P_s S_s \tag{4.4}$$

where S_s is the analyzing power, given by

$$S_s = \frac{S_L - S_R}{S_L + S_R}, \quad \text{and} \quad S_i = \int_{E_{min}}^{E_{max}} (\frac{d\sigma}{dE})_i \, E\, r(E)\, dE, \quad i = L, R \tag{4.5}$$

and $r(E)$ is the energy response function. The longitudinal polarimeter, LPOL, is capable of measuring the polarization of single bunches, small groups of bunches or all the electron bunches in the ring. The background, when running in the multi–photon mode, is negligible.

The longitudinal polarimeter has been subject to especially intense research, motivated by problems of understanding the calibration of the device during the first years of operation. A significant effort undertaken by the LPOL group [6] of the HERMES experiment has led to substantial progress in reproducing theoretically expected asymmetries and in understanding the physics of the calorimeter. In the summer of 1999 it was possible for the first time to calibrate LPOL independently of TPOL, making it a stand alone, fully calibrated polarization measurement station. Since then, the polarimeter has delivered data with exceptional reliability and very good accuracy. Nonetheless, there is still room for improvement. The design of the calorimeter used for LPOL suffers from some intrinsic problems that limit the statistical precision. It has therefore been decided to replace the existing crystal calorimeter with a sampling calorimeter for operation after the upgrade, that should have a better energy resolution and a more linear response. The new model has been built and tested and the results are promising.

One of the major advantages of LPOL over TPOL is that it has a higher analyzing power. The timing of the high intensity pulsed laser for LPOL on the other hand, makes the operation of this polarimeter more difficult. It is generally believed that the ultimate precision in polarization measurement will be delivered by a polarimeter which measures longitudinal polarization in the single photon mode. This mode has several advantages, the most important being the large asymmetries at the Compton edge and the precise knowledge of the expected energy spectra, which facilitate calorimeter calibration and help in understanding various detector effects. The main disadvantage is the sensitivity to the beam–gas background. For operation in the multi–photon mode such background is not important, but the interpretation of the detected energy spectra is less straightforward. The most severe impediment for operation of an LPOL in the single photon mode is the high continuous laser power needed to obtain a sufficient photon flux in order that essentially one Compton photon is backscattered from each bunch in the machine. Following a design originating at the CEBAF ring at the Thomas Jefferson laboratory [Fa01], the LPOL laser system will be supplemented by a more powerful system consisting of a Fabry–Perot cavity. Recent numerical studies [PZ00] show that in a single or few photon mode the problems with the large background rates in the LPOL area can be overcome. With the Fabry–Perot laser power enhancement system, it should be possible to measure the polarization with a statistical and systematic precision of better than 1 % per bunch per minute.

[6] University of Freiburg, University of Michigan and DESY, Hamburg.

Chapter 5

Models for the new Interaction Regions

5.1 Sandwich model for SLIM/SLICK

The new interaction regions of the luminosity upgraded HERA have been described in some detail in Chapter 2. In particular, the unconventional solution of placing the beam separation magnets partially inside the solenoids of the colliding beam experiments has been emphasized. It is clear that such a lattice layout requires special treatment when modelling to fit any standard optics computer code. None of the optic codes or codes for calculating and optimizing the polarization in common use at DESY contain mixed element types such as solenoid + dipole or solenoid + combined function magnet, so ways must be found to incorporate such special elements. The situation is further complicated by the fact that the design orbit inside the experimental solenoids will be curved, due to the bending action of the separator magnets. See Figure 5.1 and the discussion below. Two different approaches have been used to model these unusual features. The first method simply amounts to building mixed elements out of existing magnet types. This is the sandwich model described in this section. A more fundamental way of describing the influence of a complicated magnetic field structure on a charged particle, is to perform numerical tracking of the particle through that structure, integrating the equations of motion. With properly chosen initial conditions, maps for orbit and spin motion can be constructed. This is the subject of the next section.

To get a first estimate for the polarization expected with the upgraded HERA the spin–orbit code SLICK [Bb00], has been modified. As a first step, in order to minimize the changes to the code, the regions with overlapping solenoid, combined function magnet and corrector fields have been described as series of interleaved thin slices of these magnet types which we call "sandwiches". The separator magnets on the left and right hand sides of the IP complete/start the bending onto/away from the straight, head–on, collision direction at the IP *inside* the experimental solenoids. The design orbit inside the solenoids is therefore curved in the horizontal plane. In particular, for this work, the design orbit is defined just by the curvature in the separator magnets and has no torsion due to the solenoids. A curved design orbit implies that the beam enters and leaves the straight solenoids with a radial offset and angle. The particles on the design orbit will therefore be subject to radial field components from the solenoid end fields which will kick the beam, mainly in the vertical direction. Furthermore, in the interior of the solenoid, radial fields will effectively be present due to the curvature, which will cause a disturbance to the electron orbits as well as to the spin.

In the sandwich model, two different representations of the radial solenoid fields have been compared. The **first** and simplest way of representing the fields on the design orbit is to interleave thin corrector coil slices with slices of combined function magnet (or quadrupole or dipole) and ordinary solenoid slices. The strengths of the slices are scaled so as to maintain the correct total field integrals. The corrector coils simulate the kicks mentioned in the previous paragraph. However, to preserve the

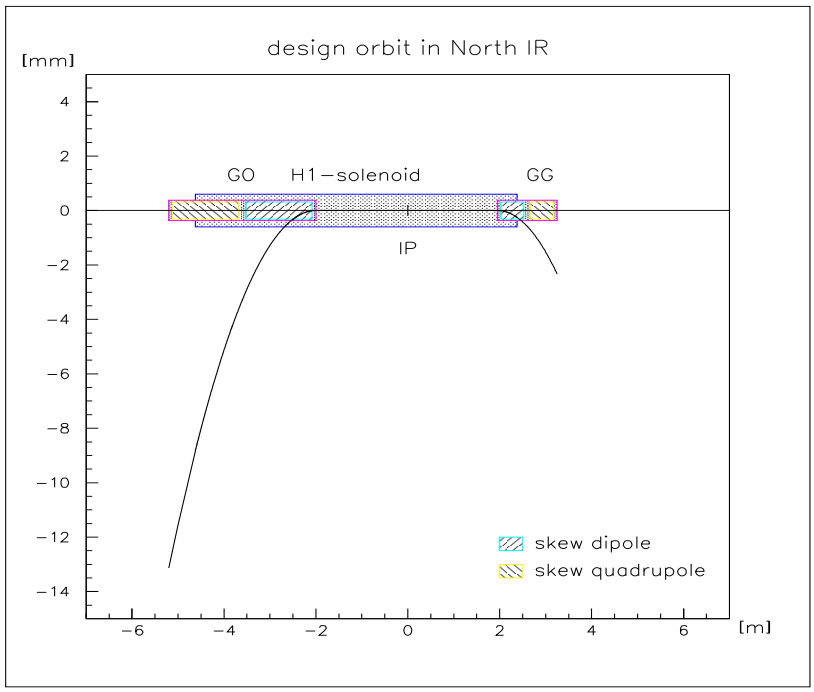

Figure 5.1: Schematic picture of the North interaction region, indicating the positions of the innermost magnets with respect to the H1 solenoid. Also shown, in another scale, is the curved design orbit in the horizontal plane.

symplecticity of the matrices for SLIM type programs — which use the orbit variables x, x', z, z' — the solenoid slices must include their radial end fields. But then the exit radial end field of a solenoid slice is separated by the combined function slice from the entry radial end field of the next solenoid slice. However, if the combined function slice is replaced by a zero length effective magnet treated in the thin lens approximation, its matrix commutes with the surrounding radial end field matrices (see eqn. (5.1) below) and these latter then "annihilate" each other. Symplecticity is thereby maintained and unphysical solenoid "internal" radial end field effects are avoided — but at the cost of using a thin lens representation for the combined function magnets. A large number of slices is then needed to maintain accuracy in this region of strong focusing. If one is just interested in some purely optical matters this should be acceptable. This is one of the approaches used for the coupling studies discussed in Section 6.1.1.

However, zero length for a combined function slice implies infinite curvature and then the effects that depend explicitly on the curvature of the design orbit, such as the radiation, need to be handled in a special way in the computer codes. This can be arranged, but there would still be problems with the representation of the spin motion. In particular, the commutation of the matrices mentioned above does not feed through to the spin motion since the spin basis, which appears in the $\mathbf{G}$ matrices, rotates in the combined function slices. Thus, so far, a solution employing many slices of finite thickness has been used which is a compromise between the need to adequately describe the optic and the spin and the need to maintain finite curvature in the combined function magnets. In practice, the slice length has been varied from a few mm up to about 100 mm, all leading to similar results for the orbit as well as the spin motion. In any case, we are still subject to the uncertainties in the exact form of the physical solenoid fields in the overlap regions.

The **second** method uses the enlarged transfer matrix $\mathbf{M}_{7\times 7}$ (eqs. (3.46) and (3.47)). In this approach the effects of the lateral and angular offsets of the solenoids with respect to the design orbit are introduced using the seventh column. In this way no artificial elements need to be introduced in

the representation. Using a hard edge approximation for the fields at the ends of a solenoid, the 7×7 transfer matrix of a solenoid with a longitudinal central field of length l takes the form [Bb85b, GR00]

$$\mathbf{M}_{sol} = \mathbf{M}_{exit} \cdot \mathbf{M}_{central} \cdot \mathbf{M}_{entrance}$$

$$\mathbf{M}_{central} = \begin{pmatrix} 1 & \frac{\mathcal{S}}{\mathcal{R}} & 0 & \frac{1-\mathcal{C}}{\mathcal{R}} & 0 & 0 & \frac{\alpha_x(\mathcal{S}-\mathcal{R}\,l)+\alpha_z(1-\mathcal{C})}{\mathcal{R}} \\ 0 & \mathcal{C} & 0 & \mathcal{S} & 0 & 0 & \alpha_x(\mathcal{C}-1)+\alpha_z\mathcal{S} \\ 0 & -\frac{1-\mathcal{C}}{\mathcal{R}} & 1 & \frac{\mathcal{S}}{\mathcal{R}} & 0 & 0 & \frac{\alpha_x(\mathcal{C}-1)+\alpha_z(\mathcal{S}-\mathcal{R}\,l)}{\mathcal{R}} \\ 0 & -\mathcal{S} & 0 & \mathcal{C} & 0 & 0 & -\alpha_x\mathcal{S}+\alpha_z(\mathcal{C}-1) \\ 0 & 0 & 0 & 0 & 1 & 0 & 0 \\ 0 & 0 & 0 & 0 & 0 & 1 & 0 \\ 0 & 0 & 0 & 0 & 0 & 0 & 1 \end{pmatrix}$$

$$\mathbf{M}_{entrance/exit} = \begin{pmatrix} 1 & 0 & 0 & 0 & 0 & 0 & 0 \\ 0 & 1 & \frac{\pm\mathcal{R}}{2} & 0 & 0 & 0 & \frac{\pm\mathcal{R}(2\,a_z+l\,\alpha_z)}{4} \\ 0 & 0 & 1 & 0 & 0 & 0 & 0 \\ \frac{\mp\mathcal{R}}{2} & 0 & 0 & 1 & 0 & 0 & \frac{\mp\mathcal{R}(2\,a_x-l\,\alpha_x)}{4} \\ 0 & 0 & 0 & 0 & 1 & 0 & 0 \\ 0 & 0 & 0 & 0 & 0 & 1 & 0 \\ 0 & 0 & 0 & 0 & 0 & 0 & 1 \end{pmatrix} \tag{5.1}$$

where $\mathcal{R} = \frac{ec}{E_0}\mathcal{B}^{s.a}_{long}$ ($\mathcal{B}^{s.a}_{long}$ is the longitudinal solenoid field on the axis), $\mathcal{S} = \sin(\mathcal{R}l)$ and $\mathcal{C} = \cos(\mathcal{R}l)$. The quantities $a_{x,z}$ and $\alpha_{x,z}$ are the transverse offsets and tilt angles respectively. The relatively simple form in (5.1) is due to the linear dependence on radius of the radial end fields. See the first line in eqn. (5.15). It has been verified in simulations using SLIM/SLICK that the results of spin–orbit calculations using the two versions of the sandwich model are in good agreement.

In the case of an optic with closed orbit distortions, the second method exploiting the seventh column of the enlarged transfer matrix becomes impractical or at least unnecessarily complicated. It requires that the matrix elements are reevaluated twice: first the motion is described with respect to the curved design trajectory and in a second iteration the distorted closed orbit with respect to this curved trajectory has to be found. The matrix elements will then be given with respect to this new (translated and distorted) closed orbit. The treatment of closed orbit distortions in the current DESY versions of SLIM and SLICK is not sufficiently complete, as it does not allow for direct displacements or strength deviations of the lattice elements, but only treats closed orbit distortions created by powering correction coils. Therefore another program from the SLIM family, SITF in combination with PETROS [Ke78] has been used for the study of the luminosity upgrade optic when applying realistic closed orbit distortions.

In the sandwich model the H1 and ZEUS solenoids are described by box shaped fields, i.e. constant longitudinal fields with hard edge end fields. This is an acceptable representation for the central parts of the solenoids, but for the end fields the approximation is crude. Concerns have risen that the spin motion could be very sensitive to the details of the solenoid fields, especially the end fields. Calculations should therefore be based upon better knowledge of, and an improved representation of the fields. To this end, measured field maps of the experimental solenoids have been used as a basis when constructing an improved model for the upgrade IRs.

5.2 Maps from numerical integration

The sandwich model presented in the previous section is attractive in its simplicity and it is also quite general — all magnet types defined in an optics code can in principle be used in a sandwich construction to represent optical elements overlapping each other without modifying software. Nevertheless, the model has some serious shortcomings as we have seen, and in order to overcome these an improved representation of the mixed fields is required.

A better description can be obtained by numerically integrating the equations of orbit and spin motion using measured fields and casting the solutions in matrix form. Using the fact that the transfer matrix is just the matrix of linearized (constant) partial differentials of the output coordinates with respect to the input coordinates — i.e. the Jacobian of the linear part of the map, numerical matrices can be constructed from numerical integration data using a small number of test trajectories. In particular the **M** and the **G** matrices in the SLIM approximation can be calculated in this way. The numerical integrations can be carried out using some standard integration scheme like fourth order Runge–Kutta or an Adams algorithm. By tracking particles with different sufficiently small initial offsets Δ with respect to the design orbit, very good approximations to linear maps for regions with arbitrarily complicated field structure can readily be computed. This then is the way adopted for improving on the sandwich model of the overlapping fields of the luminosity upgrade and for providing maps suitable for implementation into SLICK.

The design orbit around the IP is depicted in Figure 5.2, which is explained in more detail later. In Figure 5.2 particle positions transverse to the design orbit are denoted by $\tilde{x}$ and $\tilde{z}$ and the distance along the design orbit in Figure 5.2 is denoted by $\tilde{s}$. For convenience we will temporarily adopt that notation here for describing the calculation of the maps. The equations for the orbital motion [1] (A.8) and (A.9) and those for the spin motion eqn. (A.14) with (A.15 – A.17) are integrated using a Runge–Kutta scheme with adaptive stepsize control (RK45) from Numerical Recipes [Pr92]. A total of 10 initial phase space vectors at $\tilde{s}_0$: $\vec{u}_i = (\tilde{x},\ \tilde{x}',\ \tilde{z},\ \tilde{z}',\ l,\ \delta) = (\pm\Delta_1,\ 0,\ 0,\ 0,\ 0,\ 0)$, $(0,\ \pm\Delta_2,\ 0,\ 0,\ 0,\ 0)$, $(0,\ 0,\ \pm\Delta_3,\ 0,\ 0,\ 0)$, $(0,\ 0,\ 0,\ \pm\Delta_4,\ 0,\ 0)$, $(0,\ 0,\ 0,\ 0,\ 0,\ \pm\Delta_6)$ and the design orbit $(0,\ 0,\ 0,\ 0,\ 0,\ 0)$ are tracked across the IR magnets, starting outside of the solenoid at the left side of the GO magnet. The elements of the linear transfer maps are derived column wise by constructing differential quotients of the output and input phase space coordinates with respect to the design orbit, much in the same way as the section matrices in SITROS are derived. For example the first column of the map $\mathbf{M}(\tilde{s}_1, \tilde{s}_0)$ from $[\tilde{s}_0, \tilde{s}_1]$ is given by

$$\mathbf{M}(\tilde{s}_1, \tilde{s}_0)^T\,[i,1]_{i\in\{1,\ldots,6\}} = \left(\frac{\tilde{x}^+_{\tilde{s}_1} - \tilde{x}^-_{\tilde{s}_1}}{2\,|\Delta_1|}, \frac{\tilde{x}'^+_{\tilde{s}_1} - \tilde{x}'^-_{\tilde{s}_1}}{2\,|\Delta_1|}, \frac{\tilde{z}^+_{\tilde{s}_1} - \tilde{z}^-_{\tilde{s}_1}}{2\,|\Delta_1|}, \frac{\tilde{z}'^+_{\tilde{s}_1} - \tilde{z}'^-_{\tilde{s}_1}}{2\,|\Delta_1|}, \frac{\ell^+_{\tilde{s}_1} - \ell^-_{\tilde{s}_1}}{2\,|\Delta_1|}, 0\right) \tag{5.2}$$

The superscripts "+" and "−" on the output coordinates appertain to particles starting with position $\pm\Delta_1$ at $\tilde{s}_0$. The sixth element $\left(\delta^+_{\tilde{s}_1} - \delta^-_{\tilde{s}_1}\right)/2\,|\Delta_1| \equiv 0$, since no accelerating fields are present around the IP. The other columns of $\mathbf{M}(\tilde{s}_1, \tilde{s}_0)$ are constructed in an obvious analogous way except for column 5: in the absence of accelerating fields element $(5,5) = 1$ and the other elements of column 5 are zero.

For the spin part of the representation, for each initial phase space vector a set of three mutually orthogonal spin vectors needs to be tracked. The information is stored in a 3×3 rotation matrix $\mathbf{R}_0$, which describes the spin rotations on the reference trajectory (0^{th} order spin transfer maps), and ten matrices $\mathbf{R}_{\vec{u}_i}$ which give the dependence of the spin rotations on the initial phase space coordinates $\vec{u}_i$. Taken together these matrices provide the necessary information needed to construct the **G** matrices for SLICK. The relationship between the 3×3 rotation matrices and the **G** matrix is found by making

[1] Note that the orbital variables in Appendix A do not carry tildes ˜ since there the equations are meant to be generic.

the following observations, valid in the linear approximation: suppose that at the input (beginning) of an element we are given the components of the non–periodic spin basis $(\hat{n}_{0\,i}, \hat{m}_{0\,i}, \hat{l}_{0\,i})$. An initial spin vector $\widehat{S}_i$ is then transformed into $\widehat{S}_f$ by the rotation matrix $\mathbf{R}_{\vec{u}_i}$: $\widehat{S}_f = \mathbf{R}_{\vec{u}_i}\, \widehat{S}_i$. Assume now that we put $\widehat{S}_i$ parallel to $\hat{n}_{0\,i}$. Then for linearized spin motion, and denoting the spin basis at the final phase space point by $(\hat{n}_{0f}, \hat{m}_{0f}, \hat{l}_{0f})$ we have

$$\begin{aligned} \widehat{S}_f &= \mathbf{R}_{\vec{u}_i}\, \hat{n}_{0\,i} \\ &\equiv \hat{n}_{0f} + (\vec{G}_\alpha \cdot \vec{u}_i)\, \hat{m}_{0f} + (\vec{G}_\beta \cdot \vec{u}_i)\, \hat{l}_{0f} \end{aligned} \tag{5.3}$$

where $\vec{G}_\alpha$ and $\vec{G}_\beta$ in the second line are the row vectors of the $\mathbf{G}$ matrix. Compare eqs. (3.29), eqs. (3.52) and (3.56) and recall that in the SLIM code $\psi_0' = 0$ for almost all of the ring, except at the end of the lattice, so that the non–periodic and the periodic spin bases coincide for most of the ring. The $\hat{m}_{0\,i}$ and $\hat{l}_{0\,i}$ are transported from s_i to s_f by $\mathbf{R}_0$: $\hat{m}_{0f} = \mathbf{R}_0\, \hat{m}_{0\,i}$ and $\hat{l}_{0f} = \mathbf{R}_0\, \hat{l}_{0\,i}$. To get the rows of the $\mathbf{G}$ matrix we need the projection of $(\mathbf{R}_{\vec{u}_i}\, \hat{n}_{0\,i})$ on $\hat{m}_{0f}$ and $\hat{l}_{0f}$

$$\begin{aligned} \vec{G}_\alpha \cdot \vec{u}_i &= \left(\mathbf{R}_0\, \hat{m}_{0\,i}\right)^T \left(\mathbf{R}_{\vec{u}_i}\, \hat{n}_{0\,i}\right) = \hat{m}_{0\,i}^T \left(\mathbf{R}_0^T\, \mathbf{R}_{\vec{u}_i}\right) \hat{n}_{0\,i} \\ \vec{G}_\beta \cdot \vec{u}_i &= \left(\mathbf{R}_0\, \hat{l}_{0\,i}\right)^T \left(\mathbf{R}_{\vec{u}_i}\, \hat{n}_{0\,i}\right) = \hat{l}_{0\,i}^T \left(\mathbf{R}_0^T\, \mathbf{R}_{\vec{u}_i}\right) \hat{n}_{0\,i} \end{aligned} \tag{5.4}$$

The individual components of $\vec{G}_\alpha$ and $\vec{G}_\beta$ are finally derived by taking $\vec{u}_i$ to be successively the 10 starting vectors given above and averaging the values appertaining to the $\pm\Delta$ starting offsets.

The numerically derived orbit matrices and the spin 3×3 rotation matrices are calculated with a separate code for some chosen number of energy points. However, before these numerical maps can be implemented into SLICK, it must be ensured that the orbit maps are symplectic, as radiation is not included at this stage of the calculations, and that the spin maps are orthogonal. The chosen Runge–Kutta integrator is not symplectic, but the deviation from symplecticity is so small that it can be taken care of after the integration. [2] The orthogonality of the spin maps from the integrator is sufficient, so that the elements of $\mathbf{R}_{3\times3}^T\, \mathbf{R}_{3\times3} - \mathbf{I}$ are less than $5 \cdot 10^{-15}$. The symplecticity of the orbit maps is restored using a method based on mixed variable generating functions. [3] An example of this is given in Appendix D. The construction of the $\mathbf{G}$ matrices from the numerical $\mathbf{R}_0$ and $\mathbf{R}_{\vec{u}_i}$ matrices according to eqn. (5.4) is done in–line in SLICK. For a typical energy scan, covering one unit in $a\gamma$, a large number of orbit and spin matrices (of the order of one to several thousand) have to be stored and handled within the program. The numerical mapping of the HERA interaction regions has been subdivided into five segments: one map for a left and a right part of the GO magnet (together with possible overlap from the solenoid), two maps for solenoid pieces straddling the IPs and one map for the GG magnet, respectively. The main reason for this is the need to maintain a basic flexibility for diagnostic purposes. The code has been adapted so that all parts of it recognize and treat the special elements in the correct way. This is the first time that something like this has been attempted for extending analytical spin–orbit calculations to include complicated, non–standard field configurations.

[2] Note that to preserve and demonstrate symplecticity for numerical maps of sections which begin and end inside solenoid fields, artificial radial end fields are inserted in analogy with the practice for the sandwich model. However, the effects of an output end field and a subsequent input end field cancel when the maps are concatenated. See Section 5.2.1 also.

[3] The magnitude of the symplecticity breaking for a matrix $\mathbf{M}$ is given by the deviation from $\mathbf{0}$ of $\mathbf{M}^T\, \mathbf{S}\, \mathbf{M} - \mathbf{S}$, where $\mathbf{S}$ is the unit symplectic matrix from Section 3.2.1, and is a matrix with elements less than 10^{-5} for the numerical orbit maps before application of the generating functions method. The "symplectification" brings this number down to $\leq 5 \cdot 10^{-14}$. The numerical precision in the integration varies between the different regions, but is generally set as close as possible to machine precision (10^{-16}), and should therefore not affect the symplecticity.

In experimental high energy physics, a detailed knowledge of the magnetic fields in the detector area is crucial for an accurate determination of the momenta and scattering angles of charged particles. For HERA, the magnetic fields of the experimental solenoids in H1 and ZEUS were measured in 1989/1990 [Ne90, Ho93] with high precision, before commissioning the experiments. The data from the measurements are stored in field maps, covering a longitudinal range of 7 metres (H1) and 8.5 metres (ZEUS). At a "coarse level" (0.5 % measurement precision) the H1 magnetic field possesses axial symmetry, i.e. $\mathcal{B}_\phi = 0$ with ϕ the azimuthal coordinate in a cylindrical coordinate system. In addition the field has a left–right mirror symmetry, with respect to the plane of symmetry (*s.p.*) perpendicular to the magnetic axis. It should be observed that this plane of symmetry does *not* cross the magnetic axis at the IP, but is shifted in the longitudinal direction by 1.125 metres. See Figure 5.1. The H1 field measurements unfortunately only cover the central part of the field and do not extend out through the end–caps of the iron return yoke. Therefore, the knowledge of the fringe fields is poor and an extrapolation has to be made in order to estimate these fields. In the ZEUS detector area a large amount of magnetic material, mostly needed for shielding of sensitive detector equipment, modifies the field from the main solenoid. In particular the regions near the ends of the superconducting coil exhibit strong field inhomogeneities. Some of the tracking devices are located in these regions and therefore the magnetic field measurements were carried out with detail here also. The ZEUS field also exhibits a longitudinal asymmetry with respect to the IP, but much smaller than for H1, namely 0.05 metres and in the opposite direction.

To use the measured solenoid field data in the luminosity upgrade spin–orbit calculations, the measurements are summarized by parametrizations to be described in the next section. But before we turn our attention to the representation of the solenoid fields in the numerical maps, some coordinate systems will be defined that link the particle motion with the field values at various points in configuration space. In the following the symbol σ will be used to represent the distance along the magnetic axis of a solenoid. The H1 field map is given in a cylindrical coordinate system with the origin fixed at the point of symmetry on the magnetic axis, $\vec{\mathcal{B}}_{\rm H1} = \vec{\mathcal{B}}(r, \phi, \sigma)$, and with the positive σ–axis in the direction of the proton beam. The direction of the field is opposite to the direction of the $e^{+/-}$ beam. A trivial transformation brings the field data into the form $\vec{\mathcal{B}}(x_s, z_s, \sigma_s)$, where (x_s, z_s, σ_s) is a fixed right–handed Cartesian coordinate system. See Figure 5.2. The ZEUS field map data is in the form $\vec{\mathcal{B}}_{\rm ZEUS} = \vec{\mathcal{B}}(-x_s, z_s, -\sigma_s)$, with respect to our coordinate system. Particles moving in these solenoid fields, on the other hand, are described in a curvilinear coordinate system that moves along the design orbit together with a fictive ideal particle (see Appendix A). Imagine for a moment that we fix this moving coordinate system on the curved design orbit at the point of entrance to the GO magnet, as seen by the electrons. We refer to this curved coordinate frame as the $(\tilde{x}, \tilde{z}, \tilde{s})$ system, and label the snapshot of it at the entrance of GO with "in". There is no vertical curvature in the interaction regions, so that $K_z = 0$ and the design trajectory lies in the horizontal plane. Recall (Chapter 2) that by design the collisions take place at some small distance away from the solenoid axis, where the magnitude of the shift depends on which IP and lepton species is under consideration. To make these features clear in our description, yet another fixed coordinate system $(\bar{x}, \bar{z}, \bar{s})$ is introduced, in which a particle position is given with respect to the distance from and along the beam axis inside the solenoid. From the geometry on the left side of the IP we find the following relations between the coordinates of the various frames:

$$\begin{aligned} x_s &= \bar{x} - x_{shft} \\ z_s &= \bar{z} \\ \sigma_s &= \bar{\sigma} - \sigma_{s.p.} \end{aligned} \tag{5.5}$$

$$\bar{x}(\tilde{x}, \tilde{z}, \tilde{s}) = -\left(\rho_{\rm GO} - (\rho_{\rm GO} + \tilde{x}) \cos\left(\varphi_{in} - \frac{\tilde{s}}{\rho_{\rm GO}}\right)\right)$$

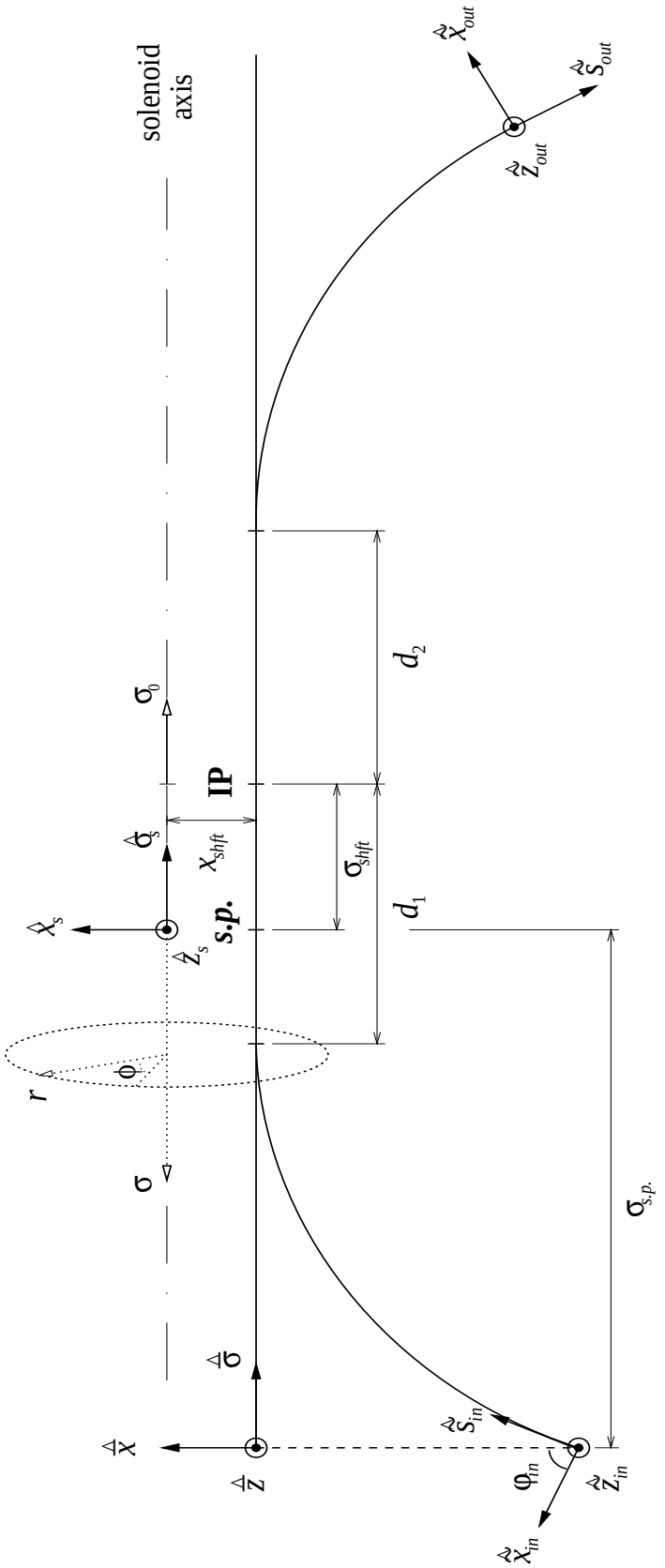

Figure 5.2: The design trajectory in the vicinity of the IP. The various coordinate systems used to describe the solenoid fields and the particle trajectories are illustrated.

$$\begin{aligned} \bar{z}(\tilde{x},\tilde{z},\tilde{s}) &= \tilde{z} \\ \bar{\sigma}(\tilde{x},\tilde{z},\tilde{s}) &= \rho_{\rm GO}\sin(\varphi_{in}) - (\rho_{\rm GO}+\tilde{x})\sin\left(\varphi_{in} - \frac{\tilde{s}}{\rho_{\rm GO}}\right) \end{aligned} \tag{5.6}$$

where $\rho_{\rm GO}$ is the radius of curvature in the GO magnet and φ_{in} is the total bending angle in GO. The numerical values for the longitudinal shifts of the symmetry plane away from the position of the IP are with our conventions $\sigma_{shft} = -1.125$ m for H1 and $\sigma_{shft} = +0.05$ m for ZEUS. The distance from the entrance of the GO magnet to the plane of symmetry measured along the solenoid axis is $\sigma_{s.p.} = \rho_{\rm GO}\sin(\varphi_{in}) + d_1 + \sigma_{shft}$, where d_1 is the distance from the exit of GO up to the IP. At H1 collisions between protons and electrons take place on the solenoid axis, whereas a horizontal shift of the beam trajectories of $x_{shft} = 7.5$ mm towards the centre of the ring is introduced when positrons are collided with the protons. At ZEUS the distance between the axis and the collision point is $x_{shft} = 10$ mm with electrons and $x_{shft} = 17.5$ mm with positrons. The shift direction of the beams with respect to the solenoid axis is the same as at H1. In the calculations presented in Chapter 6, a slightly different shift value at ZEUS for the electron case has been used ($x_{shft} = 4$ mm), corresponding to an intermediate version of the upgrade IR geometry. This will be commented on later. On the right hand side of the IP the coordinates are related in similar ways:

$$\begin{aligned} \bar{x}(\tilde{x},\tilde{z},\tilde{s}) &= -\left(\rho_{\rm GG} - (\rho_{\rm GG}+\tilde{x})\cos\left(\frac{\tilde{s}-\tilde{d}_0}{\rho_{\rm GG}}\right)\right) \\ \bar{z}(\tilde{x},\tilde{z},\tilde{s}) &= \tilde{z} \\ \bar{\sigma}(\tilde{x},\tilde{z},\tilde{s}) &= (\rho_{\rm GG}+\tilde{x})\sin\left(\frac{\tilde{s}-\tilde{d}_0}{\rho_{\rm GG}}\right) + \rho_{\rm GO}\sin(\varphi_{in}) + d_1 + d_2 \end{aligned} \tag{5.7}$$

Here $\rho_{\rm GG}$ and d_2 are the radius of curvature of the GG magnet and the distance from the IP to the entrance of GG, respectively. The $\tilde{d}_0$ is the distance along the curved design trajectory from the entrance of GO to the entrance of GG. Using the above coordinate transformations we now have the means to transform the solenoid fields from functions of fixed coordinates, with their origins on the solenoid axes, to functions of the curvilinear system, with respect to which the particle motion is described. From the field maps and the relations (5.5 – 5.7) we get

$$\vec{\mathcal{B}}(x_s,z_s,\sigma_s) = \vec{\mathcal{B}}(x_s(\tilde{x},\tilde{z},\tilde{s}),z_s(\tilde{x},\tilde{z},\tilde{s}),\sigma_s(\tilde{x},\tilde{z},\tilde{s})) \tag{5.8}$$

with components $\vec{\mathcal{B}} = (\mathcal{B}_{x_s},\mathcal{B}_{z_s},\mathcal{B}_{\sigma_s})$ in the straight coordinate system (x_s,z_s,σ_s). We are interested in the components of $\vec{\mathcal{B}}$ in the curved system $(\tilde{x},\tilde{z},\tilde{s})$. The base vectors of these two coordinate systems are related by a simple rotation:

$$\vec{\tilde{\mathcal{B}}} = (\mathcal{B}_{\tilde{x}},\mathcal{B}_{\tilde{z}},\mathcal{B}_{\tilde{s}})^{T}_{(\tilde{x},\tilde{z},\tilde{s})} = \mathbf{R}\left(\varphi(\tilde{s})\right)\,\vec{\mathcal{B}}(x_s,z_s,\sigma_s)^{T} \tag{5.9}$$

On the left side of the IP

$$\mathbf{R}\left(\varphi(\tilde{s})\right) = \begin{pmatrix} \cos\varphi(\tilde{s}) & 0 & -\sin\varphi(\tilde{s}) \\ 0 & 1 & 0 \\ \sin\varphi(\tilde{s}) & 0 & \cos\varphi(\tilde{s}) \end{pmatrix} \qquad \text{where} \qquad \varphi(\tilde{s}) = \varphi_{in} - \frac{\tilde{s}}{\rho_{\rm GO}} \tag{5.10}$$

and on the right side of the IP

$$\mathbf{R}\left(\varphi(\tilde{s})\right) \;=\; \begin{pmatrix} \cos\varphi(\tilde{s}) & 0 & \sin\varphi(\tilde{s}) \\ 0 & 1 & 0 \\ -\sin\varphi(\tilde{s}) & 0 & \cos\varphi(\tilde{s}) \end{pmatrix} \qquad \text{where} \qquad \varphi(\tilde{s}) = \frac{\tilde{s}-\tilde{d}_0}{\rho_{\mathrm{GG}}}\,. \tag{5.11}$$

With the transformed solenoid fields, using the above formulae, we are now in a position to perform Runge–Kutta integrations across the new IRs with respect to the design orbit and we finally come to the representations of the H1 and ZEUS fields.

5.2.1 H1 and ZEUS solenoid field models

For spin and orbit tracking the incomplete knowledge of the H1 solenoid fields requires that the measured information be complemented by an extrapolation of the data. This has been done by modelling the field as the superposition of the fields from two solenoids, according to an analytical expression given in [BB96, FG97]

$$\begin{aligned} \mathcal{B}_\sigma \;&=\; \frac{p_1}{p_2}\left(\frac{\sigma+p_2}{\sqrt{{p_3}^2+(\sigma+p_2)^2}} - \frac{\sigma-p_2}{\sqrt{{p_3}^2+(\sigma-p_2)^2}}\right) \\ &+\; \frac{p_4}{p_5}\left(\frac{\sigma+p_5}{\sqrt{{p_6}^2+(\sigma+p_5)^2}} - \frac{\sigma-p_5}{\sqrt{{p_6}^2+(\sigma-p_5)^2}}\right) \end{aligned} \tag{5.12}$$

This model gives a parametrization of the axial field in terms of the longitudinal coordinate, where the free parameters can be used to fit the measured data. A fit to the data with MINUIT [Ja94] gives

$$p_1 = 2.629, \quad p_2 = 4.131, \quad p_3 = 1.638, \quad p_4 = -0.01468, \quad p_5 = 0.6613, \quad p_6 = 0.4658$$

The H1 longitudinal field on the solenoid axis from the field map can be seen in Figure 5.3 together with a fitted parametrization using eqn. (5.12). In the figure, vertical lines indicate the extent of the field measurement between the solenoid end–cap regions. In the region covered by the measurements the fit is clearly good.

Assuming perfect rotational symmetry around the magnetic axis, the parametrized longitudinal field on the solenoid axis is sufficient for determination of all other field components via Maxwell's equations, expressing the components through simple Taylor expansions [FR73]. An estimation of the unknown end fields is then possible. Moreover, the parametrization of the field has the advantage over a method relying on interpolation of the field map data of higher computational speed. Accordingly, in order to fulfill Maxwell's equations, only the measured on–axis longitudinal field has been incorporated (even in regions where the measurement data contain information on the transverse fields) and away from the solenoid axis the radial and longitudinal field components are given by

$$\begin{aligned} \mathcal{B}_r \;&=\; \sum_{n=0}^{\infty} b_{2n+1}(\sigma)\, r^{2n+1} \\ \mathcal{B}_\sigma \;&=\; \sum_{n=0}^{\infty} b_{2n}(\sigma)\, r^{2n} \end{aligned} \tag{5.13}$$

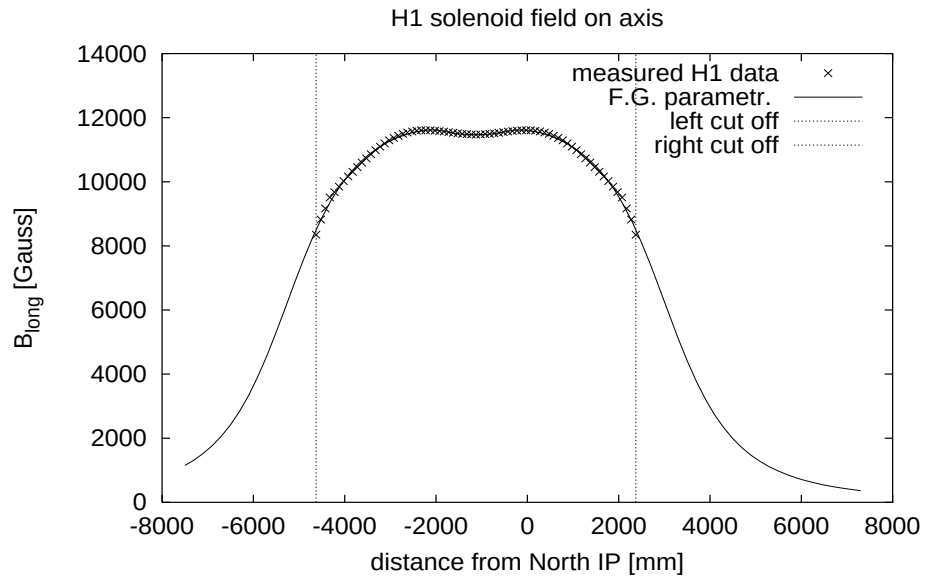

Figure 5.3: On–axis H1 solenoid field used in the numerical calculations. The crosses are the measured data from the H1 field map and the solid curve is a fit to this data using eqn. (5.12). The vertical lines indicate the limits of the measurements and the positions of the δ–function radial end fields in model A_1.

where the following recursive relationships hold

$$\begin{aligned} b_{2n+1}(\sigma) &= \frac{(-1)^{n+1}}{(2n+2)(2n!!)^2}\, b_0^{(2n+1)} \qquad \forall\, n \in \{0,1,2,\ldots\} \\ b_{2n+2}(\sigma) &= \frac{(-1)^{n+1}}{((2n+2)!!)^2}\, b_0^{(2n+2)} \qquad \forall\, n \in \{0,1,2,\ldots\} \end{aligned} \tag{5.14}$$

The implementation into the code for numerical matrix retrieval only includes the constant and linear terms of the Taylor expansions, the justification for this being the smallness of the higher order terms for particles travelling at a modest distance from the solenoid axis and increased computational speed, avoiding complicated analytical expressions and numerical ripple from quickly oscillating terms. Retaining just the zeroth and first order terms in eqn. (5.13) we are left with

$$\begin{aligned} \mathcal{B}_r &= b_1(\sigma)\, r \;=\; -\frac{1}{2}\, b_0{}'(\sigma)\, r \\ \mathcal{B}_\sigma &= b_0(\sigma) \end{aligned} \tag{5.15}$$

The resulting parametrization of the H1 solenoid field is depicted in Figures 5.4 to 5.6.

We now discuss three different ways of describing the H1 fields at and beyond the limits of the measurements. The first, called hard edge model A_1, has the parametrization (5.12) but hard edge cut offs at the positions given in Figure 5.3 and a resulting total integrated longitudinal field of

$$\int_{\mathrm{H1}} \mathcal{B}_\sigma d\sigma = 7.64169\,\mathrm{Tm}$$

However more recent information and field calculations with the POISSON code [Fe99] have shown that this value underestimates the H1 integrated field by about 8% so that one should have

$$\int_{\mathrm{H1}} \mathcal{B}_\sigma d\sigma = 8.266\,\mathrm{Tm}$$

Thus we have defined a second hard edge model. This again has the parametrization (5.12) but hard edges at positions set to give the larger integral. We refer to this as hard a edge model A_2. In mathematical terms the longitudinal fields of models A_1 and A_2 can be written as $\vec{\mathcal{B}_\sigma} = \mathcal{B}_\sigma(\sigma)\,\hat{\sigma}\,\Theta(\sigma-\sigma_1)\,[1-\Theta(\sigma-\sigma_2)]$ where Θ is the Heaviside step function, and the radial end fields appear as δ–function kicks at $\sigma=\sigma_1$ and $\sigma=\sigma_2$, using eqn. (5.15).

A physical solenoid field will of course not exhibit such a behaviour, but have a smooth decline over some distance comparable to the size of the hole for the beam pipe in the iron return yoke. Therefore a more realistic model, model B, reflecting this fact has been constructed. This uses parametrization (5.12) together with a linear fall off of the end fields arranged so as to give the the field integral of 8.266 Tm. Field calculations with OPERA2D [4] in the end field regions support this assumption, see Figure 5.7.

In summary, the various models used to represent the H1 field in the polarization calculations are as follows. All the numerical map models use the first order field approximation according to eqn. (5.15). The results of calculations of orbital and spin motion are presented in Chapter 6.

- The sandwich model with a field integral of 8.266 Tm, using the "box–field approximation", i.e. the hard edge model where all solenoid slices have the same strength.
- Numerical map model A_1. Hard edge cutoff using the lower estimate of the H1 field integral: 7.642 Tm. See Figure 5.3.
- Numerical map model A_2. Hard edge cutoff using the higher estimate of the H1 field integral: 8.266 Tm. See Figure 5.7.
- Numerical map model B. Linear fall off model using the higher estimate of the H1 field integral. See Figure 5.8.

The ZEUS field measurement data has been treated in a manner similar to the H1 field data. To fit the data to an analytical expression, only a single solenoid term is needed. As the solenoid field was measured out to a greater distance from the centre point, including the fringe field regions, the fall off of the field and the shape of the end fields are known. Therefore only one end field model has been considered for the numerical map derivations, the hard edge cutoff as illustrated in Figure 5.9. Note in particular that the field overlap with the machine magnets is smaller, as is the integrated field strength compared to H1. The ZEUS longitudinal asymmetry with respect to the IP is also quite small. For the numerical calculations, the radial field components on the solenoid axis originating from magnetic material close to the iron return yoke have been neglected, since their magnitude is small, < 400 Gauss. The ZEUS field integral on axis is

$$\int_{\mathrm{ZEUS}} \mathcal{B}_\sigma d\sigma = 4.45409\,\mathrm{Tm}$$

The ZEUS field has been parametrized using the form

[4] The Opera2D calculations were performed by M. Marx with the purpose of studying some details of the magnetic field close the the solenoid end–caps. The shape and magnitude of the central part of the field was of minor importance, suggesting an explanation for the disagreement with the field map data in this region.

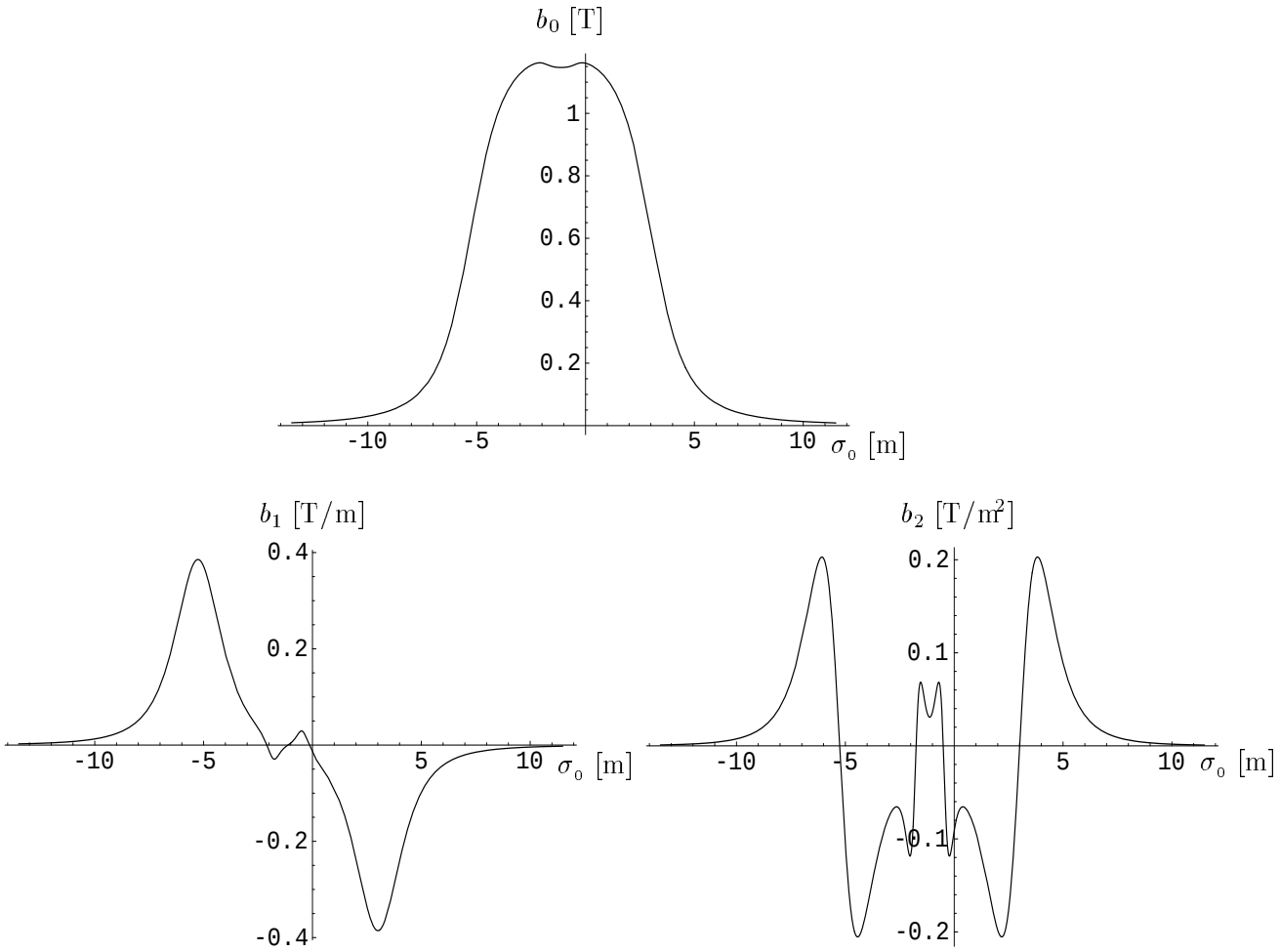

Figure 5.4: The H1 solenoid on–axis longitudinal field and the first two derivatives thereof, using the expansion (5.14) with the parametrization (5.12) where $\mathcal{B}_\sigma = b_0(\sigma_0)$. See Figure 5.2 for the definition of the longitudinal variable σ_0.

$$\mathcal{B}_\sigma = \frac{p_1}{p_2}\left(\frac{\sigma + p_2}{\sqrt{{p_3}^2 + (\sigma + p_2)^2}} - \frac{\sigma - p_2}{\sqrt{{p_3}^2 + (\sigma - p_2)^2}}\right) \tag{5.16}$$

with MINUIT fit parameters

$$p_1 = 1.166, \quad p_2 = 1.364, \quad p_3 = 0.8815$$

The longitudinal and radial field components are once again given by eqn. (5.15). Calculations using the numerical map model for ZEUS are presented in Chapter 6.

5.2.2 Implementation into SITROS

The method used to create numerical maps, representing the overlapping fields in the new interaction regions, for implementation into SLIM/SLICK can with some modifications also be used to create

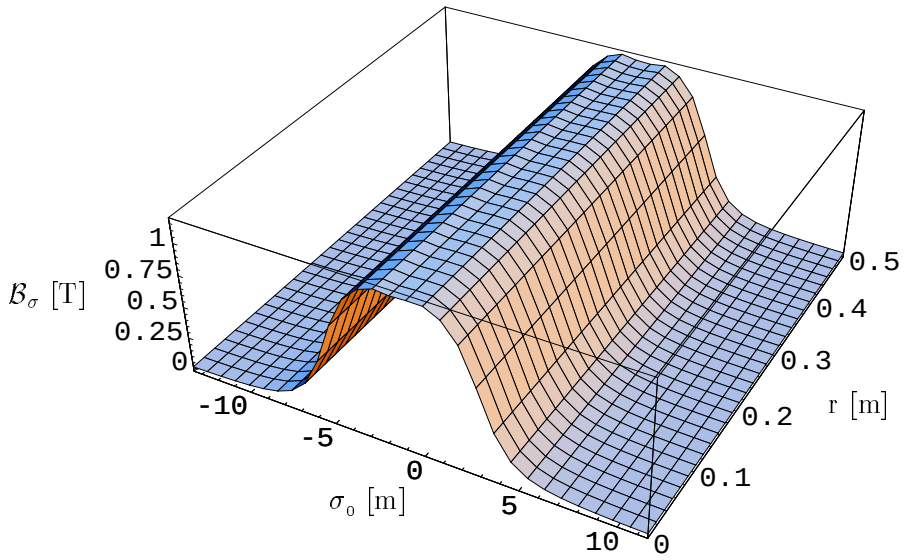

Figure 5.5: The H1 solenoid longitudinal field as given by the first order Taylor coefficients of a parametrized fit, using eqn. (5.12), to the on–axis measured longitudinal field. The cylindrical coordinates r and σ_0 are defined in Figure 5.2.

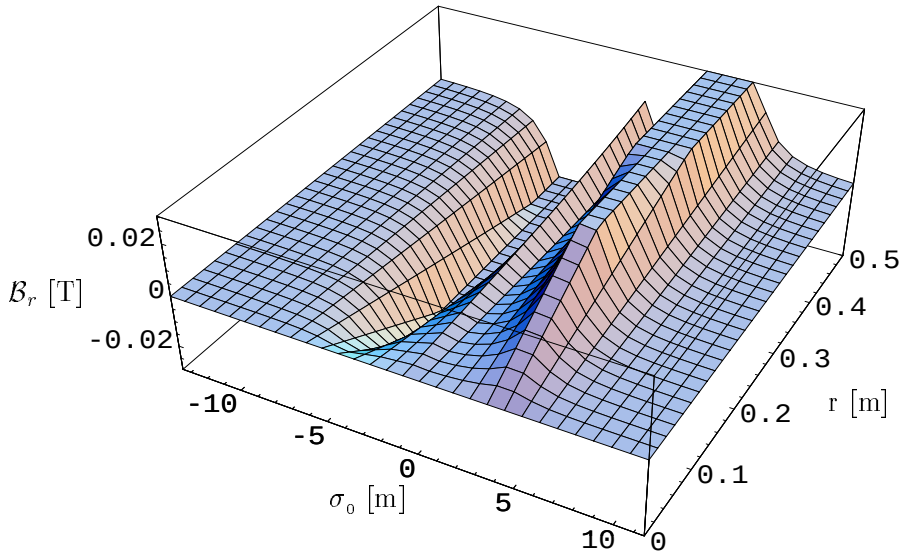

Figure 5.6: The H1 solenoid radial field as given by the first order Taylor coefficients of a parametrized fit, using eqn. (5.12) together with (5.15), to the on–axis measured longitudinal field. The cylindrical coordinates r and σ_0 are defined in Figure 5.2

maps for SITROS. For SITF, the linear part of SITROS, it is (almost) straightforward, whereas for the tracking part of SITROS a few points must be noted.

First of all, the orbit maps in SITROS contain damping and hence are not symplectic. The SLIM/SLICK maps should therefore in principle be recalculated before using them in SITROS, taking the E_0–dependent antidamping of the combined function magnets into account. For a large ring such as HERA, the contribution to the damping from a few magnets in the interaction regions, although having strong fields, is not prominent. Switching the damping off in the GO and GG magnets changes the damping partition numbers by less than 0.5%. The nondamped matrices from SLIM/SLICK can thus be used as a good approximation to the real damped maps for these few elements with

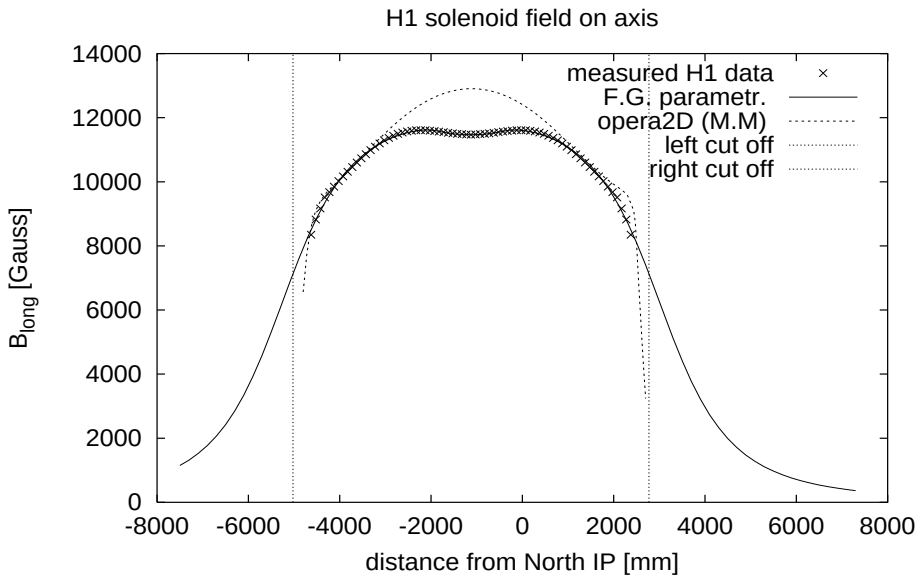

Figure 5.7: On–axis H1 solenoid field. The crosses are the measured data from the H1 field map and the solid curve is a fit to this data using eqn. (5.12). The vertical lines indicate the positions of the δ–function radial end fields in model A_2. The dashed line is a field calculation made with OPERA2D for studying the field near the end–caps.

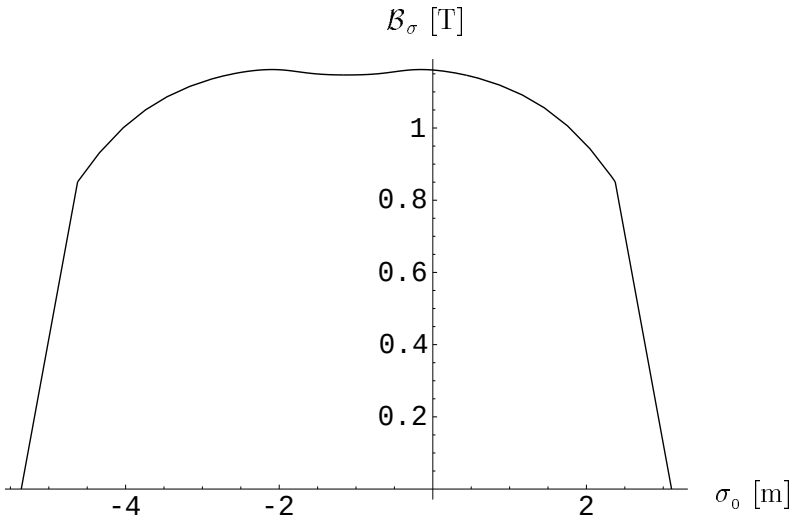

Figure 5.8: The H1 solenoid longitudinal field (measured data fitted to eqn. (5.12)) with an assumed linear fall off of field in the end regions: model B.

solenoid overlap. Furthermore, SITROS is built upon a matrix formalism where the nonlinearities up to second order in the orbital coordinates are accounted for. When constructing numerical maps for SITROS, all different two–combinations of the phase space coordinates at the starting positions should be traced across the map sections. However, the nonlinear effects in the mixed field sections, related to the solenoid end fields, are expected to be small compared to the total nonlinearity of the rest of the ring and could as a first attempt be ignored for the orbital motion. Considering the fact that the overlapping interaction region magnets only amount to a small fraction of the total number of magnets in the ring, such an approximation seems reasonable.

In contrast to SLIM/SLICK and SITF, where the spin transformations on the design and closed

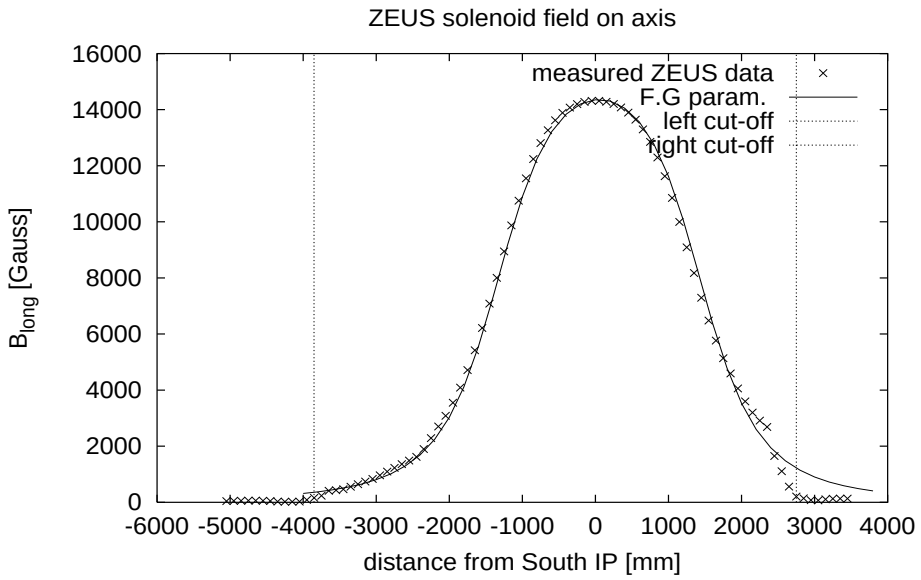

Figure 5.9: On–axis ZEUS solenoid field used in the numerical calculations. The crosses are the measured data from the ZEUS field map and the solid curve is a fit to this data using eqn. (5.16). The vertical lines indicate the positions of the δ–function radial end fields used in the model.

orbits are represented by the 3×3 rotation matrices, SITROS uses the quarternion description. Recall the definition of the unit–quarternion in Chapter 3, relation (3.85). The quarternions needed for the mapping of the spin motion through the overlapping elements in the HERA upgrade interaction regions could in principle be derived directly through integration in slices of the $\vec{\Omega}$ rotation vector (see eqn. (3.86) and eqs. (A.15 – A.17)) over the elements. However, for describing these long (thick) complex field regions, it is more convenient to use the rotation matrices evaluated for SLIM/SLICK and derive an approximation to the quarternions needed for SITROS.

It can be shown [Vo00] that for every rotation matrix $\mathbf{R} \in \mathrm{SO}(3)$ there exists a quaternion $\bar{q} = (\cos\frac{\varphi}{2}, \sin\frac{\varphi}{2}\hat{q})$ representing the same transformation. The correspondence between the representations is not one–to–one since the quarternion $\bar{q}^- = (\cos\frac{\varphi}{2}, -\sin\frac{\varphi}{2}\hat{q})$ is also a realization of $\mathbf{R}$. Adopting for simplicity the positive sign for $\sin\frac{\varphi}{2}\hat{q}$ as our preferred sign convention, the conversion from rotation matrices to quarternions is given by

$$\begin{aligned} q_0 &= \frac{1}{2}\sqrt{\mathrm{trace}(\mathbf{R})+1} \\ q_i^+ &= -\frac{\epsilon_{ijk}R_{jk}}{2\sqrt{\mathrm{trace}(\mathbf{R})+1}} \qquad \forall\, i \in \{1,2,3\} \end{aligned} \tag{5.17}$$

where ϵ_{ijk} is the anti–symmetric Levi–Civita tensor. If $\mathrm{trace}(\mathbf{R}) = -1$ so that $q_0 = 0$ there is still a non–vanishing

$$q_m^+ = \sqrt{\frac{R_{\underline{mm}}+1}{2}} \tag{5.18}$$

for some $m \in \{1,2,3\}$. The underlining of the indices indicate that they are not subject to contraction. We then have

$$q_i^+ = \frac{R_{mi}}{2q_m^+} \qquad i \neq m \tag{5.19}$$

Given the information at hand, we can write down the quarternion transformations as a truncated power expansion in the orbital coordinates

$$\bar{q} \;=\; \bar{q}_0 + \frac{\partial \bar{q}_1}{\partial x}\,\Delta x + \frac{\partial \bar{q}_1}{\partial x'}\,\Delta x' + \frac{\partial \bar{q}_1}{\partial z}\,\Delta z + \frac{\partial \bar{q}_1}{\partial z'}\,\Delta z' + \frac{\partial \bar{q}_1}{\partial \ell}\,\Delta \ell + \frac{\partial \bar{q}_1}{\partial \delta}\,\Delta \delta \tag{5.20}$$

where $\frac{\partial \bar{q}_1}{\partial \ell}\,\Delta\ell \equiv 0$. The zeroth order quarternions $\bar{q}_0$, corresponding to the $\mathbf{R}_0$'s, and the partial differentials of the first order quarternions $\bar{q}_1$, corresponding to the $\mathbf{R}_{\vec{u}_i}$'s, are calculated in–line in SITROS using eqs. (5.17 – 5.19). After summation of the terms in the expansion (5.20) the unitarity of the reconstructed quarternions must be restored by renormalization. Note that in the case of an optic with orbit distortions I have reverted to the sandwich model for practical reasons. See comments in Chapter 6.

Chapter 6

Polarization calculations for the upgraded HERA

6.1 Limitations and remedies

The luminosity upgrade of HERA is a major undertaking that has far reaching consequences for the electron machine. A brief introduction to the most important changes was given in Chapter 2 and Chapter 4. After having discussed the basic concepts of radiative spin polarization theory in Chapter 3 and the models introduced for describing the overlapping field structures in the new interaction regions in Chapter 5, we are now in a position to investigate the effects of the upgrade on the spin polarization.

The upgrade lattice is designed to allow collisions between protons and $e^{+/-}$ at the nominal HERA energies of 30 GeV for $e^{+/-}$ and 820 GeV for protons. Since it was demonstrated during 1998 machine operation that the proton ring can be run with sufficient safety margin at 920 GeV, the proton energy after the upgrade will (at least initially) be set to this value. For the $e^{+/-}$ beam the upper energy limit, as was mentioned earlier, is set by the maximum tolerable energy loss per turn and by reliability considerations. The lower energy limit is set by the spin rotators at about 26.8 GeV where the horizontal geometry in the tunnel is the limiting factor. The need to achieve a high level of spin polarization further restricts the choice of $e^{+/-}$ beam energy. In order to stay away from detrimental depolarizing resonances, the working point should be chosen such that the spin tune ν_0 is set to a half–integer value. The presence of the experiment solenoids and the spin rotators in the lattice introduces a shift of the spin tune away from $a\gamma$, where the shift related to the rotators is dominating and is about $\Delta\nu_0 = 0.05$ per pair at these energies. $E = 27.474$ GeV is therefore the smallest energy compatible with HERA operation with three pairs of rotators, corresponding to $\nu_0 = 62.5$. The corresponding energy in the old lattice with only one pair of rotators is $E = 27.519$ GeV.

For electron spin polarization, the main concerns for the upgrade are the effects of the uncompensated experiment solenoids and the influence from the overlapping fields in the interaction regions. A non–compensated solenoid in the lattice introduces coupling between horizontal and vertical betatron motion and thereby increases the vertical beam size. In addition it causes a tilt of $\hat{n}_0$. From eqn. (3.8) we see that for a particle travelling in a magnetic field of magnitude $\mathcal{B}_{||}$, parallel to its velocity, the spin $\widehat{S}$ precesses around the beam direction by an angle

$$\Delta\theta \;=\; \frac{(1+a)e}{\gamma m}\int \mathcal{B}_{||}(s)ds \tag{6.1}$$

The H1 solenoid for example, with its integrated field strength of 8.27 Tm would, if not compensated, tilt an initially vertical spin by about 90 mrad at 27.5 GeV. [1] Under such conditions the radiative polarization would be overwhelmed by depolarization. With the installation of spin rotators around the North and the South interaction zones, the design direction of $\hat{n}_0$ will be longitudinal at the IPs. The disturbance of the polarization from the uncompensated solenoids in this case is less severe, but nonetheless important. In particular particles which due to betatron motion travel through the solenoid at an angle x' or z' with respect to the solenoid axis, assuming for simplicity that the particle trajectories are straight lines in the solenoid [2], will experience kicks to their spin from the longitudinal field in the solenoid centre, and additional kicks in the solenoid end fields when the particles traverse these fields with a transverse offset. For these particles the spin matching conditions are broken. This can be understood in terms of the **G** matrix since these particles pick up nonzero contributions in columns 2 and 4 (central solenoid fields) and 1 and 3 (end fields) respectively, and these nonzero terms hence contribute to the spin diffusion. Note that for particles travelling with a fixed offset (x or z) through solenoid end fields, the end field contributions at the entrance and exit of the solenoid cancel. In the old design the effects of the experiment solenoids were almost completely compensated by anti–solenoids. The inevitable removal of these devices in the new design requires that the problems are solved in a different way. The situation in the interaction regions is further complicated by the overlap of the solenoid fields with the fields of the final focus magnets and by the lack of mirror symmetry.

Due to the larger integrated field strength of the H1 solenoid compared to the ZEUS solenoid, a larger longitudinal asymmetry and a more extensive overlap, most of the work on calculating the influence of the mixed fields in the new interaction regions on orbit and spin motion has concentrated on the North IR. For cases where both solenoids are included in the calculations, this will be explicitly mentioned. The particular optic that will be studied in the following sections is one of several revisions for the upgrade IRs and will be referred to as the Rev3.2 optic.

6.1.1 Coupling compensation

In the absence of compensating solenoids the inter–plane coupling in the new HERA design has to be minimized by other means. As a figure of merit, the ratio of the generalized vertical emittance to the horizontal one is about 6.9 % in this design with an uncompensated H1 solenoid overlapping with the GO and GG final focus magnets [3], as compared to the nominal value of 2.4 % in a lattice with three pairs of rotators, but with no solenoids. Following the successful implementation in several other machines (for example ISR and LEP) a solution utilizing skew quadrupoles has been adopted for HERA II. I will now give a summary of some theoretical methods for describing orbital coupling, which suggest ways to find the positions and relative strengths of the skew quadrupoles needed, and present some results based on these methods for the upgraded HERA electron optic.

The equations of motion (A.8) and (A.9) for the transverse particle coordinates in the presence of solenoids and skew quadrupoles can be written as [4]

$$\begin{aligned} x'' + (g + K_x^2)\, x &= (N + R')\, z + 2Rz' \\ z'' - (g - K_z^2)\, z &= (N - R')\, x - 2Rx' \end{aligned} \tag{6.2}$$

[1] Note that the resulting tilt in the machine arcs, looking at the *closed solution* for a half–integer spin tune, is about 45 mrad.

[2] i.e. ignoring the small twist of the beam generated by the solenoid and ignoring the weak focusing in the solenoid

[3] The value depends on the solenoid model; the stated value is for the sandwich model.

[4] To arrive at this form, the equations have been linearized following [MR82a] and Maxwell's equations have been used.

where

$$\begin{aligned} K_{x,z} &= \pm\frac{ec}{E_0}\{\mathcal{B}_{z,x}\}_{x=z=0} \\ g &= \frac{ec}{E_0}\{\frac{\partial B_x}{\partial z}\}_{x=z=0} = \frac{ec}{E_0}\{\frac{\partial B_z}{\partial x}\}_{x=z=0} \\ N &= \frac{1}{2}\frac{ec}{E_0}\{\frac{\partial B_x}{\partial x} - \frac{\partial B_z}{\partial z}\}_{x=z=0} \\ R &= \frac{1}{2}\frac{ec}{E_0}\{B_s\}_{x=z=0} \end{aligned}$$

We will need the notation introduced here for the following discussion. As a consequence of coupling between the transverse oscillation modes some of the horizontal dispersion will couple into the vertical plane, i.e. there will be generation of spurious vertical dispersion, which can be hazardous for the polarization. This however is not the case if the solenoid and its compensating skew quadrupoles are located in places where $D_x = 0$. In HERA the experiment solenoids are located at positions where $D_x \simeq 0$. The skew quadrupoles should therefore be placed at positions in the lattice where the horizontal dispersion is minimal. Moreover, since in general the coupling terms will only vanish in the region outside the coupling source (solenoid) and the compensating elements (skew quadrupoles in our case), for the overall machine optic it is desirable to have a local compensation of the coupling. [5] Hence the skew quadrupoles should be located as close as possible to the solenoids. In the following I will refer to the "region of interest" when discussing the region to be decoupled upstream and downstream of an experimental solenoid, between the outermost skew quadrupoles.

In the absence of coupling the 4×4 transfer matrix $\mathbf{m}$ for the transverse motion has a block diagonal form (cf. eqn. (4.1)) along any section of the ring, but when coupling is introduced the off diagonal blocks are no longer identically zero. Unlike the case of machine alignment errors, the perturbation due to an experiment solenoid is in principle known, so that the magnet may be included in the optic and one can look for settings for the skew quadrupoles which minimize the off–diagonal blocks of the transfer matrix. This will be referred to as the "matrix method". At this stage of the calculations in setting up an uncoupled optic, the radiation effects are usually not taken into account so that the transfer matrices obey the symplecticity condition $\mathbf{m}^T\,\mathbf{S}\,\mathbf{m} = \mathbf{S}$. The symplecticity ensures that only one of the off-diagonal blocks needs to be minimized, so that the number of free parameters is reduced to four. The minimum number of skew quadrupoles needed to force the off-diagonal blocks to zero is therefore four.

For the luminosity upgrade it has been decided to incorporate skew quadrupole windings in the final focus magnets GO and GG. At least one more pair of skew quadrupoles further out in the lattice is needed, but because of the limited strength of the "inner" skew components in GO and GG a solution with two more pairs has been chosen. In this way the extra freedom of choice in the settings can be used to suppress the vertical dispersion generated by the solenoids and the skew quadrupoles themselves. The choice of positions of the skew quadrupoles will be explained later in the text. Table 6.1 summarizes the settings of the six skew quadrupoles for the North IR. These were obtained using the six free parameters to minimize the sum of squares of the off–diagonal elements of the 4×4 part of the transfer matrix $\mathbf{M}$ for this region of interest and in addition the generation of vertical dispersion, i.e. requiring

$$\sqrt{w_1\,\mathrm{M}\,[1,3]^2 + w_2\,\mathrm{M}\,[1,4]^2 + w_3\,\mathrm{M}\,[2,3]^2 + w_4\,\mathrm{M}\,[2,4]^2 + w_5\,\mathrm{M}\,[3,6]^2 + w_6\,\mathrm{M}\,[4,6]^2} = 0$$

where $w_1, w_2, \ldots, w_6$ are weight factors. By weighting the dispersion compensation by a factor of 100 more than the coupling compensation an almost complete reduction of the spurious vertical dispersion

[5] In this treatment we will ignore any coupling related to machine magnet misalignments.

is accomplished, while still acquiring good coupling compensation. See Figure 6.1. However, as can be seen in Table 6.1 the skew quadrupole settings found for the various end field models of H1 have large variations. This is most likely due to the fact that the magnitude of D_z caused by the solenoid perturbation is quite modest to begin with: the solenoid contribution to the vertical dispersion is $\Delta D_z^{rms} \simeq 2.2$ mm, which should be compared with the much larger contribution from orbit distortions. See tables in Section 6.3. The system is therefore underdetermined.

	A_1	A_2	B
QSKN1	0.00035	0.00020	-0.00263
QSKN2	0.00064	0.00068	-0.00070
QSKON	0.00107	0.00038	-0.00010
QSKGN	-0.00763	-0.00768	-0.00008
QSKN3	-0.00165	-0.00214	-0.00772
QSKN4	-0.00003	0.00008	0.00165

Table 6.1: Skew quadrupole settings in the North IR, using 6 individually powered magnets (coils). Comparison between various end field models for H1. The integrated strengths are in m^{-1}.

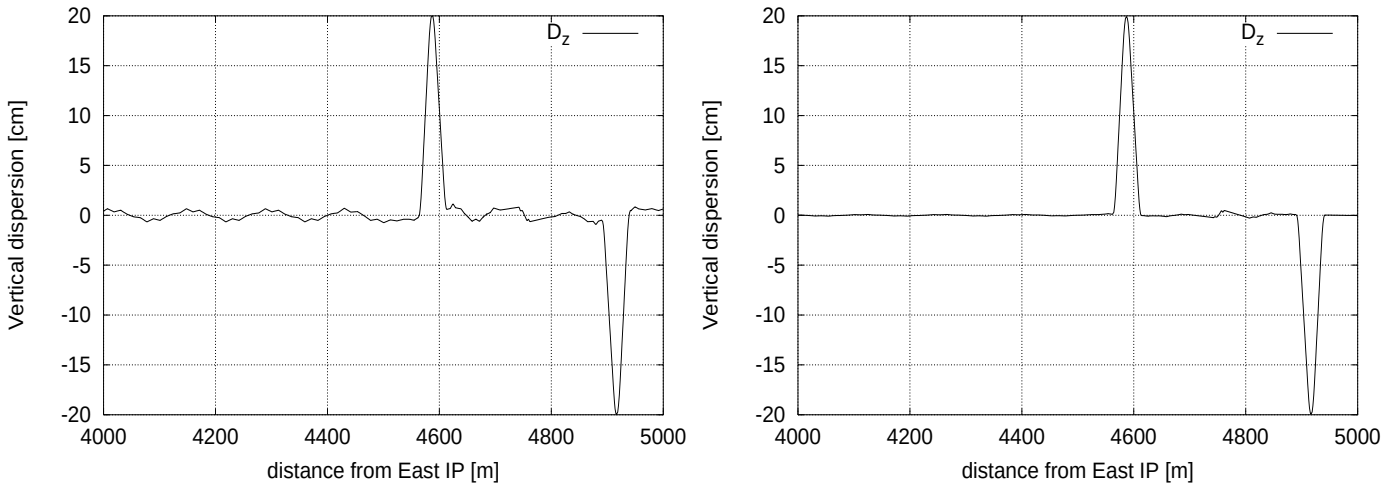

Figure 6.1: Vertical dispersion function in the North–West octant for the Rev3.2 e^- lattice including the H1 solenoid (end field model A_1) and local orbit correction. The IP North is at 4751.862 m. Observe that the 20 cm spikes correspond to the (design) vertical dispersion at the vertical bend magnets in the rotators. *Left:* No skew quadrupole compensation. *Right:* Skew quadrupole compensation with a relative weight factor of 100 favouring dispersion compensation over coupling compensation.

To get a better idea of how important the modelling of the solenoid end fields is and how this affects the skew quadrupole settings, the coupling minimization has been repeated using only the "outer" four skew quadrupoles and minimizing just the coupling, hence requiring

$$\sqrt{w_1 \,\mathrm{M}\,[1,3]^2 + w_2 \,\mathrm{M}\,[1,4]^2 + w_3 \,\mathrm{M}\,[2,3]^2 + w_4 \,\mathrm{M}\,[2,4]^2} = 0$$

The results are summarized in Table 6.2. In this table "crude" refers to a sandwiching made with only nine solenoid slices (and the same number of quadrupole and correction coil slices), whereas "thin quads" refers to a model where the focusing action is represented by a larger number of thin lens quadrupoles. In all cases the ratio of the vertical emittance to the horizontal one is reduced to 2.4 %. As can be seen, the variation in settings is now much reduced as compared to the six parameter

case and the agreement between the calculations made with the numerical IR maps and the sandwich model is also good. In the following calculations, the skew quadrupole windings on GO and GG have therefore been excluded and only the outer four skew quadrupoles are used.

	maps A_1	maps A_2	maps B	sandwich crude	sandwich thin quads
QSKN1	-0.0024	-0.0027	-0.0027	-0.0026	-0.0025
QSKN2	0.0004	-0.0010	-0.0009	0.0010	-0.0003
QSKN3	-0.0069	-0.0079	-0.0079	-0.0073	-0.0073
QSKN4	0.0017	0.0017	0.0017	0.0019	0.0017

Table 6.2: Skew quadrupole settings in the North IR, using 4 individually powered magnets. Comparison between various end field models for H1. The integrated strengths are in m^{-1}.

It should be noted that the settings of the skew quadrupoles presented here can only be used as a guide for how to power these magnets in the real machine. Even without taking further sources of coupling into account (due to, for instance, random roll–angles of the quadrupoles), one should be prepared to perform an empirical optimization. In particular, a straight forward minimization of the off diagonal blocks as in the matrix method does not tell anything about how the individual skew quadrupoles influence the coupling. It is therefore necessary to find ways to disentangle the effects that the individual skew quadrupoles have on the beam and to devise "orthogonal control knobs" for them. In order to find such knobs we have looked into a few different approaches, in particular two perturbative methods due to Guignard [Gu76] and Bassetti [Ba79] respectively.

A Perturbative harmonic approach (Guignard)

Guignard has formulated the solution to the problem of linear transverse betatron coupling utilizing a perturbative method. In his treatment the solutions of the uncoupled equations of motion are used to construct the solutions for the coupled case by the method of variation of constants. Owing to the periodicity in machine azimuth of the perturbing Hamiltonian, the perturbation can be expanded in a Fourier series and Guignard performs a detailed analysis of the two most important harmonics ($p^{\pm}$) associated with the linear sum (+) and difference (−) resonances. In the presence of pure solenoid and skew quadrupole fields and neglecting terms in R^2 (see eqn. (6.2)), the real and imaginary parts of these Fourier components are given in terms of the Courant–Snyder parameters [CS58] β and $\alpha = -\frac{\beta'}{2}$ by

$$
\begin{aligned}
\Re\mathrm{e}(+) &= \frac{1}{4\pi}\int_0^C \sqrt{\beta_x\beta_z}\left\{[N + R(\frac{\alpha_x}{\beta_x} - \frac{\alpha_z}{\beta_z})]\cos(\psi^+) + R(\frac{1}{\beta_x} - \frac{1}{\beta_z})\sin(\psi^+)\right\} ds \\
\Im\mathrm{m}(+) &= \frac{1}{4\pi}\int_0^C \sqrt{\beta_x\beta_z}\left\{[N + R(\frac{\alpha_x}{\beta_x} - \frac{\alpha_z}{\beta_z})]\sin(\psi^+) - R(\frac{1}{\beta_x} - \frac{1}{\beta_z})\cos(\psi^+)\right\} ds \\
\Re\mathrm{e}(-) &= \frac{1}{4\pi}\int_0^C \sqrt{\beta_x\beta_z}\left\{[N + R(\frac{\alpha_x}{\beta_x} - \frac{\alpha_z}{\beta_z})]\cos(\psi^-) + R(\frac{1}{\beta_x} + \frac{1}{\beta_z})\sin(\psi^-)\right\} ds \\
\Im\mathrm{m}(-) &= \frac{1}{4\pi}\int_0^C \sqrt{\beta_x\beta_z}\left\{[N + R(\frac{\alpha_x}{\beta_x} - \frac{\alpha_z}{\beta_z})]\sin(\psi^-) - R(\frac{1}{\beta_x} + \frac{1}{\beta_z})\cos(\psi^-)\right\} ds
\end{aligned}
\tag{6.3}
$$

with

$$\psi^{\pm} \equiv \mu_x \pm \mu_z - (\nu_x \pm \nu_z + p^{\pm})\frac{2\pi s}{C}$$

where μ_x and μ_z are the horizontal and vertical betatron phase advances, and $p^{\pm}$ is the closest integer to $-(\nu_x \pm \nu_z)$. Also with this formalism one finds that at least four skew quadrupoles are needed for the compensation, although these then have a somewhat different function as compared to the four emerging from the matrix method. In principle, an exact compensation of the perturbation would require the compensation of all harmonics and therefore an infinite number of skew quadrupoles. However, this is only apparently in contradiction with the matrix method. The matrix method is aiming at getting decoupled motion outside the region of interest, whereas the harmonic approach is minimizing the perturbation everywhere along the ring (in our case by requiring the four most important harmonics of the perturbation to vanish). For this reason one does not in general expect the two approaches to be equivalent. Note the analogy with the closed orbit case, where the effect of a local kick can be either confined to a short region by powering two coils close to the disturbance, forming a local "orbit bump", or can be minimized by correcting the most important Fourier harmonics of the resulting closed orbit, thus reducing the orbit distortion everywhere around the ring.

The Guignard approach is useful for recognizing the optimal locations for the skew quadrupoles. Indeed, to keep the integrated strengths of the skew quadrupoles small and to have the possibility of correcting all four coefficients one should look for places where $\sin(\psi^{\pm})$ and $\cos(\psi^{\pm})$ are not all small. For example, since the phase advances across the upgraded low beta regions are approximately equal to π in both planes, all sine terms will (nearly) vanish for positions close to the IPs. Taking this into consideration, together with the condition $D_x \simeq 0$ on the horizontal dispersion (the dispersion functions in the upgrade IRs can be seen in Figure 2.3) and additional space restrictions due to the proton ring magnets, the number of choices of suitable positions is very limited. For the HERA–e luminosity upgraded optic the most convenient locations have turned out to be at $\pm$116.3 m and $\pm$124.5 m from the IPs, and (if used) near the IPs by placing the skew quadruple windings on GO and GG on the "outer halves", i.e. on the left half of GO and on the right half of GG.

From eqn. (6.3) it is clear that for a fully symmetric IR design the solenoid would be compensated by two pairs of antisymmetric skew quadrupoles, leading to only two independent knobs. It is worth noting that this result also holds for the matrix approach. For HERA the interesting aspect of the Guignard approach is that owing to the orthogonality of the Fourier components and their linear dependence on the skew quadrupole strengths, it is possible to choose four sets of skew quadrupole strengths, such that when the strengths in a set are scaled, the corresponding harmonic is scaled by the same factor without changing the other three harmonics. The scale factors are the "orthogonal knobs" or "skew bumps" for the Guignard formalism needed for the empirical optimization mentioned above. In practice the relationships ("excitation ratios") between the skew quadrupole strengths required to excite one harmonic at a time and leaving the others unchanged are trivially obtained by solving eqn. (6.3) for $\Re\mathfrak{e}(+) = 1$ with $\Im\mathfrak{m}(+) = \Re\mathfrak{e}(-) = \Im\mathfrak{m}(-) = 0$, $\Im\mathfrak{m}(+) = 1$ with $\Re\mathfrak{e}(+) = \Re\mathfrak{e}(-) = \Im\mathfrak{m}(-) = 0$ and so on. Although the one–turn transfer matrix is not fully decoupled with this choice, calculations with SLIM/SLICK show that the residual effects of the remaining coupling on the beam dynamics and the polarization are very small. See Figure 6.11. It should however be mentioned that the remaining distortion of the vertical dispersion after compensation with four skew quadrupoles is $\Delta D_z^{rms} \simeq 7$ mm (including the distortion introduced by the skew quadrupoles themselves), i.e. larger than before the correction, since with only four skew quadrupoles this distortion cannot be controlled. The value is nevertheless small compared to the value associated with closed orbit distortions, as we will see.

B Perturbative approach (Bassetti)

Although the transfer matrix is not explicitly mentioned, Bassetti is actually considering the transfer matrix through the region of interest. In a first order approximation he finds that the block diagonal

elements are unchanged by the coupling perturbation and that the off–diagonal elements may be expressed as linear combinations of the unperturbed block diagonal elements, the coefficients of such combinations being given by the integrals on the right hand side of eqn. (6.3) with $\psi^{\pm} \equiv \mu_x \pm \mu_z$. Therefore block–diagonalization of the matrix in the Bassetti formulation amounts to requiring the integrals in (6.3), with "Bassetti phases" instead of "Guignard phases", to be zero. Owing to the specific form of the functions to be integrated in eqn. (6.3), the Bassetti approach also leads to four orthogonal "knobs".

By comparing the Bassetti and the Guignard formulas we see that for $\nu_x + \nu_z = p^+$ and $\nu_x - \nu_z = p^-$ the two approaches are equivalent. However, in practice these conditions can never be satisfied simultaneously. It is therefore better to say that the approaches are equivalent when the region of interest is short. In that case $(\nu_x \pm \nu_z + p^{\pm})\frac{2\pi s}{C} \simeq$ const. When the region of interest is short the two approaches are also conceptually equivalent. For the luminosity upgrade Rev3.2 e^- optic a comparison between the skew quadrupole settings needed for the North IR, using the matrix minimization, the Guignard and the Bassetti methods is given in Table 6.3 (simulations done with SLIM, using the sandwich mode with 34 solenoid slices). Indeed one finds that the matrix method and the Bassetti approach give very similar, although not identical, results.

	matrix method	Bassetti	Guignard
QSKN1	-0.00257	-0.00254	-0.00231
QSKN2	0.00024	0.00025	0.00028
QSKN3	-0.00747	-0.00739	-0.00649
QSKN4	0.00178	0.00175	0.00146

Table 6.3: Skew quadrupole settings in the North IR, comparing values found for the matrix method, the Bassetti and the Guignard approaches respectively. The integrated strengths are in m^{-1}.

A minimization of the four harmonics in eqn. (6.3) minimizes the overall perturbation of the Hamiltonian of the system. It should therefore be possible to use any observable as a figure of merit. One such observable is the betatron tune, whose measurement is available at any storage ring. By using the perturbative approach it is possible to show (see for instance [RW88]) that in the presence of coupling sources the horizontal and vertical motions both contain the same two frequencies, ν_I and ν_{II}. When $\nu_x^0 \simeq \nu_z^0 \equiv \nu^0$, ν_x^0 and ν_z^0 being the unperturbed tunes, these frequencies, which are the actually measurable ones, differ from each other and from the unperturbed tune ν^0 by an amount which depends on the coupling strength. Therefore decoupling is achieved when it is possible to set the machine quadrupoles so that the measurable tunes are equal. Another suitable observable is the tilt of the beam cross section. Indeed when the radial and vertical motions are uncoupled the beam cross section is an ellipse with axes aligned along the x and z axes, reflecting the fact that the x and z coordinates of the particles are independent. In the presence of coupling the beam ellipse is tilted and the tilt angle, for a given perturbation, is a function of the machine azimuth. The measurement of the tilt of the beam ellipse is therefore also a measure of the machine coupling. In HERA the beam cross section can be observed at the synchrotron light monitor (SLM) in the North–West arc, at the experiment luminosity monitors and at the transverse polarimeter. It is worth noting that a monitoring of the beam ellipse tilt merely at one azimuth in the machine would be insufficient.

This way of correcting the coupling through empirical adjustment of the four coefficients in eqn. (6.3) has been simulated with SLIM for the Rev3.2 e^- upgrade optic in the presence of the H1 solenoid (using the sandwich model). For each harmonic the strength of QSKN1, the skew quadrupole located at -124.5 m (the "leading quadrupole"), has been varied and the observables described above have been recorded. The strengths of the remaining three skew quadrupoles are slaved to the strength of QSKN1 through the excitation ratios. Figures 6.2 to 6.4 show these chosen observables plotted against the integrated strength of QSKN1 for the harmonics $\mathfrak{Re}(+)$, $\mathfrak{Re}(-)$ and $\mathfrak{Im}(-)$. The nominal tunes (without the solenoid) are pushed rather close together and are $\nu_x(\text{unp}) = 54.149$ and

$\nu_z(\mathrm{unp}) = 51.167$. [6] When the solenoid is switched on the tunes move apart to $\nu_I = 54.143$ and $\nu_{II} = 51.174$. The minimum tune separation is obtained by setting the skew quadrupoles to the values quoted in Table 6.4. This table also gives values obtained by analytically solving eqn. (6.3) with the Bassetti definition of $\psi^{\pm}$. Note that the optimal settings found by looking at the minimum tune separation are in good agreement with the values found at the minimum value of the rms beam ellipse tilt. We note that the coefficient $\Im\mathfrak{m}(-)$ in Table 6.4 shows the largest deviation. For $\Im\mathfrak{m}(+)$, which is relatively small, the scanning did not give any minimum. This can be understood by noting that the tunes are far away from the sum resonance. In fact the minimum for $\Re\mathfrak{e}(+)$ is also not pronounced. The result from the scanning indicates that in practice, the only coefficients that are expected to be measurable are the $\Re\mathfrak{e}(-)$ and $\Im\mathfrak{m}(-)$, in consistency with the fact that HERA is operated close to the difference resonance.

For the sake of consistency, the results presented above on the coupling minimization using the Bassetti and Guignard approaches are all obtained using the sandwich model in SLIM, since a complete set of results for the mixed maps in SLICK is not at hand. It should be pointed out however that the calculations have been cross checked using both methods for the major part of the results and that the results are consistent. The values found for the skew quadrupole settings are not the same with the sandwich model and with the numerical maps, but they both indicate that the optimization method is feasible.

	QSKN1	
	"analytical"	scan
$\Re\mathfrak{e}(+)$	0.00030	0.00027
$\Im\mathfrak{m}(+)$	-0.00008	–
$\Re\mathfrak{e}(-)$	-0.00160	-0.00160
$\Im\mathfrak{m}(-)$	-0.00115	-0.00100

Table 6.4: Contributions from the real and imaginary parts of the coupling coefficients to the settings of the first (upstream) of the four skew quadrupoles, compared to the corresponding contributions found by scanning each of the four skew quadrupole bumps and looking at some suitable observable(s). The integrated strengths are in m^{-1}.

C Transfer matrix measurement

Finally, we have considered the possibility of "measuring" the actual transfer matrix $\mathbf{M}$ of an experiment solenoid once it is switched on. The basic idea is simple. One excites orbit oscillations with a correction coil upstream of the solenoid and measures the beam position at the BPM's just before and after the solenoid. Knowing the initial (i) and final (f) coordinates at the solenoid entrance and exit the transfer matrix can be retrieved in a way similar to the way the numerical maps were calculated in Chapter 5. However, since the particle slopes cannot in general be measured they must be computed by making a fit to the measured position data. The closed orbit in an error free region can always be fitted by a free betatron oscillation, therefore the normal HERA correction coils may be used and one can work on difference closed orbits instead of single pass data. The procedure can be summarized as follows:

- Excite one coil upstream of the solenoid
- Fit difference orbits by using the BPMs between the coil and the solenoid
  $\rightarrow (x^i, x'^i, z^i, z'^i)$

[6] The label "unp", meaning "unperturbed", on ν_x and ν_z is equivalent to the superscript 0 used earlier.

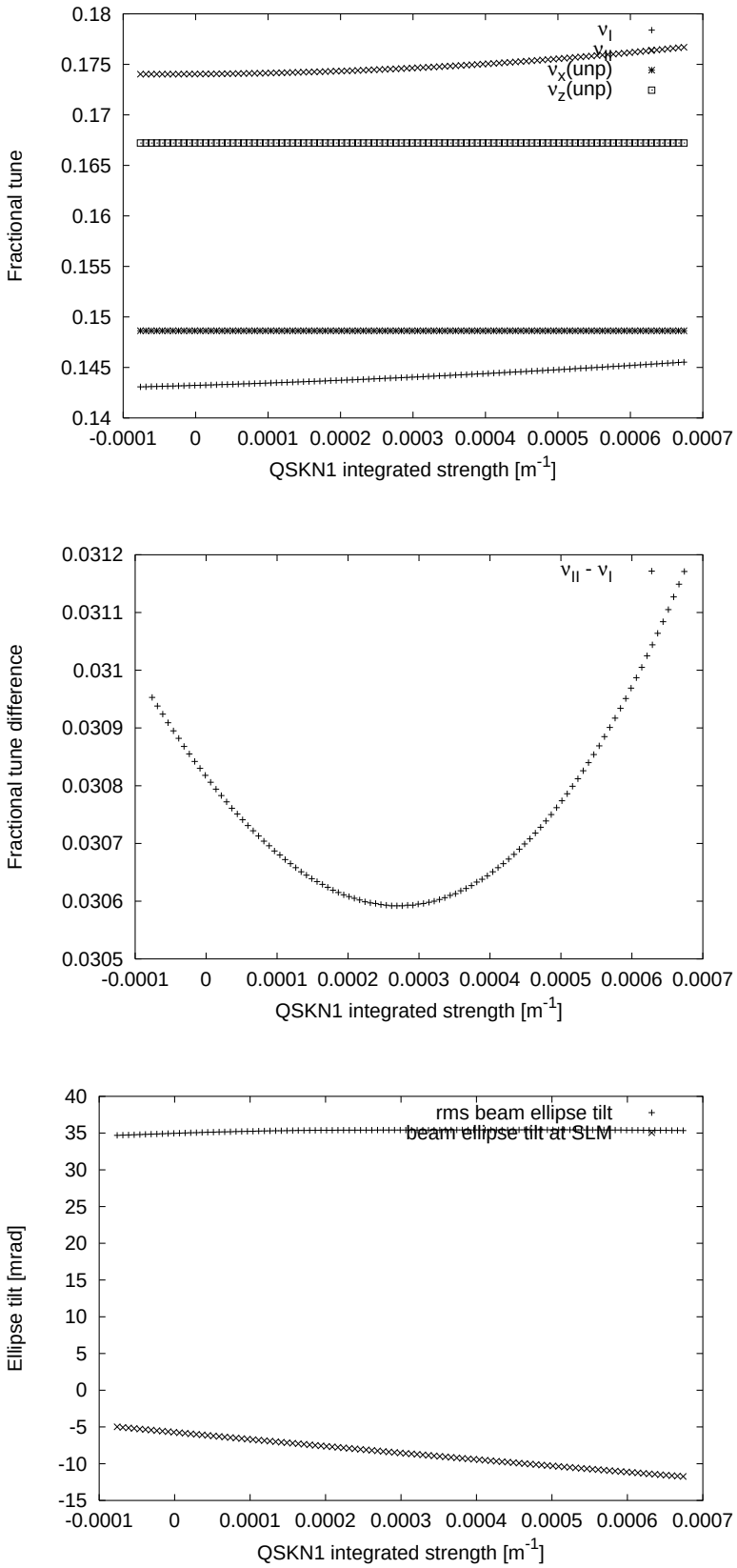

Figure 6.2: A few observables plotted against the integrated strength of QSKN1 for the $\Re\mathfrak{e}(+)$ harmonic, when minimizing the coupling in the Rev3.2 e^- lattice including the H1 solenoid (sandwich model). *Top:* Nominal (without solenoid) and perturbed tunes (with solenoid). *Middle:* Tune difference. *Bottom:* The rms beam ellipse tilt around the ring, and the beam ellipse tilt at the SLM.

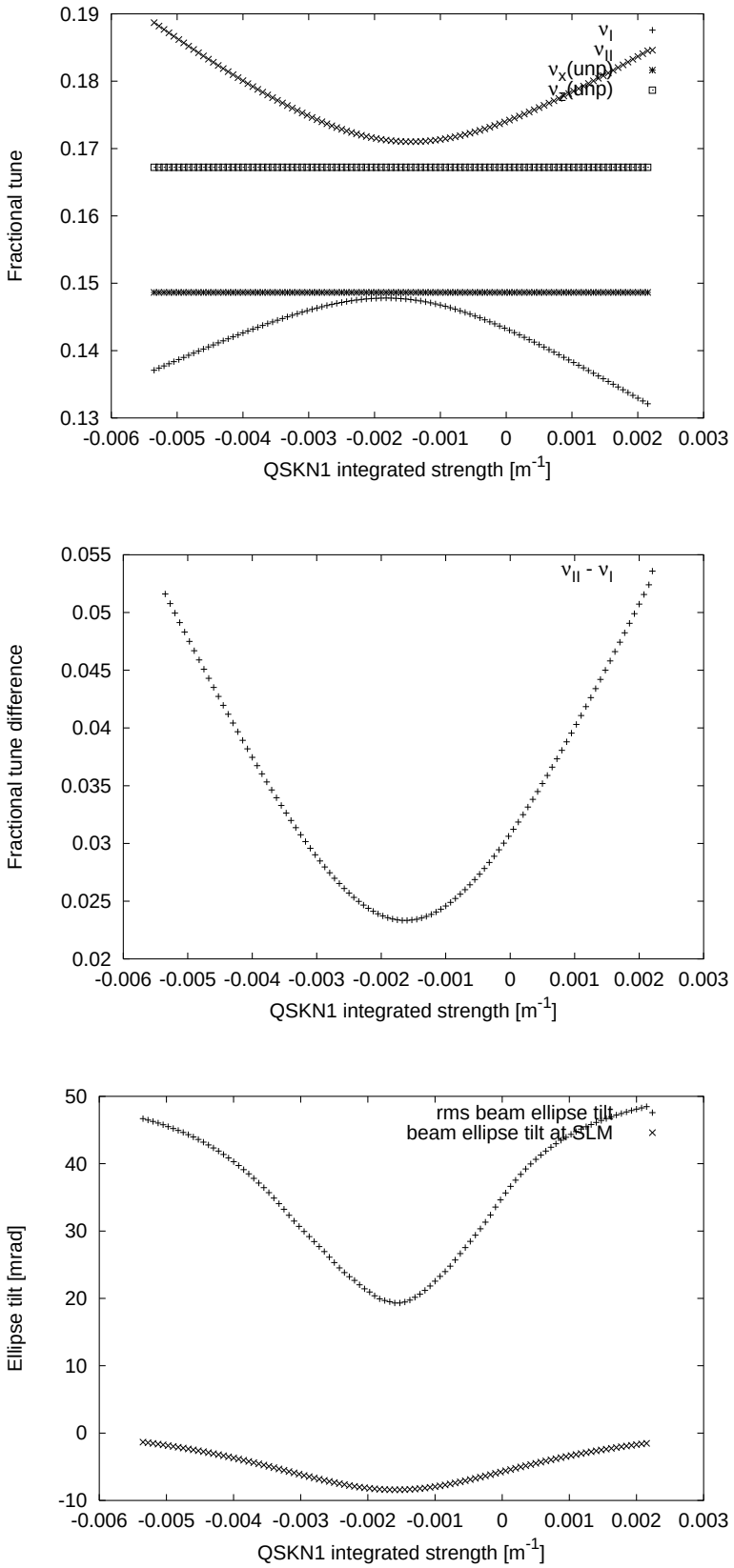

Figure 6.3: A few observables plotted against the integrated strength of QSKN1 for the $\Re\mathfrak{e}(-)$ harmonic, when minimizing the coupling in the Rev3.2 e^- lattice including the H1 solenoid (sandwich model). *Top:* Nominal (without solenoid) and perturbed tunes (with solenoid). *Middle:* Tune difference. *Bottom:* The rms beam ellipse tilt around the ring, and the beam ellipse tilt at the SLM.

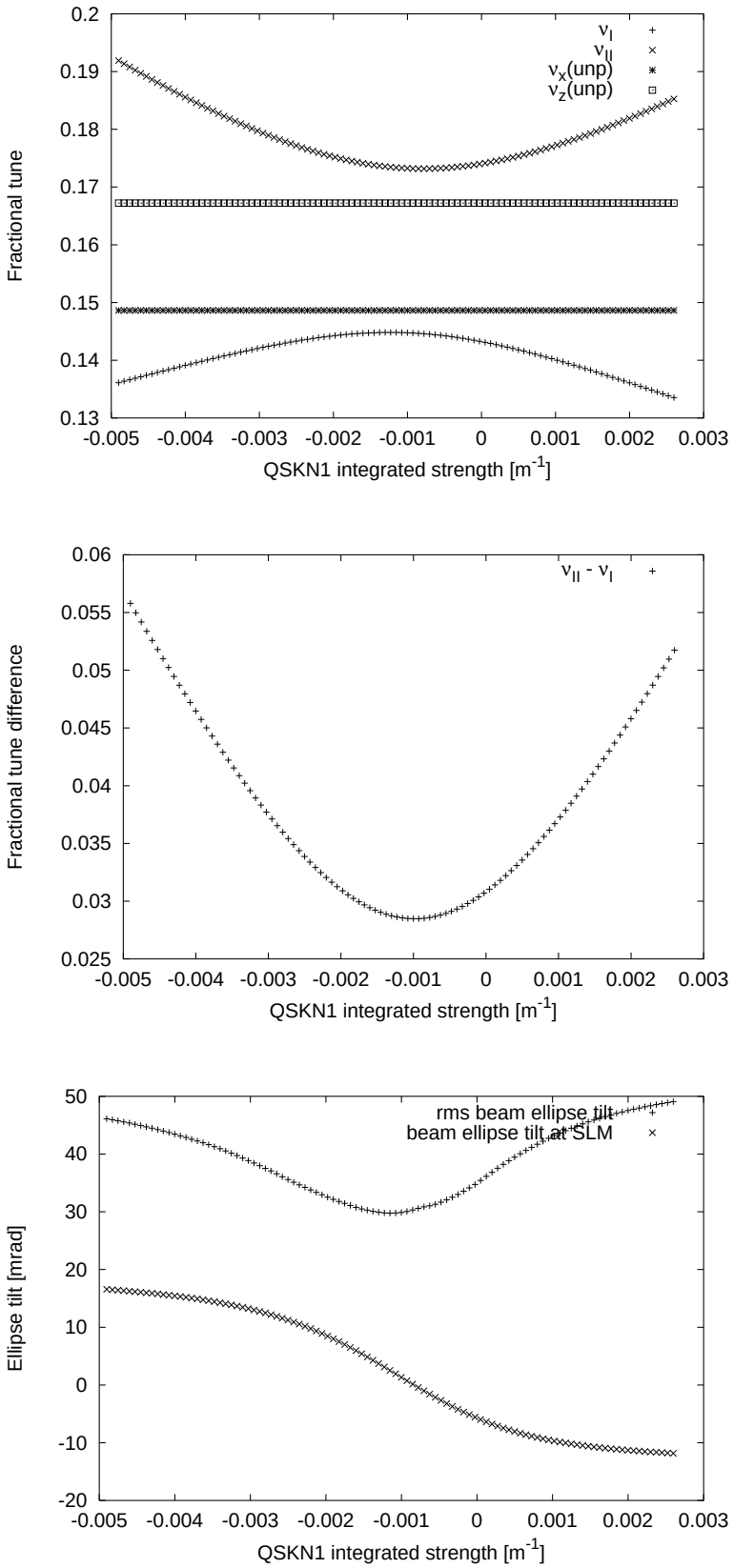

Figure 6.4: A few observables plotted against the integrated strength of QSKN1 for the $\Im\mathfrak{m}(-)$ harmonic, when minimizing the coupling in the Rev3.2 e^- lattice including the H1 solenoid (sandwich model). *Top:* Nominal (without solenoid) and perturbed tunes (with solenoid). *Middle:* Tune difference. *Bottom:* The rms beam ellipse tilt around the ring, and the beam ellipse tilt at the SLM.

- Fit difference orbits downstream of the solenoid
  $\rightarrow (x^f, x'^f, z^f, z'^f)$
- Repeat the process for 3 more coils to get a 16×16 equation system in the transfer matrix elements

$$\vec{w} = \mathbf{A}_{16\times 16}\,\vec{v}$$

with

$$\vec{w} = (x_1^f, x_1'^f, z_1^f, z_1'^f, x_2^f, \ldots, z_4'^f)$$

and

$$\vec{v} = \left(\mathrm{M}\,[1,1]\,, \mathrm{M}\,[1,2]\,, \ldots, \mathrm{M}\,[2,1]\,, \mathrm{M}\,[2,2]\,, \ldots, \mathrm{M}\,[4,4]\right)$$

where

$$\mathbf{A}\,[1,j] = (x_1^i, x_1'^i, z_1^i, z_1'^i, 0, \ldots, 0)$$

$$\mathbf{A}\,[2,j] = (0,0,0,0,x_1^i, x_1'^i, z_1^i, z_1'^i, 0, ...0)$$

$$\ldots\ldots\ldots$$

$$\mathbf{A}\,[5,j] = (x_2^i, x_2'^i, z_2^i, z_2'^i, 0, \ldots, 0)$$

$$\ldots\ldots\ldots$$

$$\mathbf{A}\,[16,j] = (0, \ldots, 0, x_4^i, x_4'^i, z_4^i, z_4'^i) \qquad \forall\, j \in \{1, \ldots, 16\}$$

- By inverting the $\mathbf{A}$ matrix (which is not singular if coils with a phase difference $\Delta\mu_{x,z} \neq n\pi$, where n is integer, are used) the solenoid transfer matrix elements are obtained, and the matrix $\mathbf{M}$ can subsequently be fed into a program minimizing the coupling with, for instance, the matrix method.

At first sight one needs at least four different orbits in order to determine the 16 matrix elements, but the symplecticity condition reduces the number of the free parameters to 10. Moreover, as we are only interested in the off–diagonal elements, using only two coils is sufficient to determine the elements $\mathrm{M}\,[1,3]$, $\mathrm{M}\,[1,4]$, $\mathrm{M}\,[2,3]$ and $\mathrm{M}\,[2,4]$. The HERA BPMs are capable of resolving orbit differences of the order of 0.05 mm. It is possible to find suitable coils among the already existing ones which, with a moderate excitation in one transverse plane, produce an rms change of the orbit in the other transverse plane that can be measured [Gi01]. Hence, this kind of measurement technique to arrive at the solenoid transfer matrix should be feasible in HERA. In particular since the experiment solenoid fields are not ramped, the measurements can be carried out at injection energy (12 GeV), reducing the amplitude of the coil kicks by a factor 2.3. However the overlapping GO and GG magnets are ramped, and measurements carried out at this energy must therefore be compared with relevant theory at the same energy.

6.1.2 Correction of distorted IR design trajectories

The radial fields experienced by particles on or close to the design orbit inside the solenoids, due to the off–axis design orbit inside the solenoids in the new design, mainly give rise to a vertical distortion of the orbits. To compensate for this and avoid a closed orbit distortion propagating from the interaction regions out into the arcs, a local compensation, utilizing the correction coil windings on the GO and GG magnets has been devised. The shape and magnitude of the distortion was first calculated with

a simple code, solving the equations of motion for orbit and spin (T–BMT equation) in a general 3–dimensional field [Gi01]. A systematic study borrowing ideas from the numerical map code for the overlapping fields in the interaction regions has subsequently been performed, investigating the optimal excitations of the correction coils in various configurations in the software. Particles starting on the design orbit on the upstream (left) side of the solenoids have been tracked across the interaction regions North and South and the strengths of the correction coils have been varied in a least squares fit program so as to minimize the expressions $\sqrt{w_1\,x^2 + w_2\,(x')^2 + w_3\,z^2 + w_4\,(z')^2}$ or $\sqrt{w_1\,z^2 + w_2\,(z')^2}$, where again w_1, w_2, w_3 and w_4 are weight factors. The coordinates x, x', z, z' were calculated at the exit of the GG magnet while the number of free parameters was set to four – two horizontal and two vertical coils – or more often just two (vertical). The skew dipole windings are placed on the right half of GO and on the left half of GG, which is favourable for the economy in powering both these coils and the skew quadrupole coils on the remaining halves of the superconducting magnets. Solutions have been found for H1 and ZEUS, given the restriction that only skew dipole fields, i.e. coils with horizontal fields correcting for motion in the vertical plane are available. A summary of the calculated settings for the vertical correction coils VGOR (GO right side) and VGGL (GG left side) in the North and the South for electrons and positrons is given in Table 6.5. A comparison between different end field models for the H1 solenoid is also given.

The uncompensated electron trajectory in the North interaction region, assuming that the H1 solenoid field can be modelled as having a linear fall off in the end field regions (end field model B) is shown in Figure 6.5. After compensation of the orbit distortion with the skew dipole windings on GO and GG, the trajectory is a closed "hump" in the vertical plane as seen in Figure 6.6. The residual uncompensated horizontal motion is very small in amplitude and can be taken care of by the ordinary correction coils in the lattice; on the scale of the vertical hump it can barely be seen in the figure.

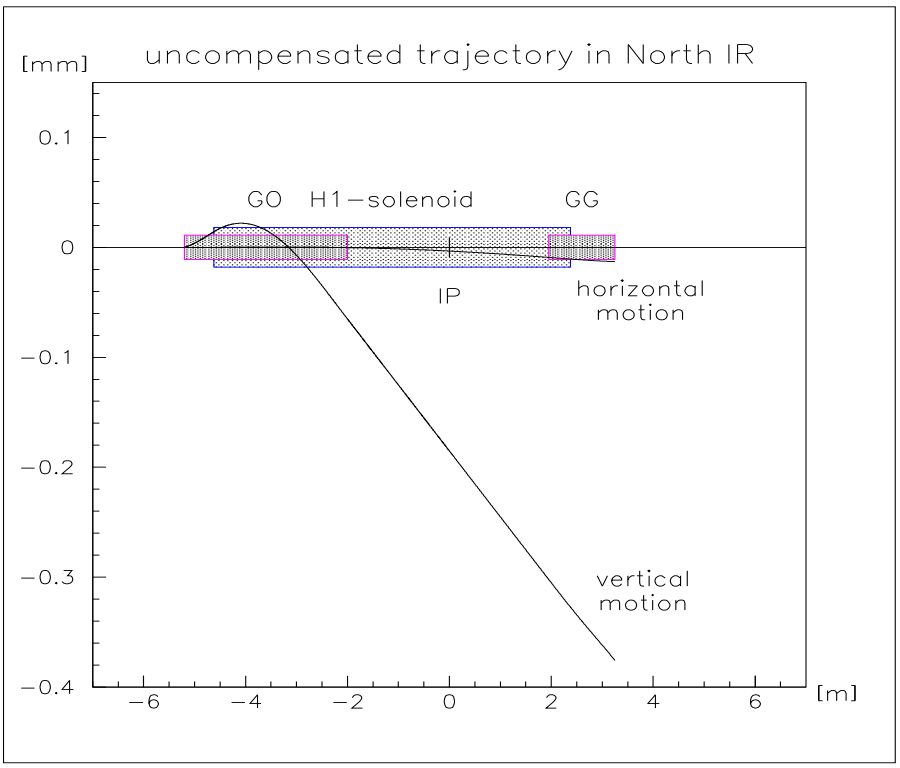

Figure 6.5: Uncompensated electron trajectory (w.r.t. design orbit) in the North interaction region, using H1 solenoid end field model B.

	skew dipole settings		maximum orbit excursion after corrections	
	VGOR [μrad]	VGGL [μrad]	horizontal [μm]	vertical [μm]
e^-				
North				
model A_1	52.8	-2.15	0.28	16
model A_2	67.2	-7.15	0.29	22
model B	67.2	-4.68	0.25	22
South				
	(-4.96)	(7.80)	(-0.036)	(-1.2)
	-15.0	20.2	-0.087	-3.0
e^+				
North				
model A_1	9.23	-53.3	4.0	-65
model A_2	-0.90	-54.2	4.2	-69
model B	1.06	-63.7	3.5	-68
South				
	28.1	-36.2	-0.15	5.1

Table 6.5: Skew dipole settings, and maximum orbit excursions after corrections of the orbit distortion introduced by the overlapping solenoid – combined function magnet fields in the new IRs. For electrons and applying the sandwich models, the rms vertical orbit shift before corrections is 1.2 mm and the rms horizontal shift is 0.13 mm. The dominant shift comes from H1 since the small overlap of the ZEUS solenoid field with GO and GG has almost no influence. In order to simplify the calculations, the lengths of the skew dipole windings in the models are 1.6 m for VGOR and 0.65 m for VGGL (half of the lengths of the parent magnets), which is a few centimeters longer than the actual coils. For the case of e^- in the South, two sets of values are given. The first ones in parenthesis are for a transverse offset of $x_{shft} = 4$ mm used in the polarization calculations in this chapter (where this particular value belongs to an older version of the optic) and the second ones are evaluated for $x_{shft} = 10$ mm, which is the offset in the Rev3.2 e^- optic.

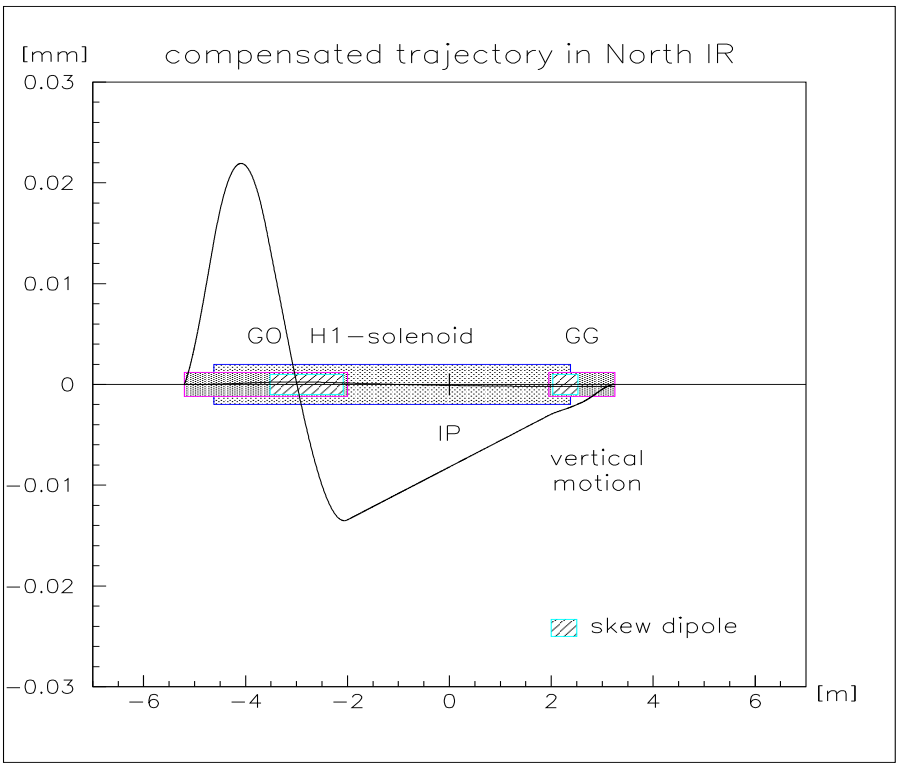

Figure 6.6: Compensated electron trajectory (w.r.t. design orbit) in the North interaction region, using H1 solenoid end field model B.

6.1.3 Local $\hat{n}_0$ tilt correction

Due to the overlap of the GO and GG magnet fields with the experiment solenoids, the nominal particle direction and $\hat{n}_0$ are not perfectly parallel to the central solenoid fields when entering these magnets. Moreover, as we have seen in Chapter 5, the H1 solenoid has a longitudinal asymmetry of 1.125 m with respect to the IP North. Together with the uncompensated orbit distortion originating in this region, this generates an rms $\hat{n}_0$ tilt of 8.8 mrad from the vertical in the arcs at 27.474 GeV. To further illustrate the impact that this region has on the spin motion, a list of the spin components at the entrance and "exit" (at a position symmetric to the entrance, from the optical point of view) of the uncompensated H1 solenoid of a spin, initially vertical along the arc upstream of the IP North, is given in Table 6.6.

	entrance	exit	exit (nominal)
$\widehat{S}_x$	-0.490	0.490	0.490
$\widehat{S}_s$	0.872	0.871	0.872
$\widehat{S}_z$	0.000	-0.006	0.000

Table 6.6: Spin components at the entrance and exit of the H1 solenoid of a spin vertical in the arcs with the input rotator magnet fields set to their nominal values for 27.474 GeV. Exit (nominal) refers to a case where the solenoid is absent.

After applying orbit corrections as described above, the rms tilt is reduced to 3.2 mrad. The remaining $\hat{n}_0$ tilt from the vertical in the arcs can be compensated for by an asymmetrical retuning of the vertical bending magnets in the spin rotators, using the already existing vertical correction coils in these magnets. This will only be necessary for the rotators straddling the North IP. With

asymmetrically retuned rotators, the tilt is reduced to a fraction of a milliradian.

6.1.4 Spin matching in the new lattice

Due to the asymmetries in the new IRs, the whole section between the centres of the rotators in a pair must be considered when designing the optics and doing spin matching. In a symmetric IR only half the section, from the IP up to the centre of one of the rotators in a pair needs to be taken into account. As indicated earlier, with the relatively large particle energy in HERA it is hoped that the experiment solenoids can be treated as perturbations. They have therefore been ignored when designing the new optics and establishing the spin match. [7] Then in the absence of solenoids and setting the rotator magnets to their nominal strengths for 27.474 GeV, 17 matching conditions — 12 for the optic and 5 for spin matching — must be fulfilled in the new IR design, which should be compared to the 9 matching conditions required in the old machine [Gi01]. Matching the new lattice has therefore been a tedious task. Figure 6.7 shows a schematic representation of the synchro–beta spin matching conditions required to obtain a spin matched HERA after the upgrade. Compare with the general recipe given in Chapter 4. In particular by choosing $\hat{l}_0$ to be vertical and $\hat{m}_0$ to be horizontal in the IR the elements $\mathrm{G}[1,1], \mathrm{G}[1,2], \mathrm{G}[2,3], \mathrm{G}[2,4]$ and $\mathrm{G}[1,6]$ must vanish [BR99]. In order to fulfill all matching conditions in the latest version of the IR design (Rev3.2), it has been necessary to independently power all quadrupoles left and right of the IPs up to the rotators, requiring 14 extra power supplies. In the starting phase however, only 7 of them will be available.

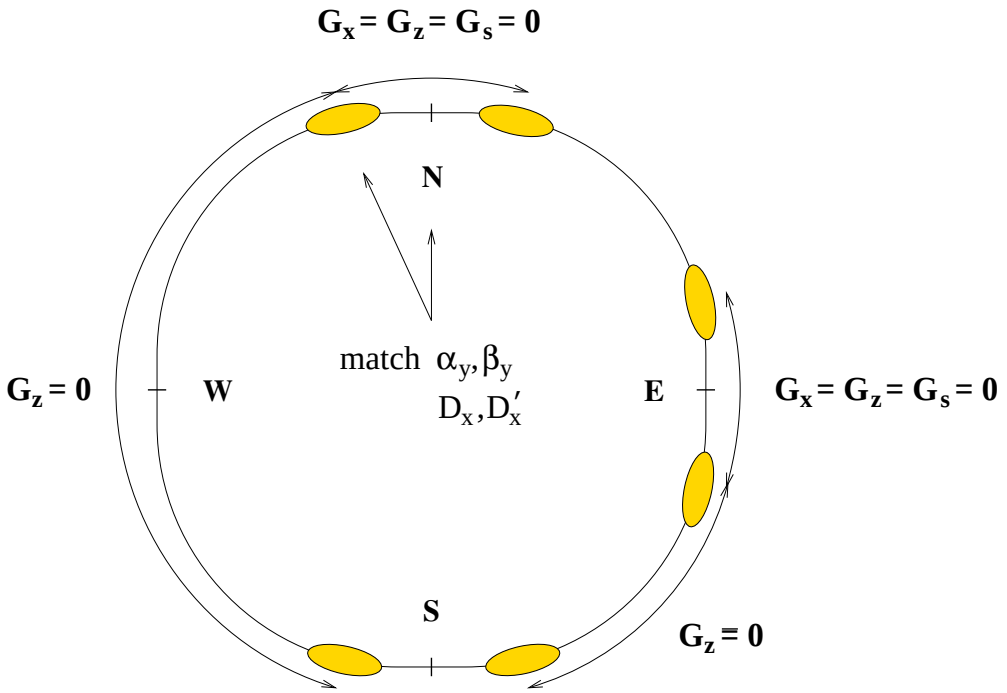

Figure 6.7: Spin matching conditions in the HERA upgrade lattice. The shaded ellipses represent the rotators.

Subsequent spin matching of the optics in the presence of the solenoids has in reality turned out to be exceedingly difficult. A mutual compensation of the H1 and ZEUS solenoids is not feasible either, mainly since this would require the phase advances between the two IPs to be multiples of π.

[7] Also the cavities are ignored in the spin match since they have little effect on the spin motion.

6.2 Polarization in the non–distorted machine

Now that the orbit distortions have been dealt with, and the spin matching strategy for the luminosity upgrade optics has been explained, we are ready to discuss the polarization in the new lattice. The results will be presented in the following order: first calculations made with SLICK for the non–distorted machine will be presented and comparisons between the various end field models, including the sandwich model, for the H1 solenoid will be made. Thereafter follows a qualitative analysis of the underlying causes of polarization reduction related to synchro–betatron motion in the new lattice. In particular the effects of artificially switching off elements in the **G** matrix for various sections of the ring will be studied. An estimate of the opening angle between $\hat{n}$ and $\hat{n}_0$, close to a resonance, from SLICK calculations will also be given. The next section investigates the effects of closed orbit distortions and misalignments, followed by a section dealing with the effect of the RF frequency shift on the polarization. In the last section a discussion of the influence on the polarization of the beam–beam interaction is given. All polarization calculations presented below are calculated for the e^- case. A spin matched e^+ optic for the upgrade also exists. The results are qualitatively similar to the e^- results and will therefore not be discussed further.

The polarization calculated with SLICK for the non–distorted Rev3.2 e^- optic (without solenoids) in the presence of 3 pairs of rotators is presented in Figure 6.8. The lattice has been spin matched as well as possible at the central energy of the interval shown according to the strategy described in the previous section. The solid line in the figure corresponds to the total (linearized) polarization whereas the dotted and dashed lines refer to the polarization related to the individual degrees of freedom of the orbital motion, for an energy scan covering one integer in $a\gamma$. The abscissa has triple labeling to emphasize the dependence of the polarization on energy, $a\gamma$ and spin tune, respectively. In many circumstances it is advantageous to plot the polarization versus $a\gamma$ or the spin tune, for instance when identifying resonances, but for our context it is sufficient to indicate the polarization dependence on energy. Therefore in the following pictures only the energy will be given on the abscissa. The large resonance dips appearing in Figure 6.8 at $E = 27.28$ GeV and $E = 27.665$ GeV correspond to the first order resonances $\nu_0 = 62 + \nu_s$ and $\nu_0 = 63 - \nu_s$, respectively. The less pronounced dips correspond to $\nu_0 = m \pm \nu_x$ and $\nu_0 = m \pm \nu_z$. The maximum polarization in the energy range $27.25 - 27.69$ GeV is (as expected) obtained for $\nu_0 \approx 62.5$ and is 77.2 %. The polarization is, as seen, limited by the synchrotron motion, and more fundamentally by the loss related to the presence of the rotators (recall Chapter 4), setting the upper limit to 83.2 % at 27.474 GeV. Note that the widths of the betatron resonances are exaggerated due to the finite energy step size (in this and following pictures $\Delta E = 0.005$ GeV). By turning off the **G** matrix for the straight sections it is found that the relatively strong vertical betatron resonance at $E = 27.605$ GeV is related to a breaking of the energy dependent spin match in the arcs at that energy.

Figure 6.9 shows what happens to the polarization when the experiment solenoids are included in the calculations. In the top left picture the H1 solenoid (end field model A_1) is strongly perturbing the polarization and causing a wide "hole" in the polarization P_s related to the synchrotron mode to develop on each side of the central energy point, because of the tilt of $\hat{n}_0$ in the arcs. In terms of the spin–orbit coupling integrals this can be understood as originating in a large contribution to $J_{\pm s}$ in eqn. (3.78) from this tilt in combination with the horizontal dispersion in the arcs. After correction of the $\hat{n}_0$ tilt by asymmetrically retuning the vertical bend magnets in the North rotators the polarization recovers but is now limited by betatron motion in the solenoid and skew quadrupoles and by propagation of the local distortions caused by the presence of the solenoid. Applying orbit and coupling corrections brings the polarization up to 70.8 %. By including also the ZEUS solenoid in the calculations, the polarization again drops by about 2.3 % for central energies. Note that as mentioned earlier asymmetrical rotator settings are only needed in the North. Finally it should be observed that the dips occurring at integer values of ν_0 (close to the outer edges in the top left picture and on the left hand side in the top right and bottom left pictures) are related to a decrease in strength of the

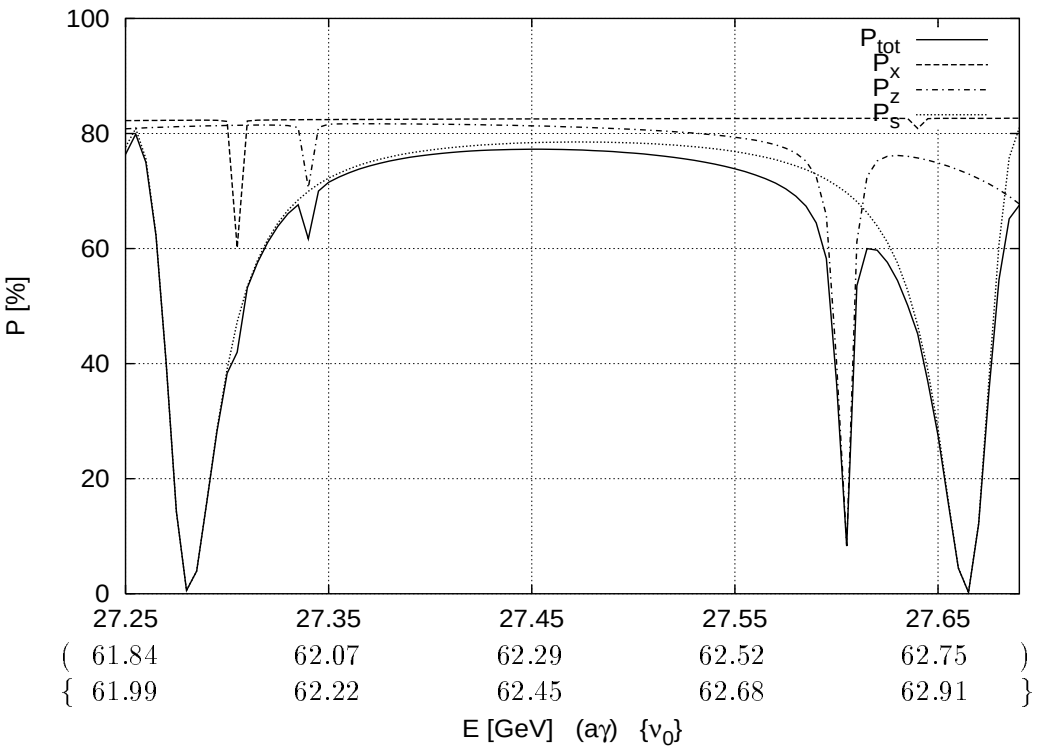

Figure 6.8: Polarization vs. energy $(a\gamma)$ {spin tune} for the Rev3.2 e^- nominal lattice with 3 pairs of rotators using standard settings.

Sokolov–Ternov driving term, caused by the strong tilt of $\hat{n}_0$ at these energies resulting from imperfect asymmetric rotator retuning. In reality these dips are very narrow, but the finite energy "binning" used in the scan produces an artificial broadening.

In Figure 6.10 a comparison between the various end field models for the H1 solenoid described in Chapter 5 is made. It is seen that the differences in the polarization between the models after orbit, coupling and $\hat{n}_0$ tilt corrections have been applied are negligible, except for a "shoulder" for the polarization associated with longitudinal orbit motion on the right hand side in the lower two plots. The total polarization at the central energy point for the sandwich model is 68.1 %, for end field model A_1 70.5 %, for end field model A_2 69.7 % and for end field model B 69.2 %. A closer study of the resonance patterns indeed shows that the various models are not identical and that end field model A_1 with its lower integrated field strength deviates most from the others. This suggests that the knowledge of the integrated field strength is in fact more important for the determination of the polarization than the exact knowledge of the shape of the end fields. However for the determination of the optical corrections mentioned above the end fields do play an important role.

Figure 6.11, already discussed in the previous section, shows that the polarization is rather insensitive to the coupling correction scheme adopted.

Figures 6.12 to 6.14 give examples of how SLIM/SLICK can be used in diagnosing which parts of the lattice are most troublesome for the polarization. In Figure 6.12 (left) the spin–orbit coupling has been deactivated in the whole of the ring, except in the East straight section, by switching off the **G** matrix for all quadrupoles, skew quadrupoles and combined function magnets. [8] It is clearly seen that the polarization is limited by the longitudinal mode, reflecting the impact of an imperfect spin match related to the horizontal dispersion in the East straight section, which is due to inherent

[8] Again the effect of the cavities can be ignored since it is anyway small.

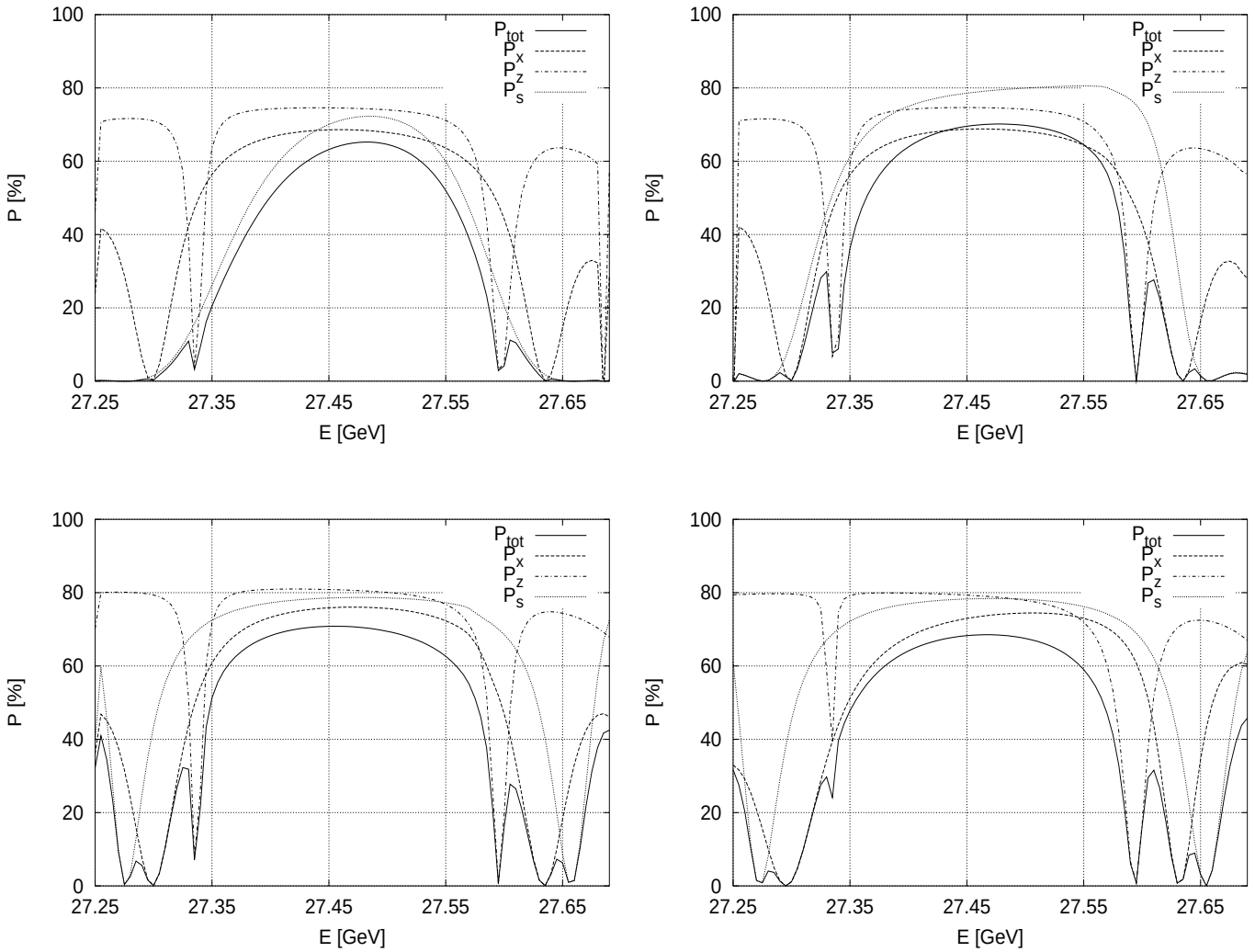

Figure 6.9: Polarization vs. energy for the Rev3.2 e^- lattice. *Top left:* Lattice including H1 solenoid. No corrections of orbit distortions and coupling. Standard rotator settings. *Top right:* Lattice including H1 solenoid. No corrections of orbit distortions and coupling. Asymmetric rotator settings around the North IR. *Bottom left:* Lattice including H1 solenoid. Local corrections of orbit distortions and coupling included. Asymmetric rotator settings around the North IR. *Bottom right:* Lattice including H1 and ZEUS solenoids. Local orbit and coupling corrections included for the North and South IRs. Asymmetric rotator settings around the North IR and standard rotator settings around the South IR. In all these calculations end field model A_1 was assumed for the H1 solenoid.

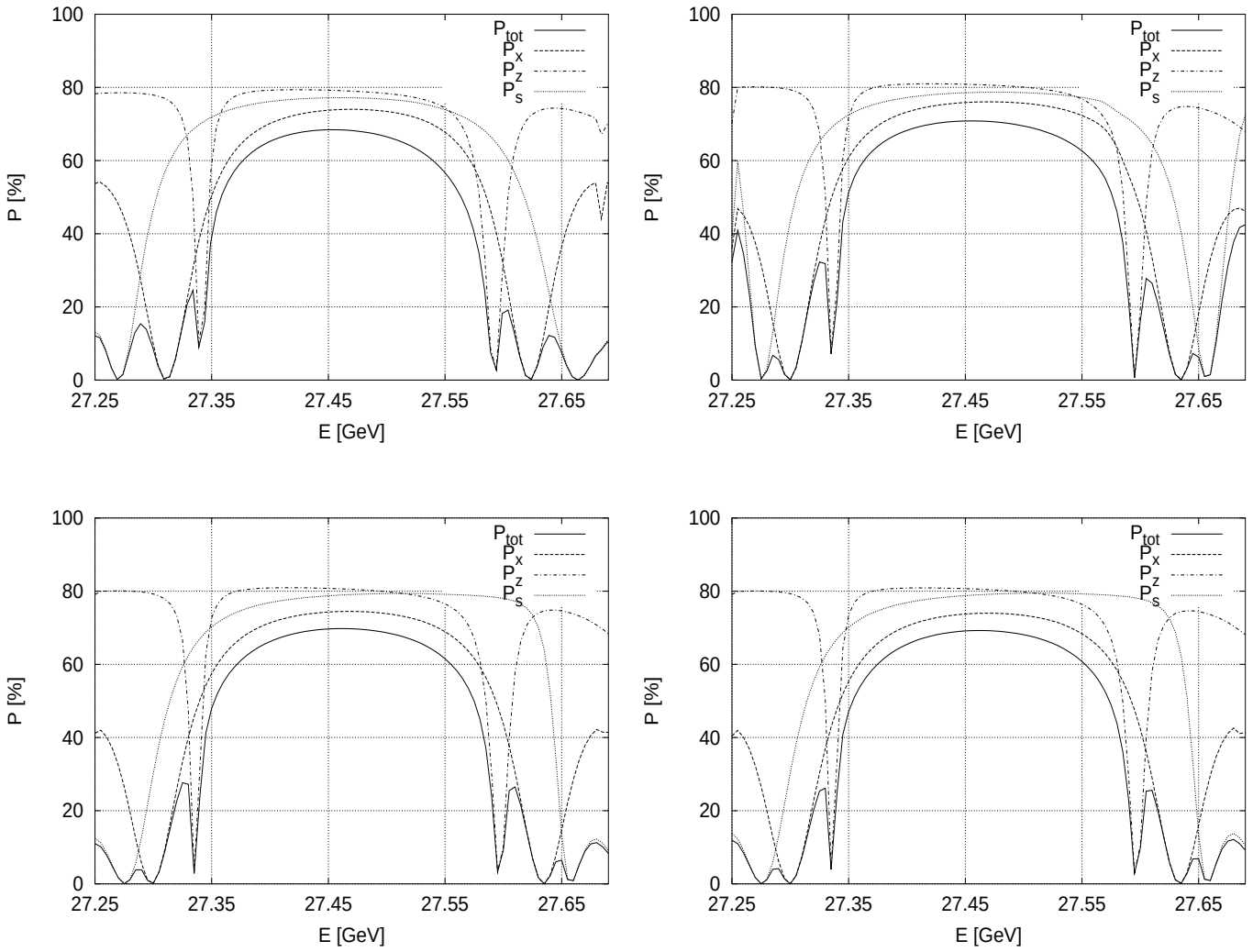

Figure 6.10: Polarization vs. energy for the Rev3.2 e^- lattice including the H1 solenoid, assuming various end field models. *Top left:* Sandwich model. *Top right:* End field model A_1. *Bottom left:* End field model A_2. *Bottom right:* End field model B.

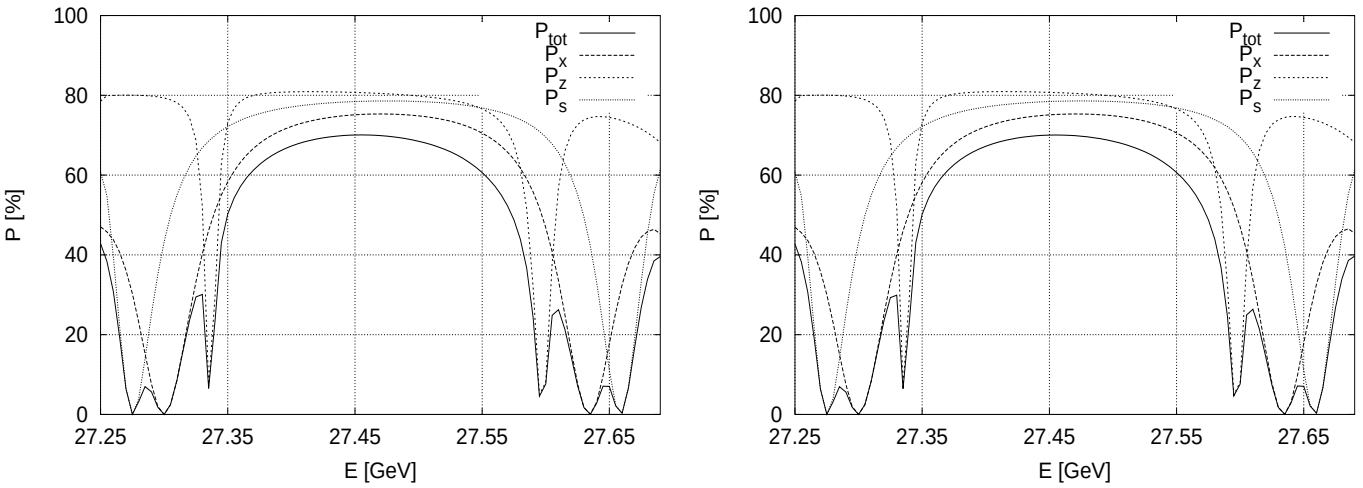

Figure 6.11: Polarization vs. energy for the Rev3.2 e^- lattice including the H1 solenoid (end field model A_1). *Left:* Local coupling compensation carried out with the matrix method (4 skew quadrupoles). *Right:* Local coupling compensation carried out with the Guignard method (4 skew quadrupoles). These pictures look identical, but a careful examination show that they are not!

limitations on the distribution of the dipoles in the East straight section. [9] In the right picture the spin–orbit coupling in the central part of the H1 solenoid has been turned on and new resonances are seen to appear, although the solenoid is locally compensated for (orbit compensation and $\hat{n}_0$ tilt compensation are active). The next two pictures, Figure 6.13, show the polarization achieved when the ZEUS solenoid is included in the calculations, but H1 not. In the left picture the spin–orbit coupling is active in the whole machine, whereas in the right picture the spin–orbit coupling is allowed to act only in the South straight section. This should be compared with the polarization in the nominal lattice, Figure 6.8, and with Figure 6.10 where only H1 is included. As can be seen, the ZEUS solenoid has a much smaller impact on the polarization than H1. Note that the loss in polarization directly related to ZEUS is separated out in the right picture and amounts to an enhancement of the betatron resonances, in agreement with expectations raised at the the beginning of this chapter. The last series of pictures in this block, Figure 6.14, again shows the polarization when only H1 is taken into account in the calculations. In these pictures the spin–orbit coupling is active only in the North straight section, and the polarization is limited by the horizontal motion. In the top left picture, a broad P_x resonance is dominating the pattern. When the spin–orbit coupling is switched off in the solenoid, this resonance is suppressed and the polarization recovers (top right picture). To investigate the importance of the solenoid radial end fields, the spin–orbit coupling is activated for these end fields (bottom picture), whereas the spin–orbit coupling is still switched off for the longitudinal field component. We note that the main limitation on the polarization comes from the horizontal betatron motion in the central part of the solenoid field, whereas the end fields contribute to a partial cancellation of the contribution to the P_z resonance from the GO and GG magnets.

An investigation has also been made on how important the radiation from the combined function magnets in the North and South IRs are. By doubling or halving, and even turning the radiation off in the strongest combined function magnets, situated at large β–function locations in these regions, it is found that the polarization, at least at the linear level, is basically uneffected. Hence one can conclude

[9] This imperfect spin match in the East straight section is also the source of the strong first order synchrotron resonances in Figure 6.8. If a dispersion spin match could be established in the East, these resonances would disappear and the polarization at 27.474 GeV would be above 80 % in that figure. Likewise it was always possible to get good spin matches with the various "pre–Upgrade" optics for the case when all three interaction regions were layed out as then planned for the North and South [Bb01, Bb90, BS86].

that the radiation from a small number of magnets in the IRs, although strong, has a marginal effect on the overall spin–orbit dynamics, compared to the radiation from the arcs. This fact has been used when implementing the numerical maps in SITROS, see Chapter 5.

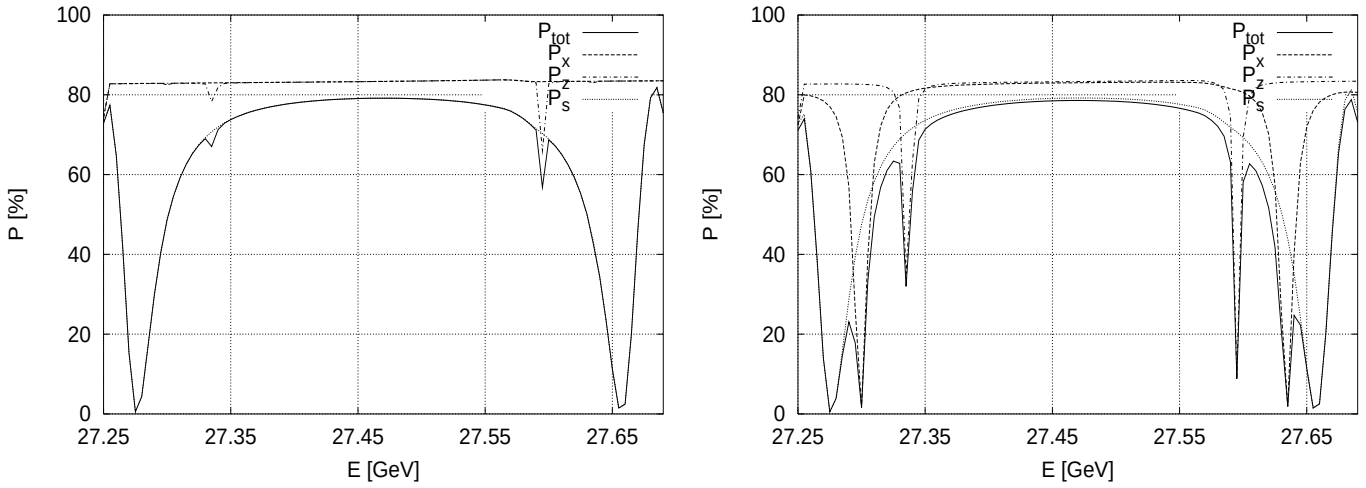

Figure 6.12: Polarization vs. energy for the Rev3.2 e^- lattice including the H1 solenoid (end field model A_1). *Left:* Spin–orbit coupling active only in the East straight section. *Right:* Same as left, but with stronger vertical mode resonances and additional resonances appearing in the horizontal mode due to switched on spin–orbit coupling in the central part of the H1 solenoid.

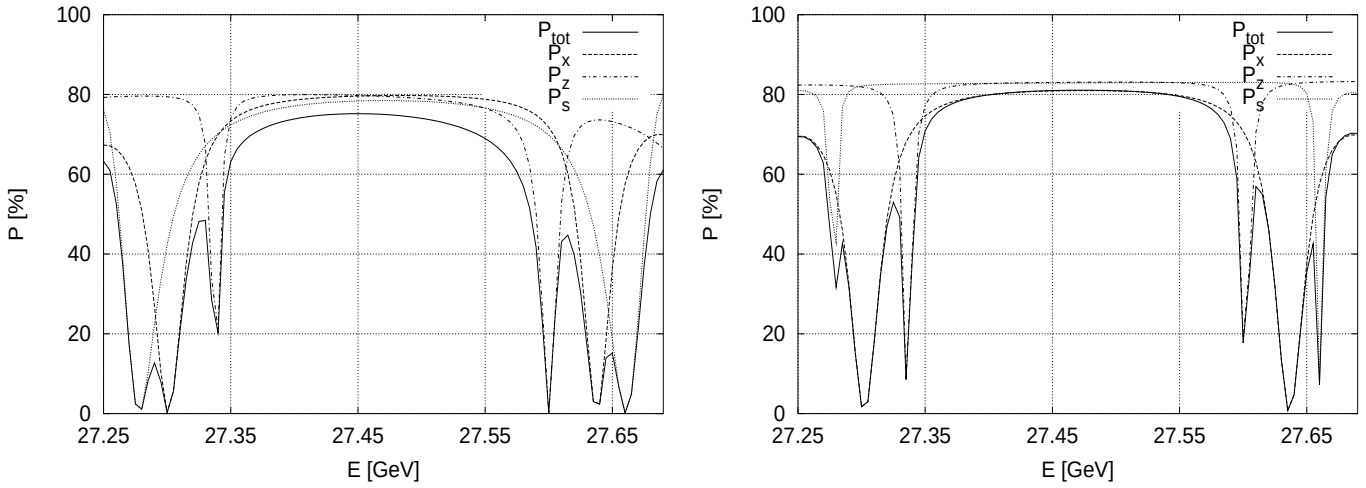

Figure 6.13: Polarization vs. energy for the Rev3.2 e^- lattice including the ZEUS solenoid. *Left:* Spin–orbit coupling active in the whole ring. *Right:* Spin–orbit coupling active only in the South straight section (including the ZEUS solenoid).

In order to further emphasize the importance of the spin–orbit coupling for the polarization, a series of three–dimensional plots, created from energy scans made with SLICK, illustrating the energy and azimuth dependence of the term $\frac{1}{|\rho|^3}\frac{11}{18}\left(\frac{\partial\hat{n}}{\partial\delta}\right)^2$ in the Derbenev–Kondratenko formula for the HERA upgrade lattice is given in Figures 6.15 to 6.17. A few qualitative features of the plots will be pointed out here. In the first illustration, Figure 6.15, the above term is plotted (for dipoles and combined function magnets (CFs) where $\frac{1}{|\rho|^3} \neq 0$) for the case of the nominal Rev3.2 e^- lattice, and is compared with the polarization calculated for the same case. Two broken "fences" stretching along the machine

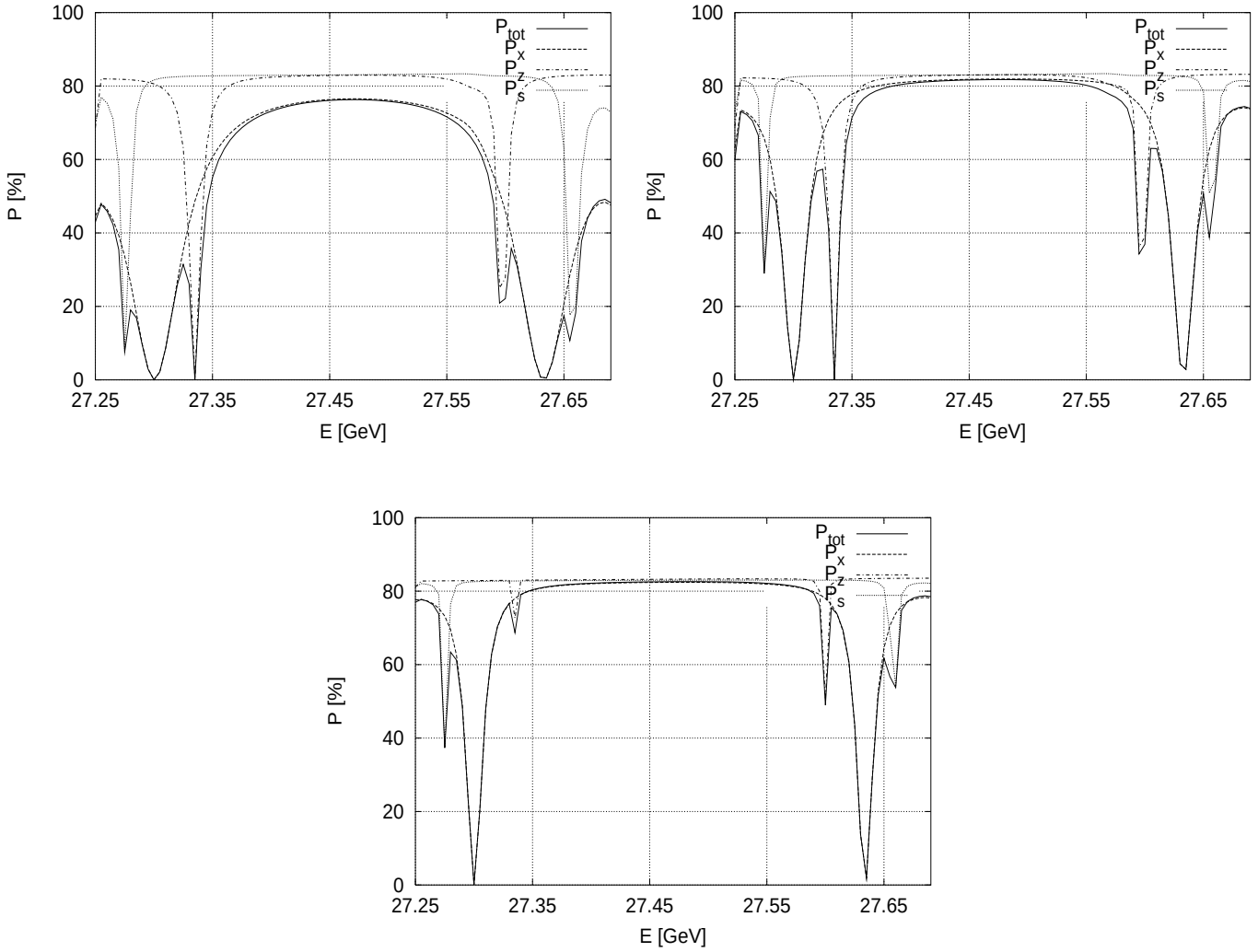

Figure 6.14: Polarization vs. energy for the Rev3.2 e^- lattice including the H1 solenoid (end field model A_1). *Top left:* Spin–orbit coupling active only in the North straight section (including the H1 solenoid). *Top right:* Same as left, but with spin–orbit coupling active only in the GO and GG magnets (i.e. not in the solenoid) in the North straight section. *Bottom:* Same as above, but without spin–orbit coupling just for the longitudinal part of the H1 solenoid.

azimuth ($s = 0$ corresponds to the East IP) at 27.28 GeV and 27.665 GeV can be clearly seen, corresponding to the strong synchrotron resonances centred at these energies. The gaps in the fences correspond to the straight sections, whereas the tips close to the gaps are related to the rotator dipoles. Note the peaks close to the centre of these gaps for azimuths around 1584 m (South IP) and 4752 m (North IP), indicating the positions of the GO and GG magnets. The pronounced spikes in the fences around 3440 m are due to the strong, short dipoles in the injection section (see Figure 1.1). Peaks can also be seen rising from the background pattern at about 27.6 GeV, related to the vertical betatron resonance at this energy and appearing, as expected, just at the azimuths corresponding to the positions of the rotator bend magnets where $v^*_{z5} \neq 0$ since $D_z \neq 0$. It should be observed that the vertical scale in the bottom plot is arbitrary and the data should only be regarded as a relative measure for how strong the spin diffusion in the various magnets and at various energies is. The reason for this is the high sensitivity of the amplitude to the chosen energy binning in the scan. If the spin diffusion term is plotted for an energy point that happens to hit a resonance condition precisely, the corresponding peak can be very much enhanced and dominate the picture completely. This may not be the case for the "mirror resonance", thus giving the false impression that the resonances should have very different strengths. Care must therefore be taken when choosing the energy binning and plotting such pictures. Note that the sensitivity to the energy binning is suppressed in the polarization plots, where one turn averages (cf. eqn. (3.20)) are taken.

Figure 6.16 illustrates what happens when the spin matching is broken by switching off the entire **G** matrix for a pair of quadrupoles in the South–West arc, close to the rotator, where the vertical beta–function is relatively large. The polarization is much decreased by the strong enhancement of the vertical betatron resonances and corresponding large peaks can be seen in the bottom plot for the spin diffusion related to vertical motion. The last figure in the series, Figure 6.17, has been added for completeness and shows how the spin diffusion term looks for the Rev3.2 e^- lattice, including the H1 (end field model B) and ZEUS solenoids. Note the more rugged structure of the "fence", and the extra spikes appearing, on the left side in the picture compared to the corresponding one in Figure 6.15, and compare this to the more smooth looking fence on the right side. This may be understood as being related to the larger influence on spin–orbit motion from the non–ramped solenoids at the low energy side. The effect can also be seen in the polarization (top plot) for instance by observing that the lower energy P_x resonance is wider than the corresponding resonance on the high energy side.

In Chapter 3 it was pointed out that the measured polarization contains a factor $\langle \hat{n} \rangle_s$ and a factor P_{DK} which is the same over all phase space and which depends on the azimuthal and phase space average of $\frac{1}{|\rho|^3}(\frac{\partial \hat{n}}{\partial \delta})^2$. It was claimed that $\langle \hat{n} \rangle_s \simeq \hat{n}_0$ even close to resonances owing to the smallness of the rms angle $\Theta_{\langle \hat{n}, \hat{n}_0 \rangle}$ between $\hat{n}$ and $\hat{n}_0$. We are now in a position to check this latter assertion in SLIM approximation for HERA and in the process present a novel way of exploiting knowledge of $\Theta_{\langle \hat{n}, \hat{n}_0 \rangle}$. As an example I will focus on the $\nu_0 = 62 + \nu_s$ resonance in Figure 6.8 at an energy of $E = 27.29$ GeV, three quarters down the resonance dip where the polarization is $P = 16.1$ %. In the SLIM approximation the rms opening angle $\Theta_{\langle \hat{n}, \hat{n}_0 \rangle, syn}$ due to the synchrotron motion is $\sqrt{\langle (\alpha^2 + \beta^2) \rangle_s}$ for the α and β associated with the synchrotron mode in eqn. (3.64). Its calculation needs the $|A_{III}|^2$ given by eqn. (3.62). In the arc dipoles one finds that $\Theta_{\langle \hat{n}, \hat{n}_0 \rangle, syn}$ is almost azimuth independent and has the value $\simeq 2.85 \cdot 10^{-3}$ at this energy. So $\langle \hat{n} \rangle_s \simeq \hat{n}_0$ as claimed. But this does not mean that $\frac{\partial \hat{n}}{\partial \delta}$ is small, since this rms opening angle is associated with a relative energy spread of $\sigma_\delta \simeq 1 \cdot 10^{-3}$! Then a first estimate of $(\frac{\partial \hat{n}}{\partial \delta})^2$ is given by $(\frac{\Theta_{\langle \hat{n}, \hat{n}_0 \rangle, syn}}{\sigma_\delta})^2$ which is $\simeq 8.1$. This number is of a magnitude similar to that of $(\frac{\partial \hat{n}}{\partial \delta})^2 = 5.8$ calculated analytically in SLICK at the same positions in the ring. Using this estimate, and the rough approximation $P_{DK} \approx \frac{0.832}{1 + \frac{11}{18}(2.85)^2}$ one finds $P_{DK} \approx 0.14$.(c.f. eqn. (3.20)). This emphasizes in concrete terms that although the opening angle is small, in our case 2.85 mrad, it appertains to a small energy spread, so that the depolarization can be large. In order to account for a polarization of 16.1 % in geometric terms, i.e. only on the basis of the opening angle, this angle would need to be of the order of 80° in order to get a small enough $|\langle \hat{n} \rangle_s|$. In Chapter 7 I will further

elaborate on this point in connection with an extension of an idealized model for synchrotron sideband resonances.

6.3 Closed orbit distortions and misalignments

To get an estimate of the polarization that can be achieved in the real HERA machine after the luminosity upgrade, the effects of random misalignment errors of the machine magnets must be included in the study. In the presence of random transverse quadrupole displacements for example, the expected rms value of the closed orbit distortion is related to the rms quadrupole displacement, $\delta_y^{\rm quad}$, by [Bo70]

$$y_{c.o}^{rms} = \frac{1}{2\sqrt{2}} \frac{\sqrt{\langle\, \beta_y \,\rangle}}{|\sin(\pi\nu_y)|} \sqrt{\sum_i m_i \beta_y^i (g_i L_i)^2}\, \delta_y^{\rm quad} \qquad (y = x, z) \tag{6.4}$$

where the m_i are the number of quadrupoles in family i, L_i are the lengths of these quadrupoles, and once again $g_i = \frac{ec}{E_0}\left(\frac{\partial \mathcal{B}_z}{\partial x}\right)^i_{x=z=0}$ are the normalized quadrupole field gradients. A similar but somewhat more complicated expression holds for the distorted dispersion ΔD_y^{rms}. The effect of such errors on the polarization is, as we already know, mainly due to the tilt of $\hat{n}_0$ in the arcs. Recall the expression (4.2) for this tilt. The error induced $\hat{n}_0$ tilt causes a massive broadening of the first order ν_s resonances, pulling down the polarization at central energies (close to half integer $a\gamma$). This is reminiscent of the effect introduced by a non–compensated solenoid as in the top left picture of Figure 6.9, only much more pronounced. Since in the new optic the quadrupoles and sextupoles are stronger than in the old one, we expect to see larger closed orbit distortions as well as larger distortions of the dispersion and of $\hat{n}_0$. From the discussion in Chapter 4 we understand the importance of a good $\hat{n}_0$ tilt correction. This will be further emphasized in what follows.

6.3.1 Investigations without solenoids

For our studies we have initially considered the Rev3.2 e^- lattice with three pairs of rotators, but excluding the experiment solenoids. The investigation covers the cases of random horizontal and vertical quadrupole displacements with assumed rms values of $\delta_x^{\rm quad} = \delta_z^{\rm quad} = 0.3$ mm with cuts at three standard deviations of the error distributions. In some cases a quadrupole roll–angle error of 0.35 mrad rms value has been added. No dipole rolls or field errors have been considered. The polarization calculations have been carried out with SITF. The results of the simulations are summarized in Tables 6.7 to 6.9. These tables are all organized in two blocks. In the upper blocks the rms orbit and dispersion distortions, the beam emittances and the rms values for the tilt of $\hat{n}_0$, together with the expected polarization at the linear level (total and individual modes) are presented, after standard orbit corrections have been carried out. In the lower blocks the rms tilts of $\hat{n}_0$ and the corresponding polarizations are shown, when in addition $\hat{n}_0$ tilt correction using the harmonic bumps (see Chapter 4) has been applied. All calculations are carried out at the energy $E = 27.474$ GeV.

In Table 6.7 results averaging over 10 random seeds for the case of quadrupole displacements in both transverse planes are displayed. Note that the orbit has been corrected down to 0.7 mm in both planes. In some cases the distortion of the dispersion is quite large and the values therefore have a large spread. Note in particular that the ΔD_y $(y = x, z)$ due to closed orbit distortions is much larger than the distortion introduced by the overlapping fields in the new IRs. The unperturbed emittances are $\varepsilon_x = 27.0$ nm rad and $\varepsilon_z = 0.75$ nm rad, respectively. As can be seen by comparing with the table, there is some blowup of the vertical emittance when the distortions are included. The average tilt of $\hat{n}_0$ is about 5 - 10 mrad larger than in the old optic (for orbit corrections down to about 1 mm in both

After usual orbit corrections					
$x_{c.o}^{rms}$ [mm] $z_{c.o}^{rms}$ [mm]	ΔD_x^{rms} [mm] ΔD_z^{rms} [mm]	ε_x [nm rad] ε_z [nm rad]	$\delta\hat{n}_0$ [mrad]	P_{lin} [%]	P_x [%] P_z [%] P_s [%]
0.71 ± 0.09 0.71 ± 0.17	35 ± 12 19 ± 14	26.2 ± 1.5 1.16 ± 0.40	30.3 ± 11.7	14.2 ± 9.8	72.4 ± 6.5 74.8 ± 4.6 13.4 ± 9.9

With harmonic bumps in addition		
$\delta\hat{n}_0$ [mrad]	P_{lin} [%]	P_x [%] P_z [%] P_s [%]
15.7 ± 3.9	69.5 ± 5.2	70.5 ± 7.0 73.5 ± 5.4 66.7 ± 9.0

Table 6.7: Expected rms value of $\delta\hat{n}_0$ and polarization (linear) in presence of random quadrupole transverse alignment errors for the Rev3.2 e^- lattice (without solenoids). Average over 10 random seeds.

planes), as is the spread in the tilt angles. In order to get the same order of magnitude of tilt as in the old optic, a more careful orbit correction has been necessary (see above). To bring the tilt down to the 10 - 20 mrad level 4, 6 or often 8 harmonic bumps (depending on the seed) have been used, whereas in the old optic 4 harmonic bumps were always sufficient. After the harmonic bump correction, the polarization levels for the three degrees of freedom are similar, which is in contrast with the previous design in which the polarization related to the longitudinal oscillation mode was clearly limiting. It should be mentioned that we have noticed that in some cases the polarization is limited by a large horizontal dispersion distortion around the North and South IPs, reflected by non–zero contributions in $\mathbf{G}_s$. It is therefore sensible for operation after the upgrade to have a dedicated dispersion correction algorithm, based on, for instance, MICADO or Singular Value Decomposition (SVD) [Pr92].

In Table 6.8 a comparison between various corrections applied to one particular realization of machine distortions is made. It can be seen that even with 8 harmonic bumps operating, the polarization reaches just 65 % with an orbit correction down to about 1 mm in both planes. Note that the rms dispersion distortion in this case is quite large, and that with 8 harmonic bumps a local vertical orbit distortion of more than 10 mm is generated. In order to reach a polarization level above 70 % for this seed, the orbit has to be corrected to better than 0.8 mm in both planes and the tilt must be brought down below 15 mrad, requiring the use of 8 harmonic bumps.

Table 6.9 shows the results of a study where in addition to the random quadrupole displacements, quadrupole roll–angle errors have been allowed (average over 6 seeds). The strategy by orbit and $\hat{n}_0$ tilt correction has been to reach the same order of magnitude of tilt after harmonic bump correction as in the case without roll–angle errors. Also here a variation in the number of applied harmonic bumps has been employed. As can be seen, the orbit correction is very stringent and even with a final average tilt of 16.2 mrad the average total polarization does not reach 62 %, perhaps indicating that harmonic bump correction is not very effective in the presence of roll–angle errors.

6.3.2 Investigations with solenoids

In the previous section we concluded that the differences in the polarization at the linear level between the various end field models for the numerical maps and the sandwich model are small. It has therefore

After usual orbit corrections					
$x_{c.o}^{rms}$ [mm] $z_{c.o}^{rms}$ [mm]	ΔD_x^{rms} [mm] ΔD_z^{rms} [mm]	ε_x [nm rad] ε_z [nm rad]	$\delta\hat{n}_0$ [mrad]	P_{lin} [%]	P_x [%] P_z [%] P_s [%]
1.0	88	29.8	39.8	5.6	71.7
1.2	24	1.11			75.1
					5.7
1.0	88	29.8	39.8	5.6	71.7
1.2	24	1.11			75.1
					5.7
0.7	41	29.1	34.7	7.4	74.7
0.8	10	1.17			76.8
					7.4
0.7	41	29.1	34.7	7.4	74.7
0.8	10	1.17			76.8
					7.4

With harmonic bumps in addition				
$\delta\hat{n}_0$ [mrad]	P_{lin} [%]	P_x [%] P_z [%] P_s [%]	Δz_{max}^{bump} [mm]	$\# h$
		74.4		
22.7	56.5	77.3	6.6	4
		58.5		
		71.4		
20.0	65.1	73.9	10.7	8
		69.2		
		75.7		
17.8	65.6	77.0	5.9	4
		67.6		
		69.4		
14.0	72.3	69.4	5.2	8
		77.8		

Table 6.8: Comparison of rms value of $\delta\hat{n}_0$ and polarization (linear) in presence of errors for one particular random seed after application of various corrections. Rev3.2 e^- lattice (without solenoids). Observe that the top and bottom blocks of the table should be read as if the bottom block would be the continuation of the top block on the right hand side.

After usual orbit corrections					
$x_{c.o}^{rms}$ [mm] $z_{c.o}^{rms}$ [mm]	ΔD_x^{rms} [mm] ΔD_z^{rms} [mm]	ε_x [nm rad] ε_z [nm rad]	$\delta\hat{n}_0$ [mrad]	P_{lin} [%]	P_x [%] P_z [%] P_s [%]
0.64 ± 0.06 0.51 ± 0.03	32 ± 18 13 ± 4	27.4 ± 1.4 0.920 ± 0.196	32.4 ± 8.0	8.8 ± 5.4	72.5 ± 10.8 78.4 ± 2.6 8.7 ± 5.3

With harmonic bumps in addition		
$\delta\hat{n}_0$ [mrad]	P_{lin} [%]	P_x [%] P_z [%] P_s [%]
16.2 ± 2.3	61.9 ± 12.0	70.4 ± 11.3 77.3 ± 2.0 59.0 ± 14.7

Table 6.9: Expected rms value of $\delta\hat{n}_0$ and polarization (linear) in presence of random quadrupole transverse alignment errors *and* quadrupole rolls for the Rev3.2 e^- lattice (without solenoids). Average over 6 random seeds.

been decided to stick to the sandwich model, thereby allowing PETROS — the code traditionally used at DESY for simulating the effects on orbital motion of random errors and also their correction — to remain unchanged. Using SITF and SITROS a study of the polarization in the presence of random quadrupole displacements in the Rev3.2 e^- lattice, including the H1 and ZEUS solenoids, has been carried out. The results are displayed in Table 6.10 and Figure 6.18.

In order to give a representative picture of the polarization that can be expected in HERA after the upgrade, the simulated orbit corrections have been made down to the realistic level of about 0.8 mm in both planes. Moreover, with the inclusion of the solenoids, guided by the experience gained in the studies without them and after some initial testing, it has been decided to investigate the effects of adding further harmonic bumps. The results collected in Table 6.10 include simulations for 8 random seeds where the highest polarization (at the linear level), comparing the use of 4, 8 and 16 harmonic bumps for each seed, have been selected. With an average rms $\hat{n}_0$ tilt of 14.8 mrad the linear polarization calculated with SITF reaches 63.8 % after harmonic bump correction. Note that a dedicated dispersion correction (using MICADO in PETROS) has been applied for most of the seeds to minimize the dispersion distortion. For the calculation of the effects of higher order resonances, SITROS has been used to track an ensemble of typically 100 – 350 particles for 10 000 turns: first 5000 turns to reach orbital equilibrium and then additionally 5000 turns to monitor the depolarization. The number of particles has been chosen such that the tracked emittances (in practice the beam sizes are monitored) have been able to converge to the analytically calculated ones from the first program module, while still keeping the tracking time within "reasonable" limits. [10] Averaged over the 8 random seeds for quadrupole displacement, the polarization from the SITROS trackings for the Rev3.2 e^- lattice, including the H1 and ZEUS solenoids (using the sandwich model), reaches 57.0 %. Figure 6.18 shows energy scans made with SITF and SITROS for a typical random seed (bottom plots), and for comparison, scans made for the non–distorted optic, including the solenoids (top plots). Note that one can see evidence in the right pictures of the expected sidebands and that

[10] As an example of the computation time needed to make an energy scan with the updated SITROS code, it should be mentioned that the SITROS polarization data plotted in Figure 6.18, obtained in trackings with 250 particles (which is certainly not excessive), have required about 4 1/2 days of CPU time per scan on a Sun Ultra–1 Sparc cluster. However, the simulations clearly point out the aspects that need to be considered.

After usual orbit corrections					
$x_{c.o}^{rms}$ [mm] $z_{c.o}^{rms}$ [mm]	ΔD_x^{rms} [mm] ΔD_z^{rms} [mm]	ε_x [nm rad] ε_z [nm rad]	$\delta\hat{n}_0$ [mrad]	P_{lin} [%]	P_x [%] P_z [%] P_s [%]
0.86 ± 0.16 0.78 ± 0.15	28 ± 20 14 ± 6	27.5 ± 1.6 1.07 ± 0.25	32.9 ± 7.6	10.3 ± 5.5	66.6 ± 4.4 74.2 ± 3.1 10.8 ± 6.2

With harmonic bumps in addition					
$\delta\hat{n}_0$ [mrad]	P_{lin} [%]	P_x [%] P_z [%] P_s [%]	ε_x^{analyt} [nm rad] ε_z^{analyt} [nm rad]	ε_x^{track} [nm rad] ε_z^{track} [nm rad]	P_{nonlin} [%]
14.8 ± 1.4	63.8 ± 2.1	67.1 ± 3.8 72.7 ± 3.7 71.5 ± 1.5	27.1 ± 1.3 1.31 ± 0.41	32.2 ± 3.3 1.43 ± 0.48	57.0 ± 3.2

Table 6.10: Expected rms value of $\delta\hat{n}_0$ and polarization (linear and higher order) in presence of random quadrupole transverse alignment errors for the Rev3.2 e^- lattice including the H1 and Zeus solenoids, using the sandwich model. Average over 8 random seeds.

the separation of these sidebands corresponds to the synchrotron tune, $\nu_s \simeq 0.06$. This is the case since SITROS deals with three–dimensional spin motion, which leads to higher order resonances. Note also the pronounced overlap of the first order resonances in the (left) SITF pictures. Because of this overlap we do not expect the simple model in Chapter 3 for describing synchrotron sidebands to be reliable, and hence we see that we need the SITROS program.

The higher order polarization in the case of the ideal optic with solenoids using the sandwich model is 61.0 %. It must be emphasized that this value is 6.4 % lower than the value obtained using the numerical maps in SITROS (end field model B), whereas the difference at the linear level (SITF) is only 1.5 %. It is therefore likely that the estimate for the polarization obtained with SITROS using the sandwich model is too low by a few, up to maybe 5, percent. In principle, many more distortion seeds should be investigated to improve the statistics, but due to the time consuming corrections this has not been possible for this work. However, the simulations clearly point out the aspects that need to be considered, in order to achieve polarization levels around 55–60 % in the luminosity upgraded HERA. These can be summarized as follows:

- The closed orbit must be corrected down to $\simeq 0.7$ mm. This may require the use of beam–based calibration techniques.
- A dedicated dispersion correction is probably needed to keep the dispersion distortion minimal.
- A good coupling compensation is necessary, which can be achieved using some of the techniques described in Section 6.1.1.
- As many as 16 harmonic bumps may be needed to correct the $\hat{n}_0$ tilt caused by the random distortions.

6.4 Effect of RF frequency shift on the polarization

In Chapter 2 it was explained that in order to achieve a horizontal emittance of 20 nm rad for the $e^{+/-}$ beam after the luminosity upgrade, besides an increase of the phase advances in the FODO cells from

60° to 72°, it is planned to operate the machine with a RF frequency offset of about +250 Hz. [11] This corresponds to an energy offset of about −0.1 %, where the energy–frequency relationship is given via

$$\frac{\Delta E}{\beta^2 E} = \frac{\gamma_t^2 \gamma^2}{\gamma_t^2 - \gamma^2} \frac{\Delta f_{RF}}{f_{RF}} \tag{6.5}$$

and where the square of the γ at transition, γ_t^2, is 1833 for the 72°/72° optic. The energy offset implies, through the horizontal dispersion, that the horizontal closed orbit shift will be nonzero by design. In particular on average there will be an inward radial offset of the $e^{+/-}$ beam in the quadrupoles in the arcs. Hence there will be a redistribution of the partition numbers, according to the Robinson Theorem, such that the horizontal emittance is decreased, whereas the bunch length and the energy spread are increased. We must now consider the implications for $e^{+/-}$ polarization. By noting that the horizontal offset in the ring sextupoles will cause these magnets to act as additional quadrupoles, an increased spin diffusion might be expected. However this contribution will be much smaller than that due to standard closed orbit distortions. This has indeed been confirmed in simulations. By introducing an equivalent energy shift according to eqn. (6.5), simulations including such a RF shift have been made with SITF [Gi01]. The results can be studied in Figure 6.19. Note the overall sideways shift of the resonance structures in the right hand side pictures, because of the energy shift of about 25 MeV. As can be seen the effect of the RF frequency shift on the maximum polarization is small, even for the case of realistic orbit distortions. To vindicate these findings, and to rule out that non–linear effects could have a detrimental effect on the polarization due to the RF shift, dedicated machine studies were carried out in a specially prepared 72°/72° optic in HERA before the shutdown [Ho00b]. The results from these studies are encouraging. In particular the increased energy spread did not cause any problems due to enhanced sideband resonances.

6.5 Beam-beam effects on spin

In Chapter 2 the influence of the beam–beam interaction at H1 and ZEUS on the luminosity after the upgrade was discussed. It was pointed out that the beam–beam forces are very nonlinear, but that for small amplitudes the interaction of the counter–rotating beams mainly causes betatron tune shifts. A self–consistent picture of the beam–beam interaction is not easy to formulate, and it is even more difficult to make analytical estimates of the impact on the polarization. In addition to the tune shifts, tune spread effects and possible distortions of the beam distributions complicate the situation and the spins of individual particles are affected both directly by the beam–beam forces and indirectly through the trajectory distortion.

Until 1996 no clear evidence of beam–beam effects on polarization had been observed in HERA. In that year the proton ring β_z^* was lowered from 0.7 m to 0.5 m (balanced by a reduction of $\beta_{z;e}^*$ in 1997). Moreover the proton beam current has been steadily increasing over the years. From the Autumn of 1996, when proton currents approaching 100 mA became routine, the resultant larger beam–beam forces started to have a marked effect on the polarization. By studying the polarization of single bunches, as measured by LPOL, it became apparent that the colliding and non–colliding bunches can have different polarization values [Be00a]. See Figure 6.20. This has been interpreted as the colliding and non–colliding bunches having different betatron tunes, so that one of these groups of bunches can be close to some depolarizing spin–orbit resonance (probably a synchrotron sideband of a parent resonance) and therefore have a lower polarization. The polarization of the colliding bunches can usually be improved by compensating for the tune shifts by adjusting the arc quadrupoles, thereby avoiding depolarizing resonances. However, it should be noted that even after tune compensation the

[11] Without the RF frequency shift the horizontal emittance in the 72°/72° optic is $\epsilon_x = 27$ nm rad.

polarization in the presence of the beam–beam effect is lower than for the case of a single beam, due to the breaking of the straight section spin match. This is illustrated by comparing Figures 6.8 and 6.9 (bottom right) with Figure 6.21, where the polarization calculated with SLICK in the presence of an artificial "beam–beam lens", and after tune compensation, is shown for the Rev3.2 e^- lattice. The tune shifts stated correspond to a proton current of 110 mA. A variation of the polarization of the colliding bunches, across a group of such bunches, has also been observed and has been attributed to a variation in the synchrotron tune, caused by dynamic beam loading effects in the RF cavities. Apart from the sensitivity to orbital tunes, it has been noted that in the presence of the beam–beam effect the rise time of polarization after injection is sometimes larger than that expected from standard radiative polarization theory, and that the polarization level is sometimes insensitive to the settings of the harmonics of the harmonic closed orbit correction scheme [Gi01].

The effect of the beam–beam interaction on the electron polarization for HERA I has been studied by Böge and Limberg [BL95] using SITROS. Strong depolarization was predicted, but such strong depolarization has not been confirmed by measurements. Even after updating the SITROS code (see Appendix C) it made pessimistic predictions. Therefore realistic simulations of beam–beam depolarization seem to be unexpectedly difficult and would probably need to be the subject of a separate project. It has however been confirmed by Fourier analysis of SITROS tracking data, that SITROS reproduces the correct linear (incoherent) tune shifts.

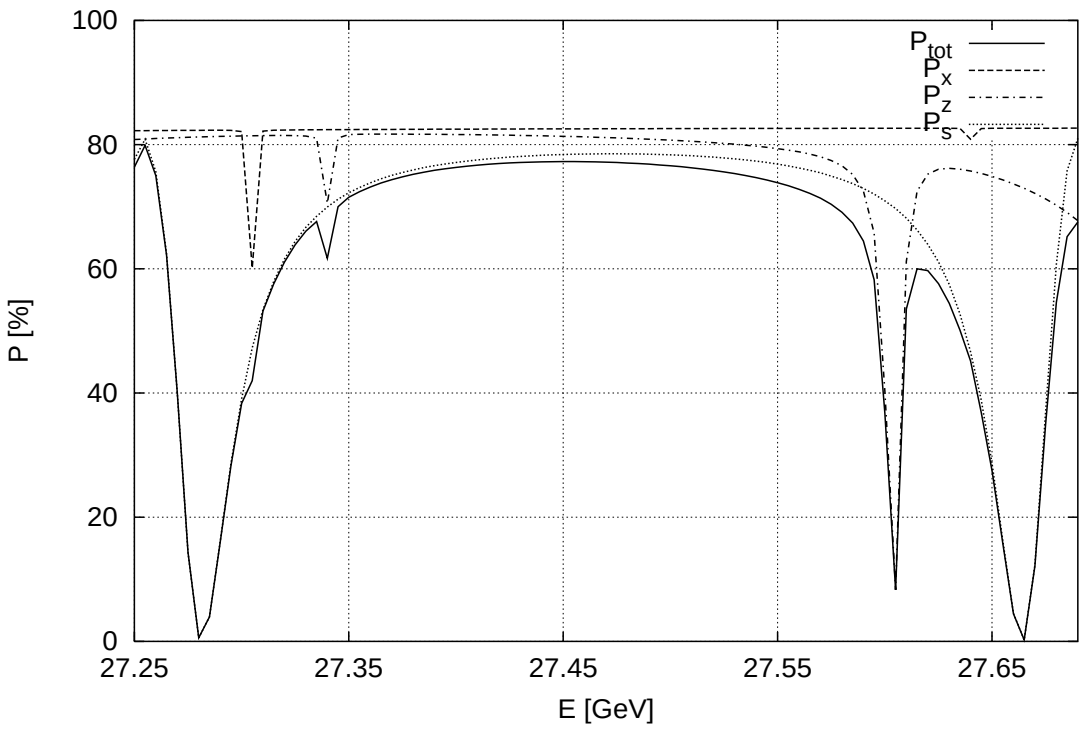

$(1/|\rho|^3)*11/18*(\partial n/\partial\delta)^2$ in Dipoles and CFs

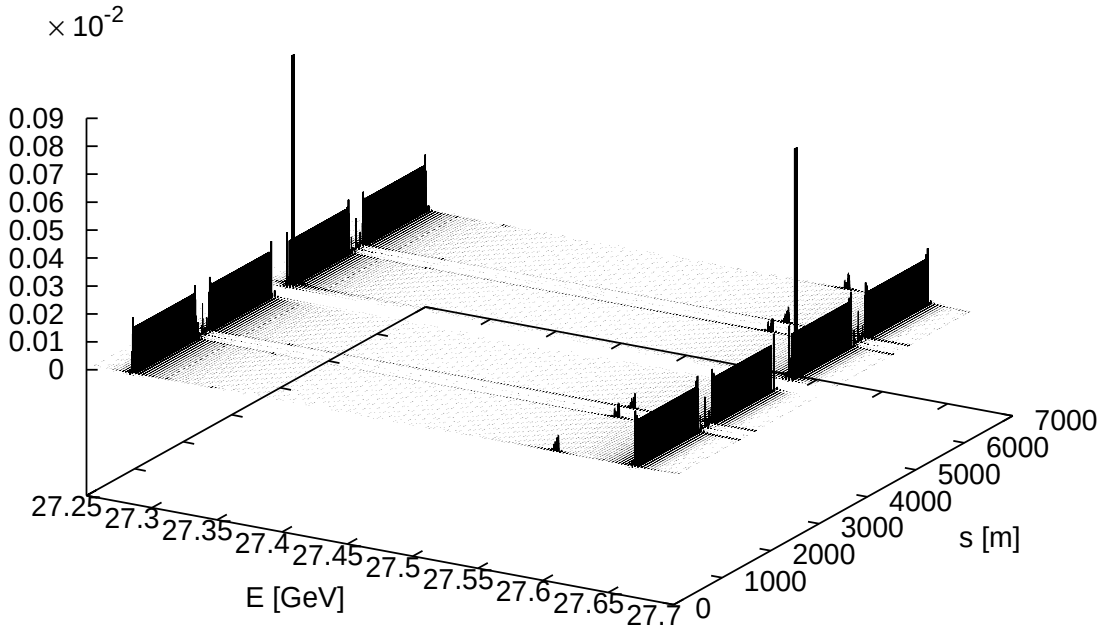

Figure 6.15: *Top:* Polarization vs. energy for the Rev3.2 e^- nominal lattice. *Bottom:* The (linearized) Derbenev–Kondratenko spin diffusion term plotted in dipoles and combined function magnets vs. energy and ring azimuth for the same case.

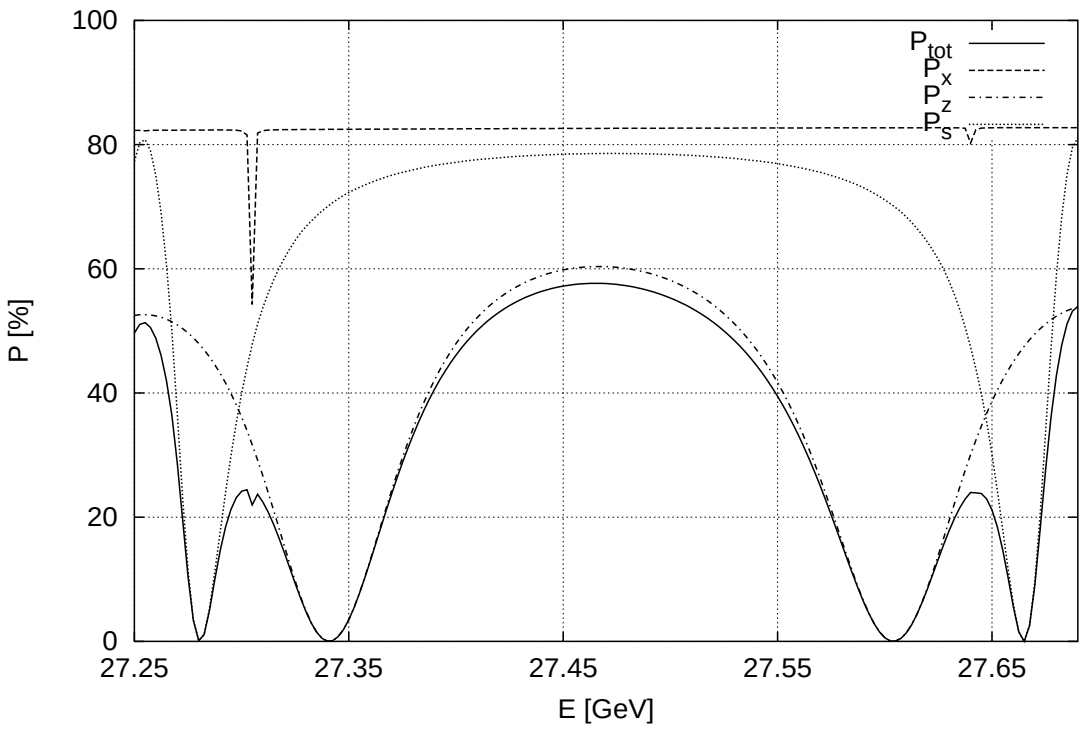

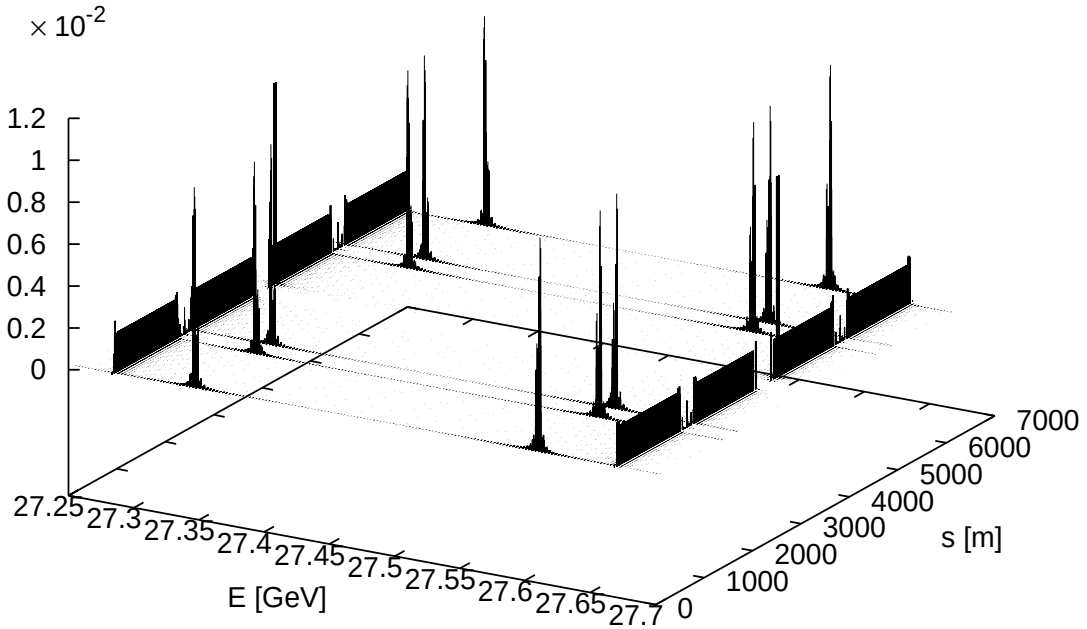

Figure 6.16: *Top:* Polarization vs. energy for the Rev3.2 e^- nominal lattice with broken (vertical) spin match in the South–West quadrant. *Bottom:* The (linearized) Derbenev–Kondratenko spin diffusion term plotted in dipoles and combined function magnets vs. energy and ring azimuth for the same case.

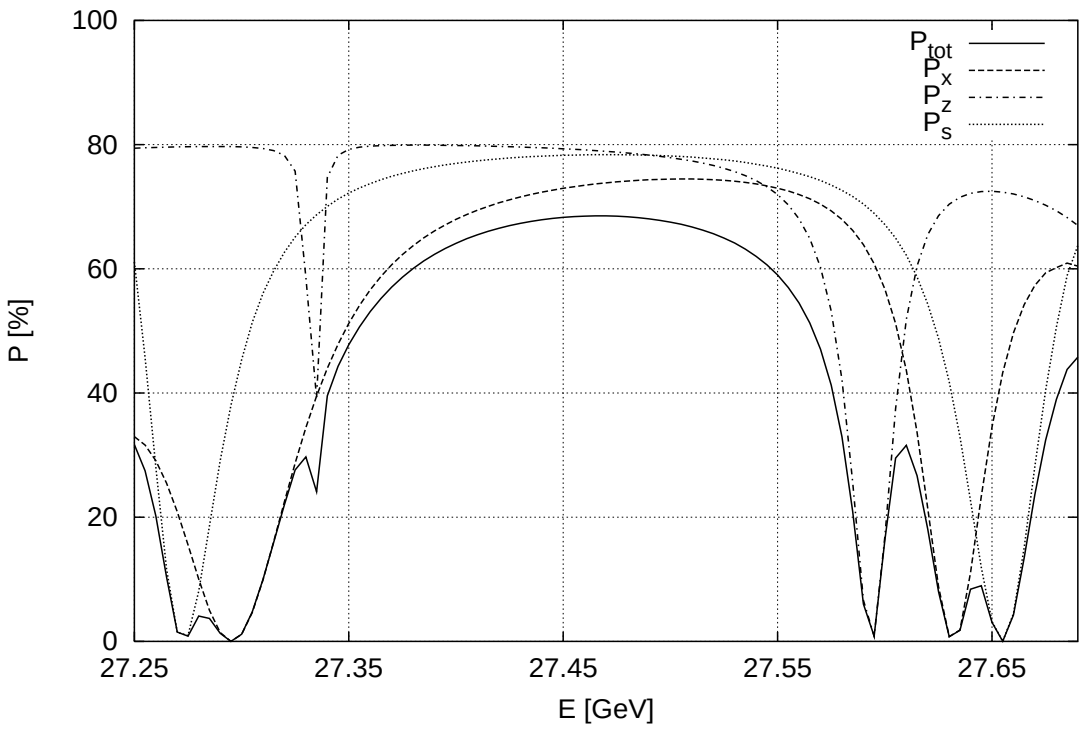

$(1/|\rho|^3)*11/18*(\partial n/\partial\delta)^2$ in Dipoles and CFs

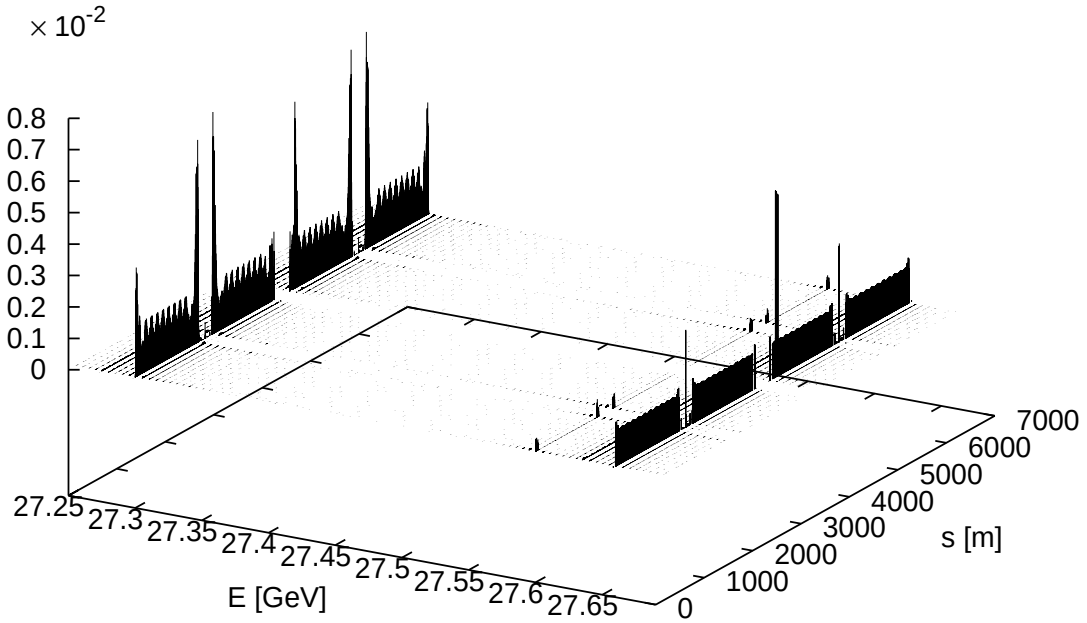

Figure 6.17: *Top:* Polarization vs. energy for the Rev3.2 e^- lattice with H1 (end field model B) and ZEUS solenoids. *Bottom:* The (linearized) Derbenev–Kondratenko spin diffusion term plotted in dipoles and combined function magnets vs. energy and ring azimuth for the same case.

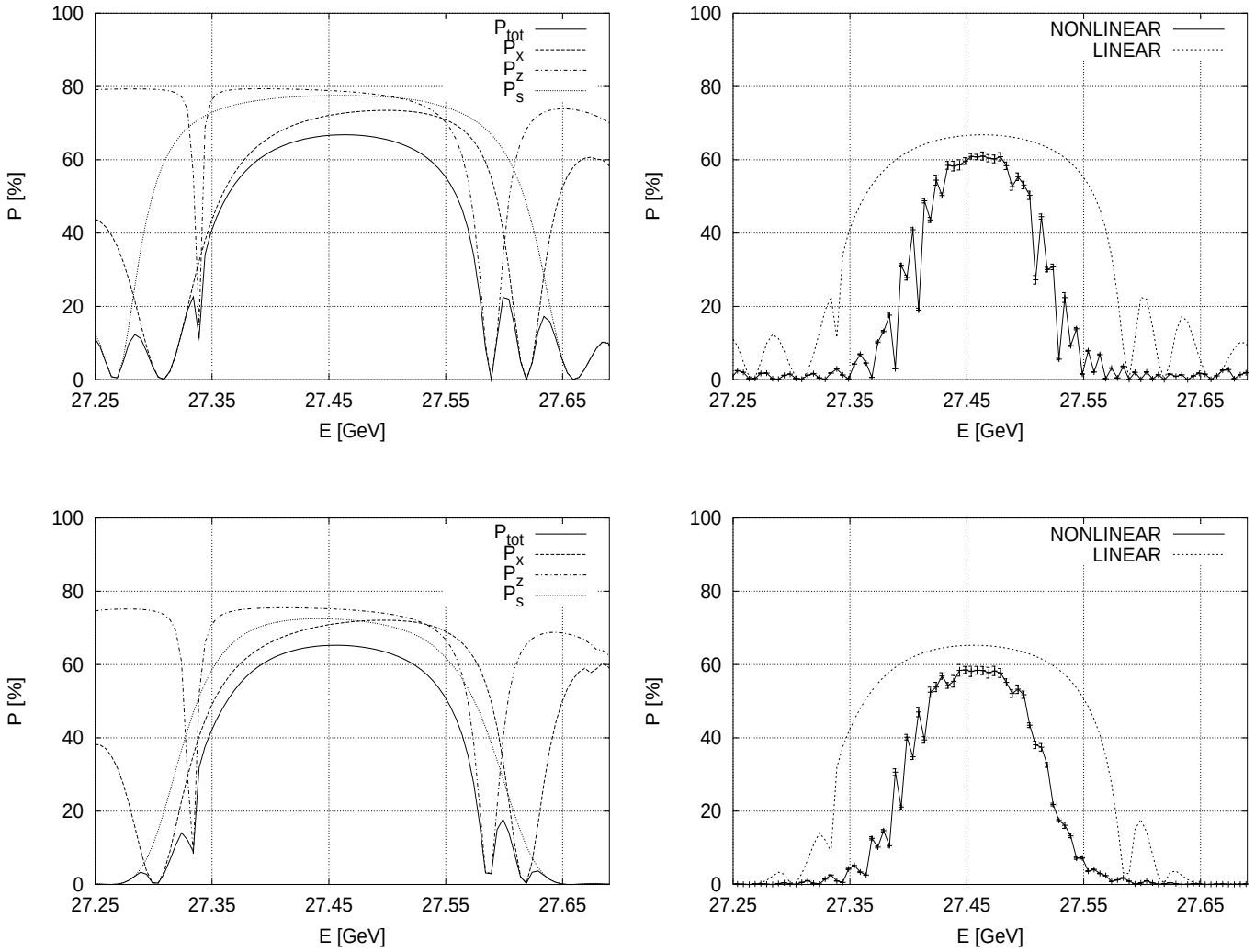

Figure 6.18: Polarization vs. energy for the Rev3.2 e^- lattice including the H1 and ZEUS solenoids, using the sandwich model. *Top left:* Linear polarization (SITF), ideal optic. *Top right:* Higher order polarization (SITROS), ideal optic. *Bottom left:* Linear polarization (SITF), typical case with distortions. *Bottom right:* Higher order polarization (SITROS), typical case with distortions.

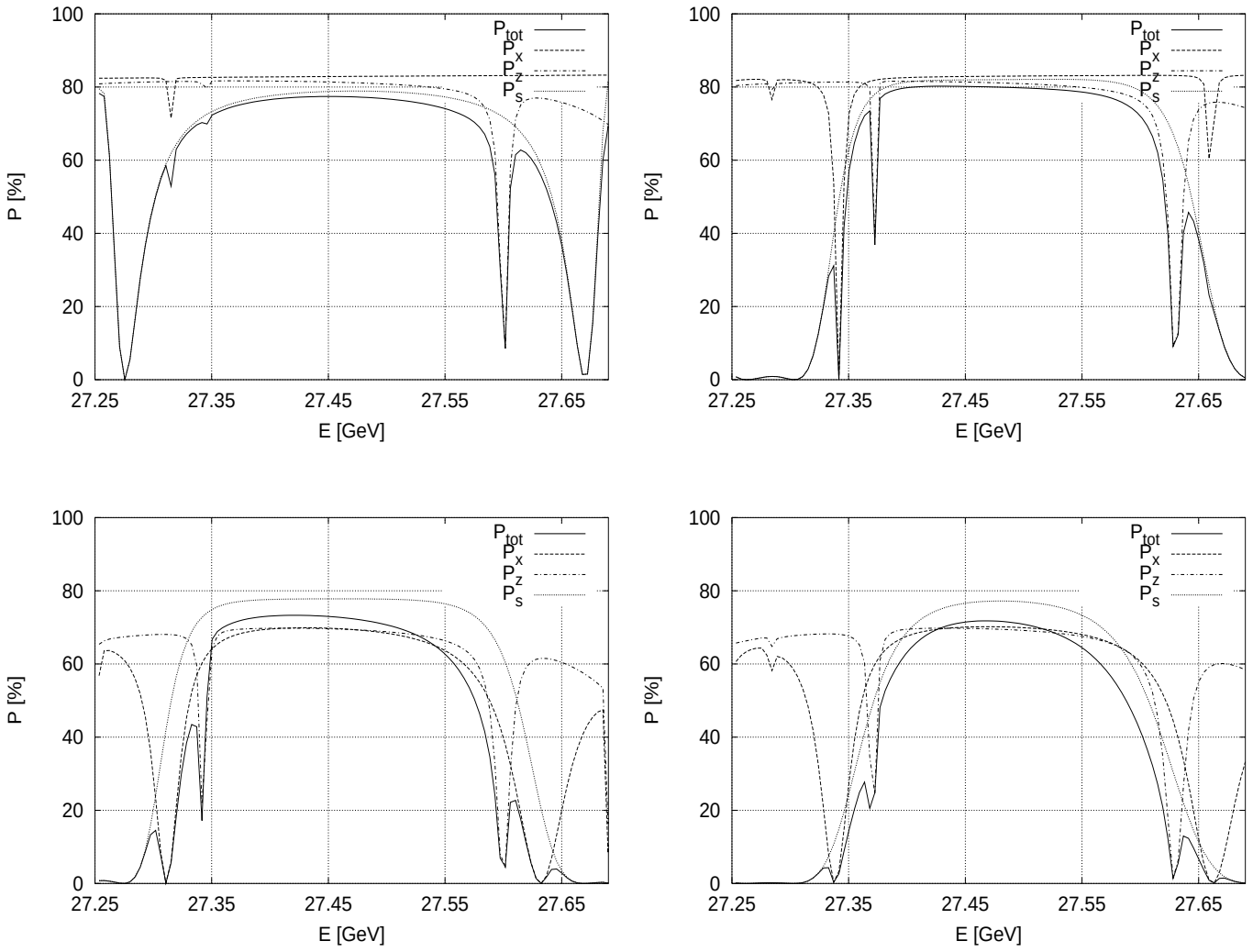

Figure 6.19: Polarization vs. energy for the Rev3.2 e^- lattice. *Top left:* Nominal lattice (no distortions, no RF shift). *Top right:* Nominal lattice with $\Delta f_{RF} = +250$ Hz. *Bottom left:* Optic with realistic distortions, no RF shift. *Bottom right:* Optic with realistic distortions and $\Delta f_{RF} = +250$ Hz. The strong broadening of the ν_s resonances when the RF shift is applied is due to a tilt of $\hat{n}_0$, caused by an energy mismatch of the rotator settings, resulting from the particular way the shift has been implemented in the code.

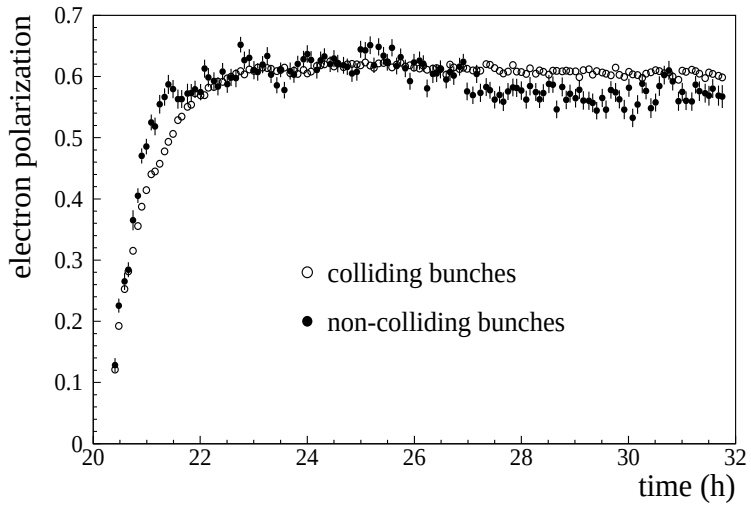

Figure 6.20: Example on the difference in polarization of the colliding and non–colliding bunches, as measured by LPOL [Be00a]. Courtesy of W. Lorenzon.

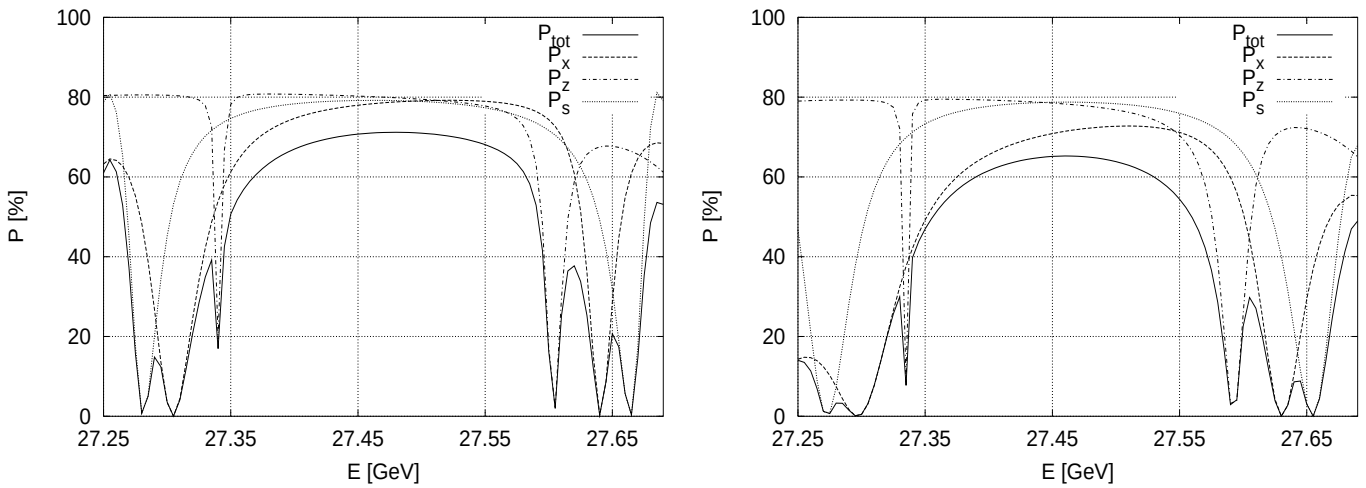

Figure 6.21: Polarization vs. energy for the Rev3.2 e^- lattice with linear beam–beam effect at the North and South IPs. The incoherent tune shifts ($\Delta\nu_x^e = 0.027$ and $\Delta\nu_z^e = 0.041$ per IP) have been compensated for by adjusting the currents of the main quadrupoles (i.e. the arc quadrupoles). *Left:* Nominal lattice. *Right:* Lattice including the H1 (end field model A_1) and ZEUS solenoids.

Chapter 7

A Unitary Model of Spin Depolarization

It was pointed out in Chapter 3 that the synchrotron part of the term $\hat{n}_0 \cdot \vec{\omega}$ in the equation of spin motion represents a modulation of the instantaneous rate of spin precession around $\hat{n}_0$ due to energy oscillations and it was explained that this leads to the generation of synchrotron sidebands of parent resonances. A brief presentation of the main result from the Yokoya–Mane approximations for synchrotron sidebands of first order parent betatron resonances was given.

The Yokoya–Mane approximation is a perturbative approach for treating isolated resonances, that does not account for interference between parent resonances. From the SLICK and SITF results for HERA presented in Chapter 6 (see for instance Figure 6.9 and the left side pictures in Figure 6.18) it is clear that the criterion of well separated parent resonances is not fulfilled in a realistic description of HERA. This model is therefore restricted in applicability. Moreover, the model does not preserve the length of spin vectors in the spin transformations, i.e. it does not preserve unitarity in an SU(2) representation. In principle one could use this model anyway and try to retrieve the main higher order resonances and this has been done for a particular HERA optic by Böge [Bö94]. It is found that the Yokoya–Mane approximate model for synchrotron sidebands is useful to get a rough view of the resonance structure, but it is not adequate for predicting the absolute polarization level because of the limitations mentioned. There is therefore no real substitute for SITROS tracking calculations or the use of SODOM [Yo92] mentioned in Chapter 3.

An alternative method for describing higher order spin motion which is based on a simple picture and thereby has the potential to provide physical insight can be found in [BL96, Le97]. However, the method presented in those texts has been applied incorrectly to $e^{+/-}$ polarization. The object of this chapter is to outline how one can nevertheless in principle still take advantage of this model if one combines it with a correct understanding of radiative depolarization theory. At this point I would like to remind the reader of the discussion on the opening angle between $\hat{n}$ and $\hat{n}_0$ in Chapter 6. By using this opening angle, as calculated by SLICK, it was possible to get a rough estimate for the spin–orbit coupling function $\frac{\partial \hat{n}}{\partial \delta}$ in the Derbenev–Kondratenko formula. We know from linear eigen–theory (see eqn. (3.64)) that the spin components of the eigenvectors, $\vec{w}_k$, are needed to calculate this opening angle. By working in the betatron–dispersion formalism, and considering for simplicity only the effect of quadrupoles, we find that the expression for these eigenvectors, eqn. (3.74), contains the one–turn integrals in eqn. (3.78). If we now make a Fourier expansion of the integrands and evaluate these integrals we find that the result is a sum of terms containing resonance factors of the kind $1/(\nu_k \pm \nu_0 - p)$, with integer p. Then the $\vec{w}_k$ diverge at $\nu_k \pm \nu_0 = \tilde{p}$ for some integer $\tilde{p}$ giving an infinite opening angle so that the perturbative treatment is completely invalid. General solutions for the spin motion also diverge. The reason is clear. At such a resonant condition, a corresponding term

$\exp i\,2\pi s(\nu_k \pm \nu_0 - \tilde{p})/C$ in the Fourier expansion becomes 1 and the integral for the first order spin solution in eqn. (3.33) increases linearly and indefinitely with distance [Yo83, BR99, Vo00]. The rate of divergence is proportional the $\tilde{p}$-th Fourier coefficient.

However, it is possible to construct a better model, which is unitary, for calculating the opening angle and handling resonance. The key to this lies in the following observation: close to a resonance the spin motion is almost coherent with the orbital motion and it is dominated by a single harmonic component equivalent to a field rotating in a plane perpendicular to $\hat{n}_0$. In the $(\hat{n}_0, \hat{m}_0, \hat{l}_0)$ frame this corresponds to the spins' seeing an almost stationary field, which rotates the spins away from $\hat{n}_0$. The situation is analogous to that encountered in nuclear magnetic resonance (NMR) experiments, where the radio frequency field acting on the spins is decomposed into two constant fields counter–rotating with the same frequencies [Ab61]. Studying the spin motion close to a spin–orbit resonance and selecting one harmonic, amounts to decomposing the field seen by the particles due to motion on synchro–betatron trajectories into two components, and selecting one of them. The Fourier coefficient for the selected harmonic gives the strength of the chosen rotating field component. By making a transformation into a frame rotating with this component, an exactly solvable model for describing the spin motion can be obtained. See for instance [Bu87, Ma88, Ma92, Le97, Vo00]. This is the so called *single resonance model* which will be briefly described below. Here, for the sake of the following argumentation I will follow the presentation in [BL96, Le97], but change the notation for certain quantities, in order not to cause confusion and break with previously introduced notation. Note that in these texts the spin motion is described in terms of two component spinors Ψ with $\widehat{S} = \langle \Psi | \vec{\boldsymbol{\sigma}} | \Psi \rangle$, and where $\vec{\boldsymbol{\sigma}}$ is a three component vector of Pauli matrices, $\vec{\boldsymbol{\sigma}} = (\boldsymbol{\sigma}_1, \boldsymbol{\sigma}_2, \boldsymbol{\sigma}_3)$. For a brief introduction to spinor algebra see [Mo84].

7.1 The single resonance model (SRM)

In terms of spinors, and using the generalized machine azimuth $\theta \equiv \frac{2\pi s}{C}$ instead of s as the independent variable, the T–BMT spin equation of motion in the presence of a single harmonic becomes

$$\frac{d\Psi}{d\theta} = -\frac{i}{2}\begin{pmatrix} a\gamma & -\epsilon_{_K}\, e^{-iK\theta} \\ -\epsilon_{_K}^{*}\, e^{iK\theta} & -a\gamma \end{pmatrix}\Psi \tag{7.1}$$

where K is the resonance tune and $\epsilon_{_K}$ is the strength (*resonance strength*) for the harmonic and is proportional to the K–th harmonic in the Fourier expansion. [1] Here, we assume that even if $\hat{n}_0$ is tilted slightly from the vertical, the closed orbit spin tune ν_0 is still given by $a\gamma$ to a very good approximation. Note that although this equation resembles a Schrödinger equation for the spinor, we are not invoking quantum mechanics here. Instead we are just using an SU(2) representation for the real vector $\hat{S}$.

By making a transformation to the *resonance precession frame* (RPF) discussed above, using

$$\Psi_K(\theta) = e^{\frac{i}{2}K\theta\sigma_3}\Psi(\theta) \tag{7.2}$$

the spinor equation of motion takes the form

[1] For a mathematical definition of resonance strength, see for example [BR99, Vo00, Ho00a]. The concept of resonance strength is most important for the acceleration of polarized protons.

$$\frac{d\Psi_K}{d\theta} \;=\; \frac{i}{2}\begin{pmatrix} \kappa & \epsilon_{_K} \\ \epsilon_{_K}{}^* & -\kappa \end{pmatrix}\Psi_K \;=\; \frac{i}{2}\left[\epsilon_R\,\boldsymbol{\sigma}_1 - \epsilon_I\,\boldsymbol{\sigma}_2 + \kappa\,\boldsymbol{\sigma}_3\right]\Psi_K \tag{7.3}$$

where ϵ_R and ϵ_I are the real and imaginary parts of $\epsilon_{_K}$, and we have introduced the *proximity parameter* $\kappa = K - a\gamma$. [2] The solution to this equation is given by

$$\Psi_K(\theta_f) \;=\; e^{\frac{i}{2}[\epsilon_R\,\sigma_1 - \epsilon_I\,\sigma_2 + \kappa\,\sigma_3](\theta_f - \theta_i)}\,\Psi_K(\theta_i) \;=\; e^{\frac{i}{2}\lambda(\theta_f-\theta_i)\,\hat{n}_r\cdot\vec{\sigma}}\,\Psi_K(\theta_i) \tag{7.4}$$

where $\lambda = \sqrt{\kappa^2 + |\epsilon_{_K}|^2}$ and

$$\hat{n}_r \;=\; \frac{1}{\lambda}\left(\epsilon_R\,\hat{x} - \epsilon_I\,\hat{s} + \kappa\,\hat{z}\right) \tag{7.5}$$

This vector represents a stationary rotation axis in the RPF. When we transform back into the original accelerator coordinate system [3], using the inverse of the transformation (7.2), we find that $\hat{n}_r$ maps back into a T–BMT solution

$$\hat{n} \;=\; \frac{1}{\lambda}\left(|\epsilon_{_K}|\cos(K\theta + \chi_1)\,,\, |\epsilon_{_K}|\sin(K\theta + \chi_1)\,,\, \kappa\right) \tag{7.6}$$

where $\chi_1 = \arctan(\epsilon_I/\epsilon_R)$ accounts for the arbitrariness of the betatron phase. The vector $\hat{n}$ in the accelerator frame is an explicit function of the betatron phase at each azimuth and is, in fact, independent of azimuth. In other words we have constructed the Derbenev–Kondratenko n–axis for the SRM. It is interesting to note that this expression for $\hat{n}$ can be derived using the SMILE algorithm [Ma92], where the potentially divergent resonant factors in the SMILE perturbation series sum up to give the non–divergent expression (7.6). The tilt of $\hat{n}$ from $\hat{n}_0$ is $\arccos(\kappa/\lambda)$ and this reaches $\pi/2$ when $\kappa = 0$, i.e. when $a\gamma = K$. Once we know the statistical distribution of $\epsilon_{_K}$ for an ensemble we can calculate the $\Theta_{\langle\hat{n},\hat{n}_0\rangle}$ (Chapter 6) for the SRM.

If we know how to express the sensitivity of the betatron amplitude and the phase to energy jumps, the SRM also allows us to calculate the derivative $\frac{\partial\hat{n}}{\partial\delta}$ needed in the Derbenev–Kondratenko formula. By comparison with the perturbative Yokoya–Mane approach, we expect this sensitivity to be given by the bracket containing Courant–Snyder parameters in eqn. (3.80). See for instance eqn. (3.3) in [Yo83]. However, one then needs a model for this function and that requires extra assumptions.

The SRM can also be extended to describe synchrotron sidebands of parent resonances [BL96, Le97]. The model developed in those texts is based on the assumption that the separations of the resonances studied are larger than their widths, but not exceedingly larger. Although not stated explicitly, it is assumed that the resonances are considered pairwise, where one of the resonances is a parent betatron resonance and the other is a synchrotron sideband. Furthermore, it is assumed that when we are close in tune space to the second resonance the tilt of $\hat{n}$ due to the first resonance is small, i.e. close to this second resonance $\hat{n}$ is nearly aligned along $\hat{n}_0$ if the sideband effect is weak. The equation of spin motion that is studied in the above texts is then

[2] Note that the symbol κ in some other descriptions of the SRM [Vo00, Ho00a] denotes the resonance position in tune space.

[3] In [BL96, Le97] a righthanded coordinate system $(\hat{x}, \hat{s}, \hat{z})$, where the particles are assumed to travel counter–clockwise is assumed.

$$\frac{d\Psi}{d\theta} = -\frac{i}{2}\begin{pmatrix} a\gamma & -\epsilon_1\, e^{-iK_1\theta} - \epsilon_2\, e^{-iK_2\theta} \\ -\epsilon_1^*\, e^{iK_1\theta} - \epsilon_2^*\, e^{iK_2\theta} & -a\gamma \end{pmatrix}\Psi \tag{7.7}$$

subject to the specified restrictions. By applying a series of spin transformations to eqn. (7.7), given in [BL96] by the eqs. (23) – (27), the spinor is brought step by step from the machine frame into the RPF of the K_2 resonance. In this frame, the spinor equation can be solved analytically and the expression for $\hat{n}$ in the accelerator frame is given by

$$\hat{n}_2 \approx \frac{1}{\lambda_2}\left(|\epsilon_2|\cos(K_2\theta + \chi_2)\,, |\epsilon_2|\sin(K_2\theta + \chi_2)\,, \kappa_2\right) \tag{7.8}$$

where $\kappa_2 = K_2 - a\gamma$ and $\lambda_2 = \sqrt{\kappa_2^2 + |\epsilon_2|^2}$, and where the $\approx$ sign indicates that approximations corresponding to the above assumptions have been made. This expression is reminiscent of the expression for the parent resonance in the usual SRM.

The model just described has been termed the "nearly overlapping resonance model", and it has been used in [BL96, Le97] to explain measurements at IUCF of the residual time averaged vertical proton polarization that would be measured by a polarimeter if a beam of vertically polarized protons were injected. The same parametrization was applied to $e^{+/-}$ polarization measurements at SPEAR. However, for SPEAR, that is clearly a misuse of the model. It should now be clear from Chapter 3 that such an approach is wholly inappropriate for the electrons in SPEAR — which became polarized by the Sokolov–Ternov effect. However, in the next section I will show how this model *can* be developed for discussing $e^{+/-}$ polarization near a synchrotron sideband. In particular, we need an estimate of the rate of depolarization. To distinguish between the original model and the extended model I will call the latter the "double resonance model". In contrast to the situation at HERA the resonances in SPEAR were quite well separated. See Figure 7.1. So the SRM and double resonance models have a chance to be relevant.

7.2 The double resonance model

We will now be more specific. We note that $\hat{n}_2$ in eqn. (7.8) is an explicit function of the phase by virtue of the term $K_2\theta + \chi_2$ in the arguments of the sine and cosine terms. As was mentioned earlier, if we know how to relate the amplitudes and phases to the energy, we are in a position to calculate the derivative $\frac{\partial \hat{n}}{\partial \delta}$. Since we are generally interested in synchrotron sidebands of parent betatron resonances, the natural starting point is to write down the expression for the energy deviation due to synchrotron oscillations. The eqn. (8) in [BL96] is such an expression. However, this particular expression lacks an arbitrary synchrotron phase factor, which will now be added in. I will also define a generalized length variable $\tilde{\ell}$, conjugate to the energy offset variable $\delta \simeq \frac{\Delta p}{p}$, and write

$$\begin{aligned} \delta &= \hat{a}\cos(\nu_s\theta + \chi_s) = \hat{a}\cos\psi_s \\ \tilde{\ell} &= \hat{a}\sin(\nu_s\theta + \chi_s) = \hat{a}\sin\psi_s \end{aligned} \tag{7.9}$$

where $\hat{a}$ is the synchrotron amplitude and χ_s is the missing phase factor. The naïve perturbation strength given in eqn. (13) in [BL96] is accordingly modified to include this phase factor

$$\epsilon_{_K}\, e^{-i\left(K\theta - \int a\gamma\, d\theta\right)} \;=\; \sum_{m_s=-\infty}^{\infty} \epsilon_{_K} J_{m_s}(\zeta) e^{-i\left[(K - a\gamma_0 - m_s\nu_s)\,\theta - m_s\chi_s\right]} \tag{7.10}$$

Here I have introduced the symbol $\zeta = \frac{\beta^2 a\gamma\,\hat{a}}{\nu_s}$ (replacing the symbol g used in [BL96, Le97]). For high energy $e^{+/-}$ machines, the Lorentz $\beta \simeq 1$ and the rms ζ is essentially equal to $\sqrt{\xi}$ from Chapter 3. For SPEAR in the energy range that we are considering the rms ζ is about 0.4. Following the argumentation in [BL96], with the aim of applying the emerging formulae initially to fit measured data from machines for which $\zeta < 1$, we apply the small argument expansion for the Bessel functions, and focus on the first order synchrotron sidebands for which the resonant tunes are given by $K \pm \nu_s$. If the strength of the parent resonance is given by $\epsilon_{_1}$, a first order sideband then has the strength $\epsilon_{_2} \approx \frac{1}{2}\zeta\epsilon_{_1}$. Inserting this estimate for the resonance strength in eqn. (7.8) and using (7.9) we get

$$\begin{aligned}
\hat{n}_{_2} \;&\approx\; \frac{1}{\lambda_{_2}}\left(\frac{1}{2}\zeta\epsilon_{_1}\cos(K\theta+\psi_s)\,, \frac{1}{2}\zeta\epsilon_{_1}\sin(K\theta+\psi_s)\,, \kappa_{_2}\right) \\
&=\; \frac{1}{\lambda_{_2}}\Big(c_{_1}\hat{a}\cos(K\theta+\psi_s)\,, c_{_1}\hat{a}\sin(K\theta+\psi_s)\,, \kappa_{_2}\Big) \\
&=\; \frac{1}{\lambda_{_2}}\Big(c_{_1}\left[\delta\cos K\theta - \tilde{\ell}\sin K\theta\right]\,, c_{_1}\left[\delta\sin K\theta + \tilde{\ell}\cos K\theta\right]\,, \kappa_{_2}\Big)
\end{aligned} \tag{7.11}$$

where $\lambda_{_2} = \sqrt{\kappa_{_2}^2 + |\epsilon_{_2}|^2}$ and where I have introduced $c_{_1} = \frac{1}{2}\frac{a\gamma}{\nu_s}\epsilon_{_1}$.

If we now take the partial derivative of this expression with respect to δ, keeping $\epsilon_{_1}$ fixed and average around the ring we obtain the following expression

$$|\langle\frac{\partial\hat{n}_{_2}}{\partial\delta}\rangle_\theta| \;=\; \sqrt{\frac{\left(c_{_1}^3\delta^2 - c_{_1}\lambda_{_2}^2\right)^2 + c_{_1}^6\delta^2\tilde{\ell}^{\,2} + c_{_1}^4\delta^2\kappa_{_2}^2}{\lambda_{_2}^6}} \tag{7.12}$$

The expression for $\hat{n}_{_2}$ in eqn. (7.11) and generally also in eqn. (7.8) contains the resonance strength $\epsilon_{_1}$ of the parent resonance, and to obtain the complete expression for $\frac{\partial\hat{n}_{_2}}{\partial\delta}$ we would need, as in the case of the simple SRM, the partial derivative of $\epsilon_{_1}$ with respect to δ. This would deliver a term additional to that obtained by differentiating $\hat{n}_{_2}$ with $\epsilon_{_1}$ fixed. The diffusion term $(\frac{\partial\hat{n}_{_2}}{\partial\delta})^2$ would then acquire an extra quadratic term and a "cross term". Since at this stage of the argument we have no model for the derivative of $\epsilon_{_1}$ we ignore the extra terms and work with the expression in eqn. (7.12). Nevertheless, this estimate of the spin–orbit coupling function puts us in a position to point at a misconception occurring in the reference texts [BL96, Le97].

As already mentioned, the nearly overlapping resonance model presented in [BL96, Le97] has been used to explain measured e^+ beam polarization data from SPEAR, first published in [Jo83]. In the paper [BL96] and in the book [Le97], the strengths of the spin–orbit resonances present in these data have been attributed entirely to the $\cos^2(\Theta_{\langle\hat{n},\hat{n}_0\rangle}) = \kappa^2/\lambda^2$. As we have stated, this would be appropriate for protons but not for electrons. We have also seen in Chapter 6 that at HERA, attributing the measured polarization to $\cos(\Theta_{\langle\hat{n},\hat{n}_0\rangle})$ leads to opening angles of tens of degrees, instead of milliradians.

Instead we need $(\frac{\partial\hat{n}_{_2}}{\partial\delta})^2$! Close to the first order synchrotron sidebands this can be calculated with eqn. (7.12).

To illustrate this point I will choose a particular parent resonance from the SPEAR data and use the corresponding values for the resonance strength given by the fit to the data in [BL96, Le97] which was based on equating the measured polarization to $0.92 \cdot \cos^2(\Theta_{\langle \hat{n}, \hat{n}_0 \rangle})$. As an estimate for the synchrotron amplitude I will initially use the value quoted in these references, $\sqrt{6}\,\sigma_\delta = 2.1 \cdot 10^{-3}$, and choose the representative phase space point $\delta = \tilde{\ell} = \sqrt{6}\,\sigma_\delta$, but this value is not critical for my illustration. In fact a smaller value based on $\sigma_\delta/\sqrt{2}$, for example, would illustrate my point even better. The parent resonance I choose is that with $\nu_0 = 3 + \nu_x$ situated at $E = 3.648$ GeV, see Figure 7.1. This resonance was presumably driven by a tilted $\hat{n}_0$ resulting from imperfections. If I now insert the parameters from the original fit in [BL96] I find that for the lower sideband resonance at about 3.63 GeV and for $\kappa_2 = 1 \cdot 10^{-3}$, corresponding to a position in tune space halfway down the resonance, $\frac{11}{18}\left(\frac{\partial \hat{n}}{\partial \delta}\right)^2$ is of the order of 250^2! at this particular position in phase space. Clearly, from the data from the SPEAR measurements [Jo83] cited in [BL96], halfway down this resonance $\frac{11}{18}\left(\frac{\partial \hat{n}}{\partial \delta}\right)^2$ must be of the order of one. So although this estimate is based on just one position in phase space, it is clear that the strength parameters from [BL96, Le97] applied to this case do not make any sense. The value of $\epsilon_1 = \epsilon_{\{3+\nu_x\}} = 0.008$ is probably massively overestimated as a result of attributing the measured polarization to the opening angle. Moreover, it is now clear that there is little point in being concerned about the absence of extra terms while the simplest estimate of $\frac{11}{18}\left(\frac{\partial \hat{n}}{\partial \delta}\right)^2$ is so large.

This analysis has been preliminary, but we could now go further and develop the full expression for $\langle \frac{11}{18}\left(\frac{\partial \hat{n}}{\partial \delta}\right)^2 \rangle$ including the rms values of ϵ_1 and of its derivative with respect to δ. Then a fit to the data might deliver values for these quantities. This will be the subject of future work and, as is often the case with simple models [He97], this investigation has already been of pedagogical value.

The obvious conclusion from this discussion is that it is misleading to treat $e^{+/-}$ spins in the same way that one would treat proton spins. $e^{+/-}$ spins diffuse due to synchrotron radiation and polarization builds up via the Sokolov–Ternov effect. Proton spins are subject to neither of these effects. This discussion shows how to proceed correctly.

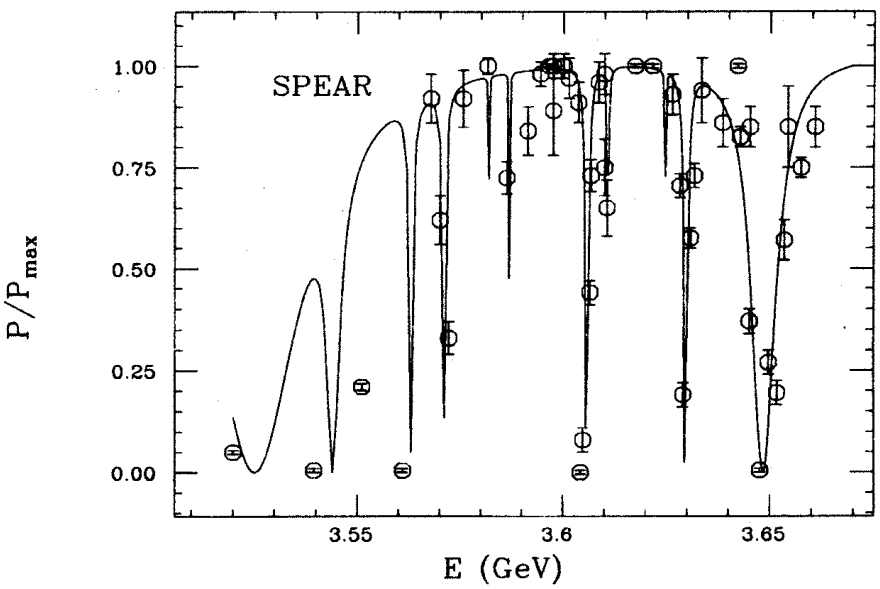

Figure 7.1: The polarization as a function of energy for single e^+ beam in SPEAR. The circles with error bars are data from measurements originally presented in [Jo83]. The solid line is a "fit to the eye" using the nearly overlapping resonance model presented in [BL96, Le97]. Source [BL96].

Chapter 8

Conclusions

The luminosity upgrade project of HERA will make operation with longitudinally polarized $e^{+/-}$ beams more difficult than in the past. Polarization is only one of the aspects of running HERA after the upgrade, but it is still very important. The interest in longitudinal $e^{+/-}$ polarization is illustrated by the large amount of time and effort spent by the polarimetry groups to upgrade the TPOL and LPOL, and by the installation of the spin rotators for H1 and ZEUS. Tracking simulations including realistic orbit distortions, and an estimate of the influence of the beam–beam interaction based on past experience, suggest that, despite the complicated field mixture in the new IRs and the uncompensated experiment solenoids, it is possible to achieve longitudinal polarization after the upgrade at the 50 % level with three pairs of spin rotators operating. This however requires very well corrected orbits and, as mentioned in Chapter 6, perhaps also a dedicated dispersion correction and use of additional harmonic bumps. It should be pointed out that the presence of the three rotator pairs, one of them being asymmetrically retuned, and the extra constraints set by the asymmetries in the new lattice will make tuning for high polarization after the upgrade especially difficult. Various effects influencing the polarization may also be difficult to disentangle in practice. The diagnostic checks made with SLICK, using various models for the overlapping field regions in the new IRs, described in Chapter 6 can then be of guidance. It has been shown for the first time how to construct numerical symplectic orbits maps and numerical orthogonal spin maps for the complicated fields at the detectors and include them in the standard programs for calculating polarization.

Since the beam–beam effect can lead to stronger depolarization in the upgraded HERA, it will be important for the future to get the beam–beam simulations in SITROS (or in alternative software) under control, in order to better understand and master the underlying dynamics. This will probably be the subject of a separate project, for which there unfortunately has been no time during the completion of this thesis.

In the last section of this work, it has been demonstrated how to use a simple, unitarity preserving model of synchrotron sidebands to derive an analytical expression for the $\frac{\partial \hat{n}}{\partial \delta}$ in the Derbenev–Kondratenko formula. It has been demonstrated that a previous treatment was incomplete, and it has been shown how that treatment can be improved.

Appendix A

Equations of motion

A.1 Orbit motion

The equations of motion for a relativistic charged particle of rest mass m in an external electric field $\vec{\mathcal{E}}$, and external magnetic field $\vec{\mathcal{B}}$, are given by the Abraham–Lorentz relation [Ja98, AM78]

$$\frac{d}{dt}\left(\frac{E}{c^2}\dot{\vec{r}}\right) = e\left(\vec{\mathcal{E}} + \dot{\vec{r}} \times \vec{\mathcal{B}}\right) + \vec{R}_{rad} \tag{A.1}$$

where E is the energy of the particle, $E = \dfrac{mc^2}{\sqrt{1 - \left(\dfrac{\dot{\vec{r}}}{c}\right)^2}} = \gamma mc^2$

and the term $\vec{R}_{rad}$ is the radiation reaction force, which can be written as the sum

$$\vec{R}_{rad} = \vec{R}^D + \delta\vec{R} \tag{A.2}$$

where

$$\vec{R}^D = -\frac{2}{3}\frac{r_e m}{c^3}\gamma^4 \dot{\vec{r}}\left(\ddot{\vec{r}}^2 + \frac{\gamma^2}{c^2}\left(\dot{\vec{r}}\ddot{\vec{r}}\right)^2\right)$$

is the continuous contribution to the energy loss due to synchrotron radiation emission which, in this formalism leads to damping of the orbital motion. The vector $\delta\vec{R}$ is the stochastic component describing the quantum fluctuations of the radiation field and ultimately leads to excitation of the orbital amplitudes.

In order to describe the particle motion in an accelerator it is customary to revert to a coordinate system in which the dynamical variables are small. This is achieved by introducing the *design orbit* $\vec{r}_0$ and writing the general particle position as

$$\vec{r}(x, z, s) = \vec{r}_0(s) + x\hat{e}_x + z\hat{e}_z \tag{A.3}$$

where s is the arc length (azimuth) along this design orbit. The unit vectors $\hat{e}_x$ and $\hat{e}_z$ are mutually orthogonal and locally normal to the design orbit. It is assumed that sections of the design orbit lie either in the horizontal or in the vertical plane. In either case $\hat{e}_x$ is in the horizontal plane whereas $\hat{e}_z$ is in the vertical plane. Together with a third unit vector $\hat{e}_s$, tangent to the design orbit and pointing

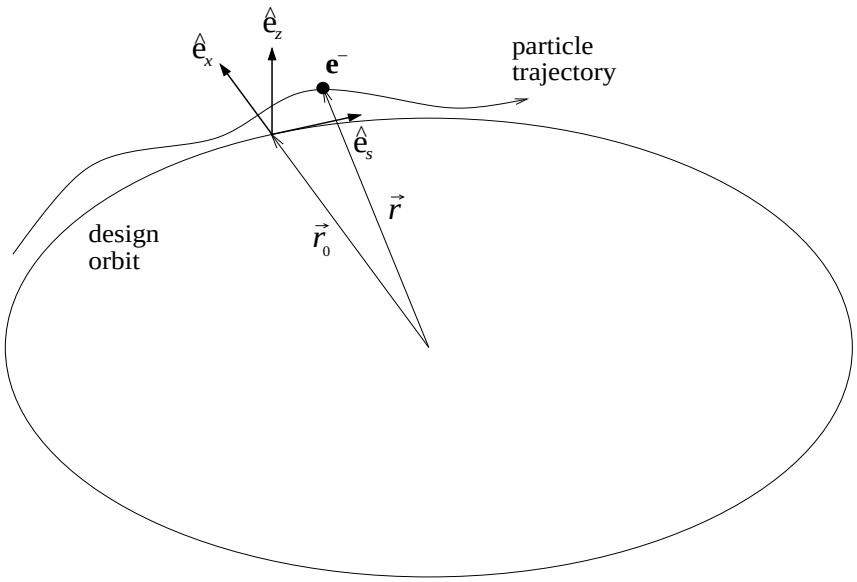

Figure A.1: Coordinate system used to describe particle motion in circular accelerators.

in the direction of motion, these unit vectors form a righthanded orthogonal "tripod". See Figure A.1. Note that even with solenoids in the machine lattice there is no torsion on the design orbit.[1] The energy of the general particle is given in terms of the design energy E_0 by introducing a small energy offset parameter $\delta = \Delta E/E_0$: $E = E_0\,(1+\delta)$. We now make a change of the independent variable from time t to arc length s via

$$\frac{d}{dt} = \frac{ds}{dl}\frac{dl}{dt}\frac{d}{ds} = \frac{v}{l'}\frac{d}{ds} \tag{A.4}$$

where l is the path length and $dl/dt = v \simeq c$ is the velocity of an ultra–relativistic particle, and make use of the relations

$$\frac{d\vec{r}_0}{ds} = \hat{e}_s\,, \quad \frac{d\hat{e}_x}{ds} = K_x\hat{e}_s\,, \quad \frac{d\hat{e}_z}{ds} = K_z\hat{e}_s\,, \quad \frac{d\hat{e}_s}{ds} = -K_x\hat{e}_x - K_z\hat{e}_z \tag{A.5}$$

where the curvatures K_x and K_z are related to the transverse magnetic fields on the design orbit and E_0 through $K_x = \frac{ec}{E_0}\mathcal{B}_z^{d.o}$ and $K_z = -\frac{ec}{E_0}\mathcal{B}_x^{d.o}$ (with $K_xK_z = 0$). The first two derivatives of the position vector $\vec{r}$ then become

$$\vec{r}\,'(x,z,s) = x'\hat{e}_x + z'\hat{e}_z + (1 + xK_x + zK_z)\,\hat{e}_s \tag{A.6}$$

$$\begin{aligned}\vec{r}\,''(x,z,s) &= \Big(x'' - K_x\,(1+xK_x)\Big)\hat{e}_x + \Big(z'' - K_z\,(1+zK_z)\Big)\hat{e}_z \\ &+ \Big(xK_x' + zK_z' + 2\,x'K_x + 2\,z'K_z\Big)\hat{e}_s\end{aligned} \tag{A.7}$$

Furthermore, we need the quantity $l' = \|\vec{r}\,'\| = \sqrt{(1+xK_x+zK_z)^2 + (x')^2 + (z')^2}$. The motion of a particle can now be described in terms of the coordinates $(x, x', z, z', \ell, \delta)$. Assuming that the particles are travelling in a region where there are no electric fields ($\vec{\mathcal{E}} = 0$) and, for the moment, disregarding

[1] For a more elaborate discussion on accelerator coordinates, where the relation of the above reference frame to the Frenet–Serret coordinate system is explained, see [Vo00] or [Ho00a].

radiation (set $\vec{R}_{rad} = 0$) it can be demonstrated that the complete equations of motion in the two transverse planes transform to [MR82a][2]

$$\begin{aligned} x'' &= K_x\,(1 + x\,K_x) + \frac{\Big((1 + x\,K_x + z\,K_z)(x\,K_x{}' + x'K_x + z\,K_z{}' + z'K_z) + x'x'' + z'z''\Big)x'}{(1 + x\,K_x + z\,K_z)^2 + (x')^2 + (z')^2} \\ &+ \frac{ec\sqrt{(1 + x\,K_x + z\,K_z)^2 + (x')^2 + (z')^2}}{E_0\,(1+\delta)}\Big(z'\,\mathcal{B}_s - (1 + x\,K_x + z\,K_z)\,\mathcal{B}_z\Big) \end{aligned} \tag{A.8}$$

$$\begin{aligned} z'' &= K_z\,(1 + z\,K_z) + \frac{\Big((1 + x\,K_x + z\,K_z)(x\,K_x{}' + x'K_x + z\,K_z{}' + z'K_z) + x'x'' + z'z''\Big)z'}{(1 + x\,K_x + z\,K_z)^2 + (x')^2 + (z')^2} \\ &+ \frac{ec\sqrt{(1 + x\,K_x + z\,K_z)^2 + (x')^2 + (z')^2}}{E_0\,(1+\delta)}\Big((1 + x\,K_x + z\,K_z)\,\mathcal{B}_x - x'\,\mathcal{B}_s\Big) \end{aligned} \tag{A.9}$$

Linear optical calculations are based on the linearized form of these equations [MR82a, MR83].

For electrons the effects of radiation must be included. It is customary to represent the stochastic part of the radiation as a Gaussian white noise process. The full linearized equations of motion for x, x', z, z' and δ are given in [MR82a, MR83]. For example, the linearized equation of motion for δ in a horizontal dipole on the design orbit is

$$\frac{d\delta}{ds} = -2C_1K_x^2\delta + \delta\mathcal{R} \tag{A.10}$$

where the (combined) symbol[3] $\delta\mathcal{R}$ represents the noise and has the properties

$$\begin{aligned} \langle\, \delta\vec{\mathcal{R}}\,\rangle &= 0 \\ \langle\, \delta\vec{\mathcal{R}}(s)\,\delta\vec{\mathcal{R}}(s')\,\rangle &= \frac{55r_e\hbar\gamma^5}{24\sqrt{3}mc}\,|K_x|^3\,\delta(s-s') \end{aligned} \tag{A.11}$$

The term $-2C_1K_x^2\delta$ with $C_1 = \frac{2}{3}r_e\gamma^3$ represents the damping. The strengths of the noise and damping terms can be derived from the radiation reaction force $\vec{R}_{rad}$ given above [Bb91]. The equations of motion for the transverse coordinates also contain damping terms [MR83, EMR99]. But the transverse beam size remains finite owing to feedthrough of the noise from the longitudinal coordinate to the transverse coordinates via the dispersion.

A.2 Spin motion

The motion of $\widehat{S}$, the normalized centre–of–mass spin expectation value of a relativistic charged non–radiating particle, in external electric and magnetic fields is given by the Thomas–BMT equation [Th27, BMT59]

$$\frac{d\widehat{S}}{dt} = \vec{\Omega}_{BMT}(\vec{r},\dot{\vec{r}};t) \times \widehat{S} \tag{A.12}$$

[2] In the cited paper by Mais and Ripken the orbital equations of motion have been derived in the *linear approximation*, i.e. by linearization of the equations with respect to the small quantities x, x', z, z' and δ.

[3] The multiple use of the symbol δ should not lead to confusion here.

with

$$\vec{\Omega}_{BMT} = -\frac{e}{\gamma m}\left((1+a\gamma)\,\vec{\mathcal{B}} - \frac{a\gamma^2}{1+\gamma}\frac{1}{c^2}\left(\dot{\vec{r}}\cdot\vec{\mathcal{B}}\right)\dot{\vec{r}} - \left(a\gamma + \frac{\gamma}{1+\gamma}\right)\dot{\vec{r}}\times\frac{\vec{\mathcal{E}}}{c^2}\right)$$

In the above equation the fields and the derivative of the position vector, $\dot{\vec{r}}$ are given in the laboratory frame. The $a = (g-2)/2$ is the gyromagnetic anomaly and γ is the Lorentz factor. By changing the independent variable from time t to arc length s according to relation (A.4) and using the definitions in (A.5), the T–BMT equation can be written as

$$\frac{d\widehat{S}}{ds} = \widehat{S}\,' = S_x{}'\,\hat{e}_x + S_z{}'\,\hat{e}_z + S_s{}'\,\hat{e}_s + (K_z\hat{e}_x - K_x\hat{e}_z)\times\widehat{S} \tag{A.13}$$

The last term, $(K_z\hat{e}_x - K_x\hat{e}_z)\times\widehat{S}$, appears because of the change of orientation of the coordinate system. It is the contribution to the spin motion from the rotation of the ideal particle co–moving coordinate frame. We will represent this here by $\vec{\Omega}_r\times\widehat{S}$. Rearranging and introducing $\vec{\Omega} = \vec{\Omega}_l - \vec{\Omega}_r$, where $\vec{\Omega}_l = l'/v\,\vec{\Omega}_{BMT} \simeq l'/c\,\vec{\Omega}_{BMT}$ describes the spin motion with respect to s in the laboratory frame, we get

$$\vec{\Omega}\,(\vec{u};s)\times\widehat{S} = S_x{}'\,\hat{e}_x + S_z{}'\,\hat{e}_z + S_s{}'\,\hat{e}_s \tag{A.14}$$

The individual components of the $\vec{\Omega}$ rotation vector, in the case of no electric field ($\vec{\mathcal{E}} = 0$), and with $\gamma = \gamma_0\,(1+\delta)$ now read [MR82b][4]

$$\begin{aligned}\Omega_x &= -\frac{ec}{E_0}\sqrt{(1+xK_x+zK_z)^2+(x')^2+(z')^2}\\ &\left(\left(\frac{1}{1+\delta}+a\gamma_0\right)\mathcal{B}_x - \frac{a\gamma_0^2}{\frac{1}{1+\delta}+\gamma_0}\frac{\left((1+xK_x+zK_z)\,\mathcal{B}_s + x'\mathcal{B}_x + z'\mathcal{B}_z\right)x'}{(1+xK_x+zK_z)^2+(x')^2+(z')^2}\right) - K_z\end{aligned} \tag{A.15}$$

$$\begin{aligned}\Omega_z &= -\frac{ec}{E_0}\sqrt{(1+xK_x+zK_z)^2+(x')^2+(z')^2}\\ &\left(\left(\frac{1}{1+\delta}+a\gamma_0\right)\mathcal{B}_z - \frac{a\gamma_0^2}{\frac{1}{1+\delta}+\gamma_0}\frac{\left((1+xK_x+zK_z)\,\mathcal{B}_s + x'\mathcal{B}_x + z'\mathcal{B}_z\right)z'}{(1+xK_x+zK_z)^2+(x')^2+(z')^2}\right) + K_x\end{aligned} \tag{A.16}$$

$$\begin{aligned}\Omega_s &= -\frac{ec}{E_0}\sqrt{(1+xK_x+zK_z)^2+(x')^2+(z')^2}\\ &\left(\left(\frac{1}{1+\delta}+a\gamma_0\right)\mathcal{B}_s - \frac{a\gamma_0^2}{\frac{1}{1+\delta}+\gamma_0}\frac{\left((1+xK_x+zK_z)\,\mathcal{B}_s + x'\mathcal{B}_x + z'\mathcal{B}_z\right)(1+xK_x+zK_z)}{(1+xK_x+zK_z)^2+(x')^2+(z')^2}\right)\end{aligned} \tag{A.17}$$

where x, x', z, z' and δ are solutions of the orbital equations of motion.

[4] Again, in the original derivation of Mais and Ripken the equations have been derived in the linear approximation of small orbital coordinates x, x', z, z' and small energy offset δ. For a nonlinear treatment by the same authors, see for instance [BM86].

Appendix B

Characteristic times of processes

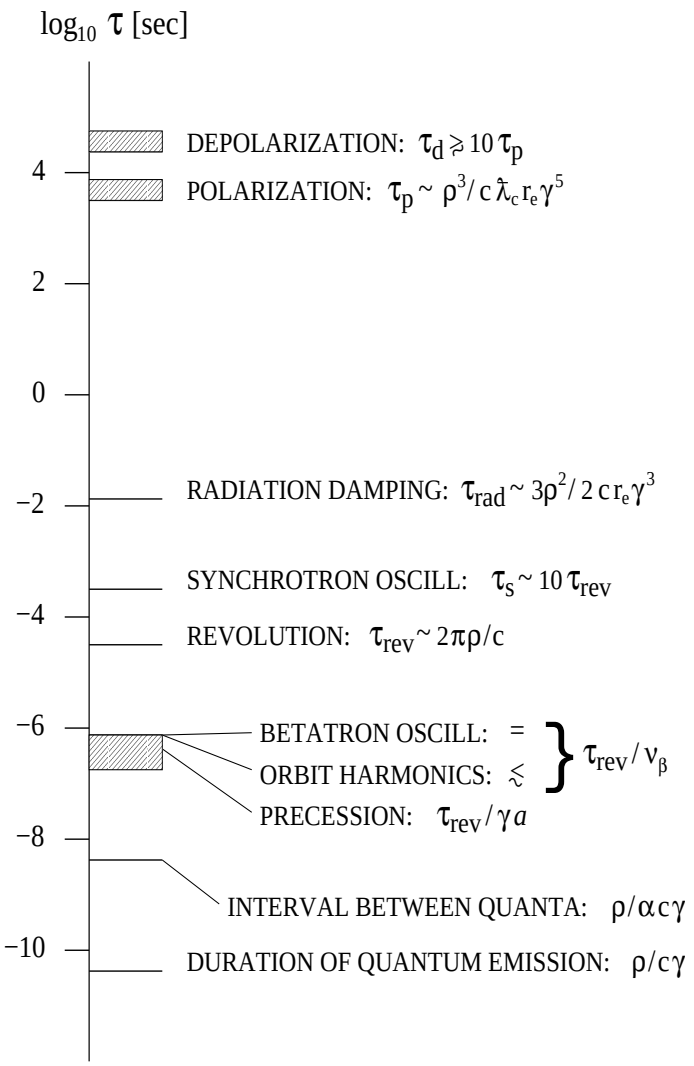

Figure B.1: Characteristic time scales in a typical 25 GeV electron storage ring [Mo84]. Legend: ρ = bending radius, $\lambda\!\!\!^{-}_c$ = Compton wavelength, r_e = classical electron radius, ν_β = betatron tune, α = fine structure constant, a = gyromagnetic anomaly. Although it is desirable that $\tau_d \geq 10\,\tau_p$, this is difficult to achieve in practice.

Appendix C

Updates of the SITROS code

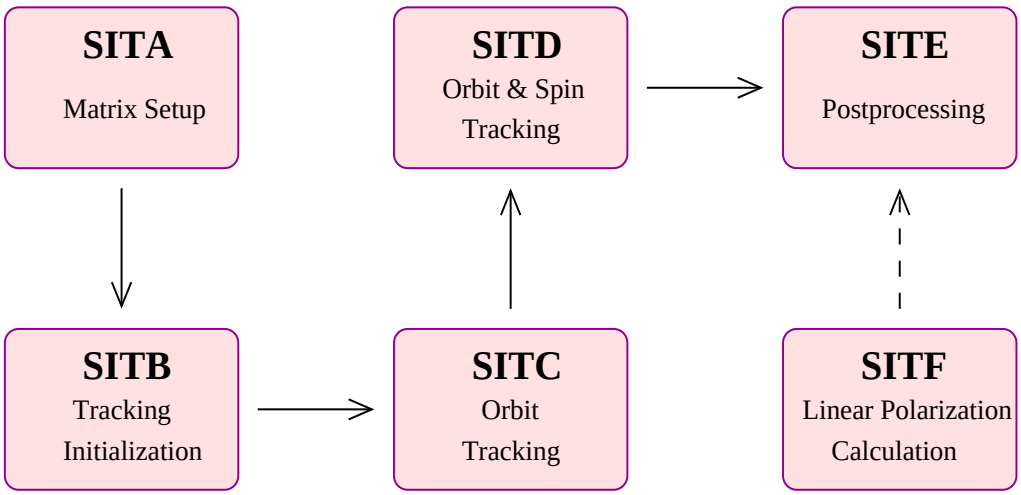

Figure C.1: Flow diagram of the SITROS code.

Listed below are the updates introduced and errors corrected in SITF and SITROS:

SITF:

- Resolved the confusion in the program concerning the use of damped and undamped eigenvectors (the DODAMP = T or F option). The eigenvector needed in the calculations of the linear approximation of $\hat{n}$, eqn. (3.64), and the partial derivative with respect to δ, eqn. (3.66), are the *undamped* eigenvectors, whereas for the damping time calculations, obviously the damping has to be switched on. Note also that the closed orbit is calculated with the damping on.
- The vertical bends' contribution to $\frac{1}{|\rho(s)|^3}$ in the emittance calculation were omitted, but has now been added.
- The arc dipoles should in principle be sliced up to get a sufficient sampling for the optical calculations. In the current version this option is omitted, since it causes trouble in the routine preparing for the tracking (SITA) where the linear calculations from SITF are repeated. In other words, this is a known artifact that should be addressed at some point. Without the extra slicing the emittance in SITF is off from the analytical value by a few percent.
- The erroneous calculation of the polarization time for the case with the rotators turned on has been corrected.

- The **G** matrix for the solenoid was not correctly implemented, but this has now been corrected. In fact, the whole implementation of the solenoids into the code was suspect, but it should be noted that up to now solenoids were generally not used with the program for HERA, since they were considered to be perfectly compensated by the "anti–solenoids".

SITROS:

- An erroneous definition of the rms beamsize in the emittance calculation has been corrected.
- The number of radiation points has been enlarged so that the radiation now takes place in every dipole and combined function magnet. This was necessary in order to reproduce the correct emittance in the luminosity upgrade optic.
- The representation of the spin components in the tracking has been changed from the vector–angle representation to a pure quarternion representation. Before that, a mixture of representations was used.
- The solenoid end fields were missing in the spin representation for the tracking — they have now been correctly introduced.
- Corrections in the beam–beam implementation have been made where the most important update is the introduction of the missing *direct* beam–beam spin kick.

Appendix D

Symplectification of maps via generating functions

The four most common generating functions of classical mechanics relate the generalized positions $\vec{q}$ and conjugate momenta $\vec{p}$ before (i) and after (f) a canonical transformation via

$$(\vec{q}_i, \vec{q}_f) = \left(\partial_{\vec{p}_i}, -\partial_{\vec{p}_f} \right) F_1 (\vec{p}_i, \vec{p}_f) \tag{D.1}$$

$$(\vec{q}_i, \vec{p}_f) = \left(\partial_{\vec{p}_i}, \partial_{\vec{q}_f} \right) F_2 (\vec{p}_i, \vec{q}_f) \tag{D.2}$$

$$(\vec{p}_i, \vec{q}_f) = \left(-\partial_{\vec{q}_i}, -\partial_{\vec{p}_f} \right) F_3 (\vec{q}_i, \vec{p}_f) \tag{D.3}$$

$$(\vec{p}_i, \vec{p}_f) = \left(-\partial_{\vec{q}_i}, \partial_{\vec{q}_f} \right) F_4 (\vec{q}_i, \vec{q}_f) \tag{D.4}$$

If, by integration, any of these generating functions can be found, it will by definition represent a symplectic transformation. This property of the generating functions can be used to construct transformations that restore the symplecticity of nearly symplectic matrices [Ho94].

Consider a nearly symplectic linear map $\mathbf{M}_{6\times 6}$ that transports the vector $\vec{u} = (x, p_x, z, p_z, \ell, \delta)$[1] from azimuth s_i to s_f so that $\vec{u}_{s_f} = \mathbf{M}_{6\times 6}\, \vec{u}_{s_i}$. Rearrange the phase space vector such that the positions and momenta are sorted as follows: $(\vec{q}, \vec{p}) = (x, z, \ell, p_x, p_z, \delta)$ and write the matrix $\mathbf{M}$ in terms of four submatrices

$$\mathbf{M} = \begin{pmatrix} \mathbf{A} & \mathbf{B} \\ \mathbf{C} & \mathbf{D} \end{pmatrix} \quad \Longrightarrow \quad \begin{pmatrix} \vec{q}_f \\ \vec{p}_f \end{pmatrix} = \begin{pmatrix} \mathbf{A} & \mathbf{B} \\ \mathbf{C} & \mathbf{D} \end{pmatrix} \begin{pmatrix} \vec{q}_i \\ \vec{p}_i \end{pmatrix} \tag{D.5}$$

Suppose that we choose F_2 as our candidate for the transformation. With the aid of eqs. (D.2) and (D.5) and after some simple algebraic manipulations we arrive at a partial differential equation problem for the coordinates in terms of the matrix elements

$$\begin{pmatrix} \vec{q}_i \\ \vec{p}_f \end{pmatrix} = \begin{pmatrix} \mathbf{I} & \mathbf{0} \\ \mathbf{C} & \mathbf{D} \end{pmatrix} \begin{pmatrix} \mathbf{A} & \mathbf{B} \\ \mathbf{0} & \mathbf{I} \end{pmatrix}^{-1} \begin{pmatrix} \vec{q}_f \\ \vec{p}_i \end{pmatrix}$$

[1] Note the use of the true canonical coordinates here.

$$= \begin{pmatrix} \mathbf{I} & \mathbf{0} \\ \mathbf{C} & \mathbf{D} \end{pmatrix} \begin{pmatrix} \mathbf{A^{-1}} & \mathbf{-A^{-1}B} \\ \mathbf{0} & \mathbf{I} \end{pmatrix} \begin{pmatrix} \vec{q}_f \\ \vec{p}_i \end{pmatrix} \tag{D.6}$$

$$\Longrightarrow \quad \begin{pmatrix} \partial_{\vec{p}_i} \\ \partial_{\vec{q}_f} \end{pmatrix} F_2 = \begin{pmatrix} \mathbf{A^{-1}} & \mathbf{-A^{-1}B} \\ \mathbf{CA^{-1}} & \mathbf{-CA^{-1}B + D} \end{pmatrix} \begin{pmatrix} \vec{q}_f \\ \vec{p}_i \end{pmatrix} \tag{D.7}$$

By introducing the notation

$$\begin{pmatrix} \mathbf{A^{-1}} & \mathbf{-A^{-1}B} \\ \mathbf{CA^{-1}} & \mathbf{-CA^{-1}B + D} \end{pmatrix} = \begin{pmatrix} \mathbf{a} & \mathbf{b} \\ \mathbf{c} & \mathbf{d} \end{pmatrix} \tag{D.8}$$

and integrating eqn. (D.7) to obtain F_2 — provided that $\mathbf{A^{-1}}$ exists — it can be shown that one possible solution to the matrix equation defined in (D.5) is given by

$$\begin{aligned} \begin{pmatrix} \vec{q}_f \\ \vec{p}_f \end{pmatrix} &= \begin{pmatrix} 2\,(\mathbf{a} + \mathbf{d}^T)^{-1} & -(\mathbf{a} + \mathbf{d}^T)^{-1}(\mathbf{b} + \mathbf{b}^T) \\ (\mathbf{c} + \mathbf{c}^T)(\mathbf{a} + \mathbf{d}^T)^{-1} & -\frac{1}{2}\left[(\mathbf{c} + \mathbf{c}^T)(\mathbf{a} + \mathbf{d}^T)^{-1}(\mathbf{b} + \mathbf{b}^T) - (\mathbf{a}^T + \mathbf{d})\right] \end{pmatrix} \begin{pmatrix} \vec{q}_i \\ \vec{p}_i \end{pmatrix} \\ &= \begin{pmatrix} \widetilde{\mathbf{A}} & \widetilde{\mathbf{B}} \\ \widetilde{\mathbf{C}} & \widetilde{\mathbf{D}} \end{pmatrix} \begin{pmatrix} \vec{q}_i \\ \vec{p}_i \end{pmatrix} = \widetilde{\mathbf{M}} \begin{pmatrix} \vec{q}_i \\ \vec{p}_i \end{pmatrix} \end{aligned} \tag{D.9}$$

where by virtue of the canonical transformation introduced via F_2 in the intermediate step, the matrix $\widetilde{\mathbf{M}}$ is symplectic. Hence we have "symplectified" $\mathbf{M}$.

Bibliography

[Ab61] A. Abragam, *The Principles of Nuclear Magnetism*, Oxford University Press, 1961.

[AM78] R. Abraham, J. E. Marsden, *Foundations of Mechanics*, 2nd ed. Reading, Mass.: Benjamin/Cummings, 1978. (Chapter 11).

[Ar92] L. Arnaudon et al., *Phys. Lett.*, **B 284**, 431 (1992).

[AS70] M. Abramowitz, I. A. Stegun, *Handbook of Mathematical Functions with Formulas, Graphs and Mathematical Tables*, Dover Publications Inc., New York, 1970. (Chapter 7).

[Ba72] V. N. Baier, *Sov. Phys. Uspekhi*, **14**, 695 (1972).

[Ba79] M. Bassetti, CERN ISR–TH 79–41 (1979).

[Bb00] SLICK is a thick lens version of SLIM by D. P. Barber and uses the matrices from [Bb85b].

[Bb01] D. P Barber, private communication.

[Bb85a] D. P. Barber, H. Mais, G. Ripken, R. Rossmanith, DESY Report 85–044, (1985).

[Bb85b] D. P. Barber et al., *Part. Acc.*, **17**, 243 (1985).

[Bb90] D.P.Barber, Proceedings of the 9th International Symposium on High Energy Spin Physics, Bonn, September 1990, Springer Verlag (1991).

[Bb91] D. P. Barber, K. Heinemann, H. Mais, G. Ripken, DESY Report 91–146, (1991).

[Bb93] D. P. Barber et al., *Nucl. Inst. Meth.*, **A329**, 79 (1993).

[Bb94] D. P. Barber et al., *Nucl. Inst. Meth.*, **A338**, 166 (1994).

[Bb95] D. P. Barber et al., *Phys. Lett.*, **B 343**, 436 (1995).

[Bb96] D. P. Barber, invited plenary talk at the 12th International Symposium on High Energy Spin Physics (SPIN96), Amsterdam 1996, World Scientific 1997.

[Bb99] D. P. Barber, five articles in the Proceedings of the ICFA Workshop on Quantum Aspects of Beam Physics, Monterey, USA, 1998, edited by P. Chen, World Scientific 1999. Also DESY–98–096A and Los Alamos Archive: physics/9901038.

[BB94] R. Brinkmann, M. Böge, Proceedings of the European Particle Accelerator Conference (EPAC94), London, Vol. 2, 938 (1994).

[BB96] M. Bassetti, C. Biscari, *Part. Acc.*, **52**, 221 (1996).

[Be68] R. Belbéoch et al., Proceedings USSR Nat. Conf. Part. Acc. 129 (1968).
The Orsay Storage Ring Group, Proceedings 8th Int. Conf. High energy Acc., CERN, Geneva 1971, 127 (1971).

[Be00a] M. Beckmann et al., DESY Report 00–106, (2000). To be published in *Nucl. Inst. Meth.* Also Los Alamos Archive: physics/0009047.

[Be00b] T. Behnke, Polarization at HERA. Status and Plans. Minutes of the POL2000 Group meetings, unpublished.

[BG98] V. Balandin, N. Golubeva, DESY Report 98–016, (1998).

[Bi99] M. Bieler et al., Proceedings Workshop on Beam–Beam Effects in Large Hadron Colliders, Geneva, Switzerland, 12 – 16 April 1999.

[BH01] K. Heinemann, D. P. Barber, *Nucl. Inst. Meth.*, **A463**, 62 and **A469**, 294 (2001).

[BHR92] D. P. Barber, K. Heinemann, G. Ripken, DESY Internal Report M–92–04, (1992), second revised version 1999.

[BL96] M. Berglund, S. Y. Lee, *Phys. Rev.*, **E 54**, 806 (1996).

[BL95] M. Böge, T. Limberg, Proceedings of the IEEE Particle Accelerator Conference (PAC95), Dallas, Vol. 4, 2901 (1995).

[BM86] D. P. Barber, H. Mais, G. Ripken, F. Willeke DESY Report 86–147, (1986).

[BMT59] V. Bargmann, L. Michel, V. L. Telegdi, *Phys. Rev. Lett.*, **2**, 435 (1959).

[BK67] V. N. Baier, V. M. Katkov, *Sov. Phys. JETP*, **25**, 944 (1967).
V. N. Baier, V. M. Katkov, *Phys. Lett.*, **24A**, 327 (1967).

[BKS70] V. N. Baier, V. M. Katkov, V. M. Strakhovenko, *Sov. Phys. JETP*, **31**, 908 (1970).

[Bo70] C. Bovet et al., CERN/MPS–SI/Int. DL/70/4 (1970).

[BO66] V. N. Baier, Yu. F. Orlov, *Sov. Phys. Dokl.*, **10**, 1145 (1966).

[Br82] H.–D. Bremer et al., DESY Internal Report M–82–26, (1982).

[BR99] *Handbook of Accelerator Physics and Engineering*,
Eds. A. W. Chao and M. Tigner, World Scientific 1999.
Section 2.7.8 by D. P. Barber and G. Ripken.
See also: http://www.wspc.com.sg/books/physics/3818.html (Errata).

[BS86] J. Buon and K. Steffen, *Nucl. Inst. Meth.*, **A245**, 248 (1986).

[Bu87] J. Buon , LAL–RT 87–09 Orsay (1987).

[BW93] R. Brinkmann, F. Willeke, Proceedings of the IEEE Particle Accelerator Conference (PAC93), Washington DC, Vol. 5, 3742 (1993).

[Bö94] M. Böge, Doctoral Thesis, DESY Report 94–087, (1994).

[Ch79] A. W. Chao, *J. Appl. Phys.*, **50**, No 2, 595 (1979).

[Ch81a] A. W. Chao, *Nucl. Inst. Meth.*, **180**, 29 (1981).

[Ch81b] A. W. Chao, American Institute of Physics (AIP) Proceedings 87, 395 (1981).

[CS58] E. D. Courant, H. S. Snyder *Annl. o. Phys.*, **3**, 1 (1958).

[CY81] A. W. Chao, K. Yokoya, KEK Report, KEK 81–7 (1981).

[DK72] Ya. S. Derbenev, A. M. Kondratenko, *Sov. Phys. JETP*, **25**, 230 (1972).

[DK73] Ya. S. Derbenev, A. M. Kondratenko, *Sov. Phys. JETP*, **37**, 968 (1973).

[EMC88] The EMC collaboration. J. Ashman et al., *Phys. Lett.*, **B 206**, 364 (1988).

[EMR99] *Handbook of Accelerator Physics and Engineering*,
Eds. A. W. Chao and M. Tigner, World Scientific 1999.
Section 2.1.4 by J. A. Ellison, H. Mais and G. Ripken.

[EY94] Yu. Eidelman, V. Yakimenko, *Part. Acc.*, **45**, 17 (1994).

[Fa01] N. Falletto et al., *Nucl. Inst. Meth.*, **A 459**, 412 (2001).

[Fe99] R. Felst, private communication.

[FG97] F. Galluccio, unpublished notes.

[FR73] E. Freytag, G. Ripken, DESY Internal Report, DESY E3/R1–73/1 (1973).

[Gu76] G. Guignard, CERN 76–06 (1976).

[Gi01] E. Gianfelice–Wendt, private communication.

[GR00] G. Ripken, unpublished notes.

[He97] K. Heinemann DESY Report 97–166 (1997).
See also the Los Alamos Archive: physics/9709025.

[HH96] K. Heinemann, G. H. Hoffstätter, *Phys. Rev. E* **54**, N^0 4, 4240 (1996).

[Ho93] The ZEUS Detector. Status Report 1993. Editor Uwe Holm.

[Ho94] G. H. Hoffstätter, Doctoral Thesis, DESY Report 94-242 (1994).

[Ho99] G. H. Hoffstätter, DESY HERA 99-04, 123 (1999).

[Ho00a] G. H. Hoffstätter, *Aspects of the Invariant Spin Field for Polarized Protons in HERA*,
Habilitation thesis Darmstadt University of Technology (2000).
Excepted for publication by Springer.

[Ho00b] HERA Accelerator Studies 2000. DESY HERA 00–07. Edited by G. H. Hoffstätter (2000).

[HS85] L. Hand, A. Skuja, DESY HERA 85-18, (1985).
The SPINOR computer code has been updated and modernized by D. P. Barber.

[IRK96] G. Ingelman, A. De Roeck, R. Klanner (eds.), *Future Physics at HERA*,
Proceedings Workshop 1995/1996 (1996).

[Ja98] J. D. Jackson, *Classical Electrodynamics*, 3rd ed. John Wiley and Sons Inc.,
New York, 1998.

[Ja94] F. James, MINUIT, CERN Program Library **D506** (1994).

[Jo83] J. R. Johnson et al., *Nucl. Inst. Meth.*, **204**, 261 (1983).

[Ke78] J. Kewisch, Diploma Work, University of Hamburg (1978).
PETROS is a beam optic program in common use at DESY.

[Ke85] J. Kewisch, DESY 85-109 (1985).
J. Kewisch et al., *Phys. Rev. Lett.*, **62**, N^0 4, 419 (1989).

[Li88] T. Limberg, Doctoral Thesis, DESY HERA, 88–14 (1988).

[Le97] S. Y. Lee, *Spin Dynamics and Snakes in Synchrotrons*, World Scientific 1997.

[Ma85] S. R. Mane, DESY Report 85-125, (1985).

[Ma86a] S. R. Mane, *Phys. Rev.*, **A36**, part I, 105 (1986).

[Ma86b] S. R. Mane, *Phys. Rev.*, **A36**, part II, 120 (1986).

[Ma88] S. R. Mane, FNAL Technical Report TM–1515, (1988).

[Ma90] S. R. Mane, *Nucl. Inst. Meth.*, **A292**, 52 (1990).

[Ma92] S. R. Mane, *Nucl. Inst. Meth.*, **A321**, 21 (1992).

[Mo84] B. Montague, *Physics Reports*, **113** (1984).

[MR82a] H. Mais, G. Ripken, DESY Internal Report, DESY M–82–05, (1982).

[MR82b] H. Mais, G. Ripken, DESY Internal Report, DESY M–82–17, (1982).

[MR83] H. Mais, G. Ripken, DESY Report 83–062, (1983).

[Ne55] J. von Neumann, *Mathematical Foundations of Quantum Mechanics*,
Princeton University Press, 1955.

[Ne90] D. Newton, H1 Internal Report, H1-8/90-143, (1990).

[pp99] Proceedings of the Workshop on Polarized Protons at High Energies —
Accelerator Challenges and Physics Opportunities, DESY May 1999.
DESY–PROC–1999–03.

[Pr92] W. H. Press, S. A. Teukolsky, W. T. Vetterling, B. P. Flannery
Numerical Recipes in FORTRAN, The Art of Scientific Computing,
Second Edition, Cambridge University Press, 1992.

[PZ00] C. Pascaud, F. Zomer, Polarization Notes, unpublished.

[Ri89] H. Risken, *The Fokker–Planck equation. Methods of solution and applications*,
Springer, 1989.

[RS85] R. Rossmanith, R. Schmidt, *Nucl. Inst. Meth.*, **A236**, 231 (1985).

[RW88] F. Willeke, G. Ripken, DESY Report 88–114, (1988).

[Sa99] *Handbook of Accelerator Physics and Engineering*,
Eds. A. W. Chao and M. Tigner, World Scientific 1999.
Section 4.5.5 by J. Safranek.

[Sc98] U. Schneekloth (ed.), *The HERA luminosity upgrade*,
Technical Report DESY HERA 98–05, (1998).

[ST64] A. A. Sokolov, I. M. Ternov, *Sov. Phys. Dokl.*, **8**, 1203 (1964).

[Th27] L. Thomas, Phil.Mag., Vol. 3, (1927).

[TLK62] I. M. Ternov, Yu. M. Loskutov, L. I. Korovina, *Sov. Phys. JETP*, **14**, 921 (1962).

[VBH98] M. Vogt, D. P. Barber, G. H. Hoffstätter Proceedings of the 13th International Symposium on High Energy Spin Physics (SPIN98), Protvino 1998, World Scientific 1999.
Physical Review Special Topics — Accelerators and Beams, Vol. 2, No 11, (1999).
Also DESY Internal Report, M–98–06G, (1998).

[Vo00] M. Vogt, Doctoral Thesis, DESY–THESIS 2000–054, (2000).

[Yo83] K. Yokoya, *Part. Acc.*, **13**, 85 (1983).

[Yo87] K. Yokoya, *Nucl. Inst. Meth.*, **A258**, 149 (1987).

[Yo92] K. Yokoya, KEK Report 92–6, (1992).
K. Yokoya, DESY Report 99–006, (1999).